MATHEMATICAL MODELLING OF HYDROCORTISONE REPLACEMENT THERAPY

by

ROSEMARY EVANS

A thesis submitted to
The University of Birmingham
for the degree of
DOCTOR OF PHILOSOPHY

School of Mathematics
College of Engineering and Physical Sciences
The University of Birmingham

Metabolism and Systems Science
College of Medicine and Health
The University of Birmingham

February 2025

Abstract

Cortisol is a stress hormone produced by the adrenal glands and is responsible for multiple processes in the body, including regulating blood pressure and sugar and managing the sleep/wake cycle. Adrenal insufficiency is a condition characterised by inadequate production of cortisol resulting in symptoms such as fatigue, weakness, and weight loss.

Hormone replacement therapy attempts to artificially regulate cortisol for patients with adrenal insufficiency, however this treatment is rarely personalised to an individual. In this thesis we develop mathematical models to predict hormone dynamics after the delivery of hydrocortisone (the term for cortisol delivered as a medication). We apply these models to assess differences in cortisol response after two commonly used delivery methods, namely a continuous intravenous infusion regime (CIV), and regular intravenous bolus injections (BIV). We fit these models to published experimental data from an in-patient study.

Driven by the desire to study the most parsimonious model that contains the dominant processes affecting blood cortisol levels, the models consider the substantial role of binding protein in changing cortisol dynamics, as well as its effects on excretion. For simplicity, other metabolic processes and distribution across physiological compartments (such as organs or tissues) are neglected. The resulting models comprise five free parameters common to both delivery modes. Additionally, by exploiting the disparity of time scales in the system we obtain asymptotically reduced models of each delivery mode, involving just four free parameters.

One critically important (but often neglected) aspect of models of this type is the desire to recover unique parameter values upon fitting to experimental data. We assess both the structural and practical identifiability of the derived models, highlighting those parameters which can be reliably inferred and those which cannot. We find that the models are practically identifiable for all model parameters except the binding and unbinding rates.

This limitation is mitigated by the relative lack of sensitivity of cortisol dynamics to the precise value of these rates; instead it is the ratio of binding versus unbinding that governs dynamics. In all cases (except in the addition of significant noise) this ratio is shown to be practically recoverable. We further consider the question of whether low time-resolution measurements of combined concentrations of free and bound circulating cortisol enable model parameters to be uniquely estimated and/or inferred.

Finally, the models are fitted using both frequentist and Bayesian approaches, the latter having the added benefit of providing estimates regarding the uncertainty in the parameters which affect the dynamics. Parameter estimates from fitting the BIV model alone, and both BIV and CIV models simultaneously show good agreement, but differ from fitting only the CIV model. These differences highlight the advantage of integrating data from multiple modes of delivery to extract the dominant mechanisms of cortisol response thereby offering the potential to tailor treatments specific to an individual patient.

ACKNOWLEDGEMENTS

I would like to thank first my PhD supervisors, Dr Meurig Gallagher and Professor David Smith for their invaluable guidance, understanding and patience. I am grateful to the University of Birmingham and the EPSRC DTP grant EP/T517926/1 for funding my studies and providing the space and resources for me to complete this thesis. I would also like to acknowledge the authors of Prete *et al.* for providing the experimental data in this work [1]. This endeavour would not have been possible without my Dad, sisters, grandparents and James. I could not have done it without all those videocalls and the endless cups of tea.

And finally, thanks to my Mum.

CONTENTS

LIST OF FIGURES

CHAPTER 1

INTRODUCTION

Approximately 650–980 thousand people globally suffer from chronic primary adrenal insufficiency, also known as Addison's disease [2]. This condition is characterised by very low natural production of the hormone cortisol, commonly caused by an auto-immune disorder or congenital adrenal hyperplasia, which results in symptoms such as weight loss, muscle weakness and low blood pressure [3]. Patients with adrenal insufficiency are commonly prescribed hormone replacement therapy and receive hydrocortisone, the term for cortisol delivered as a medication. However, current treatment strategies are unable to sufficiently mimic a healthy cortisol rhythm. We develop mathematical models to address this gap by identifying the dominant biological processes that govern cortisol dynamics to tailor treatment strategies to specific patients and situations.

Cortisol is a glucocorticoid that acts upon multiple systems in the body, in particular glucose metabolism and immune system regulation, for example, suppressing inflammation [4, 5]. When the body undergoes a stressor, cortisol is one of the main stress hormones that is readily produced by the adrenal glands to increase energy and regulate blood pressure. The production of cortisol is regulated by the hypothalamic-pituitary-adrenal (HPA) axis.

1.1 The HPA axis

Figure 1.1 shows an overview of the HPA axis [6, 7]. At the start of the process, the hypothalamus releases both corticotropin-releasing hormone (CRH) and arginine vasopressin (AVP). Both, (but predominantly CRH), lead to the stimulation of corticotrophic cells in the anterior pituitary. AVP alone has limited impact on stimulation but assists CRH. Within the pituitary, the corticotrophic cells produce pro-opiomelanocortin which then splits into adrenocorticotropic hormone (ACTH) and other polypeptides. The release of ACTH from the pituitary in turn controls the adrenal cortex of the adrenal glands. ACTH interacts with the adrenal cortex which causes cholesterol within to split and release pregnonolone which in turn causes the adrenal gland to synthesize and release cortisol [4].

Cortisol undergoes a negative feedback loop with the hypothalamus and the pituitary, that is, the increase in cortisol levels inhibits the production of both CRH and ACTH [6]. This feedback causes fluctuations in ACTH and cortisol levels within the blood serum. This also means that patients on long-term steroid treatment can suppress the full HPA system and their endogenous cortisol production for months after administration.

In a healthy individual, cortisol follows a circadian rhythm: production spikes early morning just before waking and then slowly declines over the course of the day before reaching a nadir around midnight [8]. In addition to the circadian rhythm, there are smaller amplitude pulsatile secretions throughout the day. Figure 1.2 shows a schematic of the circadian rhythm of cortisol levels over 24 hours in a healthy individual.

Adrenal insufficiency is categorised into three groups dependent on the source of the problem [9]. Tertiary adrenal insufficiency stems from the top of the HPA axis, in the hypothalamus, where there is an impaired production of CRH or AVP or both. Secondary adrenal insufficiency is from problems in the pituitary, either in a reduced release of CRH or a lack of response from the adrenals. Finally, primary adrenal insufficiency, which will be the focus in this thesis, is a consequence of problems within the adrenal cortex itself.

While in circulation, cortisol binds to corticosteroid binding globulin (CBG) with

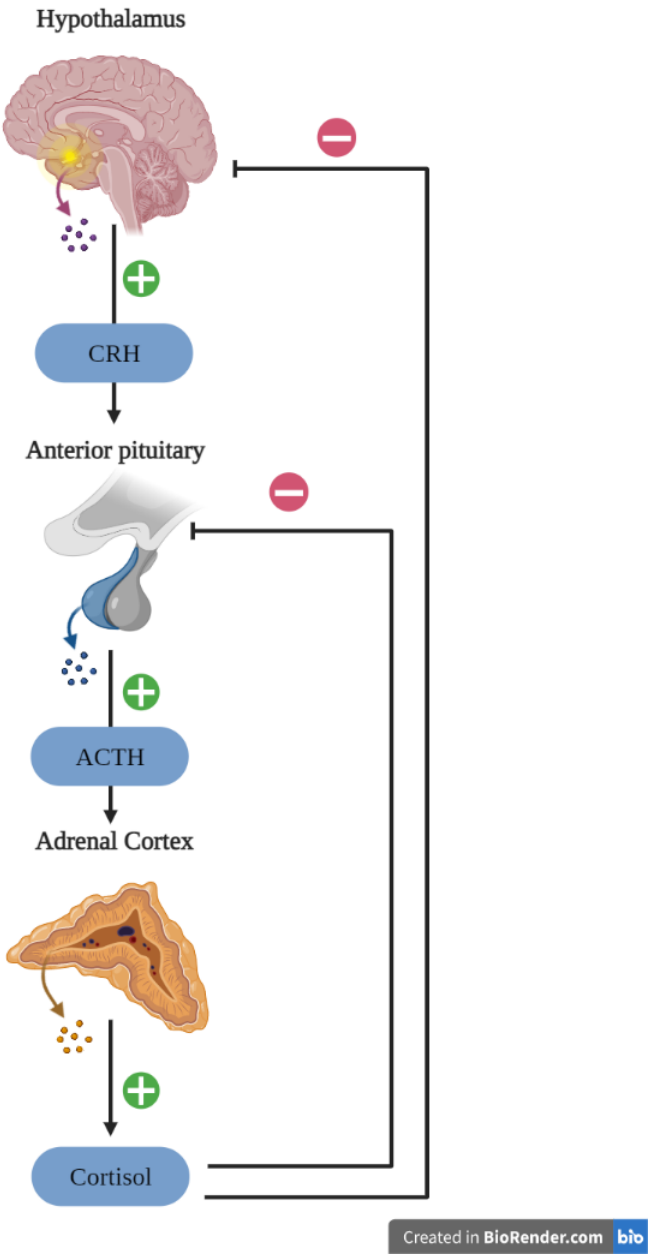

Figure 1.1: The Hypothalamas-Pituitary-Adrenal Axis. The hypothalamus releases corticotropin-releasing hormone (CRH) which stimulates the pituitary to release adrenocorticotropic hormone (ACTH). Finally, this triggers the adrenal cortex to release cortisol. Green circles indicate excitatory effects, while red circles indicate inhibitory effects.

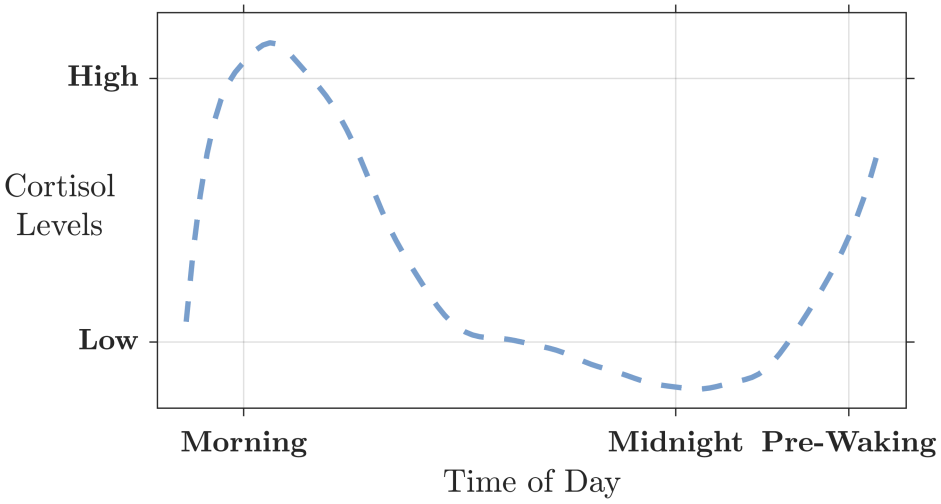

Figure 1.2: Schematic of a healthy cortisol time course. Levels peak in the morning and drop throughout the day, reaching a nadir in the middle of the night and rising again before wakening.

high affinity. Bound cortisol is stored in order to be protected from metabolisation or inactivation by the liver, and to regulate free cortisol levels when needed [10]. It may also bind to albumin at a much lower affinity, however there is a much higher concentration of albumin than CBG. It is commonly reported that approximately 80% of cortisol is bound to CBG and 10-15% is bound to albumin [6, 11, 12].

The levels of CBG and albumin play a significant role when assessing total serum cortisol levels in patients [13]. For example, during and following acute stressors, patients may be misdiagnosed with adrenal insufficiency due to difficulties in measuring total cortisol levels while CBG levels are considerably fluctuating.

Total cortisol is measured using liquid chromatography-tandem mass spectometry (LC-MS-MS) which has improved sensitivity and specificity from previous automated immunoassays [13]. Difficulties in diagnosing adrenal insufficiency can relate to how accurately cortisol can be measured, as cortisol is very structurally similar to other steroids, especially in patients with congenital adrenal hyperplasia or who have been previously treated with synthetic glucocorticoids [14]. The measurement of free cortisol is time-consuming and labour intensive and therefore not regularly used. Estimating free cortisol has been validated in healthy subjects however is yet to be validated with patients

with adrenal insufficiency. It is generally considered that an early morning measure of < 140 nmol/L is an indicator of adrenal insufficiency, however this must be corroborated with high plasma ACTH levels [13].

Hormone models attempt to simulate the biological process of a hormone (such as cortisol) in the human body over time [15]. They have great potential for medical applications, for example to make predictions about treatment regimes, in particular for treating adrenal insufficient patients with hydrocortisone [16].

Several models have been proposed to simulate the functions of the HPA axis, in particular by modelling the negative feedback mechanism of cortisol secretion by inhibiting CRH and ACTH production. Lenbury and Pornsawad (2005) and Bairagi (2008) both utilise delay-differential equations that incorporate a time delay between each stage in the HPA axis [17, 18]. Lenbury and Pornsawad did not consider cortisol inhibiting CRH production directly, but instead modelled a short term feedback loop between the pituitary and hypothalamus. Bairagi simplified the time delays in order to perform bifurcation analysis. Both models considered secretion of the three hormones only, without modelling the complex synthesis of each.

With the aim of avoiding unnecessary clinical trials, we would like to be able to predict the biological response to different dosing regimes by sufficiently mimicking the physiological time course of cortisol levels in healthy patients via pharmacokinetic modelling. As we will discuss, a balance must be drawn between creating more biologically comprehensive models and being able to obtain reliable parameter estimates in order to draw meaningful conclusions. In the following sections, we will explore the current limitations of adrenal insufficiency treatment.

1.2 Current treatment methods for adrenal insufficiency

It is very important to keep patients within a therapeutic range of cortisol levels circulating to avoid adrenal crisis. The main method of treatment for patients with primary adrenal insufficiency is glucocorticoid replacement. Hydrocortisone is a corticosteroid and is one of the most commonly prescribed hormone replacements for cortisol. It is particularly necessary to anticipate when patients may require higher doses of hydrocortisone if they undergo additional stressors such as a trauma or another illness as they are more likely to contract an infection [19].

Currently, dosing regimes are unable to closely mimic the normal physiological cortisol profile, mainly due to the immediate-release nature of hydrocortisone tablets, i.e., the dose reaches the blood stream very quickly, meaning patients have initially high levels of cortisol that decline rapidly after a dose, whereas the natural profile has a slow decline over the course of the day after an initial peak in the morning. Subsequently, patients are often given higher doses to keep levels up throughout the day which over long-term use can cause glucocorticoid excess, leading to reduced quality of life and increased morbidity and mortality such as cardiovascular disease [20, 21, 22].

Several studies have aimed to recreate the physiological cortisol profile of a healthy patient using novel drug treatments. One such method is a dual-release hydrocortisone tablet that has an immediate release coating when administered in the morning, with a delayed release core that slowly doses the patient through the day [21]. By eliminating the need for multiple dosing in a day, there is reduced spiking of cortisol levels and improved patient compliance. Compared to the conventional method of thrice-daily dosing, the dual-release method was able to replicate the natural circadian rhythm more accurately. The method had additional positive outcomes such as better quality of life factors and cardiovascular risk, in particular, improved general well-being, less fatigue and weight loss. However, a key part of the healthy circadian rhythm is the sharp increase before waking and this drug is unable to replicate this spike.

Chronocort® is a drug that was formulated in 2009 in an attempt to recreate this pre-wakening increase, where the tablet is taken just before going to sleep with a delayed release overnight so that serum levels rise just before waking [20, 23, 24]. All but one side of the tablets are insoluble, with the remaining side slowly eroding over approximately 8 hours. The dosing regime suggested is taking a large dose in the late evening with a smaller dose in the morning so that the patient's serum levels do not drop below the therapeutic range in the afternoon.

Debono *et al.* (2009) compared a modified release tablet against standard immediate release in 28 healthy volunteers [20]. In order to suppress their natural cortisol secretion during the study, the patients were administered with dexamethasone. Over several weeks, patients received various dose types and dosages which showed that *Chronocort*® was much better able to replicate the natural cortisol profile than the immediate release tablets. The second study tested 16 congenital adrenal hyperplasia patients over a 6-month period with 24-hour blood sampling every 2 months [24]. Patients who received a lower dose than the equivalent standard hydrocortisone treatment had the same efficacy in controlling their congenital adrenal hyperplasia, with the added benefit of reduced glucocorticoid excess. More research is still to be done into the long term effects of *Chronocort*®. It is also of note that effective treatment heavily relies on patient compliance, which is likely to be much higher within the environment of a clinical trial (evaluated by number of tablets returned during patient visits).

1.3 Identifiability analysis

The complexity of the biological process we are attempting to model gives rise to the issue of identifiability, that is, to create a model that reliably admits parameter values upon fitting to data. We aim to strike a balance between creating a more biologically comprehensive model whilst retaining the ability to find reliable parameter estimates in order to draw meaningful conclusions. Ideally, we would like to be able to observe every

step of the physical process; in reality, we are often limited to a number of measurable variables. If we increase the complexity of a model, 'unobservable' variables (those that we do not measure) are introduced along with unknown parameters. Identifiability analysis assesses whether the values of these parameters can be determined both accurately and uniquely [25]. Conclusions drawn from unidentifiable parameters could lead to misleading model predictions as multiple sets of parameters could fit the data equally well [26, 27]. There are various applications of identifiability analysis both within pharmacokinetics and other topics, ranging from systems biology to computer networks [28, 29, 30, 31, 32].

A model is considered to be identifiable if it is theoretically possible to extract the true values of model parameters from sufficient data [33]. In other words, if there are multiple possible sets of parameters that fit the data equally well, the conclusions drawn from the estimates could result in misleading model predictions.

Three methods of assessing structural identifiability are considered here, which is whether model parameters can be uniquely inferred from the model output given unlimited, perfect data observations. These methods are the Laplace Transform approach proposed by Bellman and Åström [34], the Taylor Series approach proposed by Pohjanpalo [35] and an extended observability method proposed by Villaverde *et al.* [36]. Structural identifiability methods in general either analyse the model outputs (such as the Taylor Series Method), the system map (such as looking at extended observability) or a mixture of the two [37].

We begin by formally defining parameter identifiability.

1.3.1 Formal definition

Consider a generalised ODE system of the form,

$$\frac{d\boldsymbol{x}}{dt} = \boldsymbol{f}(t, \boldsymbol{x}; \boldsymbol{\theta}), \tag{1.1}$$

$$\boldsymbol{y} = \boldsymbol{g}(t, \boldsymbol{x}; \boldsymbol{\theta}), \tag{1.2}$$

for $t \in [0, T]$, where $\boldsymbol{x}$ denotes the vector of state variables and $\boldsymbol{\theta}$ denotes the model parameter vector of the system. The observed variables, $\boldsymbol{y}$, are functions of the state variables and model parameters to define some measurable output.

To satisfy structural identifiability, a model must act as a bijection that transforms the parameter space and projection of solution space onto the observables. Formally,

- A system is **structurally globally identifiable** (**SGI**) if there exists a function $\boldsymbol{y} \to \boldsymbol{\theta}$. That is, the set of observable variables uniquely determines all of the corresponding model parameters.

- A system is **structurally locally identifiable** (**SLI**) if the mapping $\boldsymbol{\theta} \to \boldsymbol{y}$ is invertible on some neighbourhood of $\boldsymbol{\theta}$. If a system is SLI but not SGI then for some $\boldsymbol{\theta}$ there exists at least one other $\boldsymbol{\theta}^* \neq \boldsymbol{\theta}$ such that both $\boldsymbol{\theta}^*$ and $\boldsymbol{\theta}$ map to the same observed solution, but there are also neighbourhoods around each such $\boldsymbol{\theta}$ on which the mapping is invertible. Informally, there may be multiple discrete points within parameter space that map the state variables to the same observed solution.

- A system is **unidentifiable** if no such neighbourhood exists.

1.3.2 Laplace transform approach

In this section, we outline the Laplace Transform method of assessing structural identifiability in linear systems which was initially proposed by Bellman and Åström in 1970 [34].

Taking a Laplace transform of each of the observed variables allows for each variable to be expressed in terms of a set of rational functions. Each of these functions is written in terms of the model parameters resulting in a set of simultaneous equations that we wish to solve for the model parameters. Conclusions can then be drawn about the structural identifiability of each parameter based on the form of the solutions in terms of the rational functions. To illustrate the method and some preliminary types of indeterminacy, we consider four toy examples in appendix A.1 and discuss the limitations here.

The Laplace transform method of assessing structural identifiability is relatively uncomplicated as converting the system to a set of rational functions is straightforward [38], although this process can quickly become heavily labour-intensive depending on the size of the model and the number of observed variables. It can be unclear how the structural identifiability of a model may be changed after making modifications. Small changes may require the entire transformation and analysis to be repeated. As a result, it is difficult to draw conclusions about similar models from one example. Nevertheless, several models have been assessed using this method as can be seen in Refs. [15, 33, 38]. Another significant limitation is that it can be only applied to linear systems. Several of the models we consider in this thesis will be non-linear, and therefore other approaches are needed.

1.3.3 Taylor series approach

The first method for assessing structural identifiability in both linear and non-linear models was proposed by Pohjanpalo in 1978 [35]. The approach is based on the assumption that the measured vector (later referred to as observable states) are unique functions of time and so the coefficients of their respective expansions are also unique for a particular output. Assuming that the observable variables are infinitely differentiable, we can expand, e.g., around $t = 0$,

$$y_i(t, \boldsymbol{\theta}) = y_i(0, \boldsymbol{\theta}) + \frac{dy_i}{dt}(0, \boldsymbol{\theta})t + \cdots + \frac{d^j y_i}{dt^j}(0, \boldsymbol{j})(0, \boldsymbol{\theta})\frac{t^k}{j!} + \cdots , \tag{1.3}$$

where the coefficients yield a set of algebraic equations which we wish to solve for the original model parameters. If there is a unique solution, then the system is SGI; if there are a countable number of solutions then the system is SLI and if there are an uncountable number of solutions then the system is unidentifiable.

Pohjanpola applied this method to pharmacokinetic models with two types of saturation (Michaelis–Menten and Langmuir) in an effort to reduce the number of *in vivo* experiments needed to give estimates of different saturation parameters. The method

has also been used to assess structural identifiability in models of ship steering dynamics, microbial growth and glucose-insulin dynamics [39, 40].

In 1997, the method was extended by Gunn, Chappell and Cunningham [41] to suggest reparameterisation for unidentifiable systems. By combining the taylor series with a rank test, the methodology aimed to find possible (non-unique) reparameterisations in order to make a model locally identifiable. However, this method was limited by the varying complexity between models and reparameterisations were often only found by inspection. We consider several toy examples in appendix A.2 and discuss the limitations here.

One difficulty associated with the Taylor Series method is estimating how many coefficients will be needed to assess identifiability, with the complexity of the coefficients and therefore the algebraic equations increasing at each step. For a linear model, the maximum number of derivatives needed to prove identifiability is $2n_x - 1$, where n_x is the number of state variables [42]. However, there is currently no known upper bound for the number of derivatives needed to exhaust all possibility of identifiability in a nonlinear model. The complexity of the coefficients also quickly increases with successive differentiation, which means that local identifiability can often be easier to ascertain than global [38].

More recently, the software package SIAN (Structural Identifiability ANalyser) has been developed to address the lack of upper bound for general non-linear systems by incorporating a termination criteria based on differential algebra approaches [43, 44].

1.3.4 Extended observability

Observability means that all the model state variables are determinable from the observed outputs. We consider a method put forward by Villaverde *et al.* [25, 36, 45] that extends observability in order to assess identifiability.

The system is successively differentiated with respect to an augmented vector containing each state and parameter to create a matrix of partial derivatives. When the system is nonlinear, this matrix is constructed using Lie derivatives. The rank of the matrix is

then symbolically calculated and identifiability determined, where full rank corresponds to the model being structurally identifiable.

The method works by defining an observability-identifiability matrix, which creates a mapping from the state variables to the model output and its derivatives [25],

$$\mathcal{O}_I(\tilde{\boldsymbol{x}}) = \begin{pmatrix} \frac{\partial}{\partial \tilde{\boldsymbol{x}}} \boldsymbol{y}(\tilde{\boldsymbol{x}}, t) \\ \frac{\partial}{\partial \tilde{\boldsymbol{x}}} \left(\frac{d}{dt} \boldsymbol{y}(\tilde{\boldsymbol{x}}, t) \right) \\ \frac{\partial}{\partial \tilde{\boldsymbol{x}}} \left(\frac{d^2}{dt^2} \boldsymbol{y}(\tilde{\boldsymbol{x}}, t) \right) \\ \vdots \\ \frac{\partial}{\partial \tilde{\boldsymbol{x}}} \left(\frac{d^{(n+q-1)}}{dt^{(n+q-1)}} \boldsymbol{y}(\tilde{\boldsymbol{x}}, t) \right) \end{pmatrix}. \tag{1.4}$$

Here, $\tilde{\boldsymbol{x}}$ is an augmented state variable vector consisting of all state variables and model parameters in the system; n is the number of state variables and q is the number of model parameters.

For nonlinear systems, the matrix of partial derivatives is constructed instead using Lie derivatives [45], which are defined in this instance as:

$$L_{\boldsymbol{f}} \boldsymbol{g}(\boldsymbol{x}) = \frac{\partial \boldsymbol{g}(\boldsymbol{x})}{\partial \boldsymbol{x}} \boldsymbol{f}(\boldsymbol{x}, \boldsymbol{u}), \tag{1.5}$$

where $\boldsymbol{f} = \dot{\boldsymbol{x}}$, $\boldsymbol{g} = \boldsymbol{y}$ and $\boldsymbol{u}$ is the input. The observability-identifiability matrix now becomes:

$$\mathcal{O}_I(\tilde{\boldsymbol{x}}) = \begin{pmatrix} \frac{\partial}{\partial \tilde{\boldsymbol{x}}} \boldsymbol{g}(\tilde{\boldsymbol{x}}) \\ \frac{\partial}{\partial \tilde{\boldsymbol{x}}} L_{\tilde{\boldsymbol{f}}} \boldsymbol{g}(\tilde{\boldsymbol{x}}) \\ \frac{\partial}{\partial \tilde{\boldsymbol{x}}} L^2_{\tilde{\boldsymbol{f}}} \boldsymbol{g}(\tilde{\boldsymbol{x}}) \\ \vdots \\ \frac{\partial}{\partial \tilde{\boldsymbol{x}}} L^{n+q-1}_{\tilde{\boldsymbol{f}}} \boldsymbol{g}(\tilde{\boldsymbol{x}}) \end{pmatrix}, \tag{1.6}$$

where,

$$\tilde{\boldsymbol{f}} = \begin{pmatrix} \boldsymbol{f}(\boldsymbol{x}, \boldsymbol{u}) \\ \mathbf{0}^{q\times 1} \end{pmatrix}. \tag{1.7}$$

In order to analyse more complex biological system models, the publicly accessible software STRIKE_GOLDD (STRuctural Identifiability taKen as Extended-Generalized Observability with Lie Derivatives and Decomposition) is able to calculate the observability-identifiability matrix symbolically in MATLAB to determine local identifiability [36]. After each successive row of the observability-identifiability matrix is computed, the software symbolically calculates the rank of the matrix. If it has full rank, the algorithm concludes. Otherwise, it systematically removes each column and recalculates the rank. Each column corresponds to the partial derivatives of the observables with respect to each parameter, if the removal of one column reduces the matrix rank, then the corresponding parameter for that column from the augmented vector is identifiable at that stage. If removing a column does not reduce the rank, then the corresponding parameter is unidentifiable.

Due to the computational complexity of symbolically calculating Lie derivatives and ranks, particularly for models with large numbers of unknown parameters and few observables, Villaverde *et al.* calculated a minimum number of derivatives needed to achieve full rank [36]:

$$n_d = \left\lceil \frac{n+q}{m} \right\rceil - 1. \tag{1.8}$$

Instead of calculating the rank at each level like in the linear case, for nonlinear models STRIKE_GOLDD only calculates the rank after at least n_d have been found. Then, if full rank is not achieved, the next Lie derivative is computed and the rank determined until full rank is achieved or $n + q - 1$ derivatives have been calculated. We consider several toy examples in appendix A.3 and discuss the limitations here.

Due to the rapidly increasing complexity of coefficients generated for successive deriva-

tives, STRIKE_GOLDD may still face difficulty when large numbers of coefficients are needed. However, for smaller models it can be a swift way of determining identifiability and it is a useful tool for reducing the likelihood of human error in calculating coefficients. One limitation is that the outcome does not provide any insight into how certain parameters could be intertwined like the Laplace transform method, however an additional feature called "AutoRepar" was added in 2021 that suggests possible reparameterisations for unidentifiable models [46]. This method also only specifies local identifiability, compared to the Taylor series method which allows global identifiability to be ascertained.

Table A.1 shows a summary of the outcomes of the toy problems using the different identifiability analysis methods. In general, it is difficult to anticipate which method is most appropriate for a particular model, and it is therefore best practice to have several methods available. In this thesis, we will find that some of the non-linear models considered can be analysed using the Taylor Series method, but as the model complexity increases then the extended observability method is required.

In our drive to create identifiable models we must not lose sight of the complexity of biological realities. It is essential that we include sufficient information to capture the physiological detail.

1.4 Experimental data underpinning this thesis

The direct motivation for this thesis comes from the published data of Prete *et al.* [1]. The study investigated the influence of stressors, such as trauma or surgery, on blood cortisol levels. A pharmacokinetic study was conducted over a 4-week period on 10 patients; 9 with primary adrenal insufficiency and 1 with adrenoleukodystrophy (a genetic disease affecting the X chromosome).

We will briefly recap the study here. The patients were divided into 4 groups and each received 200 mg of hydrocortisone over 24 hours via one of the following delivery modes (abbreviations ours):

- CIV - Continuous intravenous infusion at a constant rate over 24 hours,
- BIV - 4 doses of 50 mg every 6 hours via intravenous bolus,
- IM - 4 doses of 50 mg every 6 hours via intramuscular bolus,
- OT - 4 doses via 50 mg oral tablets every 6 hours.

Blood samples were collected from patients at 30-minute intervals for two hours after each dosing times and hourly otherwise. This was repeated each week for 4 weeks so that each patient received each method of delivery in a randomised order. Figure 1.3 shows the serum cortisol levels for the continuous infusion, intravenous bolus, intramuscular and oral tablet data. From here, we will refer to this data set as [PD]. In this work, we choose to focus on the CIV and BIV delivery modes as they elicit metabolic responses to two very different rates of dosing, without the complication of accounting for absorption from oral or intramuscular compartments.

1.5 Thesis outline

Mathematical modelling allows predictions to be made, e.g., deciding on the best regime of treatment to keep individual patients in a therapeutic range. If the dose is too high for long time periods, patients may start to suffer other symptoms due to excess glucocorticoid levels; if the dose is too low the patients may experience adrenal crisis. In particular, we would like to consider whether measurements from one dosing regime in a patient could be used to predict the response to another dosing regime or dosing amount. Additionally, can an optimum dosing regime be estimated for a particular patient based on certain characteristics, for example the physiological level of binding protein or cortisol clearance rate?

One difficulty we can anticipate is in parameter estimation. The data are quite noisy and the sampling frequency (every 30 minutes to an hour) is significantly slower than some of the dynamics of the system, for example around the peaks in the BIV data in

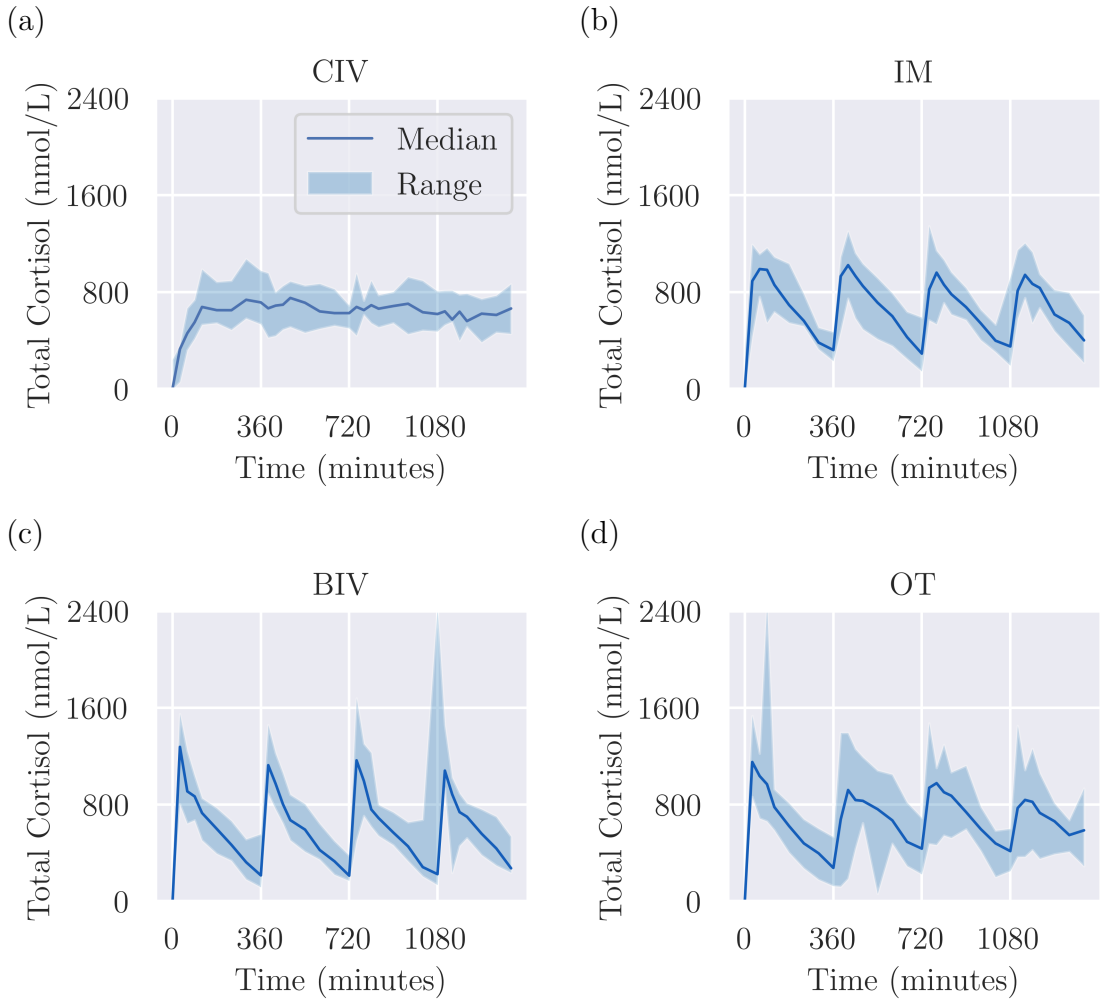

Figure 1.3: Serum cortisol levels over a 24–hour period for four modes of administration. Figures reproduced using data from [1] (CC BY 4.0).

Figure 1.3(c). There is a 30–minute gap in measurement from when the patient receives a dose to the next blood sample which creates difficulty in accurately predicting the dynamics in this interval; cortisol levels could have gently risen or sharply increased and already begun decreasing by the time of the next blood sample. Wearable technology would be able to measure a patient's total concentration levels more frequently than data [PD], and it would be beneficial to ascertain whether this increased time-resolution would aid parameter inference. Further, we study whether there are any parameters or parameter groupings that the model is insensitive to and if so, do they hold physiological importance or can they be eliminated from the model?

Statistical inference allows us to investigate two issues that relate to this problem.

Firstly, given an unlimited amount of perfect data observations, is it theoretically possible to infer unique parameter values? This corresponds to an optimisation problem whereby we want to assess whether there is a global minimum of the sum squared residual between data and model. Secondly, we aim to quantify uncertainty in parameter estimates due to imperfect data, either through low time-resolution or inaccurate measurements. Alternatively, both issues can be studied through Bayesian inference, which generates samples of the probability distributions of the parameters given the data. This method is preferable for incomplete data sets and enables prior information to be taken into account if needed [47].

In this work we will develop mathematical models for cortisol dynamics under each of CIV (Chapter 2) and BIV (Chapter 3) dosing regimes. Further, for each regime we will construct asymptotically reduced models (sections 2.5 and 3.5) which in some cases will give rise to exact solutions, and in others allow for systems of coupled differential equations to be reduced to single ODE systems. For each system, we will assess the practical identifiability by generating synthetic data and considering which model parameters can be uniquely inferred. We will combine both mathematical models of the uptake, metabolism and excretion of externally-administered hormones and approaches to parameter inference, both statistically and structurally. Some discussion of how the mathematical models could be adapted to account for the other two delivery modes (intramuscular and oral tablets) is included in appendix E. We then consider Bayesian inference (Chapter 4) to quantify the uncertainty of parameter estimates under both dosing regimes to investigate the impact of varying time-resolution, varying noise levels and prior knowledge of parameter values within the models. We begin by modelling the simplest case, that of continuous infusion of hydrocortisone.

CHAPTER 2

CONTINUOUS INTRAVENOUS INFUSION

We consider an idealised one-compartment model to replicate intravenous delivery of hydrocortisone (Figure 2.1), modelling hydrocortisone as free serum cortisol (F_f) entering and circulating blood at a rate $q(t)$. The dose is treated as an input to the model, (which we denote by the function $q(t)$) that can be chosen to replicate the delivery mode of the hydrocortisone. For the continuous infusion case considered in this chapter, we model a constant rate of dosing, i.e. $q(t) = q$. We aim to replicate the conditions of the [PD] study wherein infusion occurs at a constant rate of 200 mg over 24 hours. This dose is divided by a dilution factor, α, to account for the blood volume.

Once in the blood, we model two dominant processes involving free cortisol which are outlined below; and neglect the (relatively) less dominant interconversion with cortisone, absorption by tissue and other metabolic processes.

Firstly, free cortisol can bind with corticosteroid binding globulin (CBG) or albumin to become bound cortisol, denoted by F_b. We denote concentrations of unoccupied protein collectively by B and binding and unbinding rates as k_{fb} and k_{bf} respectively.

Secondly, free cortisol can be removed from the system at rate k_{re}. We consider removal to represent excretion via the first pass effect to the liver or kidney and neglect the interconversion to cortisone as levels of cortisone are relatively small in comparison to cortisol. Within the removal term we also include transfer into peripheral compartments, such as absorption into muscle and adipose tissue. We additionally choose to neglect

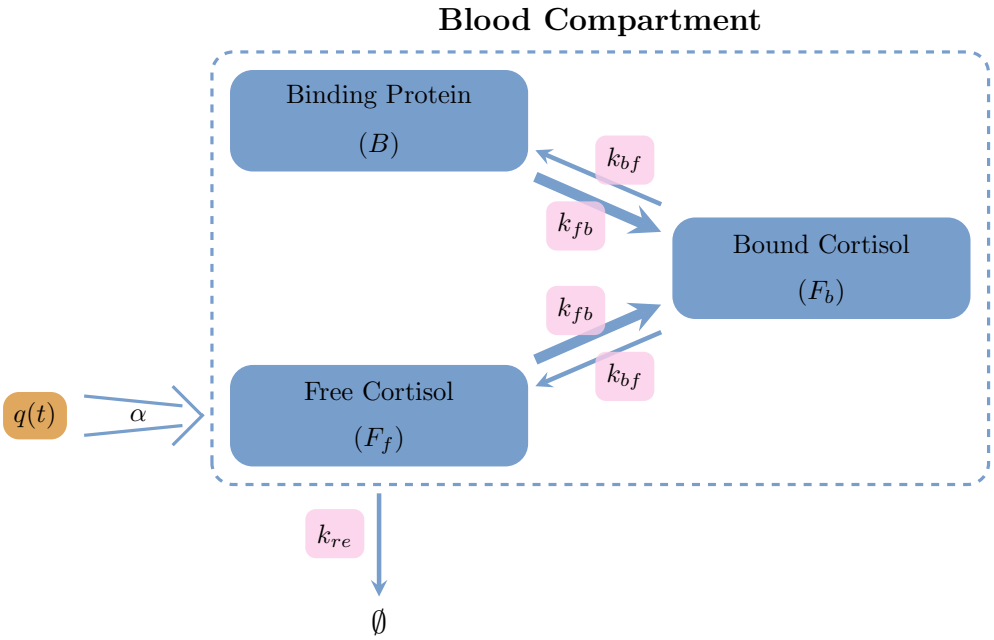

Figure 2.1: One-compartment model schematic.

removal of any binding protein or bound cortisol.

These modelling choices give rise to the following system of ordinary differential equations,

$$\frac{dF_f}{dt} = \frac{1}{\alpha}q - k_{fb}F_f B + k_{bf}F_b - k_{re}F_f, \tag{2.1}$$

$$\frac{dB}{dt} = \quad - k_{fb}F_f B + k_{bf}F_b, \tag{2.2}$$

$$\frac{dF_b}{dt} = \quad + k_{fb}F_f B - k_{bf}F_b, \tag{2.3}$$

with initial conditions $F_f(0) = F_b(0) = 0, B(0) = B_0$. In patients with adrenal insufficiency it is reasonable to assume that their cortisol levels will be extremely low compared to the input of hydrocortisone (the usual level for adrenal insufficient patients in the morning is $< 80\,\text{nmol/L}$ [48], which matches the beginning of the [PD] dosing period)[1]. We take the initial value of B to be B_0, the physiological level of binding protein. Assuming that binding protein is conserved, we are able to reduce the model to two variables, from which F_b can then be determined. We are left with a pair of ODEs with five unknown

[1]In section 2.6, we will incorporate a small initial value of cortisol into the model.

parameters,

$$\frac{dF_f}{dt} = \frac{1}{\alpha}q(t) - k_{fb}F_f B + k_{bf}(B_0 - B) - k_{re}F_f, \tag{2.4}$$

$$\frac{dB}{dt} = \quad - k_{fb}F_f B + k_{bf}(B_0 - B), \tag{2.5}$$

which from here on we will refer to as the CIV$^+$ model. The data [PD] measures total cortisol, $F(t)$, which is the sum of free and bound cortisol, hence:

$$F = F_f + F_b = F_f + (B_0 - B). \tag{2.6}$$

We investigate whether the proposed model above is structurally identifiable before attempting to fit model parameters to data [PD]. That is, we review whether it is theoretically possible to find unique parameter values if matching to perfect data.

2.1 Identifiability of the one-compartment CIV$^+$ model

In order to assess identifiability for the full continuous infusion model described by eqs. (2.4) and (2.5), we employ the Taylor series method. The model requires at least 5 independent coefficients to determine identifiability which we choose to evaluate using Maple. The first coefficient is simply the observed variable evaluated at $t = 0$:

$$F(0) = 0, \tag{2.7}$$

which provides no information on our model parameters. We calculate the next two coefficients,

$$\Phi_1 = \left.\frac{dF}{dt}\right|_{t=0} = \frac{1}{\alpha}q, \tag{2.8}$$

$$\Phi_2 = \left.\frac{d^2F}{dt^2}\right|_{t=0} = -\frac{1}{\alpha}k_{re}q. \tag{2.9}$$

The input dosing rate q is known and therefore from these two coefficients we conclude that both α and k_{re} are globally identifiable. Calculating the next 3 coefficients,

$$\Phi_3 = \left.\frac{d^3F}{dt^3}\right|_{t=0} = \frac{1}{\alpha}k_{re}q(B_0k_{fb} + k_{re}), \tag{2.10}$$

$$\Phi_4 = \left.\frac{d^4F}{dt^4}\right|_{t=0} = -\frac{1}{\alpha}k_{re}q((B_0k_{fb} + k_{re})^2 + B_0k_{fb}k_{bf}), \tag{2.11}$$

$$\Phi_5 = \left.\frac{d^5F}{dt^5}\right|_{t=0} = \frac{1}{\alpha^2}k_{re}q(\alpha(B_0k_{fb} + k_{re})^3 + \alpha B_0k_{fb}k_{bf}(2(B_0k_{fb} + k_{re}) + k_{bf}) + 3qB_0k_{fb}^2). \tag{2.12}$$

From eq. (2.10) we find the product B_0k_{fb} is identifiable. Thus, we determine from eqs. (2.11) and (2.12) that k_{bf} and k_{fb} respectively are globally identifiable and therefore B_0 is also globally identifiable. Expressing each of the model parameters in terms of the rational functions $\mathbf{\Phi} = [\Phi_1, \Phi_2, \Phi_3, \Phi_4, \Phi_5]$,

$$\alpha = \frac{q}{\Phi_1}, \tag{2.13}$$

$$k_{fb} = -\frac{(\Phi_1\Phi_3\Phi_5 - \Phi_1\Phi_4^2 - \Phi_2^2\Phi_5 + 2\Phi_2\Phi_3\Phi_4 - \Phi_3^3)}{3(\Phi_1^2\Phi_3^2 - 2\Phi_1\Phi_2^2\Phi_3 + \Phi_2^4)}, \tag{2.14}$$

$$k_{bf} = -\frac{\Phi_1(\Phi_2\Phi_4 - \Phi_3^2)}{\Phi_2(\Phi_1\Phi_3 - \Phi_2^2)}, \tag{2.15}$$

$$B_0 = \frac{3(\Phi_1^3\Phi_3^3 - 3\Phi_1^2\Phi_2^2\Phi_3^2 + 3\Phi_1\Phi_2^4\Phi_3 - \Phi_2^6)}{\Phi_1\Phi_2(\Phi_1\Phi_3\Phi_5 - \Phi_1\Phi_4^2 - \Phi_2^2\Phi_5 + 2\Phi_2\Phi_3\Phi_4 - \Phi_3^3)}, \tag{2.16}$$

$$k_{re} = -\frac{\Phi_2}{\Phi_1}. \tag{2.17}$$

As all of the parameters are structurally globally identifiable, we conclude that the model is structurally globally identifiable. We note here that this does not guarantee that pa-

rameter values are identifiable for low time-resolution, noisy data.

We confirm this result using STRIKE_GOLDD, calculating 6 Lie derivatives to build the corresponding observability-identifiability matrix [36, 45]. For this relatively small model, the software is able to build this matrix and determine the rank swiftly (execution time $\approx 0.5\,\mathrm{s}$) and concludes that all parameters are locally identifiable.

2.2 Non-dimensionalisation of the CIV$^+$ model

Now we consider physically reasonable values for each of the model parameters in the system, summarised in Table 2.1. These parameter values will guide the choice of dimensionless parameter groupings when we nondimensionalise the system. These parameter values will also allow us to test the practical identifiability of the model under varying noise and time-resolution of synthetic data within physically reasonable bounds. Approximations for the binding and unbinding rate parameters, k_{fb} and k_{bf} respectively, and the physiological level of binding protein, B_0, are taken from relevant literature [49, 50]. The dilution factor α and free cortisol removal rate k_{re} are estimated as follows:

1. α - dilution factor

   We estimate α to be roughly $55\,\mathrm{L}$ - taking body weight to be $65\,\mathrm{kg}$ minus bone weight of approximately $10\,\mathrm{kg}$.

2. k_{re} - free cortisol removal rate

   We can approximate the value of k_{re} based upon an estimate of the steady state value in the [PD] CIV data. We have:

   $$F_f^* = \frac{q}{\alpha k_{re}} \approx 700, \tag{2.18}$$

   which gives an estimate of $k_{re} \approx 0.01\,\mathrm{min}^{-1}$.

Table 2.1: Guide Model Parameters

Parameter	Description	Value	Reference
α	Blood dilution factor	$55\,\mathrm{L}$	-
k_{fb}	Binding rate	$0.1\,\mathrm{L\,nmol^{-1}\,min^{-1}}$	[49]
k_{bf}	Unbinding rate	$1\,\mathrm{min^{-1}}$	[49]
B_0	Physiological level of binding protein	$650\,\mathrm{nmol\,L^{-1}}$	[50]
k_{re}	Removal rate	$0.01\,\mathrm{min^{-1}}$	-

We assume that binding and unbinding of free cortisol to CBG occurs much faster than the dosing and removal of free cortisol. Considering the steady state solution, we define the following parameter grouping,

$$F_f^{ss} := \frac{q}{\alpha k_{re}}. \tag{2.19}$$

Dimensionless variables are introduced as,

$$F_f = B_0 F_f', \qquad B = B_0 B', \qquad t = \frac{\alpha B_0}{q} t', \tag{2.20}$$

where F_f and B are scaled with the physiological level of unoccupied binding protein, B_0, and the time scaling is chosen based on the dosing term. Finally, we define the dimensionless parameter groupings,

$$\delta = \frac{k_{bf}}{k_{fb} B_0}, \qquad \beta = \frac{\alpha k_{bf}^2}{q k_{fb}}, \qquad \rho = \frac{B_0}{F_f^{ss}}, \tag{2.21}$$

where δ is a small parameter quantifying the proportion of free to bound cortisol, ρ is an $\mathcal{O}(1)$ parameter group that quantifies the proportion of unoccupied binding protein to the amount of free cortisol being dosed (diluted), and β is an $\mathcal{O}(1)$ parameter group. Substituting these scalings into the system described by eqs. (2.4) and (2.5) yields the

dimensionless system,

$$\frac{dF'_f}{dt'} = 1 - \frac{\beta}{\delta^2}F'_f B' + \frac{\beta}{\delta}(1 - B') - \rho F'_f, \tag{2.22}$$

$$\frac{dB'}{dt'} = \quad - \frac{\beta}{\delta^2}F'_f B' + \frac{\beta}{\delta}(1 - B'). \tag{2.23}$$

We can now consider the numerical solution of system (2.22)-(2.23) within physically appropriate parameter ranges. Changes in model trajectories will reveal which parameters the model is sensitive to, and their relative importance when it comes to data fitting. If the model is insensitive to specific parameters, this may indicate practical identifiability issues and lead to difficulties in parameter fitting.

2.3 Simulating cortisol response under continuous intravenous infusion

The evolution of total cortisol concentration in the blood depends on the treatment dose together with the choice of model parameters. Returning to the dimensional model, in what follows we assess the dynamics of the full paired ODE model given by eqs. (2.4) and (2.5) when varying individual, and later pairs of, model parameters in turn.

We begin by considering the trajectory of total cortisol concentration when varying α, the dilution factor. A larger value of α results in a lower concentration of total cortisol and a longer time to reach equilibrium (see Figure 2.2(a)), which is expected as a larger α corresponds to increased dilution. Similarly, when varying α and considering the area under the curve (AUC) of total cortisol concentration over a 24-hour period, we see an almost linear decrease with increasing α (see Figure 2.3(a)). The small change in derivative as α approaches 10^3 corresponds to the total cortisol concentration level no longer reaching an equilibrium within the 24-hour period, that is, the inputted free cortisol never saturates the available binding protein.

The behaviour of the total cortisol concentration over varying k_{re}, which is the rate

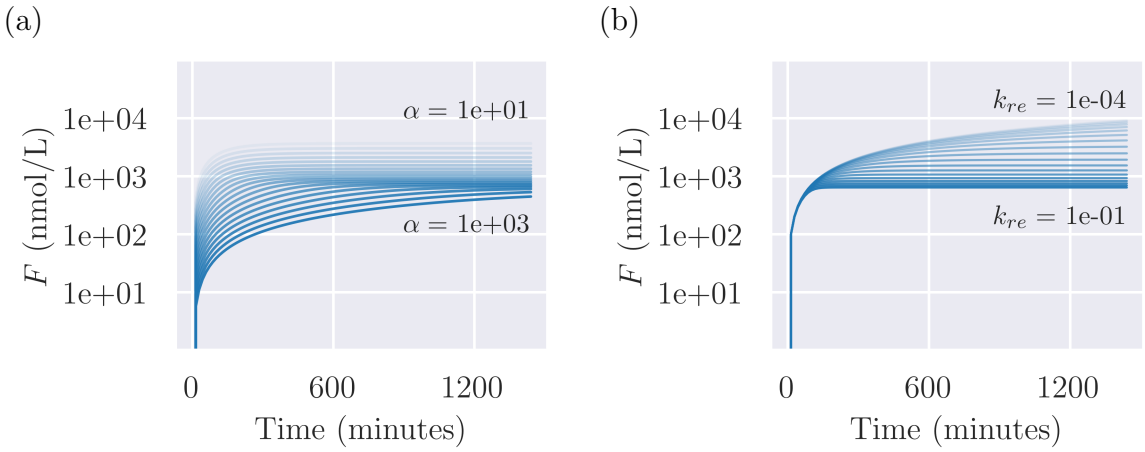

Figure 2.2: Evolution of total cortisol concentration, F, in time when varying model parameters for the CIV$^+$ model given by eqs. (2.4) and (2.5). Fixed values of parameters: $\alpha = 55\,\mathrm{L}$, $k_{fb} = 0.1\,\mathrm{L\,nmol^{-1}\,min^{-1}}$, $k_{bf} = 1\,\mathrm{min^{-1}}$, $B_0 = 650\,\mathrm{nmol\,L^{-1}}$, $k_{re} = 0.01\,\mathrm{min^{-1}}$: (a) varying dilution factor α, (b) varying rate of removal of free cortisol k_{re}.

of removal of free cortisol, shows that a smaller value of k_{re} means a longer time taken to reach equilibrium, which we see reflected in Figure 2.2(b) as k_{re} ranges from 10^{-4} to 10^{-1}. There is a similar relationship between AUC and k_{re} as there was for α, with a larger value of k_{re} leading to a smaller AUC (Figure 2.3(b)). When k_{re} is smaller than 10^{-3}, the AUC begins to flatten indicating the point at which there is effectively no removal.

We now consider varying the physiological level of unoccupied binding protein B_0. Increasing B_0 corresponds to a smaller value of δ, the parameter grouping that quantifies the relative size of free to bound cortisol. A smaller value of B_0 (larger value of δ) results in a shorter time taken for the total cortisol concentration to reach an equilibrium level (Figure 2.4(a)), which physically corresponds to the binding protein becoming saturated more quickly when there is less available initially. However, when varying the unbinding rate k_{bf} corresponding to the same range in δ (Figure 2.4(b)), we see very little difference in the trajectory for total cortisol. We anticipate that this will cause problems for parameter recovery. The AUC flattens at the point where the total dosage over the 24-hour period is equal to the level of binding protein, i.e., the AUC stops increasing when the binding protein is no longer saturated (see the dashed vertical line in Figure 2.5(a)). Larger δ leads to a lower overall AUC because there is a higher concentration of free cortisol which

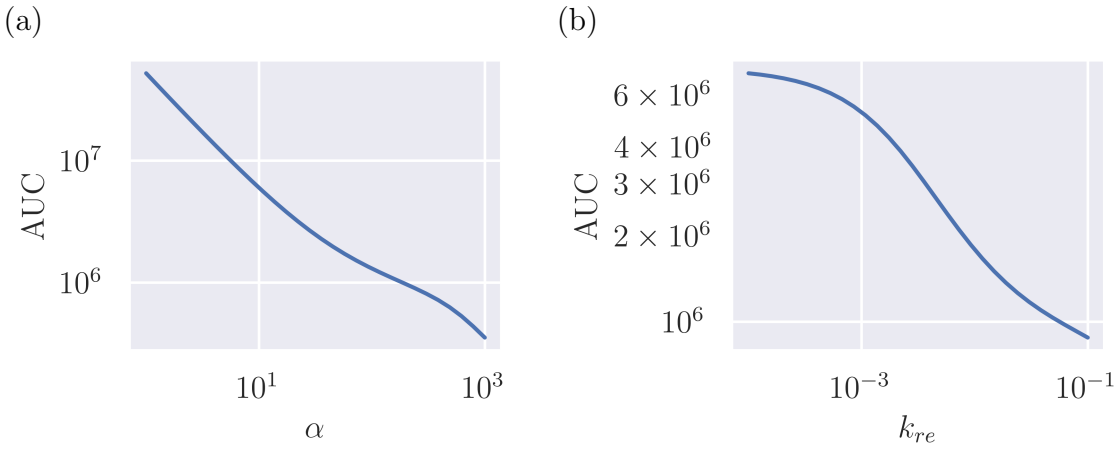

Figure 2.3: Area under the curve for total cortisol concentration, F, over a 24-hour period with varying model parameters for the CIV$^+$ model given by eqs. (2.4) and (2.5). Fixed values of parameters: $\alpha = 55\,\mathrm{L}$, $k_{fb} = 0.1\,\mathrm{L\,nmol^{-1}\,min^{-1}}$, $k_{bf} = 1\,\mathrm{min^{-1}}$, $B_0 = 650\,\mathrm{nmol\,L^{-1}}$, $k_{re} = 0.01\,\mathrm{min^{-1}}$: (a) varying dilution factor α, (b) varying rate of removal of free cortisol k_{re}.

is removed from the system (Figure 2.5(b)).

Figure 2.6 demonstrates how the AUC is affected by pairs of parameters. Firstly, in Figure 2.6(a) we see a linear relationship between increasing α and decreasing k_{re}. As α and k_{re} both increase, the AUC value decreases as we have a smaller input (more dilution) and more free cortisol removal. In Figure 2.6(b), it can be seen that increasing B_0 and decreasing k_{re} have a linear relationship. The AUC value is at the lowest in the bottom left hand corner which is when B_0 is small and k_{re} is large so the binding protein is saturated and there will be more free cortisol which will be removed at a faster rate. Finally, Figure 2.6(c) shows AUC levels for varying α and B_0. The point at which binding protein is saturated is reflected in the diagonal ridge, i.e., as α increases there is a smaller input and so the saturation point is lower.

(a)

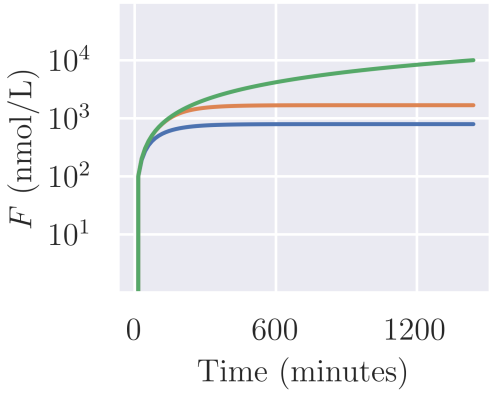

k_{fb} = 1e-01, k_{bf} = 1e+00, B_0 = 1e+02, δ = 1e-01
k_{fb} = 1e-01, k_{bf} = 1e+00, B_0 = 1e+03, δ = 1e-02
k_{fb} = 1e-01, k_{bf} = 1e+00, B_0 = 1e+05, δ = 1e-04

(b)

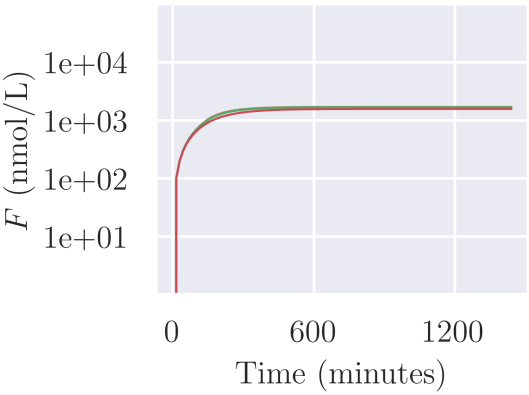

k_{fb} = 1e-01, k_{bf} = 1e-02, B_0 = 1e+03, δ = 1e-01
k_{fb} = 1e-01, k_{bf} = 1e-01, B_0 = 1e+03, δ = 1e-02
k_{fb} = 1e-01, k_{bf} = 1e+00, B_0 = 1e+03, δ = 1e-03
k_{fb} = 1e-01, k_{bf} = 1e+01, B_0 = 1e+03, δ = 1e-04

Figure 2.4: Evolution of total cortisol concentration, F, in time when varying model parameters for the CIV$^+$ model given by eqs. (2.4) and (2.5). Fixed values of parameters: $\alpha = 55\,\mathrm{L}$, $k_{re} = 0.01\,\mathrm{min}$. (a) varying physiological level of binding protein B_0, (b) varying unbinding rate k_{bf}.

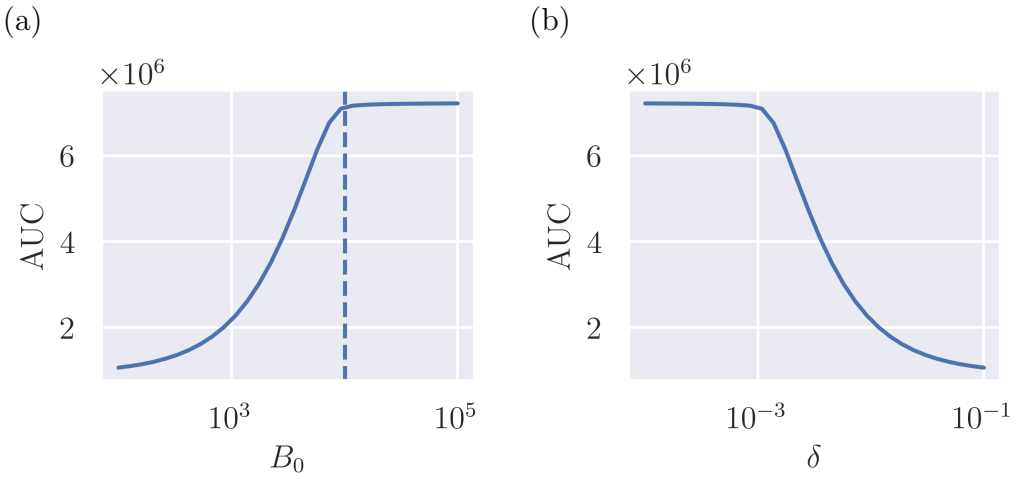

Figure 2.5: Area under the curve for total cortisol concentration, F, over a 24-hour period with varying B_0 for the CIV$^+$ model given by eqs. (2.4) and (2.5). Fixed values of parameters: $\alpha = 55\,\mathrm{L}$, $k_{fb} = 0.1\,\mathrm{L\,nmol^{-1}\,min^{-1}}$, $k_{bf} = 1\,\mathrm{min^{-1}}$, $k_{re} = 0.01\,\mathrm{min^{-1}}$.

2.4 Practical identifiability of the CIV$^+$ model using simulated data

To assess the practical identifiability of the CIV$^+$ model when attempting to estimate the parameter values corresponding to an individual in varying experimental conditions, we present the results of fitting the model to simulated data. In so doing we take a frequentist approach: first selecting values for each parameter, numerically solving the CIV$^+$ model using these parameters over a defined time-period, and adding noise before attempting to recover the original parameters through minimising a loss function between the simulated data (+ noise) and the ODE system given by eqs. (2.22) and (2.23). We choose here to numerically solve the system using the MATLAB's 'ode15s' ODE solver due to the reduced computation time compared to Python's built-in solvers for stiff systems.

That is to say, we begin by generating a set of data points for F with 'true' parameter values $\alpha = 55$, $k_{fb} = 0.1$, $k_{bf} = 1$, $B_0 = 650$, $k_{re} = 0.01$, evaluating at a chosen set of time points t and a chosen amount of noise,

$$F^{synth}(\boldsymbol{\theta}, \boldsymbol{t}, \sigma) = F(\boldsymbol{\theta}, \boldsymbol{t}) + \mathcal{N}(0, \sigma^2). \tag{2.24}$$

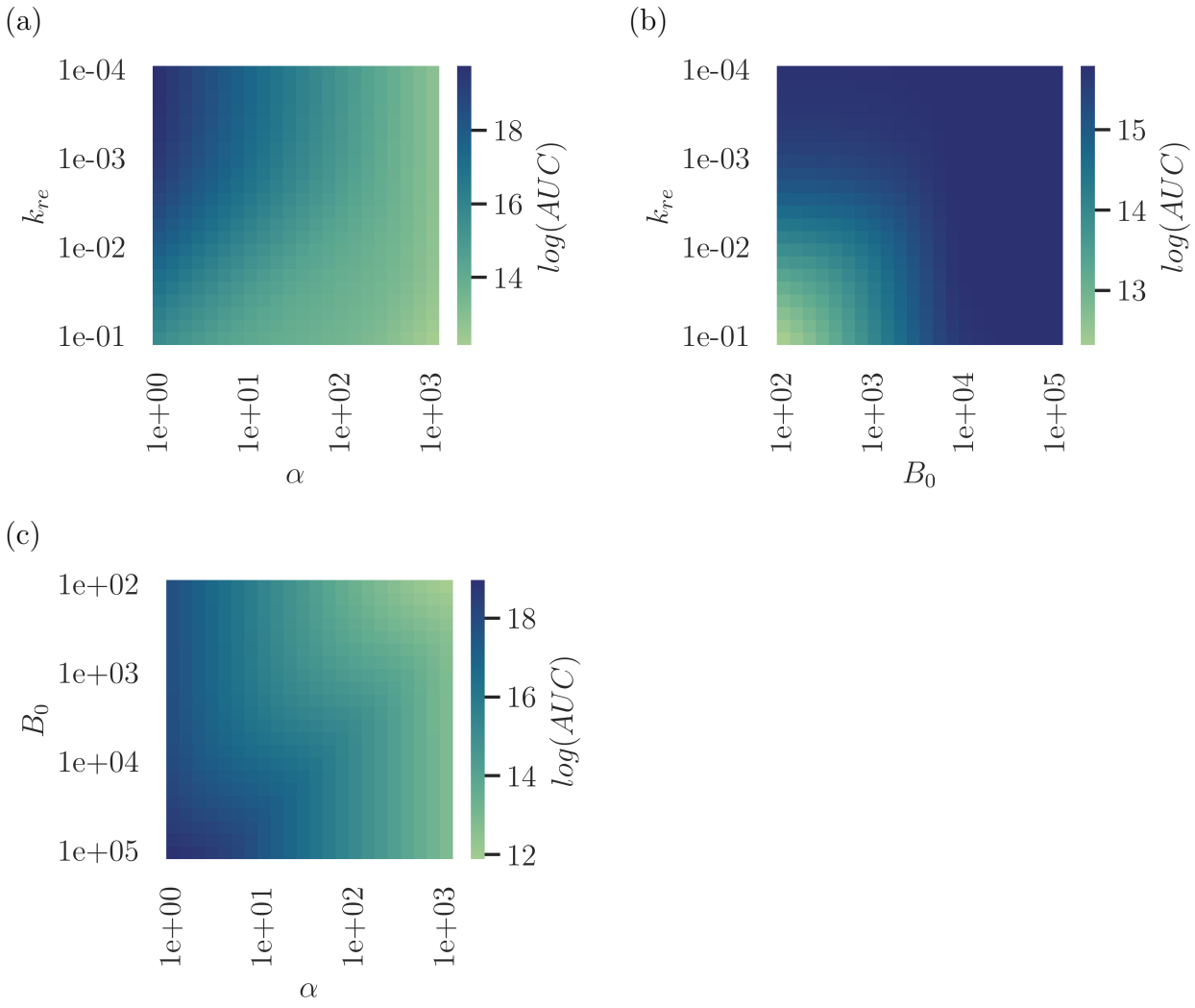

Figure 2.6: Colormap plot of the area under the curve for total cortisol concentration, F, over a 24-hour period for varying pairs of parameters for the CIV^+ model given by eqs. (2.4) and (2.5). Fixed values of parameters: $\alpha = 55\,\mathrm{L}$, $k_{fb} = 0.1\,\mathrm{L\,nmol^{-1}\,min^{-1}}$, $k_{bf} = 1\,\mathrm{min^{-1}}$, $B_0 = 650\,\mathrm{nmol\,L^{-1}}$, $k_{re} = 0.01\,\mathrm{min^{-1}}$.

We then vary each parameter in turn and recalculate the F-values at the corresponding time points and take a sum-squared error across all time points,

$$\text{LossFunc} = \sum_i (F_i(\boldsymbol{\theta}, t_i) - F_i^{synth}(\boldsymbol{\theta}^*, t_i))^2 \tag{2.25}$$

Here, $\boldsymbol{\theta} = [\alpha, k_{fb}, k_{bf}, B_0, k_{re}]$ is the parameter vector and $\boldsymbol{\theta}^*$ is the 'true' set of parameter values. A smaller loss function indicates a closer fit to the 'true' synthetic data. We initially consider the behaviour of this loss function while varying each parameter to anticipate any problems that may arise when fitting the model to noisy, low time-resolution data. Ideally, the loss function will have a single minima that corresponds to the true value of each parameter. We note here that in what follows we are presenting only one case of noisy data, however the case presented is representative of other examples seen during experimentation.

We choose to take a value of $100\,\text{nmol}\,\text{L}^{-1}$ as a realistic noise level to add to our synthetic data in order to closely resemble data [PD]. We estimate this value by applying a cubic smoothing spline to data [PD] using MATLAB's functions 'csaps' and calculating the standard deviation of the differences between the spline and data. Therefore this value is a combination of both measurement error and inter-intra subject variability. Liquid chromatography-tandem mass spectrometry (LC-MS/MS), the method used to measure serum concentration of cortisol for data [PD], has around 95% recovery for cortisol [51]. Therefore, we assume that the noise estimate of $\tilde{}100\,\text{nmol}\,\text{L}^{-1}$ is predominantly measurement error with some subject variability.

Figure 2.7 shows the loss function behaviour relative to the number of time points as each parameter varies individually. In this case, the synthetic data points have no noise added and the time resolution ranges from 0.01-100 time points per minute. For each parameter, there is a single clear minimum in the loss function that corresponds to the true value of each parameter. The loss function behaves similarly regardless of the number of time points and hence the lines appear indistinguishable in Figure 2.7 indicating that

time resolution has little influence on the ability to identify the true parameter value.

Considering the behaviour of the loss function with zero noise added while varying two parameters at once (Figure 2.8), the numerical minimum in the loss function matches the true values of each parameter for all pairs (we show a selection in Figure 2.8 but other pairs are shown in Figure B.1 in Appendix B). For varying k_{fb} and k_{bf}, the beginning of a ridge can be seen in the loss function, specifically along the line corresponding to $k_{bf}/k_{fb} = 10$, however in the zero noise case the true value is still identifiable along this ridge.

We look specifically at the values of the loss function along this ridge in Figure 2.9 (i.e., when $k_{bf}/k_{fb} = 10$). Figure 2.9(a) shows the loss function relative to the number of time points. There is a distinct minimum corresponding to the true values of k_{fb} and k_{bf} regardless of number of time points. However the loss function is no longer well-behaved which could create problems for any local optimising algorithm becoming trapped in local minima, especially once noise is added to the data. Figure 2.9(b) shows the difference between the true value of k_{fb} and the value of k_{fb} corresponding to the numerical minimum in the loss function), which for this zero noise case is always equal to zero regardless of the frequency of time sampling. Increasing the error to have standard deviation $1\,\mathrm{nmol\,L^{-1}}$, which represents a small relative error of approximately 0.1%, and considering time points used in data [PD] (every 30 minutes around dosing times and every hour otherwise), there is an increase in the width of the ridge between the parameters k_{fb} and k_{bf}. Figure 2.10(a) shows that the true value of k_{fb} still matches the numerical minimum of the loss function when fixing the other 4 parameters with this small level of noise. However, Figure 2.10(b) shows that the numerical minimum has now moved far from the true parameter values when varying both k_{fb} and k_{bf}. This shift indicates that at this time resolution it will be difficult to recover the individual values for k_{fb} and k_{bf} when fitting to patient data, however it may still be possible to recover the ratio between them.

Across the other parameters pairings, ridges begin to appear within the loss functions for even this small amount of noise (Figure 2.11). In Figure 2.11(a), the minimum point

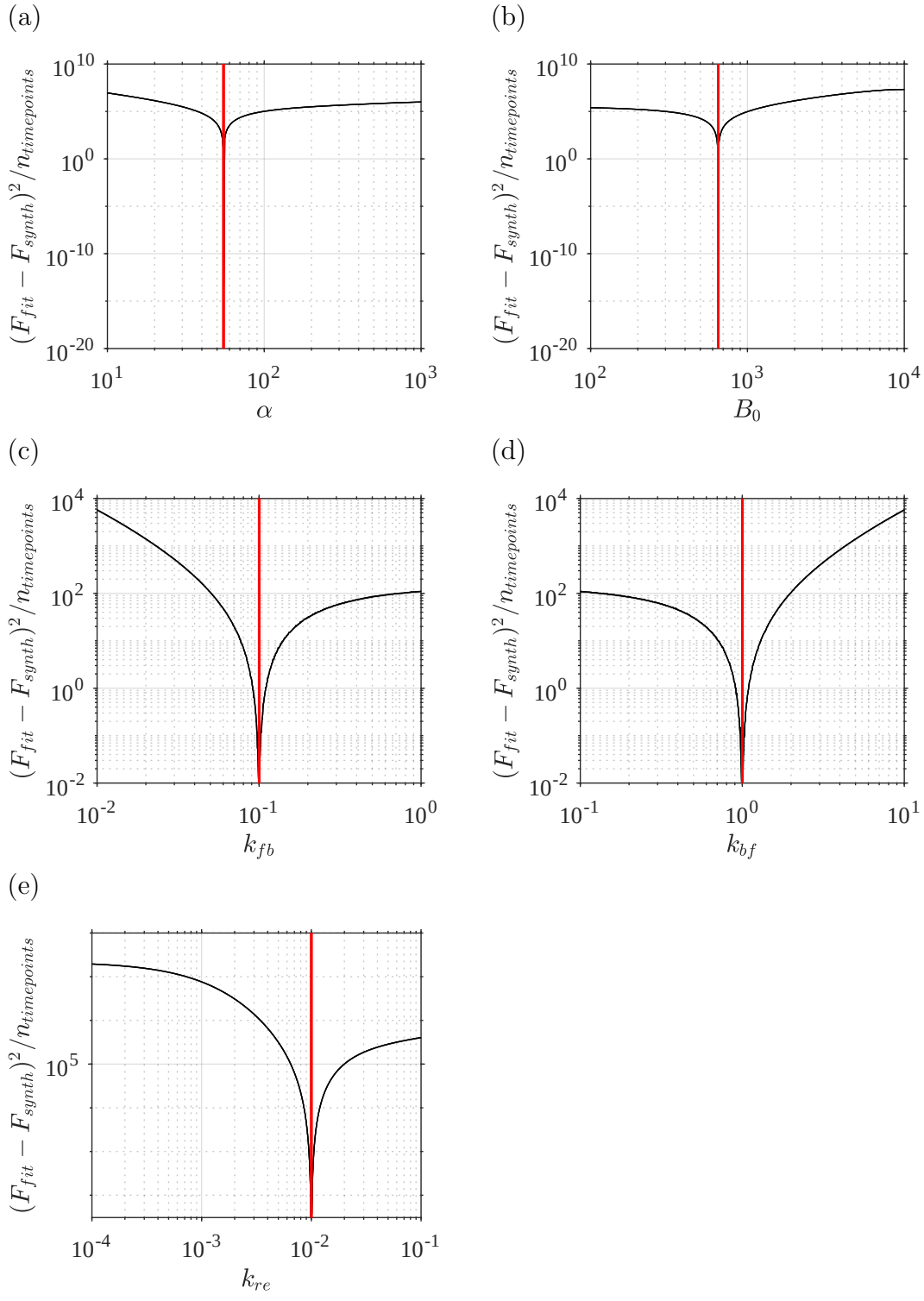

Figure 2.7: Loss function relative to sampling frequency for varying model parameters for the CIV$^+$ model given by eqs. (2.4) and (2.5) with zero noise added to synthetic data and sampling time frequency ranging from 0.01-100 time points per minute: (a) varying α, (b) varying B_0, (c) varying k_{fb}, (d) varying k_{bf}, (e) varying k_{re}. The red vertical line indicates the true parameter value.

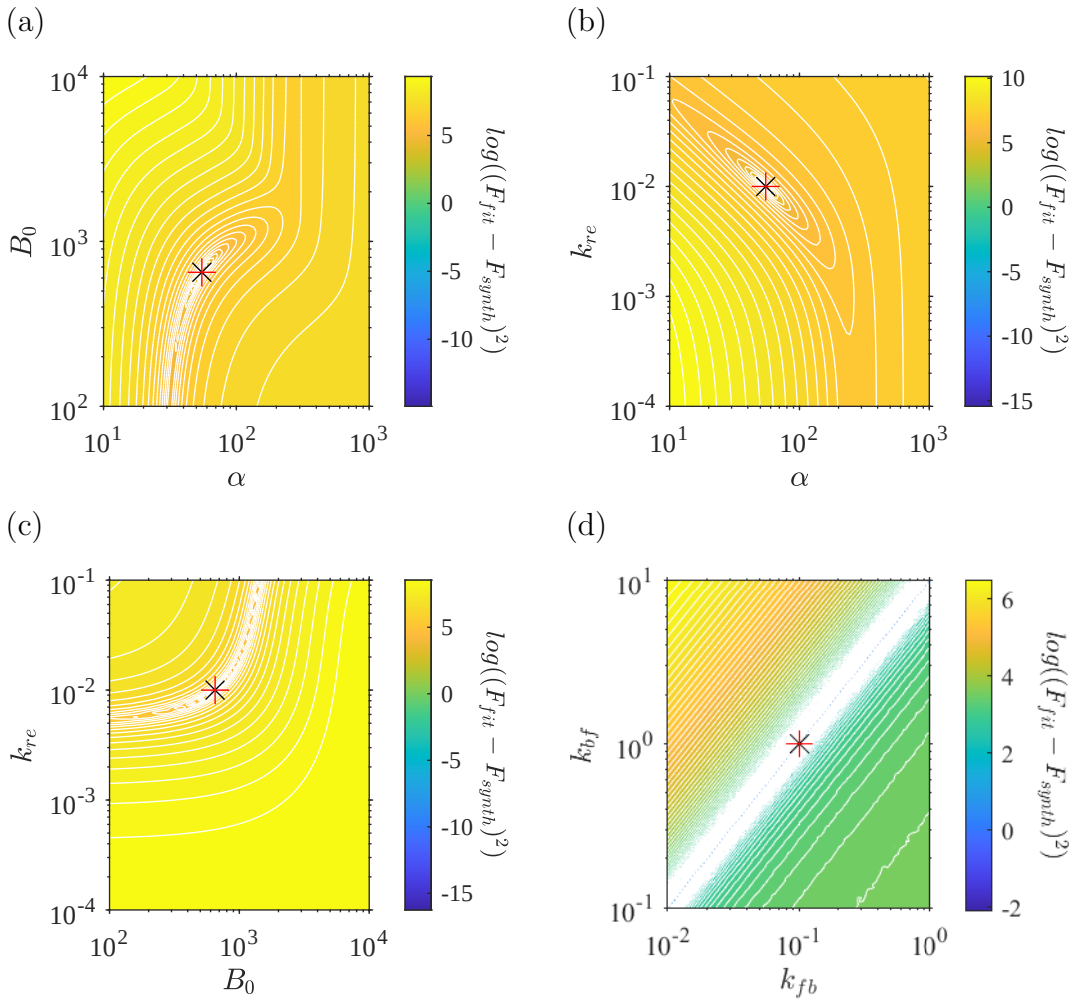

Figure 2.8: Loss function for varying pairs of model parameters for the CIV$^+$ model given by eqs. (2.4) and (2.5) with zero noise added to synthetic data and sampling time frequency corresponding to the time points used in data [PD]. The red plus indicates the true parameter value pair, while the loss function numerical minimum are shown with a black cross: (a) α versus B_0, (b) α versus k_{re}, (c) B_0 versus k_{re}, (d) k_{fb} versus k_{bf}.

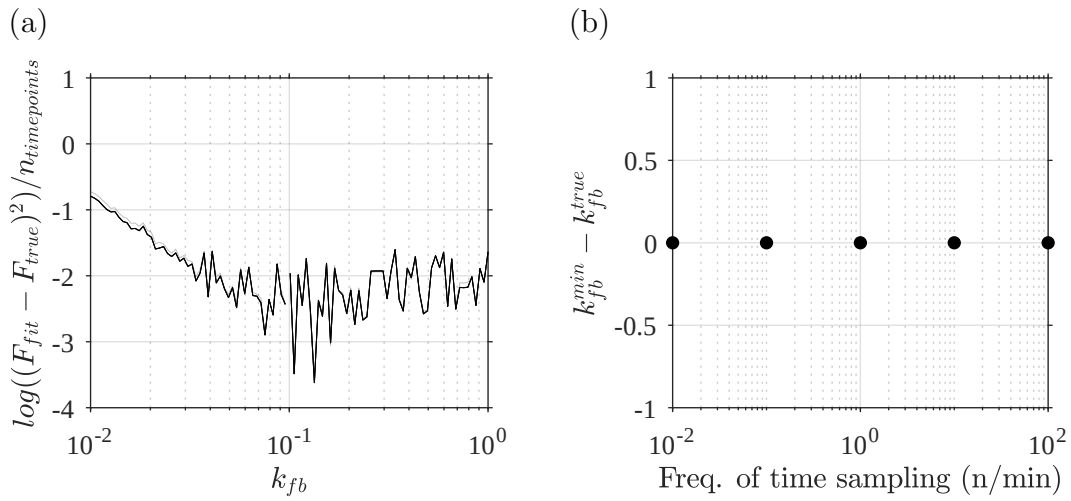

Figure 2.9: Varying k_{fb} and k_{bf} for the CIV$^+$ model given by eqs. (2.4) and (2.5) with zero noise added to synthetic data and sampling time frequency ranging from 0.01-100 time points per minute: (a) loss function relative to sampling frequency, (b) difference between true parameter value for k_{fb} and corresponding k_{fb} value that generates minimum loss function.

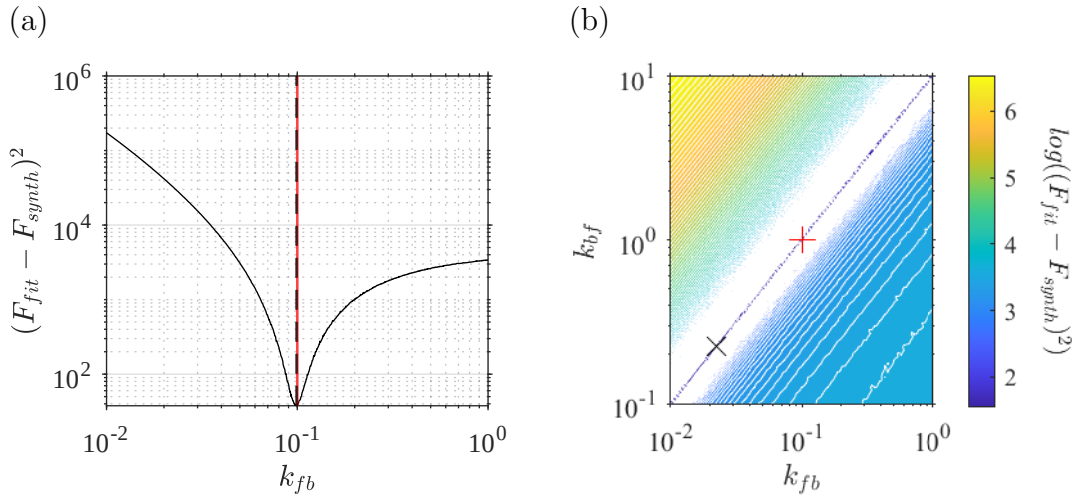

Figure 2.10: Loss function for varying model parameters for the CIV$^+$ model given by eqs. (2.4) and (2.5) with Gaussian noise added (s.d. $1\,\mathrm{nmol\,L^{-1}}$) and sampling time frequency corresponding to the time points used in data [PD]: (a) varying k_{fb} only. The red line indicates the true value of k_{fb}, while the numerical minimum is shown by the black dashed line, (b) k_{fb} versus k_{bf}. The red plus indicates the true parameter value pair, while the loss function numerical minimum is shown with a black cross.

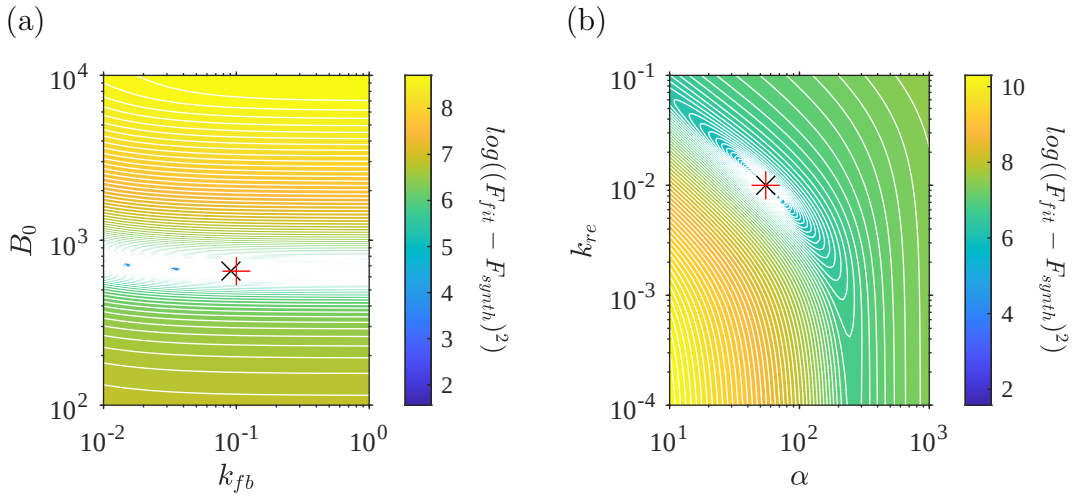

Figure 2.11: Loss function for varying pairs of model parameters for the CIV$^+$ model given by eqs. (2.4) and (2.5) with Gaussian noise (s.d. $1\,\mathrm{nmol\,L^{-1}}$) added to synthetic data and sampling time frequency corresponding to the time points used in data [PD]. The red plus indicates the true parameter value pair, while the loss function numerical minimum is shown with a black cross: (a) k_{fb} versus B_0, (b) α versus k_{re}.

for the pairing (k_{fb}, B_0) has begun to move away from the true parameter values, but there is still a match for (α, k_{re}).

By increasing the time-resolution of the data points with this small amount of noise, it becomes possible to identify the individual values of k_{fb} and k_{bf}. Figure 2.12 (a) shows the loss function along the ridge from Figure 2.10(b) for increasing time-resolution. By eye, the loss function looks flat for high time-resolution. However Figure 2.12 shows that with increasing time resolution the minimum for the loss function becomes closer to the true value of k_{fb} (and similarly k_{bf}, see Figure B.2 in Appendix B) and by 100 time points per minute the minimum in the loss function corresponds to the true value of k_{fb}.

Now increasing the error further to a more realistic value for data [PD] ($\sim 100\,\mathrm{nmol\,L^{-1}}$), the ability to trace back to the ratio between k_{fb} and k_{bf} is lost and the ridge we see in the 2D plane has become a flat plane (Figure 2.13(b)). Figure 2.13(a) shows that when varying k_{fb} and fixing the other four parameters, the value of k_{fb} that corresponds to the minimum in the loss function no longer matches the true value.

Figure 2.14 shows the ratio between the k_{fb} and k_{bf} values that correspond to the minimum in the loss function for increasing time resolution. Similarly to the small error

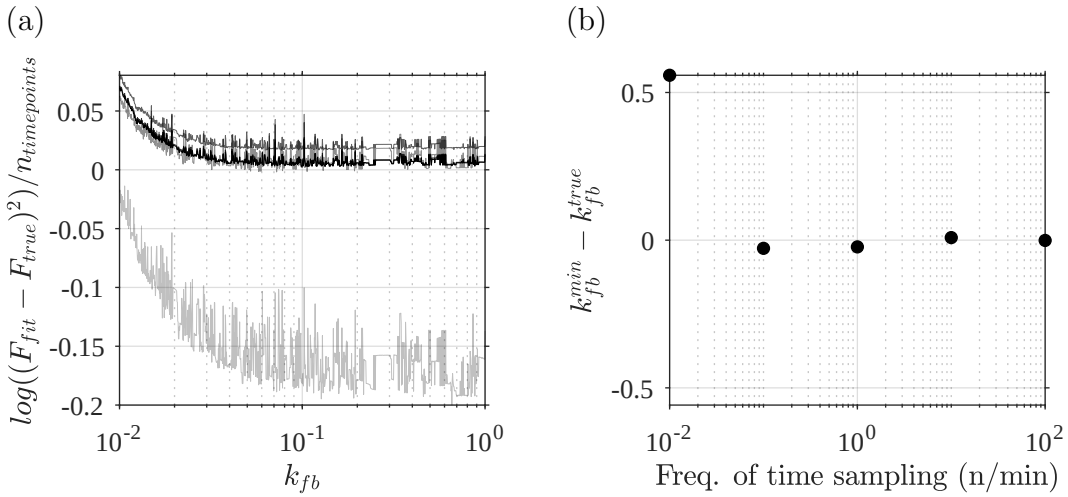

Figure 2.12: Varying k_{fb} and k_{bf} for the CIV$^+$ model given by eqs. (2.4) and (2.5) with Gaussian noise (s.d. $1\,\mathrm{nmol\,L^{-1}}$) added to synthetic data and sampling time frequency ranging from 0.01-100 time points per minute: (a) loss function relative to sampling frequency with darker lines indicating a higher time resolution, (b) difference between true parameter value for k_{fb} and corresponding k_{fb} value that generates minimum loss function.

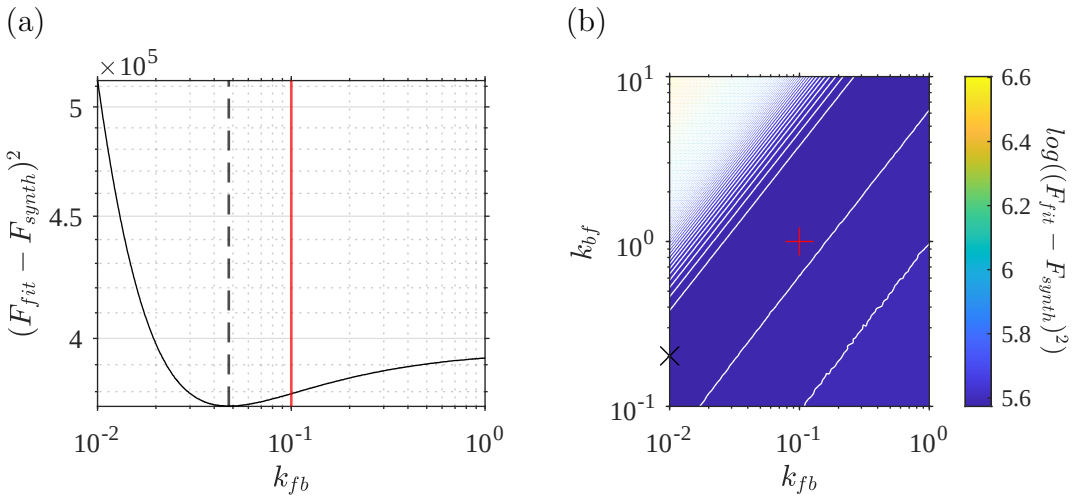

Figure 2.13: Loss function for varying model parameters for the CIV$^+$ model given by eqs. (2.4) and (2.5) with Gaussian noise added (s.d. $100\,\mathrm{nmol\,L^{-1}}$) and sampling time frequency corresponding to the time points used in data [PD]: (a) varying k_{fb} only. The red line indicates the true value of k_{fb}, while the numerical minimum is shown by the black dashed line, (b) k_{fb} versus k_{bf}. The red plus indicates the true parameter value pair, while the loss function numerical minimum is shown with a black cross.

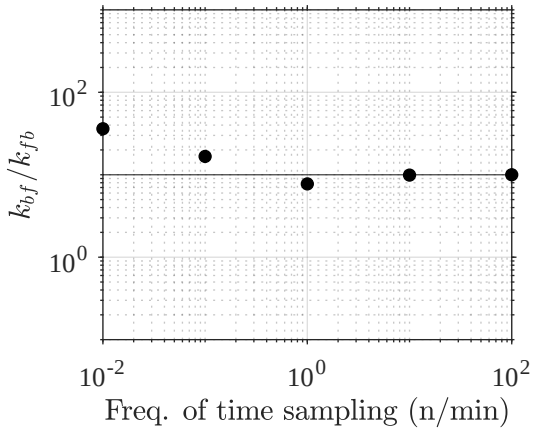

Figure 2.14: Difference between true parameter value ratio for k_{bf}/k_{fb} and corresponding numerical ratio using k_{fb} and k_{bf} that correspond to the minimum value of the loss function for the CIV^+ model given by eqs. (2.4) and (2.5) with Gaussian noise (s.d. $100\,\mathrm{nmol\,L^{-1}}$) added to synthetic data and sampling time frequency ranging from 0.01-100 time points per minute.

case, increasing the time-resolution leads to the numerical ratio becoming closer to the true value (=10).

Comparing the low and high time-resolution contour plot (Figures 2.13 and 2.15 respectively), we see that the high time-resolution numerical minimum sits on the ridge when $k_{bf}/k_{fb} = 10$, but neither match the true individual values of k_{fb} and k_{bf}.

Figure 2.16 summarises when k_{fb} and k_{bf} can be traced back to their true values via the loss function for varying time-resolution and level of noise. For zero noise, we have no issues. When adding a small amount of noise, we immediately lose the ability to trace the true values of binding and unbinding rate parameters, however by increasing time-resolution we can mitigate this issue. For large noise, which we see in data [PD], we are unlikely to be able to find the true values with physically feasible time-resolution and hence we may consider whether we can fix these values when parameter fitting.

Frequentist parameter recovery

The flat plane in the loss function created between the parameters k_{fb} and k_{bf} leads to problems when using frequentist fitting methods to estimate the model parameters. Using

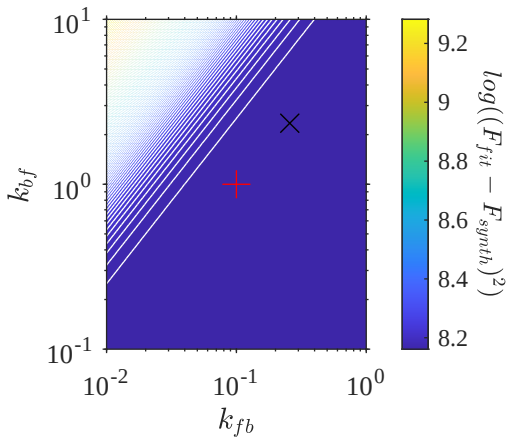

Figure 2.15: Loss function for varying k_{fb} and k_{bf} for the CIV$^+$ model given by eqs. (2.4) and (2.5) with Gaussian noise added (s.d. $100\,\mathrm{nmol\,L^{-1}}$) and sampling time frequency every 0.1 min. The red plus indicates the true parameter value pair, while the loss function numerical minimum are shown with a black cross.

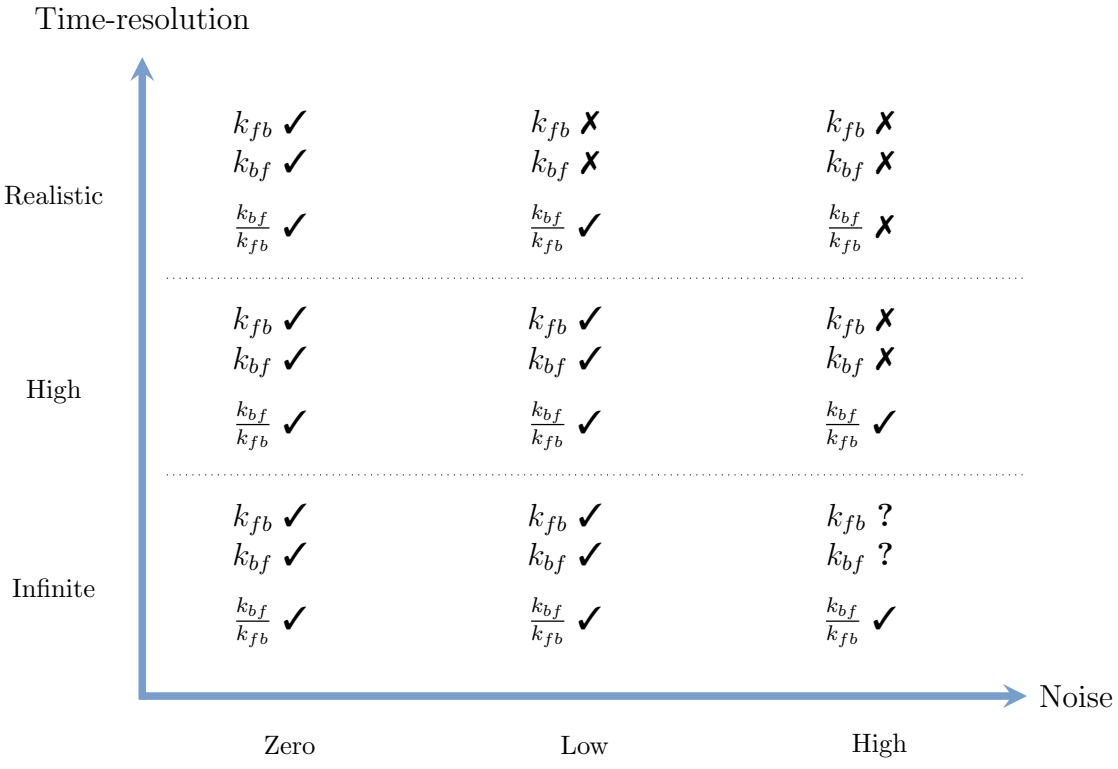

Figure 2.16: Schematic showing whether the true parameter values of k_{fb} and k_{bf} or their ratio can be traced back via the loss function for varying amounts of noise and varying time-resolution.

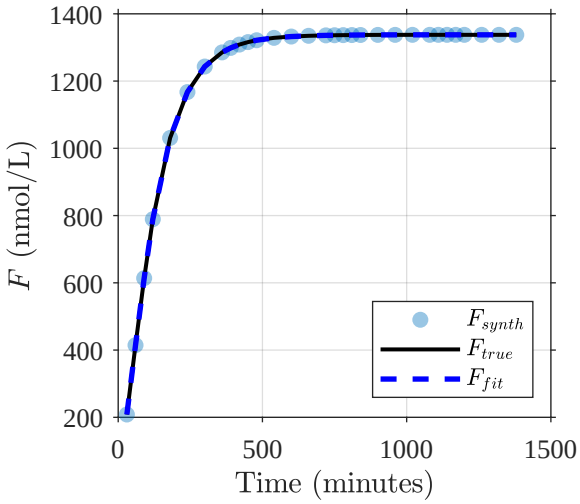

Figure 2.17: Frequentist fit of model trajectory of total cortisol, F, with zero noise and sampling time frequency corresponding to the time points used in data [PD] for the CIV$^+$ model given by eqs. (2.4) and (2.5) for all 5 model parameters. Parameter estimates are $\alpha = 55\,\mathrm{L}$, $k_{fb} = 0.1\,\mathrm{L\,nmol^{-1}\,min^{-1}}$, $k_{bf} = 1\,\mathrm{min^{-1}}$, $B_0 = 650\,\mathrm{nmol\,L^{-1}}$, $k_{re} = 0.01\,\mathrm{min^{-1}}$.

the MultiStart algorithm in MATLAB with the built-in `fmincon` routine for finding the minimum of a constrained nonlinear multivariate function using the interior-point algorithm, the estimates match the true value of each parameter at zero noise (Figure 2.17). For small noise, the estimates for α, B_0 and k_{re} have remained fairly close to the true solutions (Figure 2.18). The estimates for k_{fb} and k_{bf} have moved further from their true values, however the ratio between them has remained near the true value, reflecting the widening ridge for even small noise added to the F trajectory.

Finally, for large noise the estimates for k_{fb}, k_{bf} and B_0 have moved drastically and the ratio between k_{fb} and k_{bf} is far from the true value (Figure 2.19). The fitted curve has moved minimally from the true curve, however the estimates are poor particularly for the level of unoccupied binding protein. This poor estimate was expected as changes in the value of k_{bf} had little effect on the trajectory, so when the ratio of k_{bf} and k_{fb} moves away from the true value, a much larger estimate for B_0 maintains a physically feasible value of δ and allows for a reasonable fit to the data.

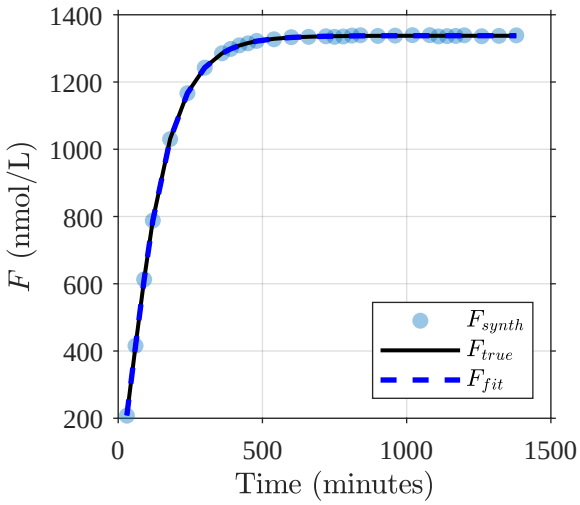

Figure 2.18: Frequentist fit of model trajectory of total cortisol, F, with Gaussian noise added (s.d. $1\,\mathrm{nmol\,L^{-1}}$) and sampling time frequency corresponding to the time points used in data [PD] for the CIV^+ model given by eqs. (2.4) and (2.5) for all 5 model parameters. The parameter estimates are $\alpha = 54.877\,\mathrm{L}$, $k_{fb} = 0.719\,45\,\mathrm{L\,nmol^{-1}\,min^{-1}}$, $k_{bf} = 8.6587\,\mathrm{min^{-1}}$, $B_0 = 652.17\,\mathrm{nmol\,L^{-1}}$, $k_{re} = 0.010\,024\,\mathrm{min^{-1}}$ with a resulting ratio of $k_{bf}/k_{fb} = 12.035$. The true values are listed in Table 2.1.

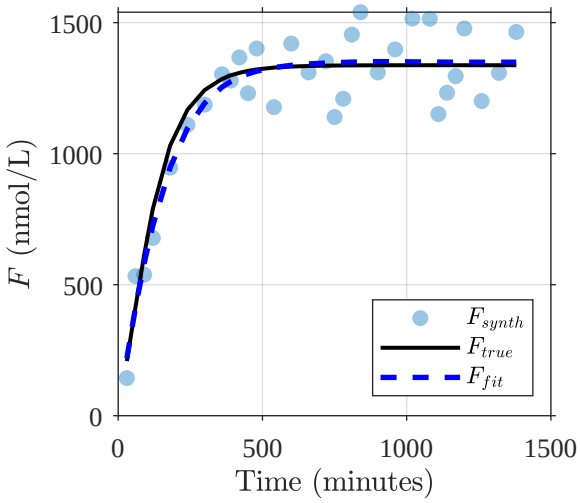

Figure 2.19: Frequentist fit of model trajectory of total cortisol, F, with Gaussian noise added (s.d. $100\,\mathrm{nmol\,L^{-1}}$) and sampling time frequency corresponding to the time points used in data [PD] for the CIV^+ model given by eqs. (2.4) and (2.5) for all 5 model parameters. The parameter estimates are $\alpha = 48.847\,\mathrm{L}$, $k_{fb} = 0.010\,\mathrm{L\,nmol^{-1}\,min^{-1}}$, $k_{bf} = 1.489\,\mathrm{min^{-1}}$, $B_0 = 3645.3\,\mathrm{nmol\,L^{-1}}$, $k_{re} = 0.1\,\mathrm{min^{-1}}$ with a resulting ratio of $k_{bf}/k_{fb} = 148.9$. The true values are listed in Table 2.1.

2.5 The reduced CIV$^-$ model

It is possible to rationally reduce the one-compartment model by using dimensional analysis and matched asymptotic analysis to separate the system rates in both the CIV and BIV case. This reduction will aid with parameter estimation when fitting the model to patient data by either reducing computation time or by reducing the number of model parameters to be fit [15].

We begin by recalling the dimensionless system for the CIV dosing method (2.22)-(2.23),

$$\begin{aligned}\frac{dF_f'}{dt'} &= 1 - \frac{\beta}{\delta^2}F_f'B' + \frac{\beta}{\delta}(1-B') - \rho F_f',\\ \frac{dB'}{dt'} &= \quad -\frac{\beta}{\delta^2}F_f'B' + \frac{\beta}{\delta}(1-B').\end{aligned}$$

At the beginning of the dosing period, we know that the unoccupied binding protein will be $\mathcal{O}(1)$ and the free cortisol will be $\mathcal{O}(\delta)$. Hence, we rescale free cortisol with,

$$F_f' = \delta\hat{F}_f', \qquad\qquad B' = \hat{B}', \tag{2.26}$$

to find the system,

$$\delta\frac{d\hat{F}_f'}{dt'} = 1 - \frac{\beta}{\delta}\hat{F}_f'\hat{B}' + \frac{\beta}{\delta}(1-\hat{B}') - \delta\rho\hat{F}_f', \tag{2.27}$$

$$\frac{d\hat{B}'}{dt'} = \quad -\frac{\beta}{\delta}\hat{F}_f'\hat{B}' + \frac{\beta}{\delta}(1-\hat{B}'). \tag{2.28}$$

Seeking a solution of the form,

$$\hat{F}_f' = \hat{F}_{f0}' + \delta\hat{F}_{f1}' + \cdots, \qquad\qquad \hat{B}' = \hat{B}_0' + \delta\hat{B}_1' + \cdots, \tag{2.29}$$

we find at leading order,

$$\hat{F}'_{f0} \approx \frac{1-\hat{B}'_0}{\hat{B}'_0}. \tag{2.30}$$

Subtracting eq. (2.28) from eq. (2.27),

$$\delta \frac{d\hat{F}'_f}{dt'} - \frac{d\hat{B}'}{dt'} = 1 - \delta\rho\hat{F}'_f, \tag{2.31}$$

and eliminating $\hat{F}'_f$ using eq. (2.30), we obtain a single ODE for $\hat{B}'$,

$$\frac{d\hat{B}'}{dt'} = \left(\delta\frac{1}{\hat{B}'^2}+1\right)^{-1}\left(-1+\delta\rho\frac{1-\hat{B}'}{\hat{B}'}\right). \tag{2.32}$$

Upon returning to original dimensionless variables, we obtain

$$F'_f = \delta\left(\frac{1-B'}{B'}\right), \qquad \frac{dB'}{dt'} = \left(\delta\frac{1}{B'^2}+1\right)^{-1}\left(-1+\delta\rho\frac{1-B'}{B'}\right). \tag{2.33}$$

This asymptotic solution still contains an ODE for B' which is separable and an implicit solution can be found (see appendix B.3.1). However, for the purpose of parameter fitting, it is quicker to solve the ODE numerically. The asymptotic approximation is compared to the numerical solution of the full system CIV^+ (calculated with the solver RK45 in Python) in Figure 2.20, with $\delta = 0.01$ and $\rho = 1.92$. The quasi-steady approximation follows very closely to the full solution for all time.

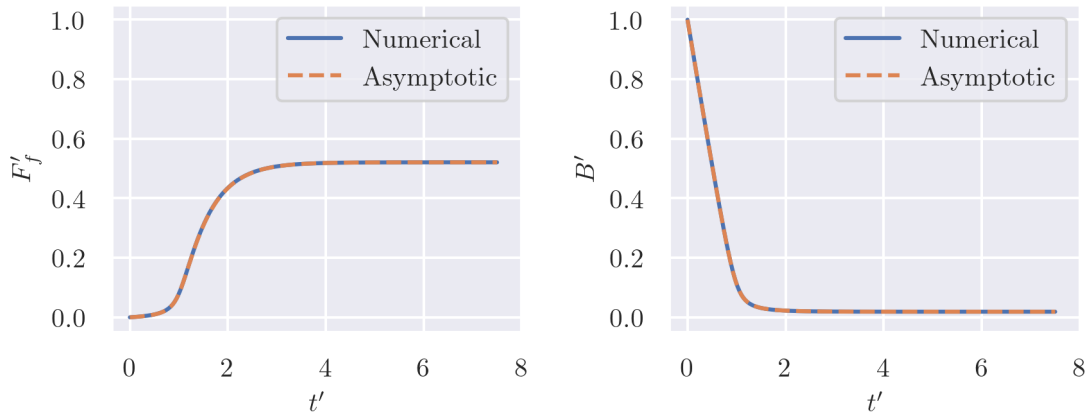

Figure 2.20: Comparison between the asymptotic model given by eqs. (2.34) to (2.36) and the numerical solution of the CIV$^+$ given by eqs. (2.4) and (2.5).

2.5.1 Identifiability of the CIV$^-$ model

On redimensionalising the reduced model, we obtain a 4–parameter system ($[\alpha, \delta, B_0, k_{re}]$), namely

$$\frac{dB}{dt} = \frac{-qB^2 + \alpha\delta k_{re} B_0 B(B_0 - B)}{\alpha(B^2 + \delta B_0^2)}, \tag{2.34}$$

$$F_f = \delta \frac{B_0}{B}(B_0 - B), \tag{2.35}$$

where the observed variable F is expressed as,

$$F = \left(\delta \frac{B_0}{B} + 1\right)(B_0 - B). \tag{2.36}$$

From here on, we will refer to this model as CIV$^-$. To establish the identifiability of this model, we proceed by calculating successive Taylor coefficients to determine the identifiability for each model parameter. As previously, the first coefficient is zero and so

we need at least another 4 coefficients,

$$\Phi_1 = \left.\frac{dF}{dt}\right|_{t=0} = \frac{q}{\alpha}, \tag{2.37}$$

$$\Phi_2 = \left.\frac{d^2F}{dt^2}\right|_{t=0} = -\frac{q}{\alpha}\frac{\delta k_{re}}{1+\delta}, \tag{2.38}$$

$$\Phi_3 = \left.\frac{d^3F}{dt^3}\right|_{t=0} = -\frac{q}{\alpha}\frac{\delta k_{re}}{1+\delta}\left(\frac{2q}{\alpha B_0(1+\delta)^2} - \frac{\delta k_{re}}{1+\delta}\right), \tag{2.39}$$

$$\Phi_4 = \left.\frac{d^4F}{dt^4}\right|_{t=0} = \frac{q}{\alpha}\frac{\delta k_{re}}{1+\delta}\left(\frac{6q^2(\delta-1)}{\alpha^2 B_0^2(1+\delta)^4} + \frac{8q}{\alpha B_0(1+\delta)^2}\frac{\delta k_{re}}{1+\delta} - \left(\frac{\delta k_{re}}{1+\delta}\right)^2\right). \tag{2.40}$$

Using MAPLE, we are able to express each model parameter as a function of the rational functions above,

$$\alpha = \frac{q}{\Phi_1}, \tag{2.41}$$

$$\delta = -\frac{2\Phi_1^2\Phi_2\Phi_4 - 3\Phi_1^2\Phi_3^2 - 2\Phi_1\Phi_2^2\Phi_3 + 3\Phi_2^4}{3\left(\Phi_1^2\Phi_3^2 - 2\Phi_1\Phi_2^2\Phi_3 + \Phi_2^4\right)}, \tag{2.42}$$

$$B_0 = \frac{9\Phi_2\left(\Phi_1^2\Phi_3^2 - 2\Phi_1\Phi_2^2\Phi_3 + \Phi_2^4\right)\left(\Phi_1\Phi_3 - \Phi_2^2\right)}{2\left(\Phi_1\Phi_2\Phi_4 - 3\Phi_1\Phi_3^2 + 2\Phi_2^2\Phi_3\right)^2}, \tag{2.43}$$

$$k_{re} = -\frac{2\Phi_2\left(\Phi_1\Phi_2\Phi_4 - 3\Phi_1\Phi_3^2 + 2\Phi_2^2\Phi_3\right)}{2\Phi_1^2\Phi_2\Phi_4 - 3\Phi_1^2\Phi_3^2 - 2\Phi_1\Phi_2^2\Phi_3 + 3\Phi_2^4}, \tag{2.44}$$

confirming that all parameters are structurally globally identifiable meaning that the model as a whole is structurally globally identifiable. We confirm this result using STRIKE_GOLDD which concludes that all 4 parameters are locally identifiability. As expected, only the reduced set of 4 parameters are identifiable. We cannot uniquely determine the original binding and unbinding rate parameters k_{fb} and k_{bf} from this reduced model.

2.5.2 Practical identifiability of the CIV$^-$ model using simulated data

To assess the practical identifiability of the CIV$^-$ model, we once more take a frequentist approach to anticipate any difficulties in parameter fitting. We now look at the loss

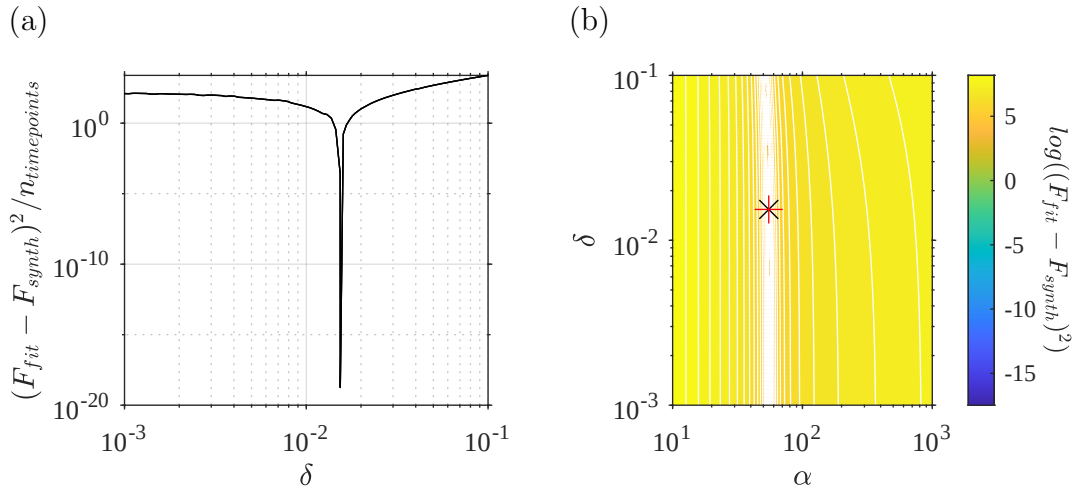

Figure 2.21: Loss function for varying model parameters for the CIV$^-$ model given by eqs. (2.34) to (2.36) with zero noise: (a) varying δ only and sampling time frequency ranging from 0.01-100 time points per minute, (b) α versus δ with sampling time frequency corresponding to the time points used in data [PD]. The red plus indicates the true parameter value pair, while the loss function numerical minimum is shown with a black cross.

function across varying δ values for the reduced model. With zero noise added, there is a unique minimum in the loss function when changing δ values (Figure 2.21 (a)). However, a ridge is formed when varying both α and δ simultaneously (Figure 2.21 (b)), which behaves similarly to the CIV$^+$ case when varying α and k_{fb} and k_{bf} (see Figure B.1(a) and (b)).

The ridge widens and the loss function becomes non-smooth for smaller values of δ in Figure 2.22 when just a small amount of noise is added to the synthetic data.

Finally, looking at Figure 2.23, the numerical minimum of the loss function has now moved away from the true parameter value of δ when noise is large. The ridge between α and δ has also widened further and the true parameter pair is no longer equal to the loss function minimum.

Frequentist parameter recovery

The increased noise creates problems with parameter fitting similar to the full model. Figure 2.25 shows the results of the frequentist fit for large noise, which demonstrates

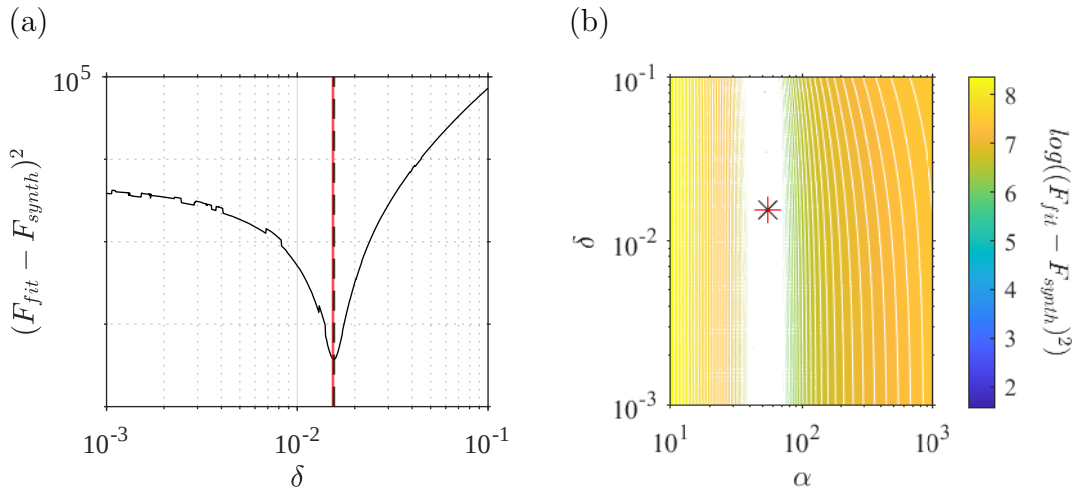

Figure 2.22: Loss function for varying model parameters for the CIV$^-$ model given by eqs. (2.34) to (2.36) with Gaussian noise added (s.d. $1\,\mathrm{nmol\,L^{-1}}$) and sampling time frequency corresponding to the time points used in data [PD]: (a) varying δ only. The red line indicates the true value of δ, while the numerical minimum is shown by the black dashed line, (b) α versus δ. The red plus indicates the true parameter value pair, while the loss function numerical minimum is shown with a black cross.

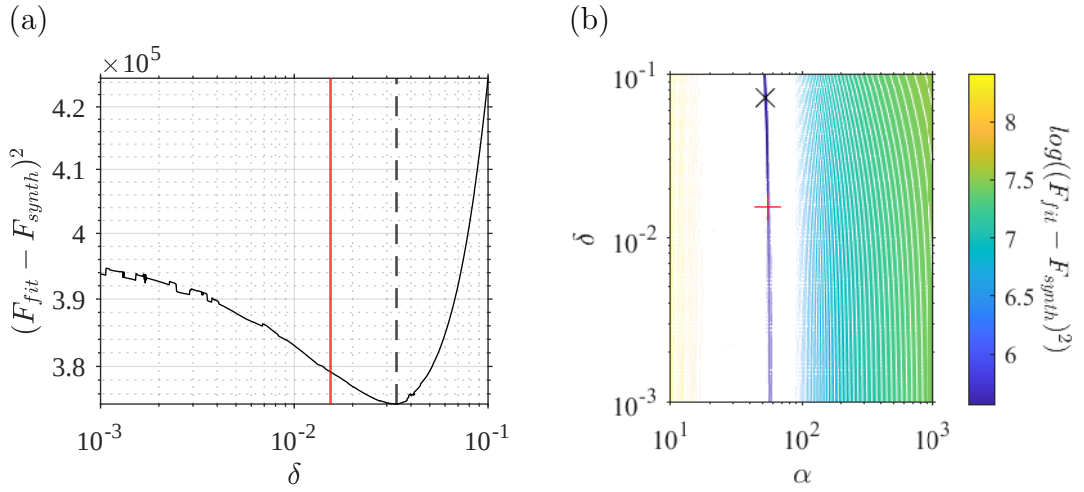

Figure 2.23: Loss function for varying model parameters for the CIV$^-$ model given by eqs. (2.34) to (2.36) with Gaussian noise added (s.d. $100\,\mathrm{nmol\,L^{-1}}$) and sampling time frequency corresponding to the time points used in data [PD]: (a) varying δ only. The red line indicates the true value of δ, while the numerical minimum is shown by the black dashed line, (b) α versus δ. The red plus indicates the true parameter value pair, while the loss function numerical minimum are shown with a black cross.

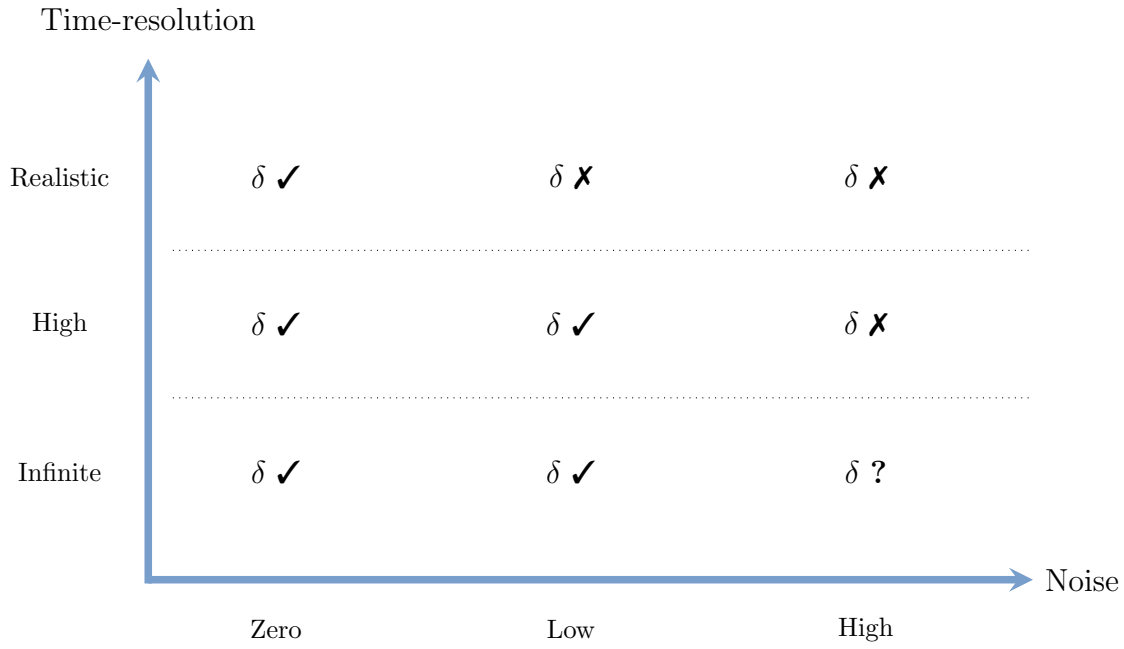

Figure 2.24: Schematic showing whether the true parameter value of δ can be traced back via the loss function for varying amounts of noise and varying time-resolution.

similar behaviour to the full model. The fitted line undershoots the true trajectory, and the corresponding parameter estimates are far from the true values, particularly parameters α, δ and k_{re}.

Figure 2.24 summarises when δ can be traced back to the true value via the loss function for varying time resolution and level of noise. We conclude here that the time-resolution in data [PD] is not sufficient to trace back the true value of the model parameters with the order of noise expected, even after taking a quasi-steady approximation that combines parameters k_{fb} and k_{bf}. Increasing the time-resolution of the data is unable to mitigate the impact of the noise levels.

2.6 Incorporating a non-zero initial level of cortisol

Patients with adrenal insufficiency are likely to still have a low-level of cortisol within their blood stream. We consider incorporating an initial level of total cortisol into the model for the CIV case. Returning to the original model given by eqs. (2.1) and (2.3) and

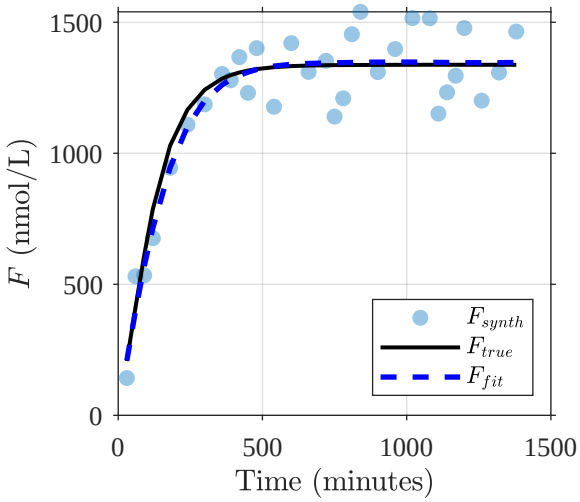

Figure 2.25: Frequentist fit of model trajectory of total cortisol, F, with Gaussian noise added (s.d. $100\,\mathrm{nmol\,L^{-1}}$) and sampling time frequency corresponding to the time points used in data [PD] for the CIV$^-$ model given by eqs. (2.34) to (2.36) for 4 model parameters. Parameter estimates are $\alpha = 51.491\,\mathrm{L}$, $\delta = 0.090465$, $B_0 = 2397.3\,\mathrm{nmol\,L^{-1}}$, $k_{re} = 0.0373\,\mathrm{min^{-1}}$. The true values are listed in Table 2.1.

considering now the modified initial conditions,

$$F_f(0) = F_{f0}, \qquad B(0) = B_0 - F_{b0}, \qquad F_b(0) = F_{b0}. \tag{2.45}$$

Due to total cortisol being the sum of free and bound cortisol, we have the relation,

$$F_0 = F_{f0} + F_{b0}. \tag{2.46}$$

We introduce a rescaled variable for the bound cortisol,

$$F_b = B_0 F_b', \tag{2.47}$$

and recall our previous dimensionless scalings for F_f and B given by eq. (2.20) and dimensionless parameter groupings given by eq. (2.21) to obtain the dimensionless system,

$$\frac{dF_f'}{dt'} = 1 - \frac{\beta}{\delta^2}F_f'B' + \frac{\beta}{\delta}F_b' - \rho F_f', \tag{2.48}$$

$$\frac{dB'}{dt'} = \quad - \frac{\beta}{\delta^2}F_f'B' + \frac{\beta}{\delta}F_b', \tag{2.49}$$

$$\frac{dF_b'}{dt'} = \quad + \frac{\beta}{\delta^2}F_f'B' - \frac{\beta}{\delta}F_b'. \tag{2.50}$$

Initially, we know that dimensionless free cortisol will be $\mathcal{O}(\delta)$ and so scale the system accordingly with $F_f' = \delta\hat{F}_f'$,

$$\delta\frac{d\hat{F}_f'}{dt'} = 1 - \frac{\beta}{\delta}\hat{F}_f'B' + \frac{\beta}{\delta}F_b' - \delta\rho\hat{F}_f', \tag{2.51}$$

$$\frac{dB'}{dt'} = \quad - \frac{\beta}{\delta}\hat{F}_f'B' + \frac{\beta}{\delta}F_b', \tag{2.52}$$

$$\frac{dF_b'}{dt'} = \quad + \frac{\beta}{\delta}\hat{F}_f'B' - \frac{\beta}{\delta}F_b'. \tag{2.53}$$

Hence we obtain the following leading order relation,

$$F_b' \approx \hat{F}_f'B'. \tag{2.54}$$

We sum eq. (2.52) and eq. (2.53) and use the initial condition to obtain a second relation,

$$B' + F_b' = 1. \tag{2.55}$$

We also substitute the initial conditions into eq. (2.54) to find the third relation,

$$F_{b0} \approx \frac{F_{f0}B_0}{\delta B_0 + F_{f0}}. \tag{2.56}$$

These three relations allow us to eliminate F_b from the system to leave us with the coupled system (returning to dimensional variables),

$$\frac{dF_f}{dt} = \frac{q(t)}{\alpha} - k_{fb}F_f B + k_{bf}\left(B_0 - B\right) - k_{re}F_f, \tag{2.57}$$

$$\frac{dB}{dt} = \qquad - k_{fb}F_f B + k_{bf}\left(B_0 - B\right). \tag{2.58}$$

with the initial conditions,

$$F_f(0) = \frac{-(\frac{k_{bf}}{k_{fb}} + B_0 - F_0) + \sqrt{(\frac{k_{bf}}{k_{fb}} + B_0 - F_0)^2 + 4\frac{k_{bf}}{k_{fb}}F_0}}{2}, \tag{2.59}$$

$$B(0) = \frac{k_{bf}B_0}{k_{fb}F_f(0) + k_{bf}}, \tag{2.60}$$

which we obtain by substituting eq. (2.56) into eq. (2.46) which yields a quadratic in F_{f0}:

$$F_{f0}^2 + (\delta B_0 + B_0 - F_0)F_{f0} - \delta B_0 F_0 = 0. \tag{2.61}$$

Identifiability

We now consider the identifiability of the extended model with an additional parameter F_0.

We proceed as before calculating the first 6 coefficients,

$$\Phi_1 = F(0) \qquad = F_0, \tag{2.62}$$

$$\Phi_2 = \left.\frac{dF}{dt}\right|_{t=0} = \frac{1}{2\alpha k_{fb}}\left(k_{fb}\left(\alpha k_{re}\left(B_0 - F_0\right) + 2q\right) - \alpha k_{re}\left(R - k_{bf}\right)\right), \tag{2.63}$$

$$\Phi_3 = \left.\frac{d^2F}{dt^2}\right|_{t=0} = -\frac{k_{re}}{2\alpha k_{fb}}\left(k_{fb}\left(\alpha k_{re}\left(B_0 - F_0\right) + 2q\right) - \alpha k_{re}\left(R - k_{bf}\right)\right), \tag{2.64}$$

$$= -k_{re}\Phi_2,$$

$$\Phi_4 = \left.\frac{d^3F}{dt^3}\right|_{t=0} = \frac{k_{re}}{2\alpha k_{fb}}\frac{\left(k_{fb}\left(\alpha k_{re}(B_0 - F_0) + 2q\right) - \alpha k_{re}\left(R - k_{bf}\right)\right)}{\left(-k_{fb}\left(B_0 - F_0\right) + R + k_{bf}\right)} \cdot \left(k_{fb}\left(2k_{bf}B_0 - k_{re}(B_0 - F_0)\right) + k_{re}\left(R + k_{bf}\right)\right) \tag{2.65}$$

$$= -\Phi_3\frac{\left(k_{fb}\left(2k_{bf}B_0 - k_{re}(B_0 - F_0)\right) + k_{re}\left(R + k_{bf}\right)\right)}{\left(-k_{fb}\left(B_0 - F_0\right) + R + k_{bf}\right)},$$

$$\Phi_5 = \left.\frac{d^4F}{dt^4}\right|_{t=0} = -\frac{k_{re}\left(-R\alpha k_{re} + \left(\alpha k_{re}(B_0 - F_0) + 2q\right)k_{fb} + \alpha k_{bf}k_{re}\right)}{\alpha k_{fb}\left(-\left(B_0 - F_0\right)k_{fb} + R + k_{bf}\right)^2}. \tag{2.66}$$

$$\left(R\left(-B_0k_{bf}k_{fb}^2\left(B_0 - F_0\right) + k_{fb}\left(B_0k_{bf}^2 + 2B_0k_{re}k_{bf} - k_{re}^2\left(B_0 - F_0\right)\right) + k_{bf}k_{re}^2\right) + B_0k_{bf}k_{fb}^3\left(B_0 - F_0\right)^2\right.$$

$$\left.+k_{fb}^2\left(2B_0\left(B_0 + F_0\right) - 2B_0k_{re}k_{bf}^2\left(B_0 - F_0\right)k_{bf} + k_{re}^2\left(B_0 - F_0\right)^2\right) + k_{bf}k_{fb}\left(B_0\,k_{bf}^2 + 2B_0k_{re}k_{bf} + 2F_0\,k_{re}^2\right) + k_{bf}^2k_{re}^2\right),$$

where,

$$R = \sqrt{\left(B_0 - F_0\right)^2k_{fb}^2 + 2k_{bf}\left(B_0 + F_0\right)k_{fb} + k_{bf}^2} \tag{2.67}$$

Maple is able to solve the set of algebraic equations in terms of the rational functions,

$$\alpha = qQ, \tag{2.68}$$

$$k_{fb} = -\frac{\Phi_2\Phi_4\Phi_6 - \Phi_2\Phi_5^2 - \Phi_3^2\Phi_6 + 2\Phi_3\Phi_4\Phi_5 - \Phi_4^3}{3\left(\Phi_2\Phi_4 - \Phi_3^2\right)^2}, \tag{2.69}$$

$$k_{bf} = -\frac{(\Phi_2\Phi_4 - \Phi_3^2)(Q\Phi_2 - 1)}{\Phi_3\left(Q\Phi_1\Phi_3 - R\Phi_2^2 + \Phi_2\right)}, \tag{2.70}$$

$$B_0 = \frac{Qd + \Phi_2^2(\Phi_2\Phi_4\Phi_6 - \Phi_2\Phi_5^2 - \Phi_3^2\Phi_6 + 2\Phi_3\Phi_4\Phi_5 - \Phi_4^3)}{Q\Phi_2\Phi_3\left(\Phi_2\Phi_4\Phi_6 - \Phi_2\Phi_5^2 - \Phi_3^2\Phi_6 + 2\Phi_3\Phi_4\Phi_5 - \Phi_4^3\right)}, \tag{2.71}$$

$$k_{re} = -\frac{\Phi_3}{\Phi_2}, \tag{2.72}$$

$$F_0 = \Phi_1, \tag{2.73}$$

where,

$$Q = RootOf\left((a)\_Z^2 + c + (b)\_Z\right), \tag{2.74}$$

$$\begin{aligned} a = {} & \Phi_1\Phi_2^3\Phi_3\Phi_4\Phi_6 - \Phi_1\Phi_2^3\Phi_3\Phi_5^2 - \Phi_1\Phi_2^2\Phi_3^3\Phi_6 - \Phi_1\Phi_2^2\Phi_3^2\Phi_4\Phi_5 + 2\Phi_1\Phi_2^2\Phi_3\Phi_4^3 \\ & + 3\Phi_1\Phi_2\Phi_3^4\Phi_5 - 3\Phi_1\Phi_2\Phi_3^3\Phi_4^2 - \Phi_2^5\Phi_4\Phi_6 + \Phi_2^5\Phi_5^2 + \Phi_2^4\Phi_3^2\Phi_6 + \Phi_2^4\Phi_3\Phi_4\Phi_5 \\ & + \Phi_2^4\Phi_4^3 - 3\Phi_2^3\Phi_3^3\Phi_5 - 6\Phi_2^3\Phi_3^2\Phi_4^2 + 9\Phi_2^2\Phi_3^4\Phi_4 - 3\Phi_2\Phi_3^6, \end{aligned} \tag{2.75}$$

$$\begin{aligned} b = {} & -\Phi_1\Phi_2^2\Phi_3\Phi_4\Phi_6 + \Phi_1\Phi_2^2\Phi_3\Phi_5^2 + \Phi_1\Phi_2\Phi_3^3\Phi_6 - 2\Phi_1\Phi_2\Phi_3^2\Phi_4\Phi_5 + \Phi_1\Phi_2\Phi_3\Phi_4^3 \\ & + 2\Phi_2^4\Phi_4\Phi_6 - 2\Phi_2^4\Phi_5^2 - 2\Phi_2^3\Phi_3^2\Phi_6 + \Phi_2^3\Phi_3\Phi_4\Phi_5 - 2\Phi_2^3\Phi_4^3 + 3\Phi_2^2\Phi_3^3\Phi_5 \\ & + 6\Phi_2^2\Phi_3^2\Phi_4^2 - 9\Phi_2\Phi_3^4\Phi_4 + 3\Phi_3^6, \end{aligned} \tag{2.76}$$

$$c = -\Phi_2^3\Phi_4\Phi_6 + \Phi_2^3\Phi_5^2 + \Phi_2^2\Phi_3^2\Phi_6 - 2\Phi_2^2\Phi_3\Phi_4\Phi_5 + \Phi_2^2\Phi_4^3. \tag{2.77}$$

As $k_{fb} > 0$, we must have,

$$\Phi_2\Phi_4\Phi_6 - \Phi_2\Phi_5^2 - \Phi_3^2\Phi_6 + 2\Phi_3\Phi_4\Phi_5 - \Phi_4^3 < 0, \tag{2.78}$$

which means we can rearrange c as,

$$c = -\Phi_2^2(\Phi_2\Phi_4\Phi_6 - \Phi_2\Phi_5^2 - \Phi_3^2\Phi_6 + 2\Phi_3\Phi_4\Phi_5 - \Phi_4^3) > 0 \tag{2.79}$$

From the expression for k_{re}, we also can say that Φ_2 and Φ_3 have opposite signs.

There are up to two solutions for Q so the system is structurally local identifiability. Numerically it can be shown that for sufficiently large q, only one of the roots will satisfy the constraint that all parameters are positive. Therefore the model is locally identifiable for all parameters and for a physically plausible input dose there is only 1 solution that satisfies positive constraints.

Initial investigation of the loss function as we have for the CIV$^{\pm}$ models shows that the behaviour is very similar between the original 5 parameters. A few ridges are apparent between the new parameter F_0 and the 3 parameters α, B_0 and k_{re}, however the calculated minima have not moved far from the true parameter pairs under high noise (see Figure E.1 in appendix E.1.1).

2.7 Discussion

In this section, we have found the CIV^{+} model to be structurally identifiable. However, the model is not practically identifiable under physically plausible levels of noise with low time-resolution data. Specifically, realistic levels of noise create identifiability issues in retrieving the binding and unbinding parameters, k_{fb} and k_{bf}. For small levels of additive noise, the binding and unbinding rate parameters can be uniquely determined if the time-resolution is sufficiently high. As noise increases, the ratio between binding and unbinding rates can be retrieved for high time-resolution. In appendix B.2, we begin to consider how the time sampling can be optimised to an individual, however we show therein that optimisation depends on *a priori* knowledge of the binding and unbinding rates.

Utilising the fast binding of cortisol to unbound binding protein allows a quasi-steady approximation that reduces the coupled model to a single ODE with 4 free parameters. This reduced model is structurally identifiable, but does not remove the practical identifiability issues discovered in the full model. In particular, large noise creates a problem with identifying δ, which is a parameter grouping quantifying the proportion of free to

bound cortisol. This parameter grouping is a combination of binding and unbinding, so the unidentifiability under large noise from the full model has been reduced from two parameters (k_{fb} and k_{bf}) to one (δ).

These results suggest that when looking for characteristics to inform an individual's optimum dosing regime, knowledge of the specific binding and unbinding rates may be of little practical use. Instead, having an estimate of the physiological level of binding protein would be more informative when predicting the response to CIV dosing as this parameter has more of an influence on the model trajectory and is also poorly estimated by frequentist methods.

We find that even with the addition of relatively small levels of noise atop the synthetic data, the loss function is no longer well-behaved and may create issues for frequentist methods of parameter recovery. Therefore we are motivated to investigate the use of Bayesian parameter inference methods so that parameter space can be more efficiently explored. Bayesian methods provide posterior distributions for parameter estimates which better quantifies the uncertainty of estimates and are easier to scale when increasing the model complexity.

Finally, the addition of a small initial level of free cortisol increased the complexity when considering structural identifiability. All parameters are found to be locally identifiable and that for a reasonably large dose of hydrocortisone, the model will have a single feasible solution due to the positive constraint on all model parameters. Assessing the loss function showed that behaviour was similar to the CIV$^{\pm}$ models. In summary, the addition of a low level of initial cortisol does not appear to introduce any major practical identifiability issues.

We now move to model the BIV dosing method, which consists of four intravenous bolus injections. Here, the input function $q(t)$ will no longer be continuous.

CHAPTER 3

INTRAVENOUS BOLUS INJECTIONS

We now look to another dosing regime in data [PD] which involved using an intravenous bolus dose of cortisol. This regime creates a very different trajectory in total cortisol so may offer more insight into the model parameters. Additionally, this method is less invasive than a continuous infusion and the multiple larger doses are more similar to the oral tablet regime. Tablets offer the most practical long-term management of adrenal insufficiency as they do not require hospital visits and provide patients with more control of their condition. Therefore, it would be beneficial if this regime provided sufficient information to predict patient response to differing dosing amounts and regimes.

We return to the one-compartment model,

$$\frac{dF_f}{dt} = \frac{1}{\alpha}q(t) - k_{fb}F_f B + k_{bf}(B_0 - B) - k_{re}F_f, \tag{3.1}$$

$$\frac{dB}{dt} = \qquad - k_{fb}F_f B + k_{bf}(B_0 - B), \tag{3.2}$$

where in place of the constant term used in the CIV case, we instead employ a step function for the dosing term,

$$q(t) = \begin{cases} D, & 0 \leq t \leq 1, \\ 0, & 1 < t. \end{cases} \tag{3.3}$$

In the [PD] study one intravenous bolus of 50 mg is administered at the start of every 6–

hour period. We approximate the delivery of an intravenous bolus to be around 1 minute. In all numerical simulations that follow, we will simulate the dosing method for the entire 24 hours by taking the end values of the previous 6–hour period and taking those to be initial conditions for the next dosing period.

From here on, we will refer to this system of equations as the BIV$^+$ model. In this chapter, we consider the structural identifiability of this system considering the alternative input function. We then assess the practical identifiability as in Chapter 2 for the BIV dosing method. Further, we reduce the BIV$^+$ model using matched asymptotic analysis by considering the dosing and post-dosing period separately and then analyse how these reductions impact the identifiability of model parameters.

3.1 Identifiability of the one-compartment BIV$^+$ model

To account for the step function dosing term, the complete model for the BIV dosing method can be written as four ODEs. The first two ODEs describe the dosing period (in the first minute) and the last two describe the post-dosing period (remaining time in a 6–hour period),

$$\frac{dF_f^D}{dt} = \frac{1}{\alpha}D - k_{fb}F_f^D B^D + k_{bf}(B_0 - B^D) - k_{re}F_f^D, \qquad F_f^D(0) = 0, \tag{3.4}$$

$$\frac{dB^D}{dt} = -k_{fb}F_f^D B^D + k_{bf}(B_0 - B^D), \qquad B^D(0) = B_0, \tag{3.5}$$

$$\frac{dF_f^{PD}}{dt} = -k_{fb}F_f^{PD} B^{PD} + k_{bf}(B_0 - B^{PD}) - k_{re}F_f^{PD}, \qquad F_f^{PD}(0) = \Omega_1, \tag{3.6}$$

$$\frac{dB^{PD}}{dt} = -k_{fb}F_f^{PD} B^{PD} + k_{bf}(B_0 - B^{PD}), \qquad B^{PD}(0) = \Omega_2. \tag{3.7}$$

Later we will find a asymptotically reduced solution (eq. (3.38)) which yields,

$$\Omega_1 = \frac{1}{\alpha}D - B_0, \qquad \Omega_2 = \frac{\alpha k_{bf} B_0}{k_{fb}(D - \alpha B_0)}, \tag{3.8}$$

however, in practice we find Ω_1 and Ω_2 numerically. If we assume that the observed variables are,

$$\boldsymbol{y} = [F_f^D + B_0 - B^D, F_f^{PD} + B_0 - B^{PD}], \tag{3.9}$$

then STIKE_GOLDD concludes that the model is structurally locally identifiable. This is expected as the structural identifiability test assumes there will be time points in the dosing period which is the same as the CIV$^+$ model and all parameters were found to be identifiable.

3.2 Non-dimensionalisation of the BIV$^+$ model

For the BIV case, we take the following scalings,

$$F_f = B_0 F_f', \qquad B = B_0 B', \qquad t = \tau t', \qquad q(t) = \frac{D}{\tau} q'(t'), \tag{3.10}$$

where the timescale, τ, is now based upon the dosing time of the intravenous bolus, which is of the order of 1 minute. We define the following dimensionless groupings,

$$\delta = \frac{k_{bf}}{k_{fb} B_0}, \qquad \beta = \frac{k_{bf}^2 \tau}{k_{fb} B_0}, \qquad \rho = \frac{\alpha B_0}{D}, \tag{3.11}$$

where we have retained the small parameter grouping δ, and β remains an $\mathcal{O}(1)$ parameter grouping. The parameter grouping ρ has been adjusted to account for the bolus dose. Substituting (eq. (3.11)) alongside the (temporarily defined) additional scaling $\mu = k_{re}\tau$ into the full system eqs. (3.1) and (3.2) yields the dimensionless system,

$$\frac{dF_f'}{dt'} = \rho^{-1} q'(t') - \frac{\beta}{\delta^2} F_f' B' + \frac{\beta}{\delta}(1 - B') - \mu F_f', \tag{3.12}$$

$$\frac{dB'}{dt'} = - \frac{\beta}{\delta^2} F_f' B' + \frac{\beta}{\delta}(1 - B'). \tag{3.13}$$

We will establish the as-yet unknown group μ through considering the relationship with the other parameter groupings in the long-time solution, which will allow us to estimate the order of magnitude of μ. Long after the dose is administered, free cortisol will be almost all removed and the binding protein will be returning to pre-dosing levels. Hence, unoccupied binding protein will be $\mathcal{O}(1)$ and free cortisol will be $\mathcal{O}(\delta)$. As we are looking at long-time, we also have time as $\mathcal{O}(\delta^{-1})$. The scalings are therefore,

$$F_f' = \delta \bar{F}_f', \qquad B' = \bar{B}', \qquad t' = \delta^{-1}\bar{t}' \tag{3.14}$$

The rescaled system becomes,

$$\delta^2 \frac{d\bar{F}_f'}{d\bar{t}'} = -\frac{\beta}{\delta}\bar{F}_f'\bar{B}' + \frac{\beta}{\delta}(1-\bar{B}') - \mu\delta\bar{F}_f', \tag{3.15}$$

$$\delta \frac{d\bar{B}'}{d\bar{t}'} = -\frac{\beta}{\delta}\bar{F}_f'\bar{B}' + \frac{\beta}{\delta}(1-\bar{B}'). \tag{3.16}$$

Therefore, at leading order we have the relation,

$$\bar{F}_{f0}' = \frac{1-\bar{B}_0'}{\bar{B}_0'} \tag{3.17}$$

Subtracting (eq. (3.16)) from (eq. (3.15)),

$$\delta \frac{d\bar{F}_f'}{d\bar{t}'} - \frac{d\bar{B}'}{d\bar{t}'} = -\mu\bar{F}_f', \tag{3.18}$$

so at leading order we find a separable equation with solution,

$$\bar{B}_0' = 1 + W_0(-A\exp(-\mu\bar{t}')), \tag{3.19}$$

where A is an integration constant and W_0 is the principal branch of the Lambert W function. Considering the term within the exponential and returning back to dimensional

variables, we have,

$$\mu\bar{t}' = k_{re}\tau\delta t' = k_{re}\frac{k_{bf}}{k_{fb}B_0}t. \tag{3.20}$$

From data [PD] it can be seen that a patient's total cortisol level does not entirely return to zero by the time of the next intravenous bolus injection so the removal of cortisol is happening over at least 6 hours. Therefore, we suggest that k_{re} is of roughly the order of tens of hours. Additionally, as discussed in section 2.2, binding happens approximately 10 times faster than unbinding. This means that the term $\mu = k_{re}\tau$ is of a similar order of magnitude to δ and so state that,

$$\mu = \psi\delta, \tag{3.21}$$

where we define a $\mathcal{O}(1)$ parameter grouping,

$$\psi := k_{re}\tau\frac{k_{fb}B_0}{k_{bf}}. \tag{3.22}$$

Finally, we substitute this new parameter grouping ψ into the dimensionless model to yield,

$$\frac{dF_f'}{dt'} = \rho^{-1}q'(t') - \frac{\beta}{\delta^2}F_f'B' + \frac{\beta}{\delta}(1-B') - \delta\psi F_f', \tag{3.23}$$

$$\frac{dB'}{dt'} = \qquad\qquad - \frac{\beta}{\delta^2}F_f'B' + \frac{\beta}{\delta}(1-B'). \tag{3.24}$$

This BIV dimensionless system accounts for the much-faster dosing than removal rate as the dosing and removal terms are no longer of comparable order in eq. (3.23), unlike the CIV case (see eq. (2.22)). As with the CIV case, we now consider the numerical solution of the system within physically appropriate parameter ranges.

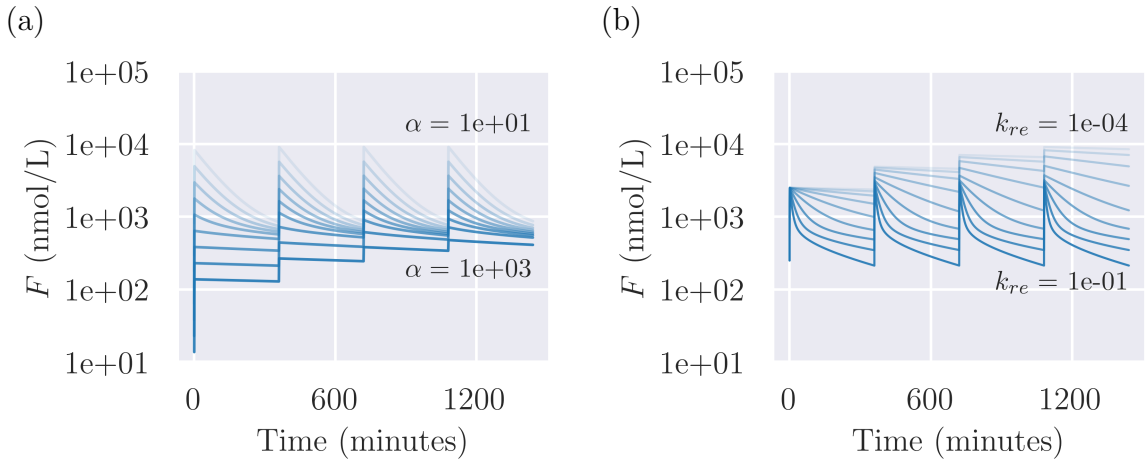

Figure 3.1: Evolution of total cortisol concentration, F, in time when varying model parameters for the BIV$^+$ model given by eqs. (3.1) and (3.2). Fixed values of parameters: $\alpha = 55\,\mathrm{L}$, $k_{fb} = 0.1\,\mathrm{L\,nmol^{-1}\,min^{-1}}$, $k_{bf} = 1\,\mathrm{min^{-1}}$, $B_0 = 650\,\mathrm{nmol\,L^{-1}}$, $k_{re} = 0.01\,\mathrm{min^{-1}}$: (a) varying dilution factor α, (b) varying rate of removal of free cortisol k_{re}.

3.3 Simulating cortisol response under intravenous bolus injections

Figure 3.1 shows the trajectory of total cortisol concentration for the dimensional paired model given by eqs. (3.1) and (3.2) when varying the dilution factor and the removal rate. We find a larger dilution factor leads to a lower concentration of total cortisol as in the CIV$^+$ model. In contrast to the CIV$^+$ model, the total cortisol does not reach a steady state by 6 hours when the next dose is delivered for these parameter values, so we see a higher peak in total cortisol for the subsequent doses compared to the first.

Figure 3.2(a) shows the total cortisol trajectory when varying the physiological level of unoccupied binding protein. It can be seen that when B_0 is large (therefore δ is correspondingly small), the binding protein is not saturated over the course of a single dose. In particular when $B_0 = 10^5$, the total level of cortisol continues to increase for all 4 doses due to the entirety of the free cortisol binding to the protein and so less is removed from the system. We also see in Figure 3.2(b) that when varying the unbinding rate k_{bf}, the total cortisol levels are very similar, although the trajectory begins to qualitatively change (total cortisol reaches a lower value at the end of each 6 hour period) when $k_{bf} = 10$.

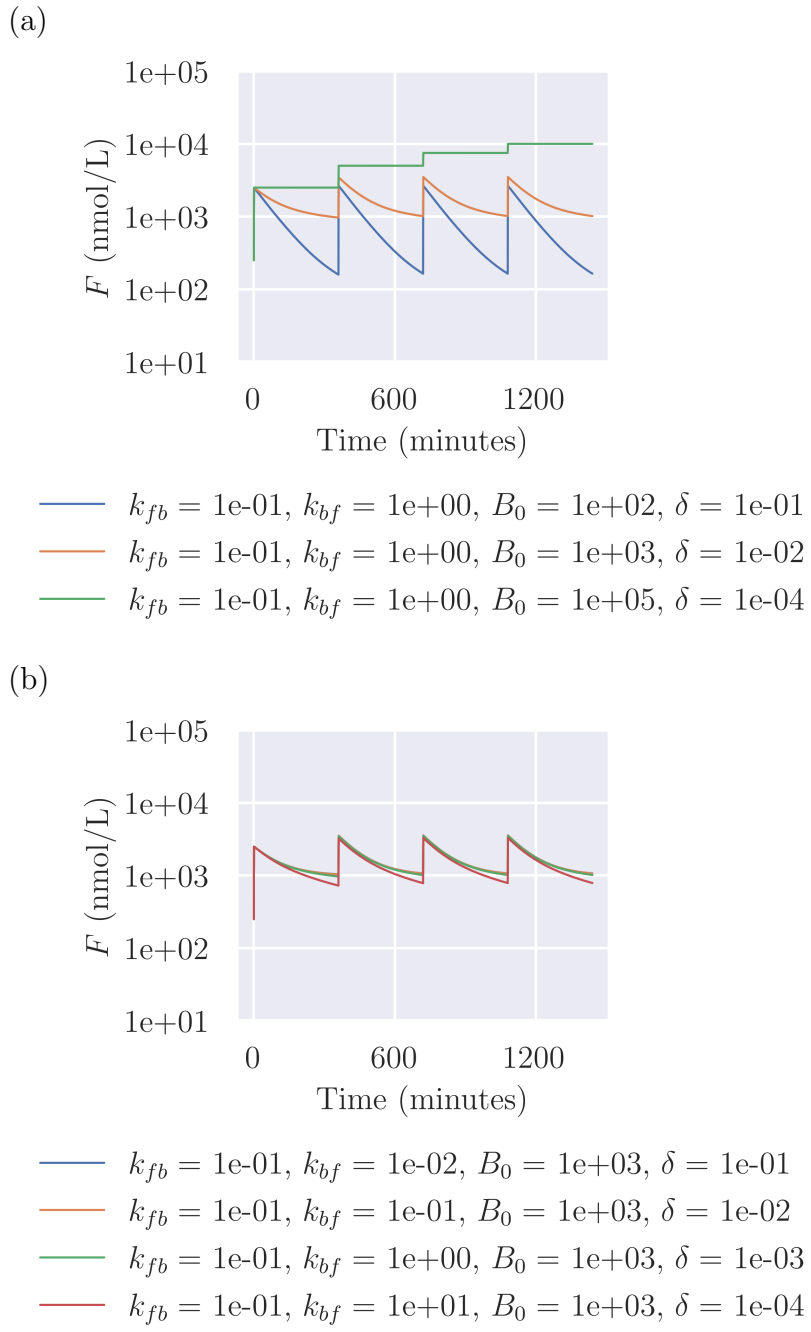

Figure 3.2: Evolution of total cortisol concentration, F, in time when varying model parameters for the BIV$^+$ model given by eqs. (3.1) and (3.2). Fixed values of parameters: $\alpha = 55\,\mathrm{L}$, $k_{re} = 0.01\,\mathrm{min}$. (a) varying physiological level of binding protein B_0, (b) varying unbinding rate k_{bf}. Blue, orange and green lines all exhibit similar behaviour. The trajectory begins to qualitatively change for the red line when $k_{bf} = 10$.

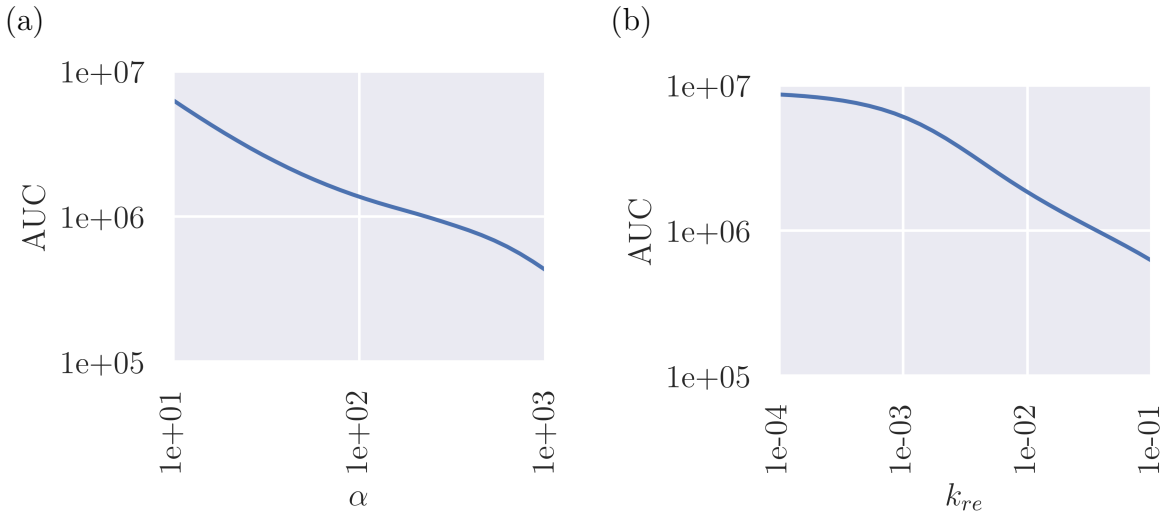

Figure 3.3: Area under the curve for total cortisol concentration, F, over a 24–hour period with varying model parameters for the BIV$^+$ model given by eqs. (3.1) and (3.2). Fixed values of parameters: $\alpha = 55\,\mathrm{L}$, $k_{fb} = 0.1\,\mathrm{L\,nmol^{-1}\,min^{-1}}$, $k_{bf} = 1\,\mathrm{min^{-1}}$, $B_0 = 650\,\mathrm{nmol\,L^{-1}}$, $k_{re} = 0.01\,\mathrm{min^{-1}}$: (a) varying dilution factor α, (b) varying rate of removal of free cortisol k_{re}.

The AUC of total cortisol concentration over a 24–hour period for varying each parameter is shown in Figures 3.3 and 3.4. As expected, they show similar behaviour to the CIV dosing regime as over 24 hours the same amount of cortisol is being delivered.

3.4 Practical identifiability of the BIV$^+$ model using simulated data

We now consider whether this model will behave similarly to the models CIV$^\pm$ under noise, that is, whether the practical identifiability issues that arose in Section 2.4 are apparent for intravenous bolus dosing. Looking at the behaviour in the previous section suggests that the BIV$^+$ model may be able to retain more information about the binding/unbinding ratio than the CIV$^\pm$ models. In Figure 3.2(b), there are more qualitative changes at the end of each 6–hour section compared to Figure 2.4(b) where the trajectories are very similar for varying δ.

Figure 3.5 shows the loss function behaviour relative to the number of time points as each parameter varies individually. In this case, the synthetic data points have no

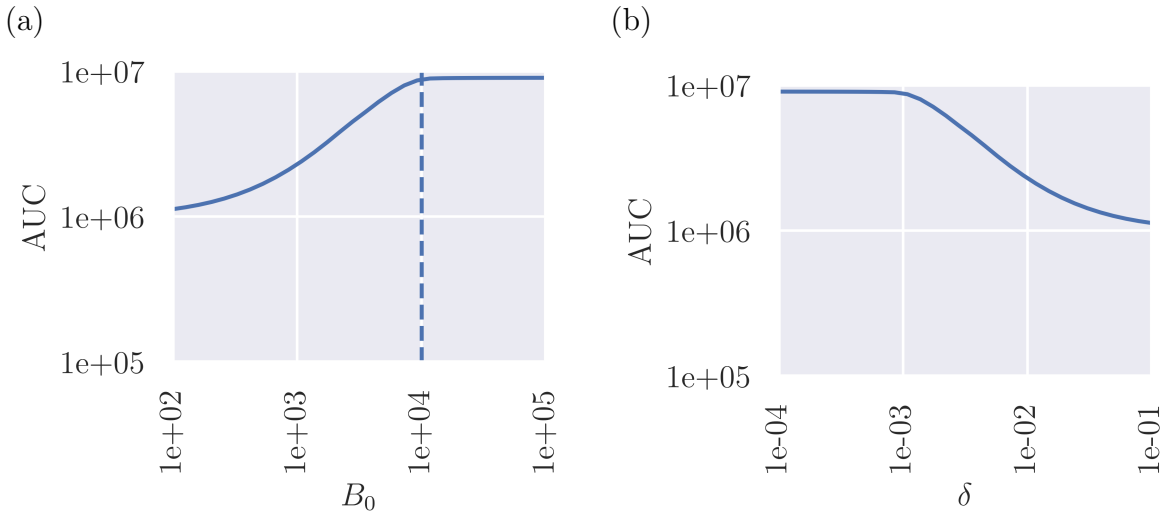

Figure 3.4: Area under the curve for total cortisol concentration, F, over a 24–hour period with varying B_0 for the BIV$^+$ model given by eqs. (3.1) and (3.2). Fixed values of parameters: $\alpha = 55\,\mathrm{L}$, $k_{fb} = 0.1\,\mathrm{L\,nmol^{-1}\,min^{-1}}$, $k_{bf} = 1\,\mathrm{min^{-1}}$, $k_{re} = 0.01\,\mathrm{min^{-1}}$.

noise added and the time resolution ranges from 0.01-100 time points per minute. For each parameter, there is a single clear minimum in the loss function that corresponds to the true value of each parameter. Differing from the CIV case marginally, the BIV loss function does become sharper around the true value of each parameter for higher number of time points. Therefore, time resolution has more of an influence in identifying true parameter values for an intravenous bolus compared to a continuous infusion. This is likely because at low time resolution (0.01 time points per minute) time measurements are not taken during the dosing period where the concentration of binding protein and free cortisol are rapidly changing.

Considering the loss function behaviour when varying pairs of parameters (Figure 3.6), the calculated minimum in the loss function matches the true values of each parameter for all pairs. The overall behaviour here is similar to the CIV case, however the loss function in Figure 3.6(d) is much less smooth than the CIV case.

We take a closer look at the loss function along the ridge between k_{fb} and k_{bf} relative to the number of time points (see Figure 3.7(a)). As in the CIV case, there is a distinct minimum corresponding to the true value of k_{fb} and k_{bf} regardless of number of time points (see Figure 3.7(b)). The loss function is no longer well-behaved which is likely to

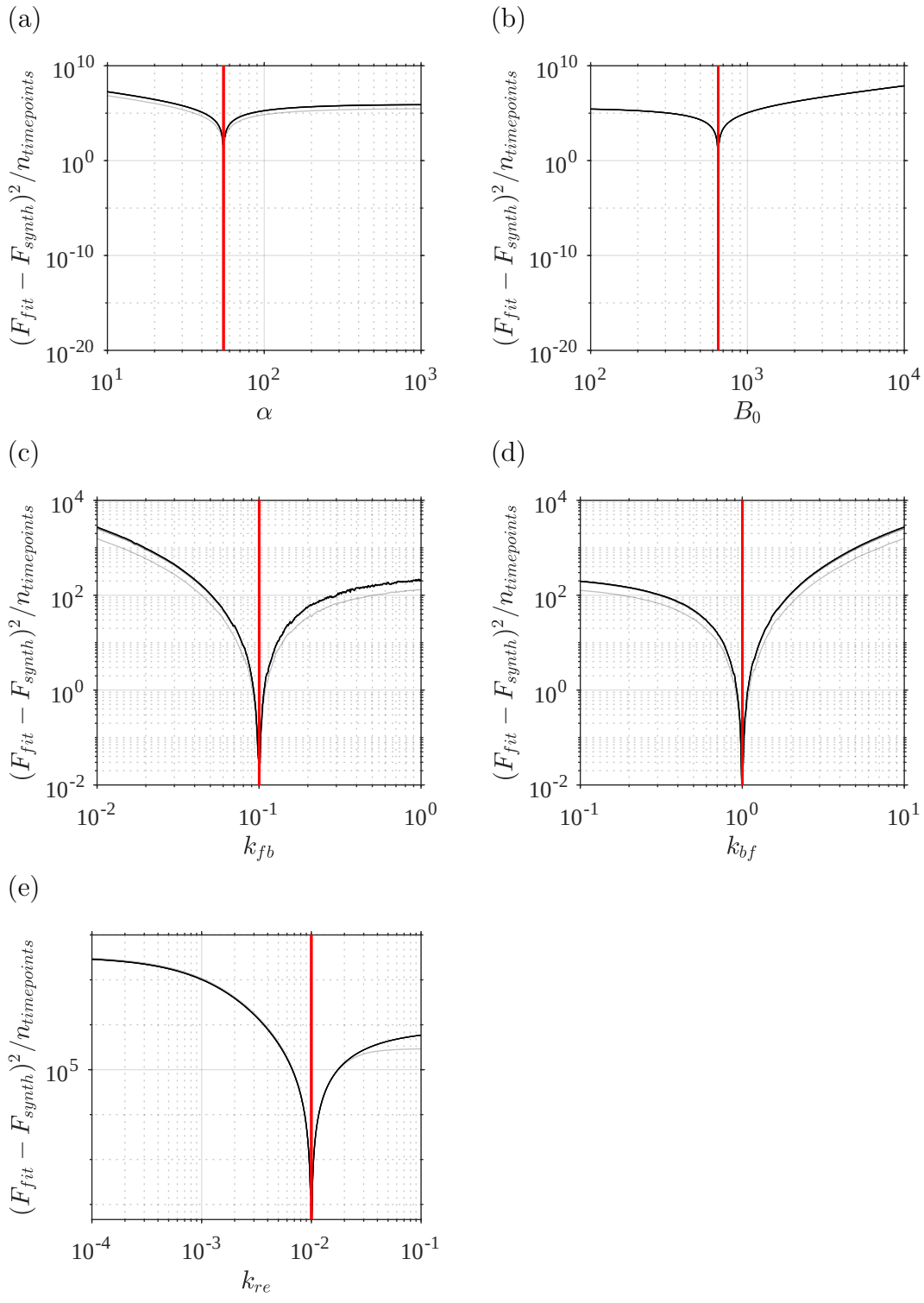

Figure 3.5: Loss function relative to sampling frequency for varying model parameters for the BIV$^+$ model given by eqs. (3.1) and (3.2) with zero noise added to synthetic data and sampling time frequency ranging from 0.01-100 time points per minute: (a) varying α, (b) varying B_0, (c) varying k_{fb}, (d) varying k_{bf}, (e) varying k_{re}. The red vertical line indicates the true parameter value.

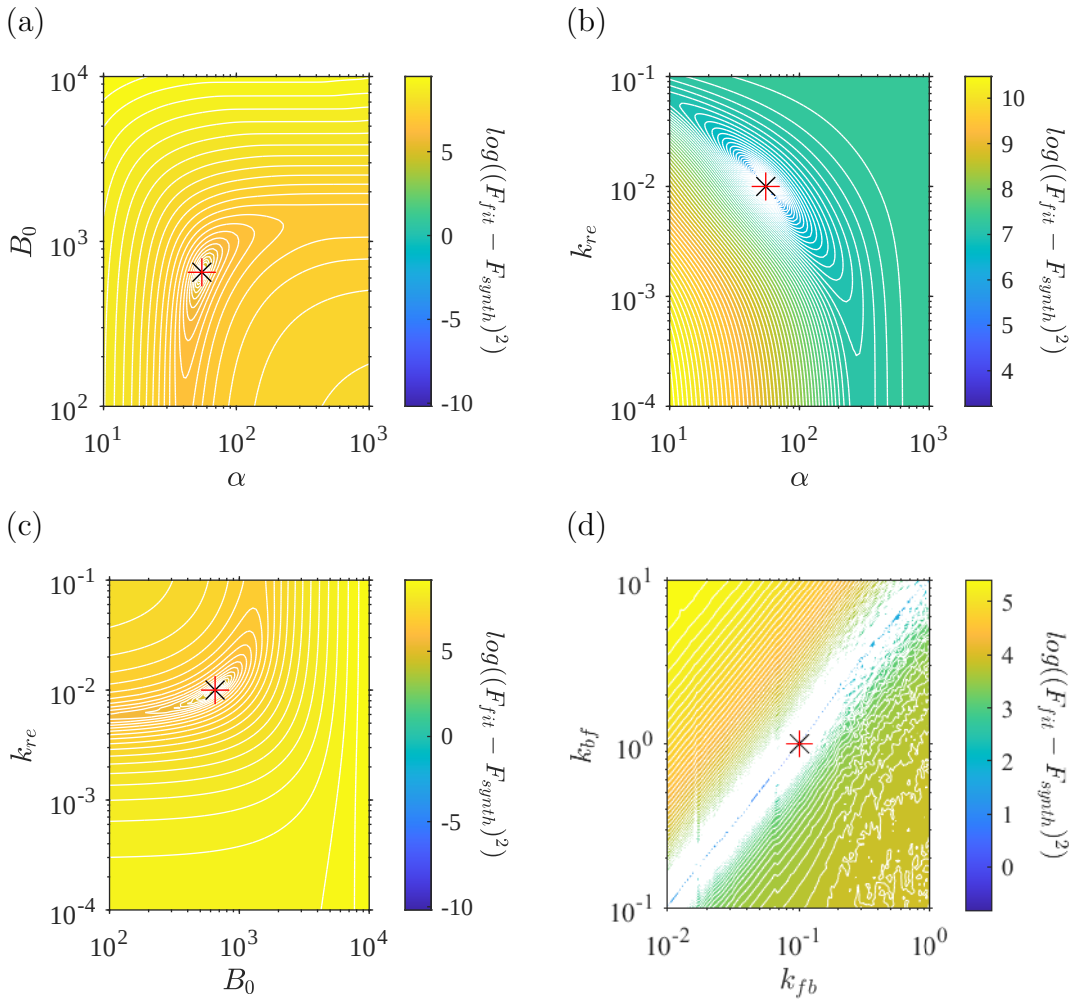

Figure 3.6: Loss function for varying pairs of model parameters for the BIV$^+$ model given by eqs. (3.1) and (3.2) with zero noise added to synthetic data and sampling time frequency corresponding to the time points used in data [PD]. The red plus indicates the true parameter value pair, while the loss function calculated minimum is shown with a black cross: (a) α versus B_0, (b) α versus k_{re}, (c) B_0 versus k_{re}, (d) k_{fb} versus k_{bf}.

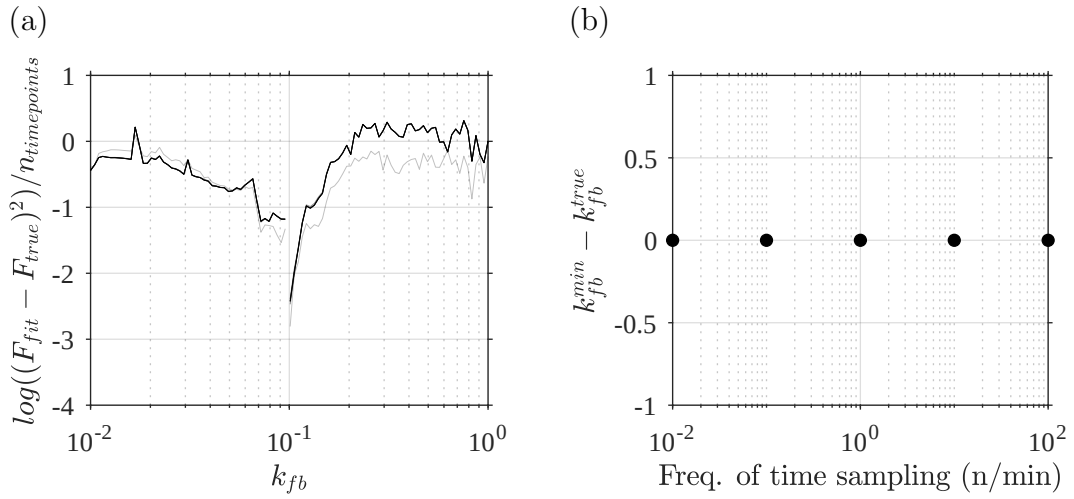

Figure 3.7: Varying k_{fb} and k_{bf} for the BIV$^+$ model given by eqs. (3.1) and (3.2) with zero noise added to synthetic data and sampling time frequency ranging from 0.01-100 time points per minute: (a) loss function relative to sampling frequency, (b) difference between true parameter value for k_{fb} and corresponding k_{fb} value that generates minimum loss function.

create problems when optimising, however the numerical minimum is easier to identify than in the CIV case (see Figure 2.9(a)).

As for the CIV case, we consider adding a small additive error term with standard deviation $1\,\text{nmol}\,\text{L}^{-1}$ and consider a time resolution that matches data [PD]. Figure 3.8(a) shows that the true value of k_{fb} is a small distance from the calculated minimum of the loss function when fixing the other 4 parameters with this small level of noise. Figure 3.8(b) shows that the calculated minimum has also moved a small distance from the true parameter values when varying both k_{fb} and k_{bf}, but this distance is smaller than in the CIV case. Additionally, there is a slight increase in the width of the ridge between the binding and unbinding rate parameters k_{fb} and k_{bf}.

Across the other pairs of model parameters, ridges begin to appear within the loss functions for even a small amount of noise (Figure 3.9) but these pairs show similar behaviour to the CIV case. In Figure 3.9(a), the calculated minimum point for the pairing (k_{fb}, B_0) no longer matches with the true parameter values, but there is still a match for (α, k_{re}). However we note that for BIV dosing, the loss function is more robust to values of B_0 compared to the CIV case (Figure 2.11(a)). The ridge is flat in the BIV

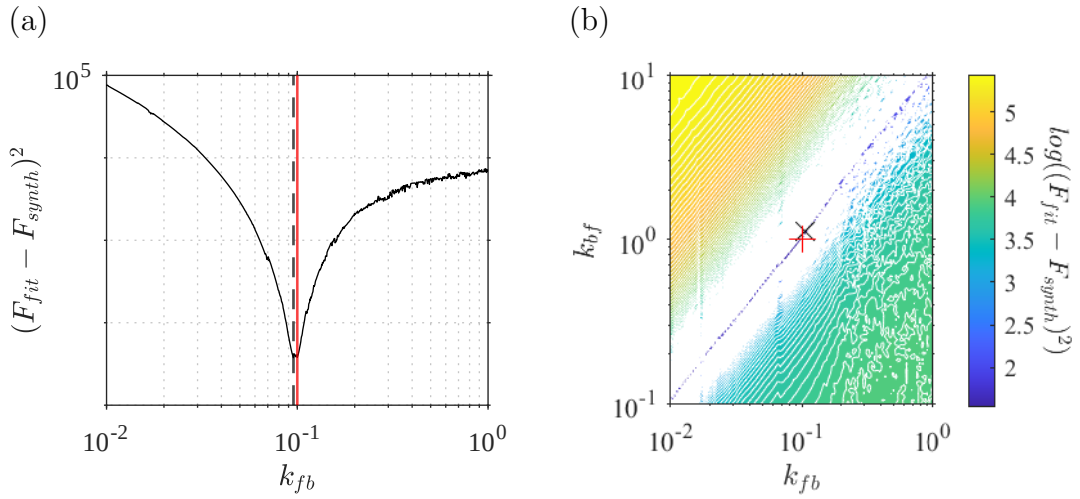

Figure 3.8: Loss function for varying model parameters for the BIV$^+$ model given by eqs. (3.1) and (3.2) with Gaussian noise added (s.d. $1\,\mathrm{nmol\,L^{-1}}$) and sampling time frequency corresponding to the time points used in data [PD]: (a) varying k_{fb} only. The red line indicates the true value of k_{fb}, while the calculated minimum is shown by the black dashed line, (b) k_{fb} versus k_{bf}. The red plus indicates the true parameter value pair, while the loss function calculated minimum is shown with a black cross.

case (matching the true B_0 value) however is slghtly curved in the CIV case, suggesting that the BIV case will be better able to recover the value of B_0.

By increasing the time-resolution of the data points with this small amount of noise, it becomes possible to identify the individual values of binding and unbinding rate parameters k_{fb} and k_{bf}. Figure 3.10(a) shows the loss function appears to maintain a minimum closer to the true value of k_{fb} unlike the CIV case which is near flat even at small noise.

However Figure 3.10 shows that with increasing time resolution the minimum for the loss function becomes closer to the true value of k_{fb} (and similarly k_{bf}) and crucially at 1 time point per minute and higher the minimum in the loss function corresponds to the true value of k_{fb}. A time resolution of 1 time point per minute indicates that we capture a single value at the end of the dosing period.

As previously, we now consider increasing the error further to a more plausible physical value for data [PD] ($\sim 100\,\mathrm{nmol\,L^{-1}}$). Figure 3.11(a) shows that when varying the binding rate k_{fb} and fixing the other four parameters, the value of k_{fb} that corresponds to the minimum in the loss function no longer matches the true value with a larger shift than was

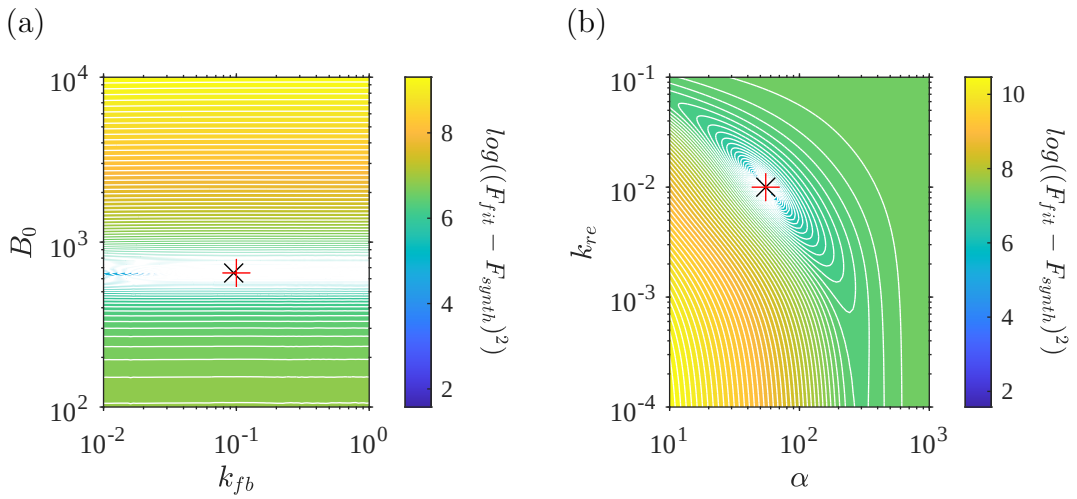

Figure 3.9: Loss function for varying pairs of model parameters for the BIV$^+$ model given by eqs. (3.1) and (3.2) with Gaussian noise (s.d. $1\,\mathrm{nmol\,L^{-1}}$) added to synthetic data and sampling time frequency corresponding to the time points used in data [PD]. The red plus indicates the true parameter value pair, while the loss function calculated minimum is shown with a black cross: (a) k_{fb} versus B_0, (b) α versus k_{re}.

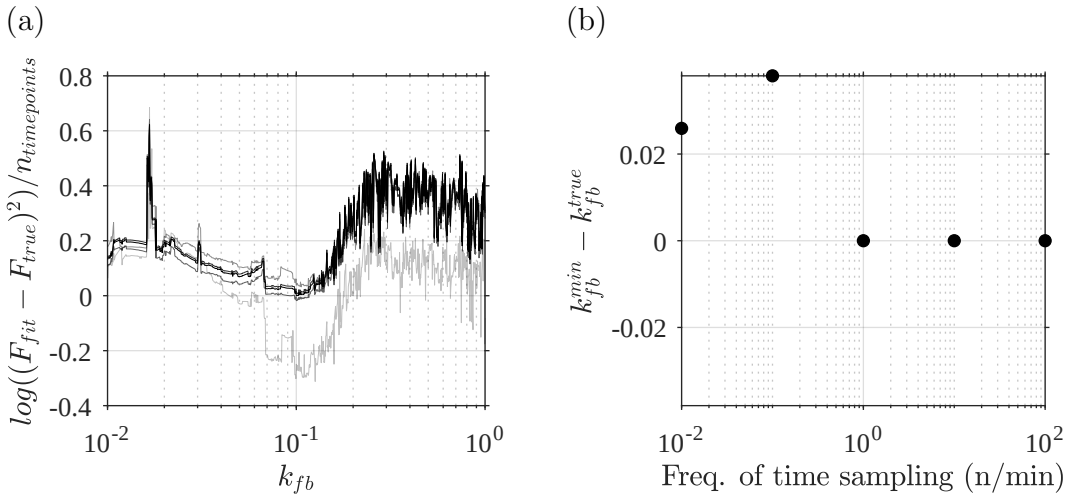

Figure 3.10: Varying k_{fb} and k_{bf} for the BIV$^+$ model given by eqs. (3.1) and (3.2) with Gaussian noise (s.d. $1\,\mathrm{nmol\,L^{-1}}$) added to synthetic data and sampling time frequency ranging from 0.01-100 time points per minute: (a) loss function relative to sampling frequency with darker lines indicating a higher time resolution, (b) difference between true parameter value for k_{fb} and corresponding k_{fb} value that generates minimum loss function.

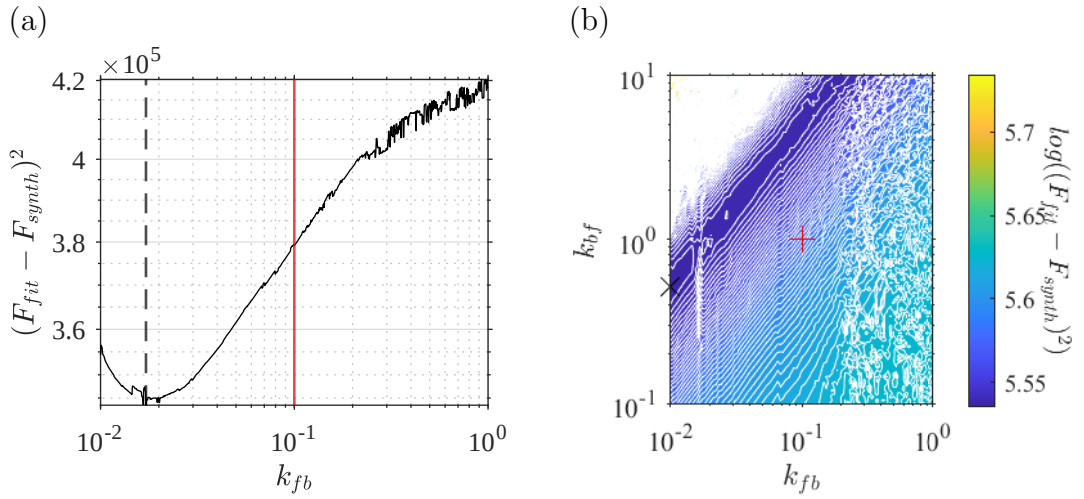

Figure 3.11: Loss function for varying model parameters for the BIV$^+$ model given by eqs. (3.1) and (3.2) with Gaussian noise added (s.d. 100 nmol L^{-1}) and sampling time frequency corresponding to the time points used in data [PD]: (a) varying k_{fb} only. The red line indicates the true value of k_{fb}, while the calculated minimum is shown by the black dashed line, (b) k_{fb} versus k_{bf}. The red plus indicates the true parameter value pair, while the loss function calculated minimum is shown with a black cross.

found for the CIV case. Figure 3.11(b) shows that the minimum ridge has shifted from where the true values of k_{fb} and k_{bf} lie. In the CIV case we had a flat plane at this level of noise but for BIV$^+$ dosing the ridge has shifted away from the true ratio. This suggests that we may be unable to retrieve the correct ratio between binding and unbinding rate parameters when parameter fitting in addition to not being able to retrieve the individual parameter values.

We find that the loss function is much smoother when using finer time sampling of every 10 minutes which roughly simulates the current ability of implantable or wearable sensors (see Figure 3.12(a)) [52, 53]. The ridge has returned to around the true ratio between unbinding and binding rates allowing a closer estimate to be found. We also find similar behaviour when sampling more finely (5 time points in 1 minute) within the dosing period only (and using the same time points as data [PD] in the post dosing region) (see Figure 3.12(b)). This sampling regime has roughly half the points of the uniform time sampling however finds a narrower ridge around the true ratio line, suggesting that key information about the binding and unbinding rates is lost when sampling the post dosing

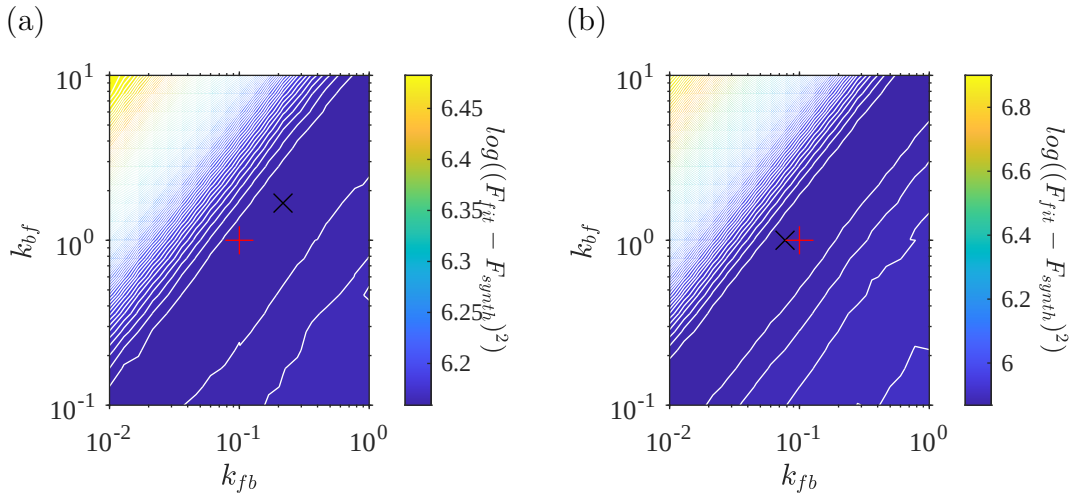

Figure 3.12: Loss function for varying model parameters for the BIV$^+$ model given by eqs. (3.1) and (3.2) with Gaussian noise added (s.d. 100 nmol L^{-1}) for varying k_{fb} and k_{bf}: (a) sampling time frequency every 10 minutes. (b) time points as in data [PD] plus 10 time points in the first minute of each dosing period. The red plus indicates the true parameter value pair, while the loss function calculated minimum is shown with a black cross.

region only.

Frequentist parameter recovery

Once again using the MultiStart algorithm in MATLAB, we consider how well the estimates match the true parameter values for varying levels of noise. For zero to small noise, the parameter estimates and model fit is good (see Figure 3.13). The model fit remains good in Figure 3.14 for large Gaussian noise and the parameter estimates are improved from the CIV case. The estimate for B_0 is much closer to the true value and the ratio between k_{bf}/k_{fb} has remained close to the true value. The qualitative behaviour of the trajectory in the BIV case is more sensitive to the unbinding rate k_{bf}, which restricts the estimate for B_0 while maintaining a physically feasible value of δ.

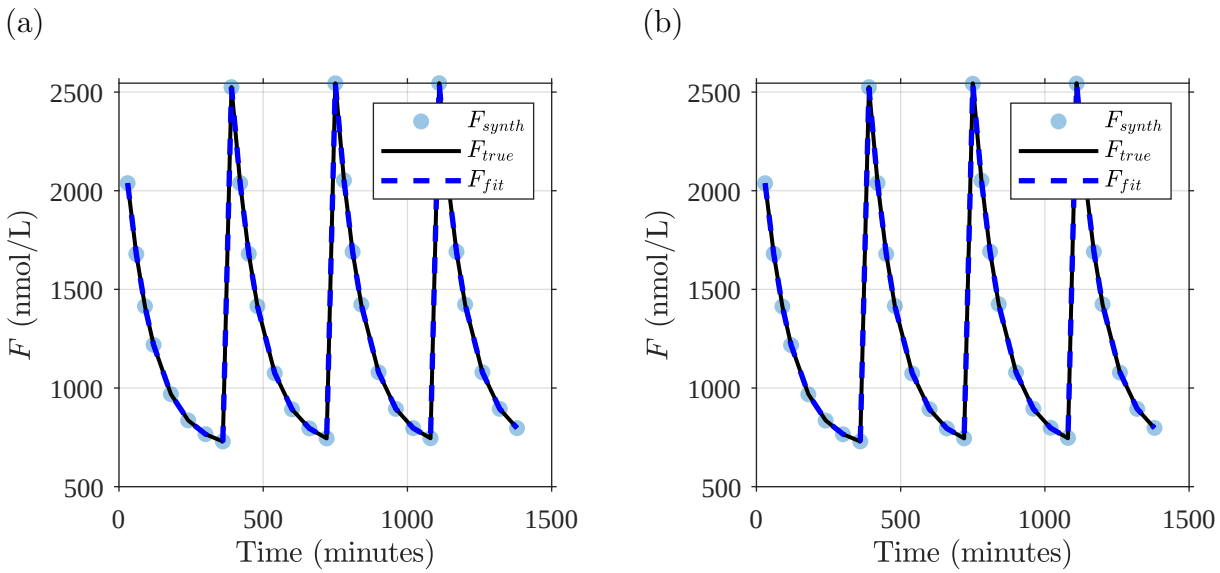

Figure 3.13: Frequentist fit of model trajectory of total cortisol, F, with sampling time frequency corresponding to the time points used in data [PD] for the BIV$^+$ model given by eqs. (3.1) and (3.2) for all 5 model parameters: (a) zero noise. Parameter estimates are $\alpha = 55\,\mathrm{L}$, $k_{fb} = 0.1\,\mathrm{L\,nmol^{-1}\,min^{-1}}$, $k_{bf} = 1\,\mathrm{min^{-1}}$, $B_0 = 650\,\mathrm{nmol\,L^{-1}}$, $k_{re} = 0.01\,\mathrm{min^{-1}}$. (b) Gaussian noise added (s.d. $1\,\mathrm{nmol\,L^{-1}}$). Parameter estimates are $\alpha = 54.966\,\mathrm{L}$, $k_{fb} = 0.0121\,\mathrm{L\,nmol^{-1}\,min^{-1}}$, $k_{bf} = 0.132\,\mathrm{min^{-1}}$, $B_0 = 649.51\,\mathrm{nmol\,L^{-1}}$, $k_{re} = 0.010\,\mathrm{min^{-1}}$ with a resulting ratio of $k_{bf}/k_{fb} = 10.9$. The true values are listed in Table 2.1.

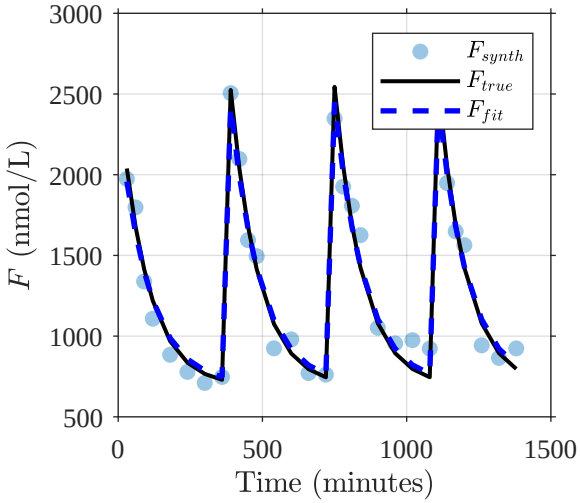

Figure 3.14: Frequentist fit of model trajectory of total cortisol, F, with Gaussian noise added (s.d. $100\,\mathrm{nmol\,L^{-1}}$) and sampling time frequency corresponding to the time points used in data [PD] for the BIV$^+$ model given by eqs. (3.1) and (3.2) for all 5 model parameters. Parameter estimates are $\alpha = 58.565\,\mathrm{L}$, $k_{fb} = 0.010\,\mathrm{L\,nmol^{-1}\,min^{-1}}$, $k_{bf} = 0.290\,\mathrm{min^{-1}}$, $B_0 = 637.45\,\mathrm{nmol\,L^{-1}}$, $k_{re} = 0.009\,27\,\mathrm{min^{-1}}$ with a resulting ratio $k_{bf}/k_{fb} = 29$. The true values are listed in Table 2.1.

3.5 The reduced BIV$^-$ model

We seek to reduce the BIV$^+$ model to aid parameter inference. The addition of a step function dosing function means that the BIV$^+$ model is approximately 3 times slower to solve than the CIV$^+$ model, so a reduction in computation time would be beneficial for both local optimiser algorithms and for Bayesian inference which require the ODEs to be solved thousands of times.

For the BIV case, we initially consider a single dose.

3.5.1 Dosing period

Initial Binding

Recalling the dimensionless system for the BIV dosing method,

$$\frac{dF_f'}{dt'} = \rho^{-1}q'(t') - \frac{\beta}{\delta^2}F_f'B' + \frac{\beta}{\delta}(1-B') - \delta\psi F_f', \tag{3.25}$$

$$\frac{dB'}{dt'} = - \frac{\beta}{\delta^2}F_f'B' + \frac{\beta}{\delta}(1-B'). \tag{3.26}$$

We initially consider the first minute during which the input dose is non-zero. The first region that can be identified is when both independent variable t' and dependent variables F_f', B' are order 1. Seeking a solution of the form,

$$F_f' = F_{f0}' + \delta F_{f1}' + \cdots, \qquad B' = B_0' + \delta B_1' + \cdots, \tag{3.27}$$

we find a leading order relation,

$$F_{f0}'B_0' \approx 0. \tag{3.28}$$

We know initially that the level of unoccupied binding protein is equal to B_0, hence we assume that $F_{f0}' = 0$. Subtracting eq. (3.26) from eq. (3.25) yields a single, easily solvable

ODE for B_0',

$$\frac{dB_0'}{dt'} = -\rho^{-1}q'(t'), \tag{3.29}$$

where $q'(t') = 1$ and hence,

$$B_0' = -\rho^{-1}t' + c. \tag{3.30}$$

Using the initial condition, we find $c = 1$. Taking next order terms we find an expression for F_{f1}' and find the leading order solution for this region,

$$F_f' = \delta\frac{t'}{\rho - t'} + \mathcal{O}(\delta^2), \qquad\qquad B' = \frac{\rho - t'}{\rho} + \mathcal{O}(\delta). \tag{3.31}$$

where the integration constant has been determined using the initial condition, however this would change for subsequent doses.

This solution tends to infinity as $t' \to \rho$, ($t \to \frac{B_0\tau}{\alpha D}$). This asymptotic approximation is compared to the numerical solution of the system (calculated with the stiff solver "bdf" in Python) in Figure 3.15, with $\delta = 0.01$ and $\rho = 0.53$. The initial binding solution very closely follows the numerical solution but begins to diverge on the approach to $t' = \rho$ as expected. When the dose does not saturate binding protein, this will cause no issue. However, once the dose saturates binding protein, then another region appears which will need consideration.

Increase in free cortisol

At the end of the dosing period, the binding protein has been saturated and free cortisol is now beginning to increase rapidly. We therefore suggest the new scalings,

$$F_f' = \tilde{F}_f', \qquad B' = \delta\tilde{B}', \qquad t' = \tilde{t}' + t_{cr}, \qquad q'(t') = \tilde{q}'(\tilde{t}'), \tag{3.32}$$

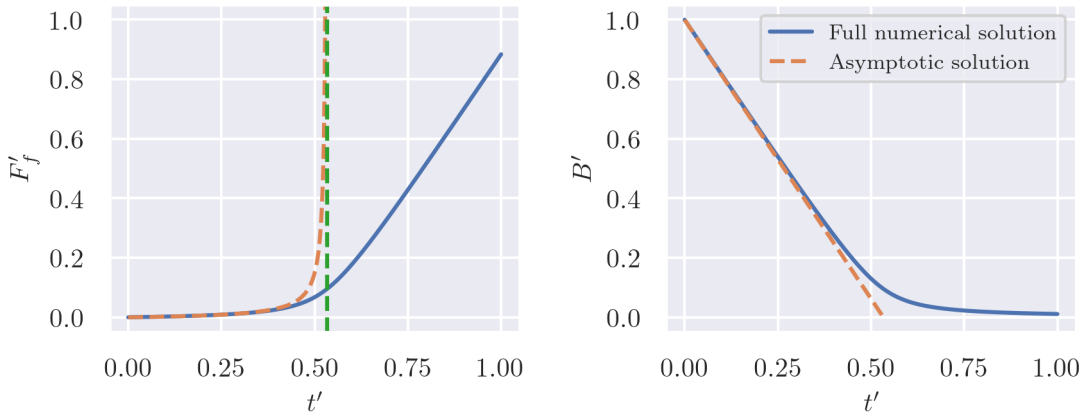

Figure 3.15: Comparison between asymptotic and full numerical solutions given by eq. (3.31) and eqs. (3.25) and (3.26) respectively during the initial binding region with $\delta = 0.01$, $\rho = 0.53$, $\beta = \psi = 1$. The vertical green line corresponds to $t' = \rho$.

which leads to the rescaled system,

$$\frac{d\tilde{F}'_f}{d\tilde{t}'} = \rho^{-1}\tilde{q}'(\tilde{t}') - \frac{\beta}{\delta}\tilde{F}'_f\tilde{B}' + \frac{\beta}{\delta}(1 - \delta\tilde{B}') - \delta\psi\tilde{F}'_f, \tag{3.33}$$

$$\delta\frac{d\tilde{B}'}{d\tilde{t}'} = \quad - \frac{\beta}{\delta}\tilde{F}'_f\tilde{B}' + \frac{\beta}{\delta}(1 - \delta\tilde{B}'). \tag{3.34}$$

Once more seeking asymptotic expansions of the form,

$$\tilde{F}'_f = \tilde{F}'_{f0} + \delta\tilde{F}'_{f1} + \cdots, \qquad \tilde{B}' = B'_0 + \delta\tilde{B}'_1 + \cdots, \tag{3.35}$$

we find a leading order relation,

$$\tilde{F}'_{f0}\tilde{B}'_0 \approx 1. \tag{3.36}$$

Now subtracting eq. (3.34) from eq. (3.33) and using the leading order approximation, we can reduce the paired system (eqs. (3.33) and (3.34)) to a single ODE for $\tilde{F}'_{f0}$. Thus,

$$\tilde{F}'_f = \rho^{-1}\tilde{t}' + c_2, \qquad \tilde{B}' = \frac{1}{\rho^{-1}\tilde{t}' + c_2}, \tag{3.37}$$

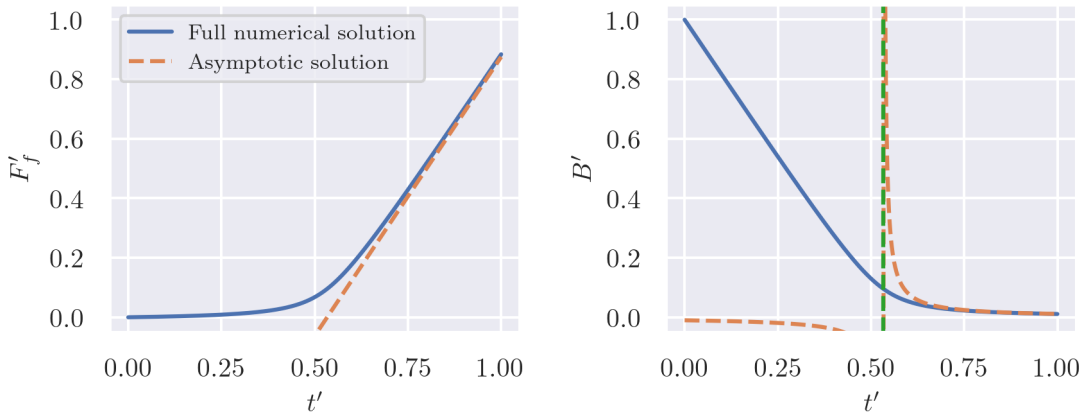

Figure 3.16: Comparison between asymptotic (eqs. (3.25) and (3.26)) and full numerical solution (eq. (3.38)) towards the end of the dosing region when binding protein has been saturated and free cortisol levels are increasing. The vertical green line corresponds to time $t' = \rho$.

where we determine $c_2 = 0$ as $\tilde{F}'_f(\tilde{t}' \to 0) \to 0$. Returning to original dimensionless variables,

$$F'_f = \rho^{-1}(t' - t_{cr}) + \mathcal{O}(\delta), \qquad B' = \delta \frac{1}{\rho^{-1}(t' - t_{cr})} + \mathcal{O}(\delta^2). \tag{3.38}$$

Figure 3.16 compares the asymptotic and numerical solution for this region, where we choose the time shift based on the blow up point from the initial binding region (i.e., $t_{cr} = \rho$). The asymptotic solution follows the numerical solution for large t', however the solution for B' tends to infinity as $t' \to \rho$ from above. Therefore, we seek a solution that more accurately matches the full numerical solution near $t' = \rho$.

Crossover Region

We wish to match the previous two regions, when B' is no longer $\mathcal{O}(1)$ and F'_f is no longer $\mathcal{O}(\delta)$. Taking the following scalings,

$$F'_f = \delta^{\frac{1}{2}} \breve{F}'_f, \qquad B' = \delta^{\frac{1}{2}} \breve{B}', \qquad t' = \delta^{\frac{1}{2}} \breve{t}' + t_{cr}, \tag{3.39}$$

the rescaled system is then,

$$\frac{d\breve{F}'_f}{d\breve{t}'} = \rho^{-1}q'(\breve{t}') - \frac{\beta}{\delta}\breve{F}'_f\breve{B}' + \frac{\beta}{\delta}(1-\delta^{\frac{1}{2}}\breve{B}') - \delta^{\frac{3}{2}}\psi\breve{F}'_f, \tag{3.40}$$

$$\frac{d\breve{B}'}{d\breve{t}'} = \qquad\qquad - \frac{\beta}{\delta}\breve{F}'_f\breve{B}' + \frac{\beta}{\delta}(1-\delta^{\frac{1}{2}}\breve{B}'). \tag{3.41}$$

Seeking an expression of the form,

$$\breve{F}'_f = \breve{F}'_{f0} + \delta^{\frac{1}{2}}\breve{F}'_{f1} + \cdots, \qquad\qquad \breve{B}' = \breve{B}'_0 + \delta^{\frac{1}{2}}\breve{B}'_1 + \cdots, \tag{3.42}$$

we have the leading order relation,

$$\breve{F}'_{f0}\breve{B}'_0 \approx 1. \tag{3.43}$$

Now subtracting eq. (3.41) from eq. (3.40), we can use the leading order relation to find a quadratic in $\breve{B}'_0$,

$$\breve{B}'_0 = \frac{-(\rho^{-1}\breve{t}' + c_3) \pm \sqrt{(\rho^{-1}\breve{t}' + c_3)^2 + 4}}{2}, \tag{3.44}$$

where we take the positive square root as $\breve{B}'_0 > 0$. By matching to the initial binding region we find $c_3 = 0$. Therefore we have,

$$\breve{F}'_{f0} = \frac{2}{-\rho^{-1}\breve{t}' + \sqrt{(\rho^{-1}\breve{t}')^2 + 4}}, \qquad \breve{B}'_0 = \frac{-\rho^{-1}\breve{t}' + \sqrt{(\rho^{-1}\breve{t}')^2 + 4}}{2}. \tag{3.45}$$

Returning to original dimensionless variables,

$$F'_f = \frac{2\delta}{-\rho^{-1}(t' - t_{cr}) + \sqrt{(\rho^{-1}(t' - t_{cr}))^2 + 4\delta}} + \mathcal{O}(\delta^{\frac{3}{2}}), \tag{3.46}$$

$$B' = \frac{-\rho^{-1}(t' - t_{cr}) + \sqrt{(\rho^{-1}(t' - t_{cr}))^2 + 4\delta}}{2} + \mathcal{O}(\delta^{\frac{1}{2}}). \tag{3.47}$$

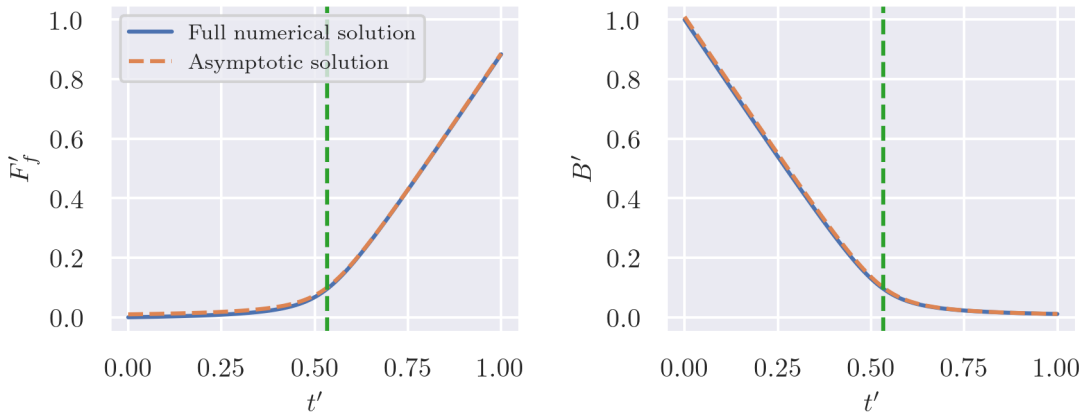

Figure 3.17: Comparison between the crossover asymptotic solution (eq. (3.46)) and numerical solution (eq. (3.25)) during the dosing period.

This asymptotic approximation is compared to the numerical solution in Figure 3.17. We find that this solution matches very well for the entire dosing period, however does not fit as well as the initial binding solution for the beginning of the region.

Fast-slow analysis

We now consider solving the entire dosing period as one. Recalling the dimensionless BIV model given by eqs. (3.25) and (3.26), we define a new, slow variable, $x' = F'_f - B'$, and eliminate F'_f from the system,

$$\frac{dB'}{dt'} = -\frac{\beta}{\delta^2}(x' + B')B' + \frac{\beta}{\delta}(1 - B'), \tag{3.48}$$

$$\frac{dx'}{dt'} = \rho^{-1}q'(t') - \delta\psi(x' + B'), \tag{3.49}$$

recalling that $q'(t') = 1$. The system now has one fast variable, B', and one slow variable, x', variable instead of two fast variables, B' and F'_f. We suggest an asymptotic expansion of the form,

$$x' = x'_0 + \delta x'_1 + \cdots, \tag{3.50}$$

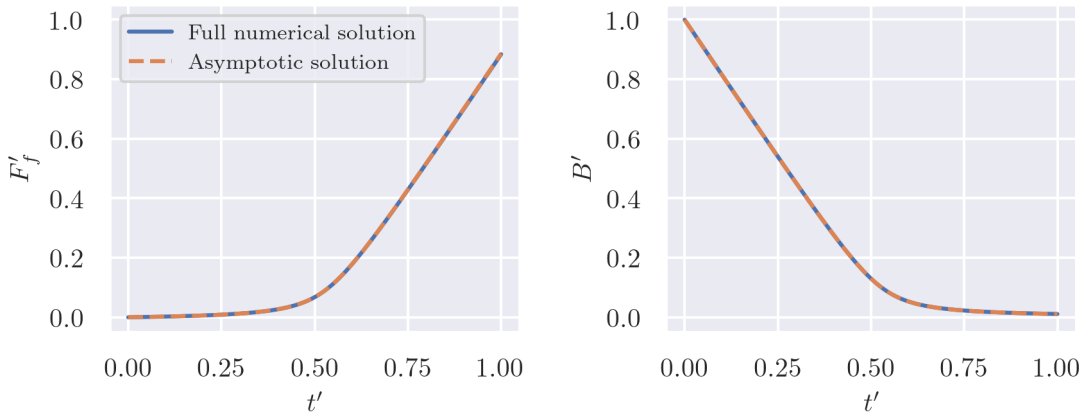

Figure 3.18: Comparison between the fast-slow asymptotic solution (eq. (3.53)) and the full numerical solution (eq. (3.25)) during the dosing period.

which gives the leading order solution,

$$x' \approx \rho^{-1}t' + c_4, \tag{3.51}$$

where c_4 can be determined using the initial condition ($c_4 = -1$), which will change upon subsequent doses. Substituting this solution into the ODE for B' eq. (3.26) allows us to find an approximate solution for the entire dosing region with a single ODE,

$$\frac{dB'}{dt'} = -\frac{\beta}{\delta^2}B'^2 - \frac{\beta}{\delta^2}(\rho^{-1}t' + c_4 + \delta)B' + \frac{\beta}{\delta}, \tag{3.52}$$

with a corresponding solution for F'_f,

$$F'_f = \rho^{-1}t' + c_4 + B'. \tag{3.53}$$

We note that eq. (3.52) is in the form of the Riccati equation. Figure 3.18 compares the solution to this equation against the numerical solution to the full system. This fast-slow analysis replaces a series of three asymptotic algebraic solution with a single asymptotic numerical solution and follows more closely to the full numerical solution (see Figures 3.22 and 3.23 for a comparison of the asymptotic solutions). We see a significantly smaller error for the fast-slow solution at the beginning of the region, and the error remains lower

than the other three solutions for all of the dosing region.

The non-linear ODE given by eq. (3.52) can be converted into a second order linear differential equation using the substitution $B' = \frac{\delta^2}{\beta}\frac{1}{u}\frac{du}{dt}$,

$$\frac{d^2u}{dt'^2} = -\frac{\beta}{\delta^2}(\rho^{-1} + c_4 + \delta) + \frac{\beta^2}{\delta^2}. \tag{3.54}$$

Letting $C = \rho^{-1}\frac{\beta}{\delta^2}$, $D = \frac{\beta}{\delta^2}(c_4 + \delta)$ and $q_0 = -\frac{\beta^2}{\delta^3}$,

$$\frac{d^2u}{dt'^2} + (Ct' + D)\frac{du}{dt'} + q_0 u = 0, \tag{3.55}$$

which has solution,

$$u(t') = \exp\left(-\frac{1}{2}t'(Ct' + 2D)\right)\left(c_5 H_r(z) + c_{61}F_1\left(-\frac{r}{2}; \frac{1}{2}; z^2\right)\right), \tag{3.56}$$

where $H_r(z)$ denotes the Hermite function, ${}_1F_1$ denotes the confluent hypergeometric function and,

$$r = \frac{q_0}{C} - 1, \qquad z = \frac{Ct' + D}{\sqrt{2C}}. \tag{3.57}$$

In practice, it suffices to use a numerical solver on the fast-slow solution (eq. (3.52)) instead of using the analytic expression above.

3.5.2 Post dosing period

Midterm behaviour

We now consider the period after dosing, recalling our dimensionless system and neglecting the dosing term,

$$\frac{dF'_f}{dt'} = -\frac{\beta}{\delta^2}F'_f B' + \frac{\beta}{\delta}(1 - B') - \delta\psi F'_f, \tag{3.58}$$

$$\frac{dB'}{dt'} = -\frac{\beta}{\delta^2}F'_f B' + \frac{\beta}{\delta}(1 - B'). \tag{3.59}$$

Introducing the scalings (see appendix B.3.2 for investigation over choice of scalings),

$$F'_f = \delta^{\frac{1}{2}}\check{F}'_f, \qquad B' = \delta^{\frac{1}{2}}\check{B}, \qquad t' = \delta^{-1}\check{t}' + t_{cr}, \tag{3.60}$$

we find the rescaled system,

$$\delta^{\frac{3}{2}}\frac{d\check{F}'_f}{d\check{t}'} = -\frac{\beta}{\delta}\check{F}'_f\check{B}' + \frac{\beta}{\delta}(1 - \delta^{\frac{1}{2}}\check{B}') - \delta^{\frac{3}{2}}\psi\check{F}'_f, \tag{3.61}$$

$$\delta^{\frac{3}{2}}\frac{d\check{B}'}{d\check{t}'} = -\frac{\beta}{\delta}\check{F}'_f\check{B}' + \frac{\beta}{\delta}(1 - \delta^{\frac{1}{2}}\check{B}'). \tag{3.62}$$

Seeking a solution of the form,

$$\check{F}'_f = \check{F}'_{f0} + \delta^{\frac{1}{2}}\check{F}'_{f1} + \cdots, \qquad \check{B}' = \check{B}'_0 + \delta^{\frac{1}{2}}\check{B}'_1 + \cdots, \tag{3.63}$$

at leading order we find the relation,

$$\check{F}'_{f0}\check{B}'_0 \approx 1. \tag{3.64}$$

Subtracting eq. (3.62) from eq. (3.61) and using the leading order relation, we can find a separable equation for $\check{B}_0$. Thus, we find solutions for $\check{B}'_0$ and $\check{F}'_{f0}$ in terms of the Lambert

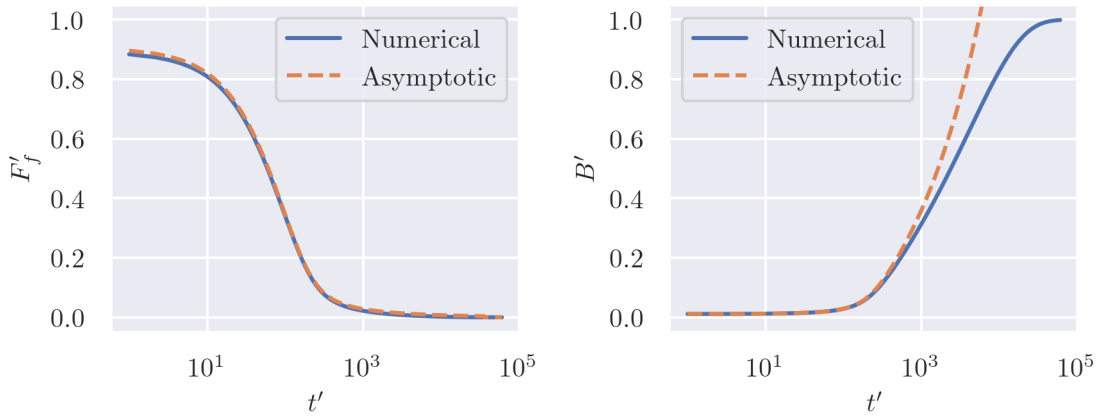

Figure 3.19: Comparison of the mid-term region asymptotic solution given by eq. (3.66) and the full numerical solution given by eq. (3.25) during the post dosing period.

W function, taking only the principal branch due to the constraint that $\check{B}'_0 > 0$:

$$\check{F}'_{f0} = \frac{1}{(W_0(A_1 \exp(2\psi \check{t}')))^{\frac{1}{2}}}, \qquad \check{B}'_0 = (W_0(A_1 \exp(2\psi \check{t}')))^{\frac{1}{2}}. \tag{3.65}$$

Returning to original dimensionless variables,

$$F'_f = \frac{\delta^{\frac{1}{2}}}{(W_0(A_1 \exp(2\delta\psi(t' - t_{cr}))))^{\frac{1}{2}}}, \qquad B' = \delta^{\frac{1}{2}}(W_0(A_1 \exp(2\delta\psi(t' - t_{cr}))))^{\frac{1}{2}}, \tag{3.66}$$

where A_1 is determined by matching to the previous region from the dosing period and t_{cr} is now chosen as 1 minute. A comparison of this solution against the full numerical solution is shown in Figure 3.19. The asymptotic solution follows closely for free cortisol levels, however begins to diverge from the levels of binding protein in the full solution for large time. We therefore seek a long-time solution that better captures the dynamics in amount of binding protein.

Long-term behaviour

We now consider the asymptotic dynamics of the long-term state of the system, when free cortisol has returned to very low levels and unoccupied binding protein is approaching

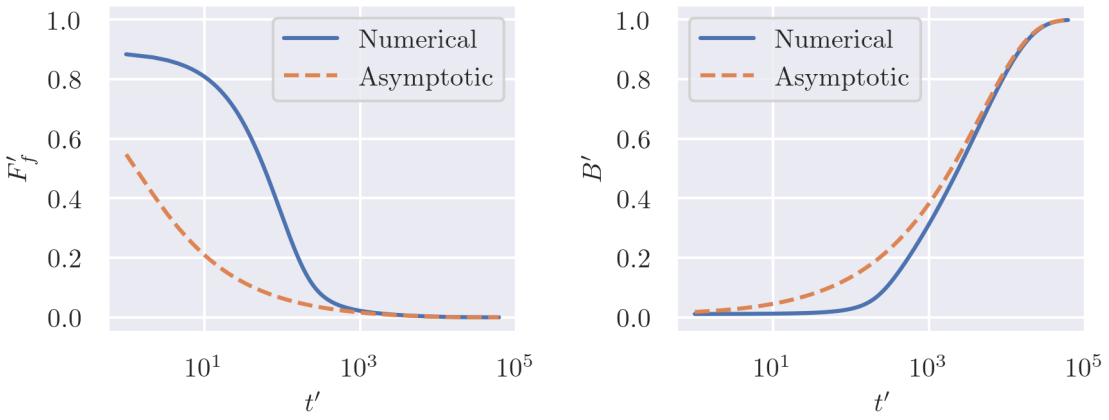

Figure 3.20: Comparison of the long time asymptotic solution given by eq. (3.69) to the full numerical solution given by eq. (3.25).

pre-dosing levels. As in section 3.2, we use the following scalings:

$$F'_f = \delta \bar{F}'_f, \qquad B' = \bar{B}', \qquad t' = \delta^{-2}\bar{t}' + t_{cr}. \tag{3.67}$$

We find solutions for $\bar{B}'$ and $\bar{F}'_f$ in terms of the Lambert W function, taking only the principal branch due to the constraint that $\bar{B}'_0 > 0$:

$$\bar{F}'_{f0} = -\frac{W_0(-A_2 \exp(-\psi \bar{t}'))}{1 + W_0(-A_2 \exp(-\psi \bar{t}'))}, \qquad \bar{B}'_0 = 1 + W_0(-A_2 \exp(-\psi \bar{t}')). \tag{3.68}$$

Returning to original dimensional variables,

$$F'_f = -\frac{\delta W_0(-A_2 \exp(-\delta^2 \psi (t' - t_{cr})))}{1 + W_0(-A_2 \exp(-\delta^2 \psi (t' - t_{cr})))}, \quad B' = 1 + W_0(-A_2 \exp(-\delta^2 \psi (t' - t_{cr}))), \tag{3.69}$$

where we determine the constant A_2 by matching to the end of the dosing region. Figure 3.20 compares this asymptotic solution to the full numerical solution in the post dosing region. The solutions match only for very large time, and hence we seek a solution that would bridge the gap between our midterm and long term solutions.

Slow manifold

Returning to the midterm region scalings, we recall the system given by eqs. (3.61) and (3.62). By setting $\delta = 0$, we find no isolated solution to the degenerate system and therefore refer to this as a singular singularly perturbed system [54]. Instead of taking the leading order solution as we did previously, we choose to introduce the new, slow variable $\check{x}' = \check{F}'_f - \check{B}'$. To obtain the full solution, we could choose either $\check{F}'_f$ or $\check{B}'$ as the fast equation. Choosing $\check{B}'$ yields,

$$\delta^{\frac{3}{2}} \frac{d\check{B}'}{d\check{t}'} = -\frac{\beta}{\delta}(\check{x}' + \check{B}')\check{B}' + \frac{\beta}{\delta}(1 - \delta^{\frac{1}{2}}\check{B}'), \tag{3.70}$$

$$\frac{d\check{x}'}{d\check{t}'} = -\psi(\check{x}' + \check{B}'). \tag{3.71}$$

Suggesting an asymptotic expansion of the form,

$$\check{B}' = \check{h}'(\check{B}', \check{x}', \delta) = \check{h}'_0(\check{x}') + \delta^{\frac{1}{2}}\check{h}'_1(\check{x}') + \ldots, \tag{3.72}$$

which we substitute into the invariant (eq. (3.70)),

$$-\delta^{\frac{3}{2}}\psi(\check{x}' + \check{h}'_0 + \delta^{\frac{1}{2}}\check{h}'_1 + \ldots)\frac{\partial}{\partial \check{x}'}(\check{h}'_0 + \delta^{\frac{1}{2}}\check{h}'_1 + \ldots) \tag{3.73}$$

$$= -\frac{\beta}{\delta}(\check{x}' + \check{h}'_0 + \delta^{\frac{1}{2}}\check{h}'_1 + \ldots)(\check{h}'_0 + \delta^{\frac{1}{2}}\check{h}'_1 + \ldots) \tag{3.74}$$

$$+ \frac{\beta}{\delta}(1 - \delta^{\frac{1}{2}}(\check{h}'_0 + \delta^{\frac{1}{2}}\check{h}'_1 + \ldots)). \tag{3.75}$$

Equating first and second order terms yields the corresponding second order approximation of the slow motion of the system:

$$\check{F}'_f = \check{x}' + \check{B}', \qquad \check{B}' = \check{h}'_0 + \delta^{\frac{1}{2}}\check{h}'_1, \tag{3.76}$$

where,

$$\frac{d\check{x}'}{d\check{t}'} = -\psi(\check{x}' + \check{h}_0' + \delta^{\frac{1}{2}}\check{h}_1') + \mathcal{O}(\delta), \tag{3.77}$$

with,

$$\check{h}_0'(\check{x}') = \frac{-\check{x}' + (\check{x}'^2 + 4)^{\frac{1}{2}}}{2}, \tag{3.78}$$

$$\check{h}_1'(\check{x}') = \frac{\check{x}' - (\check{x}'^2 + 4)^{\frac{1}{2}}}{2(\check{x}'^2 + 4)^{\frac{1}{2}}}. \tag{3.79}$$

Here, we have taken the positive square root due to the constraint that $\check{B}' > 0$ and the initial condition is determined by matching to the dosing region. Returning to original dimensionless variables,

$$F_f' = x' + B', \qquad\qquad B' = h_0' + \delta^{\frac{1}{2}}h_1', \tag{3.80}$$

where,

$$\frac{dx'}{dt'} = -\delta\psi(x' + h_0' + \delta^{\frac{1}{2}}h_1') + \mathcal{O}(\delta^2), \tag{3.81}$$

with,

$$h_0'(x') = \frac{-x' + (x'^2 + 4\delta)^{\frac{1}{2}}}{2}, \tag{3.82}$$

$$h_1'(x') = \delta^{\frac{1}{2}}\frac{x' - (x'^2 + 4\delta)^{\frac{1}{2}}}{2(x'^2 + 4\delta)^{\frac{1}{2}}}. \tag{3.83}$$

We compare this slow manifold solution to the full numerical solution in Figure 3.21 and find very strong agreement for all time post-dosing, with just one ODE (eq. (3.81)) describing the entirety of this region.

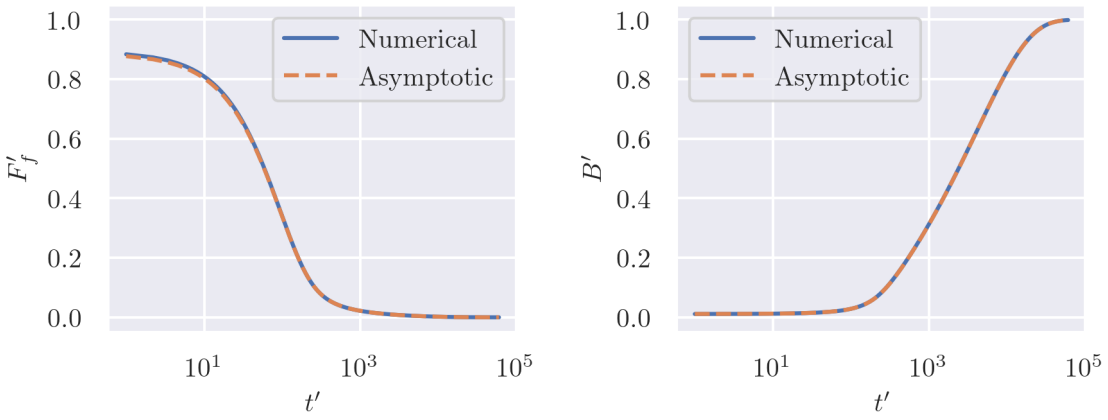

Figure 3.21: Comparison of the manifold asymptotic solution given by eq. (3.80) to the full numerical solution given by eq. (3.25).

3.5.3 Summary of asymptotic regions

We are now able to summarise the set of asymptotic regions for the entire BIV dosing case and a comparison against the full numerical solution is shown in Figures 3.22 and 3.23.

Dosing Period

For the dosing period, we have a set of three regions with explicit solutions:

1. $F'_f = \mathcal{O}(1)$, $B' = \mathcal{O}(1)$, $t' = \mathcal{O}(1)$

   An explicit solution exists for the initial binding of free cortisol to binding protein, given by

$$F_f = \delta \frac{t'}{\rho - t'} + \mathcal{O}(\delta^2), \qquad B' = \frac{\rho - t'}{\rho} + \mathcal{O}(\delta). \tag{3.84}$$

2. $F'_f = \mathcal{O}(\delta^{\frac{1}{2}})$, $B' = \mathcal{O}(\delta^{\frac{1}{2}})$, $t' = \mathcal{O}(\delta^{\frac{1}{2}})$

   An explicit solution exists for the crossover region where neither free cortisol or

binding protein are order 1, given by

$$F_f' = \frac{2\delta}{-\rho^{-1}(t'-t_{cr}) + \sqrt{(\rho^{-1}(t'-t_{cr}))^2 + 4\delta}} + \mathcal{O}(\delta^{\frac{3}{2}}), \tag{3.85}$$

$$B' = \frac{-\rho^{-1}(t'-t_{cr}) + \sqrt{(\rho^{-1}(t'-t_{cr}))^2 + 4\delta}}{2} + \mathcal{O}(\delta^{\frac{1}{2}}). \tag{3.86}$$

3. $\underline{F_f' = \mathcal{O}(1),\ B' = \mathcal{O}(\delta),\ t' = \mathcal{O}(1)}$

   An explicit solution exists for the end of the dosing period where free cortisol is increasing, given by

$$F_f' = \rho^{-1}(t'-t_{cr}) + \mathcal{O}(\delta), \qquad B' = \delta\frac{1}{\rho^{-1}(t'-t_{cr})} + \mathcal{O}(\delta^2). \tag{3.87}$$

Alternatively, we can describe the entire dosing period with a single ODE. We have,

1. $\underline{F_f' = \mathcal{O}(1),\ B' = \mathcal{O}(1),\ t' = \mathcal{O}(1)}$

   A single ODE system exists, given by

$$F_f' = \rho^{-1}t' - 1 + B', \qquad \frac{dB'}{dt'} = -\frac{\beta}{\delta^2}B'^2 - \frac{\beta}{\delta^2}(\rho^{-1}t' - 1 + \delta)B' + \frac{\beta}{\delta}, \tag{3.88}$$

Post dosing period

For the post dosing period, we have a set of two regions with explicit solutions:

1. $\underline{F_f' = \mathcal{O}(\delta^{\frac{1}{2}}),\ B' = \mathcal{O}(\delta^{\frac{1}{2}}),\ t' = \mathcal{O}(\delta^{-1})}$

   An explicit solution exists for the initial behaviour post dosing, given by

$$F_f' = \frac{\delta^{\frac{1}{2}}}{(W_0(A_1\exp(2\delta\psi(t'-t_{cr}))))^{\frac{1}{2}}} + \mathcal{O}(\delta), \tag{3.89}$$

$$B' = \delta^{\frac{1}{2}}(W_0(A_1\exp(2\delta\psi(t'-t_{cr}))))^{\frac{1}{2}} + \mathcal{O}(\delta). \tag{3.90}$$

2. $\underline{F_f' = \mathcal{O}(\delta),\ B' = \mathcal{O}(1),\ t' = \mathcal{O}(\delta^-2)}$

An explicit solution exists for the long term behaviour, given by

$$F_f' = -\frac{\delta W_0(-A_2 \exp(-\delta^2 \psi(t' - t_{cr})))}{1 + W_0(-A_2 \exp(-\delta^2 \psi(t' - t_{cr})))} + \mathcal{O}(\delta^{\frac{3}{2}}), \tag{3.91}$$

$$B' = 1 + W_0(-A_2 \exp(-\delta^2 \psi(t' - t_{cr}))) + \mathcal{O}(\delta^{\frac{1}{2}}). \tag{3.92}$$

Alternatively, we can describe the entire post dosing region with a single ODE. We have,

1. $\underline{F_f' = \mathcal{O}(\delta^{\frac{1}{2}}),\ B' = \mathcal{O}(\delta^{\frac{1}{2}}),\ t' = \mathcal{O}(\delta^{-1})}$

   A single ODE describes the slow manifold solution, given by

$$\frac{dx'}{dt'} = -\delta\psi(x' + h_0' + \delta^{\frac{1}{2}} h_1') + \mathcal{O}(\delta^2), \tag{3.93}$$

   such that the solution for the free cortisol and binding protein are given by

$$F_f' = x' + B', \qquad\qquad B' = h_0' + \delta^{\frac{1}{2}} h_1', \tag{3.94}$$

   where,

$$h_0'(x') = \frac{-x' + (x'^2 + 4\delta)^{\frac{1}{2}}}{2}, \tag{3.95}$$

$$h_1'(x') = \delta^{\frac{1}{2}} \frac{x' - (x'^2 + 4\delta)^{\frac{1}{2}}}{2(x'^2 + 4\delta)^{\frac{1}{2}}}. \tag{3.96}$$

Saturation version non-saturation of binding protein

Figure 3.24 shows an example of the dose either saturating or not saturating the physiological level of binding protein, comparing the full numerical solution to asymptotic solutions. When the dose is low enough such that the binding protein is not saturated, the first asymptotic solution given by eq. (3.84) is sufficient to match the dosing period. Additionally, when dosing ceases, the binding protein has not dropped sufficiently low to

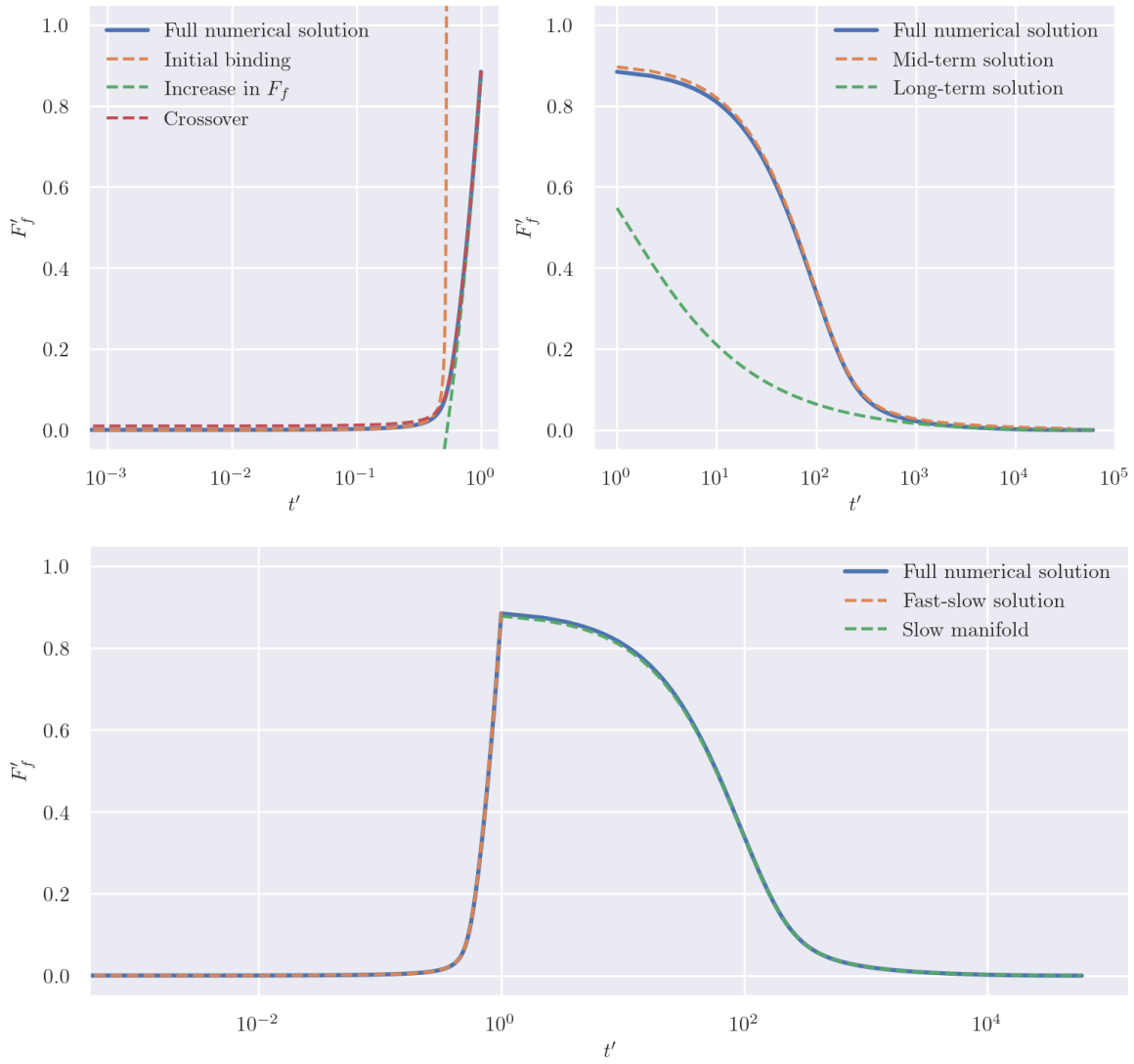

Figure 3.22: Comparison of all the asymptotic solutions for F_f' for the BIV$^+$ model given by eqs. (3.25) and (3.26). Top left: a combination of three separate asymptotic solutions to approximate the dosing period. Top right: a combination of two separate asymptotic solutions to approximate the post-dosing period. Bottom: The preferred reduced solution with the fast-slow solution for the dosing period and the slow manifold solution for the post-dosing period.

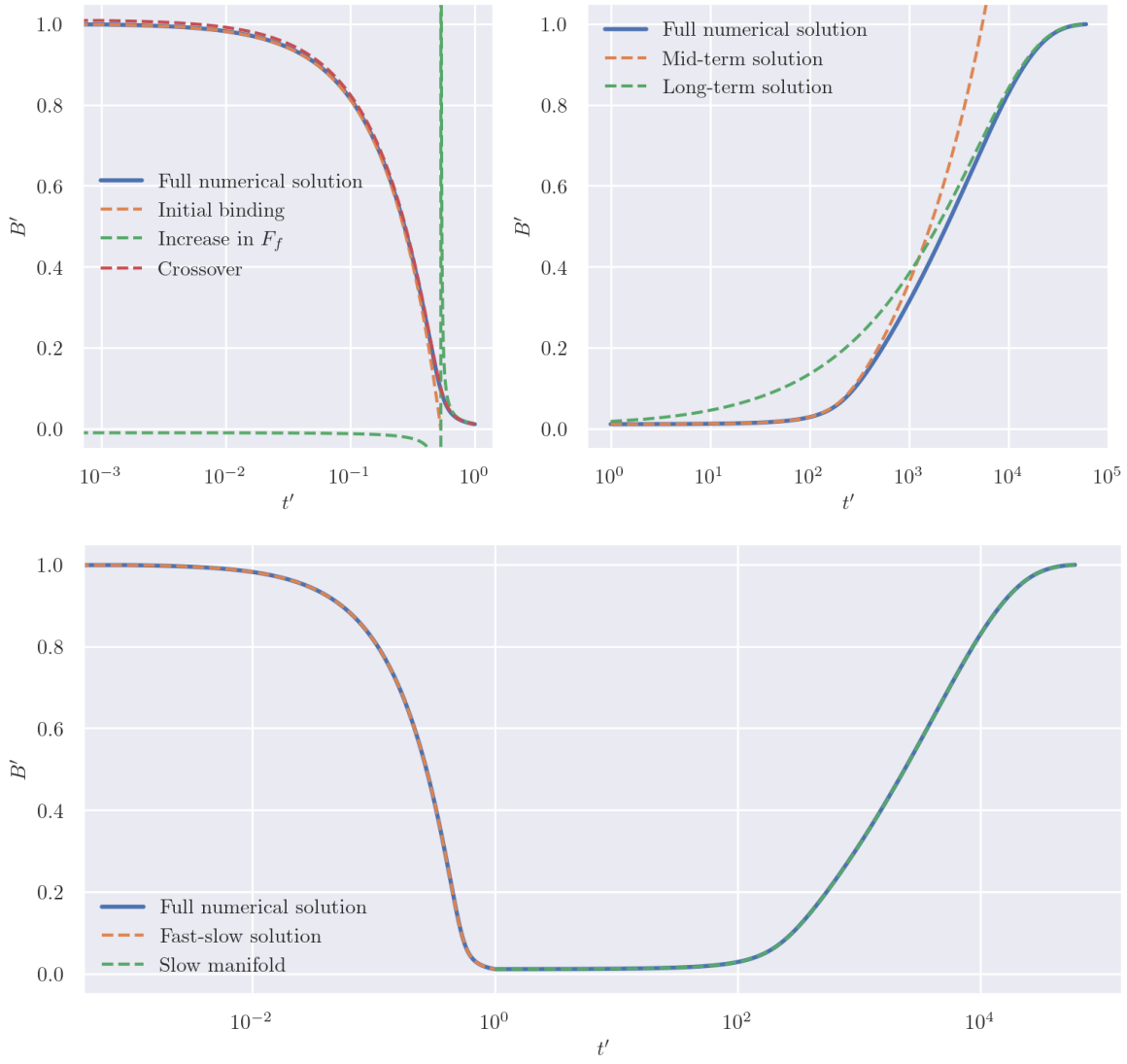

Figure 3.23: Comparison of all the asymptotic solutions for B' for the BIV$^+$ model given by eqs. (3.25) and (3.26). Top left: a combination of three separate asymptotic solutions to approximate the dosing period. Top right: a combination of two separate asymptotic solutions to approximate the post-dosing period. Bottom: The preferred reduced solution with the fast-slow solution for the dosing period and the slow manifold solution for the post-dosing period.

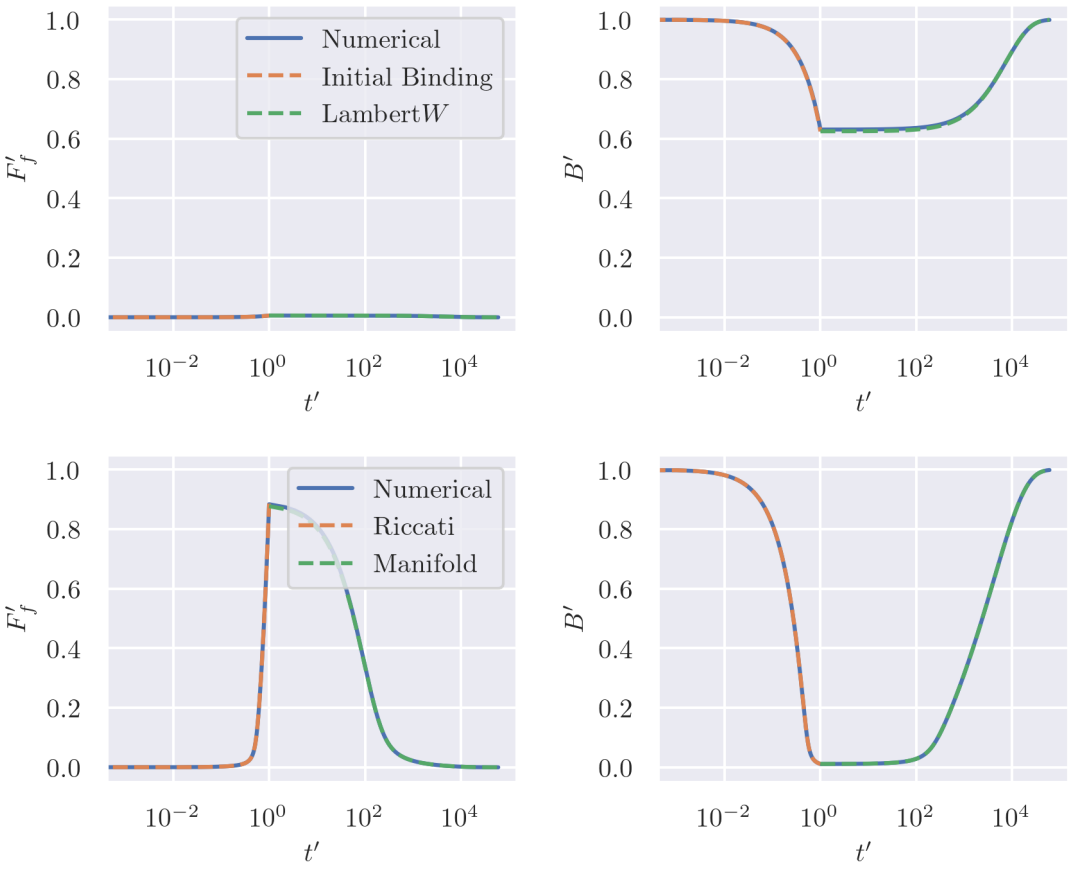

Figure 3.24: Asymptotic fits for all time for a low dose and high dose case. Top row: low dose, $\rho = 2.67$. The asymptotic fits in this case are the initial binding region given by eq. (3.31) and the LambertW solution given by eq. (3.69). Bottom row: high dose, $\rho = 0.53$. The asymptotic fits in this case are the fast-slow analysis solution given by eq. (3.53) and the slow manifold solution given by eq. (3.80).

require the manifold solution and so the longtime behaviour given by eq. (3.91) matches well for the rest of time.

For a high dose, where binding protein is saturated during the dosing period, the fast-slow solution given by eq. (3.88) is the best fit during the dosing region. Post dosing, the manifold solution given by eqs. (3.93) to (3.96) allows us to describe the rest of time with a single ODE as binding protein increases up to pre-dosing levels.

3.5.4 Identifiability of the BIV$^-$ model

We now consider the identifiability of the BIV$^-$ model, which we take to be the fast-slow solution given by eq. (3.88) followed by the slow manifold solution given by eqs. (3.93) to (3.96). Initially we look at the dosing period solution for total cortisol. We return to dimensional variables,

$$F^D = \frac{1}{\alpha} Dt - B_0(c_4 - 1) \tag{3.97}$$

where $c_4 = 1$ for the initial dose. Using the Taylor series method, we evaluate the observed variable and its derivative at $t = 0$,

$$F^D(0) = -B_0(c_4 - 1), \tag{3.98}$$

$$\left.\frac{dF^D}{dt}\right|_{t=0} = \frac{1}{\alpha} D, \tag{3.99}$$

hence we can readily see that α is identifiable. B_0 will be identifiable under the assumption that we have multiple doses.

In the post dosing period, we take eqs. (3.93) to (3.96) and return to dimensional

variables to describe the observed variable, F^{PD},

$$\frac{dx}{dt} = -k_{re}\left(x + B_0\delta^{\frac{1}{2}}\left(\frac{-x + (x^2 + 4B_0^2\delta)^{\frac{1}{2}}}{2B_0\delta^{\frac{1}{2}}} + \delta^{\frac{1}{2}}\frac{x - (x^2 + 4B_0^2\delta)^{\frac{1}{2}}}{2(x^2 + 4B_0^2\delta)^{\frac{1}{2}}}\right)\right), \tag{3.100}$$

$$x(0) = \Omega_3 \tag{3.101}$$

$$F^{PD} = x + B_0, \tag{3.102}$$

where similar to the full model, we define an initial condition for x using eq. (3.8),

$$\Omega_3 = \frac{1}{\alpha}D - B_0 - \frac{\alpha B_0^2\delta}{D - \alpha B_0}, \tag{3.103}$$

however in practice we will find Ω_3 numerically. From here on, we refer to eq. (3.97)-eq. (3.103) as the BIV$^-$ model. This requires calculation of F_f and B individually in the dosing period, which means we require the parameters k_{fb} and k_{bf} individually and cannot combine them into the parameter grouping δ. If we assume that we have the following observed variables,

$$\boldsymbol{y} = [F^D, F^{PD}]. \tag{3.104}$$

Using the Taylor Series method, aided by MAPLE, we find that 3 parameters ($[\alpha, \delta, B_0]$) are globally identifiable and k_{re} is locally identifiable with up to 2 two solutions (see appendix A.4). Numerically it can be shown that for physically plausible values, only one of the solutions will satisfy the constraint that k_{re} is positive. STRIKE_GOLDD finds all parameters to be locally identifiable.

3.5.5 Practical identifiability of the BIV$^-$ model using simulated data

We now consider whether the model reductions obtained above will alter any of the practical identifiability issues that arose for the BIV$^+$ model under different levels of

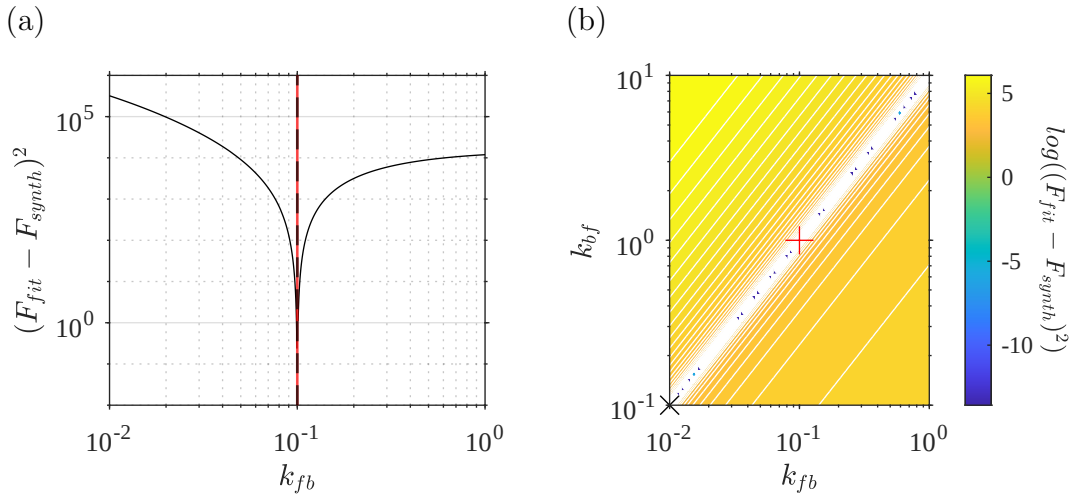

Figure 3.25: Loss function for varying model parameters for the BIV$^-$ model given by eqs. (3.97) and (3.100) with zero noise added and sampling time frequency corresponding to the time points used in data [PD]: (a) varying k_{fb} only. The red line indicates the true value of k_{fb}, while the numerical minimum is shown by the black dashed line, (b) k_{fb} versus k_{bf}. The red plus indicates the true parameter value pair, while the loss function numerical minimum is shown with a black cross.

noise. Figure 3.25(a) shows the behaviour of the loss function when no noise is added to the model and when varying k_{fb} individually. With the remaining 4 parameters fixed, there is a single minimum which matches the true value of k_{fb}, which is in line with the behaviour of the BIV$^+$ model. However, we see in Figure 3.25(b) that when varying both binding and unbinding rates simultaneously, the minimum in the loss function does not match the true value pair. This finding is because we are sampling in the post dosing region only and the binding and unbinding rate parameters only appear in ratio with each other during this period.

For large noise, Figure 3.26(a) shows a smoother loss function compared to the BIV$^+$ model and is more centred around the true value of k_{fb}. The smoother behaviour justifies the use of asymptotics to simplify the dynamics in this model. Similarly, when varying k_{fb} and k_{bf} simultaneously, the ridge, although wide as expected for large noise, is centred about the true ratio.

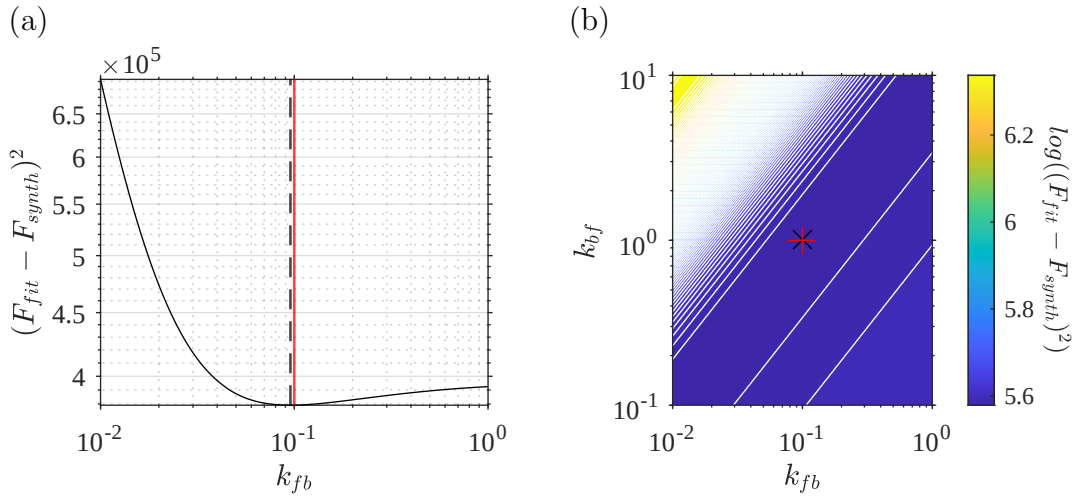

Figure 3.26: Loss function for varying model parameters for the BIV$^-$ model given by eqs. (3.97) and (3.100) with Gaussian noise added (s.d. 100 nmol L^{-1}) and sampling time frequency corresponding to the time points used in data [PD]: (a) varying k_{fb} only. The red line indicates the true value of k_{fb}, while the numerical minimum is shown by the black dashed line, (b) k_{fb} versus k_{bf}. The red plus indicates the true parameter value pair, while the loss function numerical minimum is shown with a black cross.

Frequentist parameter recovery

When attempting to recover all 5 parameters using synthetic data, the BIV$^-$ model is unable to retain the true ratio between binding and unbinding rate parameters unlike the BIV$^+$ model (see Figure 3.27). However, unlike the CIV case, the BIV$^-$ model is still able to recover a good estimate for the initial level of available binding protein, B_0. The BIV$^-$ fit appears to qualitatively fit the true model curve as well as the full model, which suggests that the total cortisol trajectory is fairly insensitive to the ratio between binding and unbinding rates.

3.6 Simultaneous parameter fitting of the CIV and BIV models

Finally, we combine both models to fit data for CIV and BIV synthetic data simultaneously. Table 3.2 has a summary of all of the parameter estimates for individual and combinations of models. Firstly, when combining both CIV$^-$ and BIV$^-$ models and

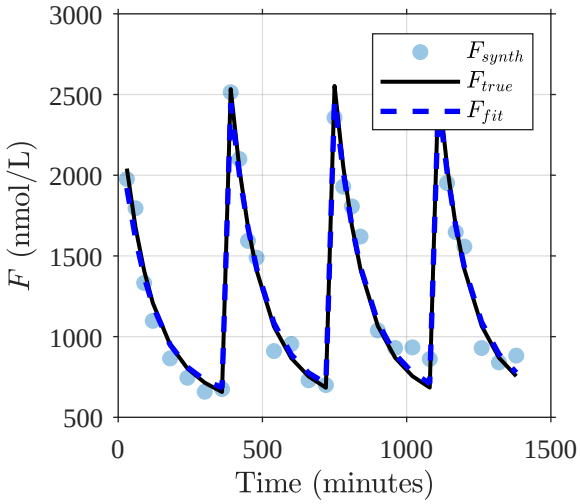

Figure 3.27: Frequentist fit of model trajectory of total cortisol, F, with Gaussian noise added (s.d. $100\,\mathrm{nmol\,L^{-1}}$) and sampling time frequency corresponding to the time points used in data [PD] for the BIV$^-$ model given by eqs. (3.97) and (3.100) for all 5 model parameters. Parameter estimates are $\alpha = 59.647\,\mathrm{L}$, $k_{fb} = 0.999\,83\,\mathrm{L\,nmol^{-1}\,min^{-1}}$, $k_{bf} = 0.1\,\mathrm{min^{-1}}$, $B_0 = 619.96\,\mathrm{nmol\,L^{-1}}$, $k_{re} = 0.009\,113\,9\,\mathrm{min^{-1}}$ with a resulting ratio $k_{bf}/k_{fb} = 0.1$. The true values are listed in Table 2.1.

attempting to recover parameters for synthetic data with Gaussian noise added (see Figure 3.28), there is a reasonable fit for both sets of data, and the estimates for the dilution factor, the physiological level of binding protein and the free cortisol removal rate are fairly close to the true values.

The CIV$^-$ model alone significantly over estimated B_0, which shows that simultaneous fitting allows for more information to be retained. However, the estimates for k_{fb} and k_{bf} are far from their true values and do not maintain their true ratio. The CIV$^-$ model alone has a reasonable estimate for $\delta(\sim 10^{-2})$, but the estimate for this simultaneous fit (calculating from the other parameter estimates) is $\sim 7 \times 10^{-4}$, suggesting that the minimising function is dominated by the BIV data. We have also seen in Figure 2.4 that the qualitative behaviour of the model trajectory was insensitive to changes of k_{bf} which kept δ between 10^{-2} and 10^{-4}, which supports the conclusion that the dynamics are predominantly governed by B_0.

If we choose instead to fit the BIV$^+$ model with the CIV$^-$ model, the qualitative fit is very similar for both sets of data (Figure 3.29). The estimated ratio between binding and

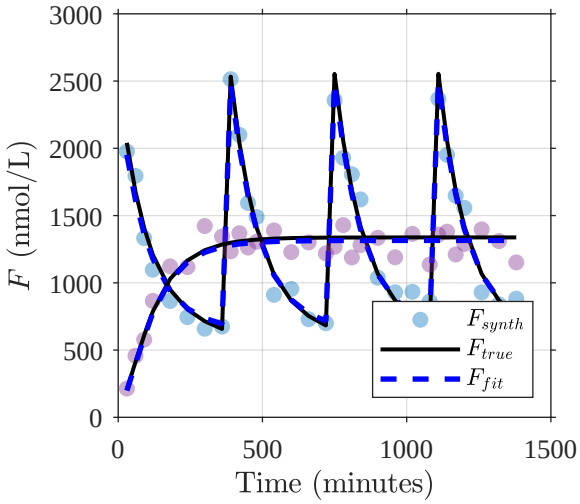

Figure 3.28: Frequentist fit of model trajectory of total cortisol with Gaussian noise added (s.d. $100\,\mathrm{nmol\,L^{-1}}$) and sampling time frequency corresponding to the time points used in data [PD] for simultaneous CIV$^-$ given by eqs. (2.34) to (2.36) and BIV$^-$ model given by eqs. (3.97) and (3.100) for all 5 model parameters. Parameter estimates are $\alpha = 57.832\,\mathrm{L}$, $k_{fb} = 0.255\,28\,\mathrm{L\,nmol^{-1}\,min^{-1}}$, $k_{bf} = 0.121\,74\,\mathrm{min^{-1}}$, $B_0 = 649.49\,\mathrm{nmol\,L^{-1}}$, $k_{re} = 0.009\,447\,\mathrm{min^{-1}}$ with a resulting ratio of $k_{bf}/k_{fb} = 0.48$. The true values are listed in Table 2.1.

unbinding rate parameters is similar to the true ratio, and the other parameter estimates are similarly close to the true values (B_0 is slightly overestimated). As we found when comparing the BIV$^\pm$ models, the BIV$^+$ model is able to retain more information about the ratio between k_{bf} and k_{fb}. However, there is a trade-off here in computation time. To solve the BIV$^-$ model takes approximately 60% of the time taken to solve the BIV$^+$ model using the MATLAB 'ode15s' ODE solver. Therefore we have to consider whether the additional information of using the BIV$^+$ model is worth the increased computation time.

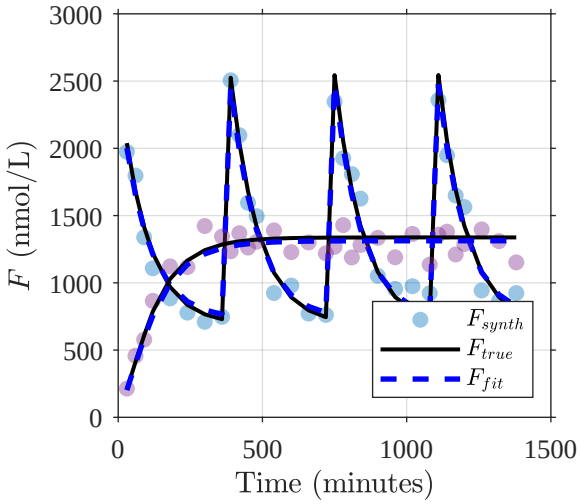

Figure 3.29: Frequentist fit of model trajectory of total cortisol with Gaussian noise added (s.d. $100\,\mathrm{nmol\,L^{-1}}$) and sampling time frequency corresponding to the time points used in data [PD] for simultaneous CIV$^-$ given by eqs. (2.34) to (2.36) and BIV$^+$ model given by eqs. (3.97) and (3.100) for all 5 model parameters. Parameter estimates are $\alpha = 56.137\,\mathrm{L}$, $k_{fb} = 0.029\,375\,\mathrm{L\,nmol^{-1}\,min^{-1}}$, $k_{bf} = 0.749\,97\,\mathrm{min^{-1}}$, $B_0 = 672.8\,\mathrm{nmol\,L^{-1}}$, $k_{re} = 0.010\,27\,\mathrm{min^{-1}}$ with a resulting ratio of $k_{bf}/k_{fb} = 25.5$. The true values are listed in Table 2.1.

3.7 Discussion

In this chapter, we found the BIV$^+$ model to be structurally identifiable. We find that the total cortisol trajectory is heavily governed by the amount of available binding protein, and less sensitive to changes in unbinding rates. When there is little to no additive noise, the binding and unbinding rates can be retrieved if the time-resolution is sufficiently high. The same ridge between the binding and unbinding rate parameters as in the CIV case appears when considering the loss function behaviour, however this is more readily distinguished from the value of B_0 when trialling frequentist parameter fitting.

Matched asymptotic analysis is used to simplify the model into two regions: a dosing period and a post-dosing period, and this model is found to be structurally locally identifiable (and numerically found to be globally identifiable for physically plausible parameter values). This reduction simplifies the loss function dynamics considerably. In contrast to the CIV case, the CIV$^-$ model does retain the ability to trace the value of B_0 while reducing computation time by $\sim 40\%$. However, the CIV$^-$ model is unable to retrace

Table 3.1: Summary of which parameters can be retrieved (✓) and which parameters are poorly estimated (✗) using frequentist parameter recovery under high noise with time sampling corresponding to data [PD]. Where parameters groupings are not fitted directly, an estimate is calculated from the other model parameters to assess whether a reasonable value is found.

	α	k_{fb}	k_{bf}	B_0	k_{re}	k_{bf}/k_{fb}	δ
CIV^+	✓	✗	✓	✗	✗	✗	✓
CIV^-	✓	✗	✗	✗	✗	✗	✓
BIV^+	✓	✗	✗	✓	✓	✓	✓
BIV^-	✓	✗	✗	✓	✓	✗	✗
CIV^- and BIV^-	✓	✓	✗	✓	✓	✗	✗
CIV^- and BIV^+	✓	✗	✓	✓	✓	✓	✓

the ratio between binding and unbinding when attempting to recover all parameters for synthetic data under high noise.

Some preliminary simultaneous data fitting suggests that the BIV data dominates the parameter estimates, but is able to give reasonably good qualitative fits to both sets of synthetic data. For both CIV and BIV, high levels of noise reduce the accuracy of parameter estimates and high time-resolution is unable to mitigate against this.

In terms of optimising dosing strategies for patients, these findings suggest that obtaining a patient's response to BIV dosing would provide information to suggest a reasonable prediction of their response to CIV dosing, but not the reverse. Table 3.1 summarises model parameters/chosen parameter groupings and whether they were recoverable through frequentist methods.

Either BIV model would allow inference of the physiological level of binding protein and using the BIV^+ model would allow the ratio to be traced, although this would be at the cost of higher computation time.

Table 3.2: Frequentist parameter recovery summary.

				α	k_{fb}	k_{bf}	B_0	k_{re}	δ
True Values				55	0.1	1	650	0.01	0.015385
Model	CIV$^+$	Noise	0	55	0.1	1	650	0.01	-
			1	54.877	0.71945	8.6587	652.17	0.010024	-
			100	48.847	0.010157	1.489	3645.3	0.1	-
	CIV$^-$	Noise	0	55	-	-	650	0.1	0.015385
			1	54.841	-	-	652.3	0.018691	0.010031
			100	51.491	-	-	2397.3	0.090465	0.037296
	BIV$^+$	Noise	0	55	0.1	1	650	0.01	-
			1	54.966	0.012109	0.13194	649.51	0.010002	-
			100	58.565	0.01012	0.28989	637.45	0.009271	-
	BIV$^-$	Noise	0	55	0.1	1	650	0.01	-
			1	55.056	0.014463	0.13794	648.31	0.0099801	-
			100	59.647	0.99983	0.1	619.96	0.0091139	-
	Simultaneous CIV$^-$ and BIV$^-$	Noise	0	55	0.1	1	650	0.01	-
			1	55.035	0.064607	0.6213	649.23	0.0099931	-
			100	57.832	0.255238	0.12174	649.49	0.009447	-
	Simultaneous CIV$^-$ and BIV$^+$	Noise	0	55	0.1	1	650	0.01	-
			1	54.997	0.010004	0.1	651.1	0.010022	-
			100	56.137	0.029375	0.74997	672.8	0.01027	-

CHAPTER 4

A BAYESIAN APPROACH TO PATIENT PARAMETER INFERENCE

Frequentist fitting in Chapters 2 and 3 highlighted the pitfalls of local optimisation when attempting to retrieve model parameter values of a complex biological system when data is measured at low time-resolution with large amounts of noise. The loss functions became non-smooth even under small amounts of noise and identifying a unique minimum parameter value became impossible for the binding and unbinding rate parameters in the system.

Bayesian inference has been widely used across multiple fields including ecology, psychology and physics [55, 56, 57, 58]. The approach has multiple benefits over frequentist methods including the ability to incorporate prior knowledge, quantify the uncertainty in parameter estimates and the ability to extend the Bayesian principles to complex models [59].

Bayesian inference utilises Bayes' theorem to estimate a posterior distribution for the model parameters, that is, a probability distribution for the parameters given the observed data, using the relation:

$$p(\boldsymbol{\theta}|\boldsymbol{y}) = \frac{p(\boldsymbol{y}|\boldsymbol{\theta})p(\boldsymbol{\theta})}{p(\boldsymbol{y})}. \tag{4.1}$$

Here, $p(\boldsymbol{y}|\boldsymbol{\theta})$ is the likelihood function, which is the probability of the observed data, $\boldsymbol{y}$, given the parameter set, $\boldsymbol{\theta}$. Prior knowledge about the parameter set is included via

the term $p(\boldsymbol{\theta})$ and is an estimate of parameter values before the observed data is known. Finally, we have the marginal likelihood,

$$p(\boldsymbol{y}) = \int_{\boldsymbol{\Theta}} p(\boldsymbol{y}|\boldsymbol{\theta}) p(\boldsymbol{\theta}) d\boldsymbol{\theta}, \tag{4.2}$$

that is the likelihood of the data where the parameter set has been integrated out. The marginal likelihood is usually intractable and therefore approximated by using approaches such as Monte Carlo Markov Chain (MCMC) algorithms which are very well established [60]. In order to explore high-dimensional parameter space more effectively than traditional MCMC algorithms, Hamiltonian Monte Carlo Markov chain sampling is implemented in Stan [61, 62, 63]. We now recap the main steps in this method.

Hamiltonian Monte Carlo Markov Chains

Stan uses the following algorithm to generate the required samples to produce an estimate of the true posterior distribution for each model parameter [61, 64, 65]:

1. Given $\theta_i \in \mathbb{R}^q$, start with an initial sample (θ_i, p_i) where $p_i \sim \mathcal{N}_q(0, M)$ and M is a positive-definite, symmetric "mass matrix".

2. Solve the following Hamiltonian initial value problem with $\theta(0) = \theta_i$, $p(0) = p_i$ on the time interval $[0, T]$:

$$\frac{d\theta}{dt} = \frac{\partial \mathcal{H}}{\partial p}, \tag{4.3}$$

$$\frac{dp}{dt} = -\frac{\partial \mathcal{H}}{\partial \theta}. \tag{4.4}$$

   where

$$\mathcal{H}(\theta, p) = -\log(Q(\theta|y)) + \frac{1}{2} p^T M^{-1} p + c, \tag{4.5}$$

is the negative log-posterior joint density known as the 'Hamiltonian' and,

$$Q(\theta|y) = p(\theta)p(y|\theta), \tag{4.6}$$

is the unnormalised posterior. The Hamiltonian can be interpreted as the sum of the kinetic and potential energy of the proposed new sample. This step is solved using Stan's leapfrog algorithm [61]. The algorithm parameters such as the step size T and the matrix M are tuned during the warm-up phase of sampling.

3. Set proposal parameters $\theta_i' = \theta(T)$, $p_i' = -p(T)$.

4. Accept proposal parameters with probability:

$$\min\{1, \exp(-\mathcal{H}(\theta_i', p_i') + \mathcal{H}(\theta_i, p_i))\}$$

5. Take the next sample as:

$$(\theta_{i+1}, p_{i+1}) = \begin{cases} (\theta_i', p_i') & \text{if proposal accepted} \\ (\theta_i, p_i) & \text{otherwise} \end{cases}$$

We now use this framework to extract Bayesian approximations for the model parameters in both the CIV and BIV models.

4.1 Parameter inference in the CIV$^+$ model

As in the frequentist fitting section, we generate synthetic data based on the parameter values discussed in section 2.2. For both the CIV and BIV models, the likelihood function is the model output of total cortisol plus some additive normal error.

We begin by considering Bayesian approximations using Stan on synthetic data generated using the CIV$^+$ model and imposing normal prior distributions. The prior distri-

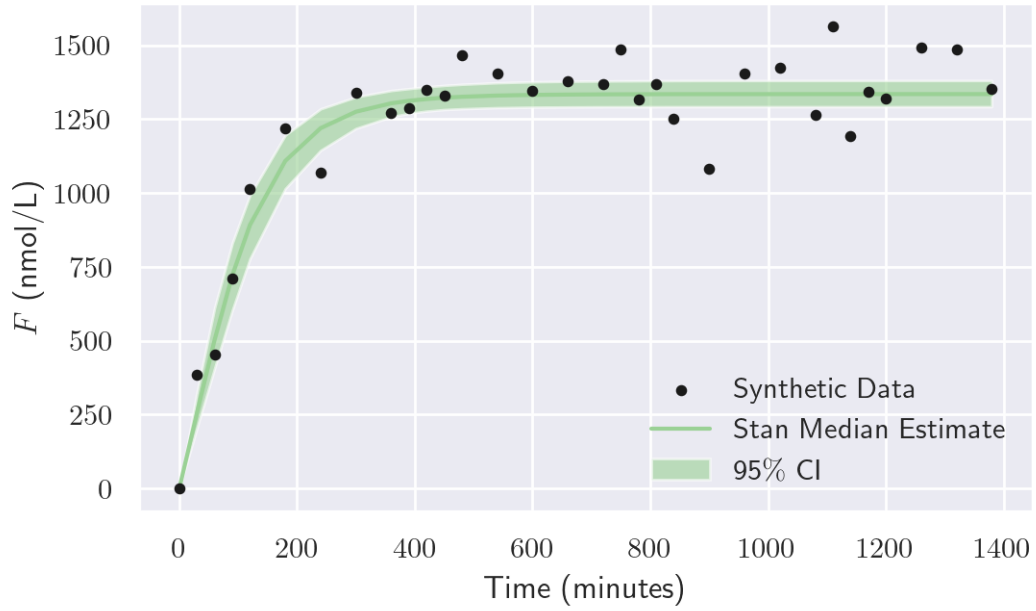

Figure 4.1: Bayesian approximation using normal prior distributions of synthetic data generated using the CIV^+ model given by eqs. (2.4) and (2.5) with Gaussian noise added (s.d. $100\,\mathrm{nmol\,L^{-1}}$) and sampling time frequency corresponding to the time points used in data [PD].

butions were chosen to generate trajectories that are qualitatively similar to data [PD], which were tested using prior predictive checks. Other sets of prior distributions were investigated during experimentation, however the set presented here is representative of reasonable physical bounds on each parameter. Figure 4.1 shows the Bayesian approximation of the trajectory against the data which is a good qualitative match and we will see in Table 4.5 a summary of the posterior distributions for the model parameters. We look at the estimates for each of the model parameters in turn.

Firstly, for the dilution factor α, the posterior is much narrower than the imposed normal prior (Figure 4.2(c)). However, the ground truth value of α is very close to the border of the 95% credible interval, although still within this interval, which could suggest that the posterior is biased due to noise on the data as in the global identifiable toy problem (appendix C.2.1). We run a Bayesian approximation for smaller amounts of additive noise and find that the ground truth sits closer to the mean and median of the posterior (Figure 4.2(a)). Considering the estimates for binding and unbinding rates, k_{fb}

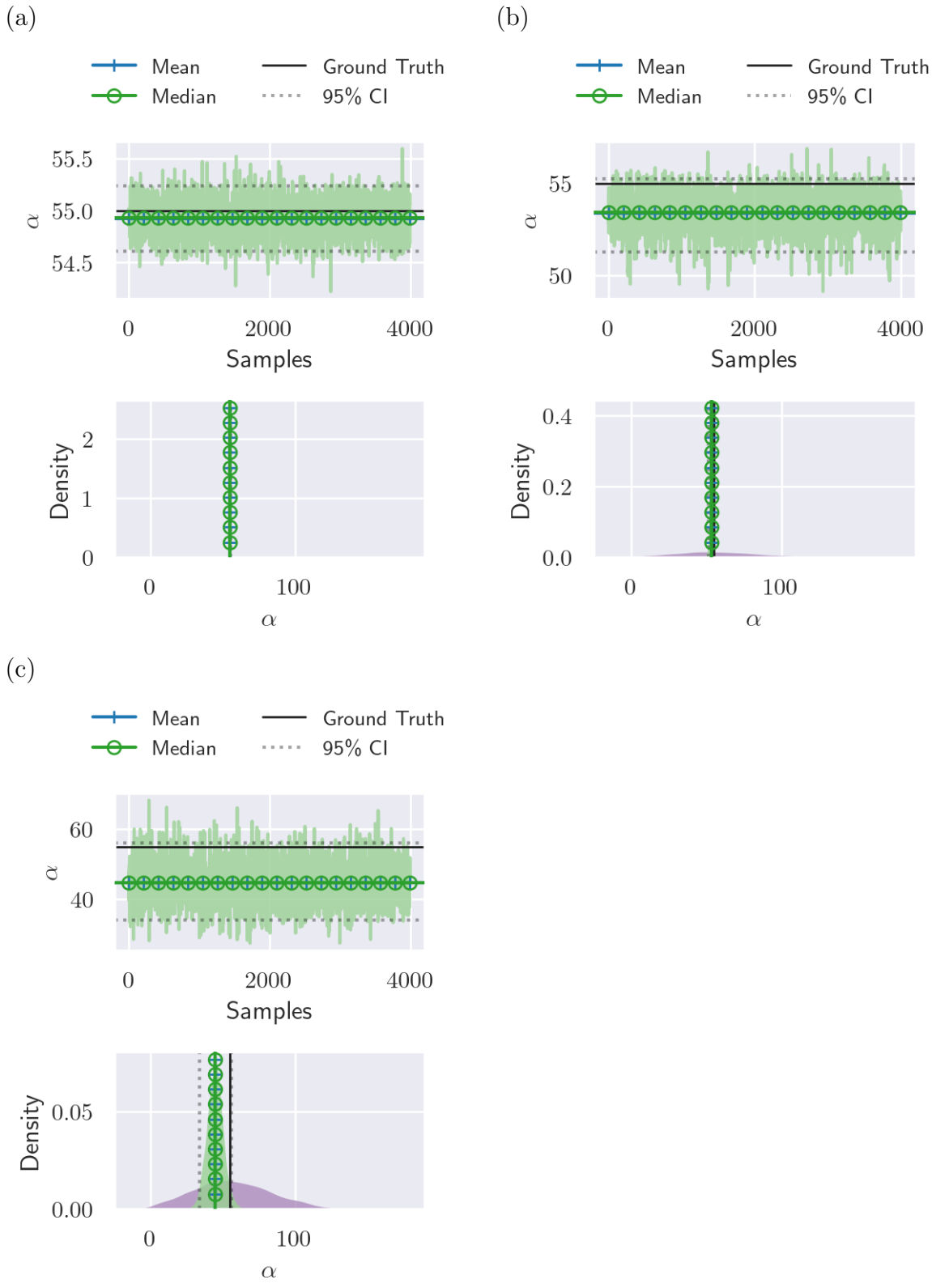

Figure 4.2: Trace, prior distributions (purple) and posterior distributions (green) of dilution factor, α, for the Bayesian approximation of the CIV$^+$ model given by eqs. (2.4) and (2.5) with sampling time frequency corresponding to the time points used in data [PD] and varying amounts of noise: (a) $1\,\mathrm{nmol\,L^{-1}}$, (b) $10\,\mathrm{nmol\,L^{-1}}$, (c) $100\,\mathrm{nmol\,L^{-1}}$.

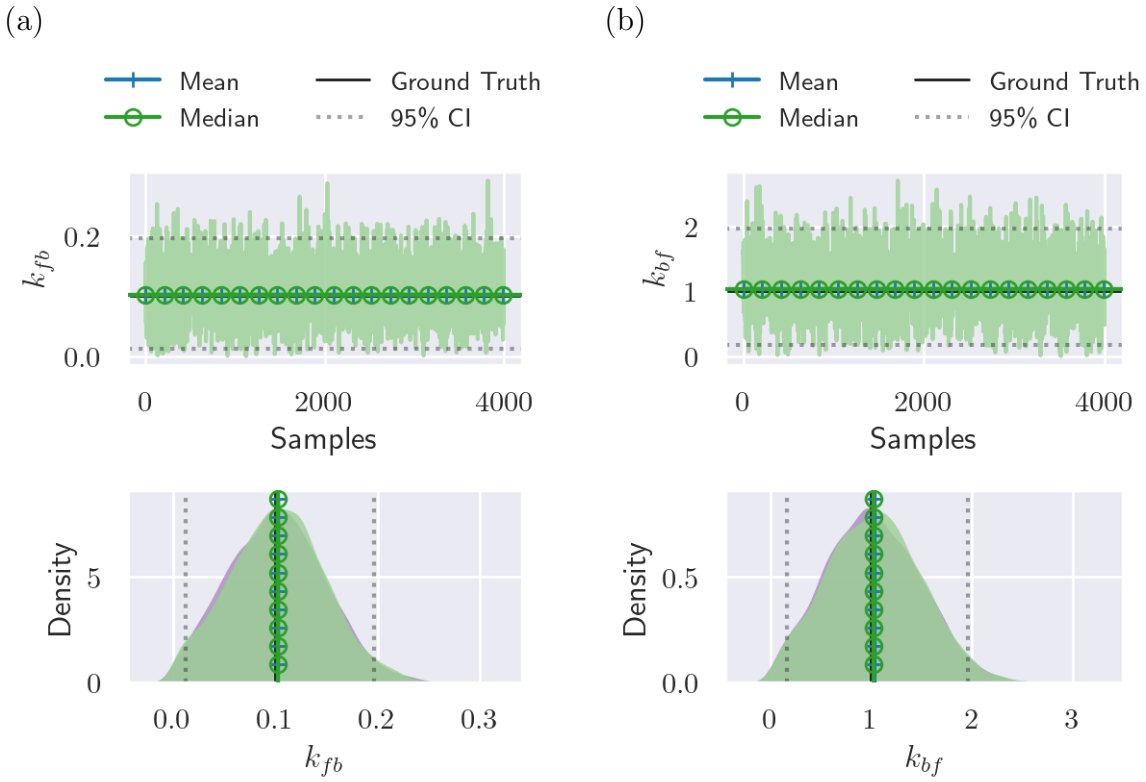

Figure 4.3: Trace, prior distributions and posterior distributions of binding and unbinding rates, k_{fb} and k_{bf} respectively, for the Bayesian approximation of the CIV$^+$ model given by eqs. (2.4) and (2.5) with Gaussian noise added (s.d. 100 nmol L^{-1}) and sampling time frequency corresponding to the time points used in data [PD].

and k_{bf}, the posterior distributions in Figure 4.3 remain wide and similar to the prior distributions (standard deviation of k_{fb} prior is 0.05 versus a posterior standard deviation of 0.046, see Table 4.2). These results reflect the finding in section 2.3, where we concluded the model with this high level of noise (s.d. approximately 100 nmol L^{-1}) is insensitive to the specific binding and unbinding rates. However, the added advantage here is that we now have a quantification of the uncertainty. We also note that in Figure 4.5 that there is no obvious correlation between these two parameters due to the high level of noise.

Figure 4.4 shows that the posterior distributions for clearance rate parameter k_{re} and physiological level of binding protein B_0 have narrowed from the prior distributions somewhat, but not as much as the estimate for α (the posterior distributions for B_0 and k_{re} are ∼59% and ∼52% of the width of their respective prior distributions compared to the posterior for α which is ∼18% of the width of the prior). However, this estimate for

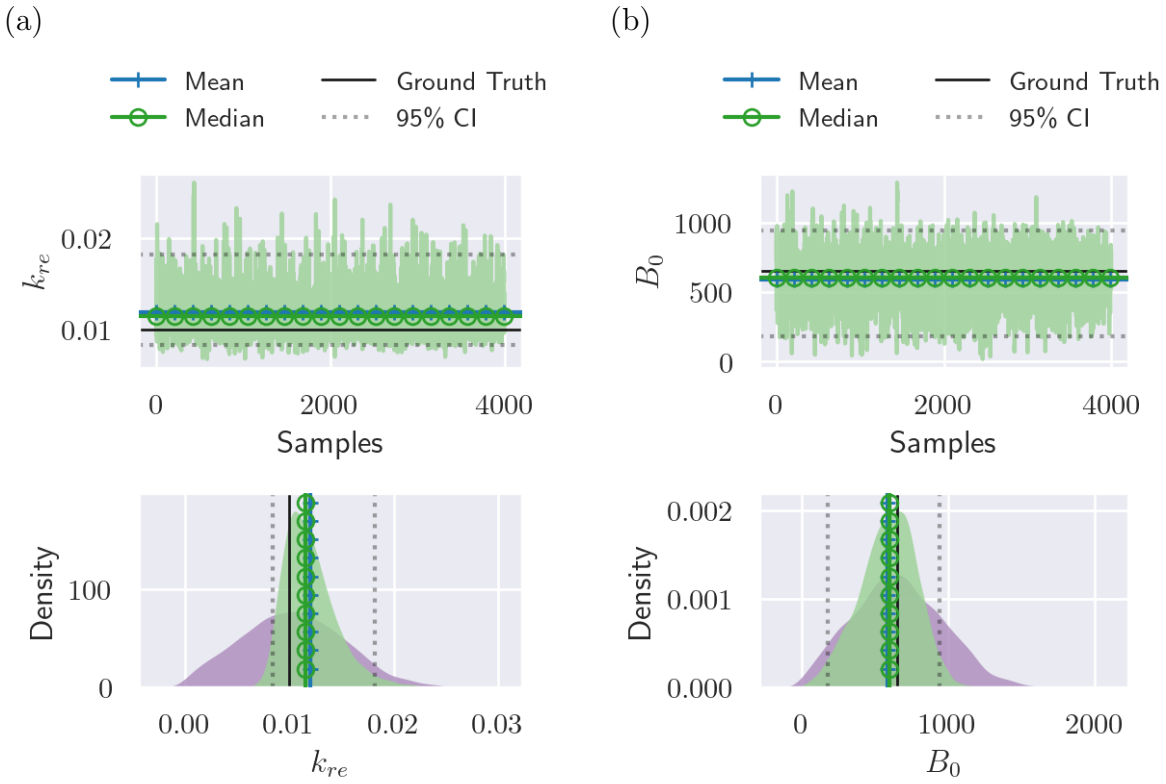

Figure 4.4: Trace, prior distributions and posterior distributions of clearance rate parameter k_{re} and physiological level of binding protein B_0, for the Bayesian approximation of the CIV$^+$ model given by eqs. (2.4) and (2.5) with Gaussian noise added (s.d. 100 nmol L^{-1}) and sampling time frequency corresponding to the time points used in data [PD].

B_0 is an improvement from the frequentist fitting which was unable to recover the true value under high noise, suggesting that this parameter benefits from having some prior knowledge of the value imposed. There is a relationship between these two parameters in the scatter matrix (Figure 4.5), which can also be seen in Chapter 2 in Figure 2.8(c). This could be due to both parameters having similar effects on the model trajectory, where a higher physiological level of binding protein allows more cortisol to be bound, hence slowing removal. The posterior distribution for σ is centred close to the true value (Figure 4.6) with a standard deviation that is $\sim$ 30% the width of the imposed prior. We trial treating σ as known to see whether this improve the Bayesian approximations and see little change in the fitting results. There is no reduction in fitting time, and posterior distributions are similar for all other parameters. The ground truth for α has moved marginally outside the credible interval (see Figure D.1 in appendix D.1), which

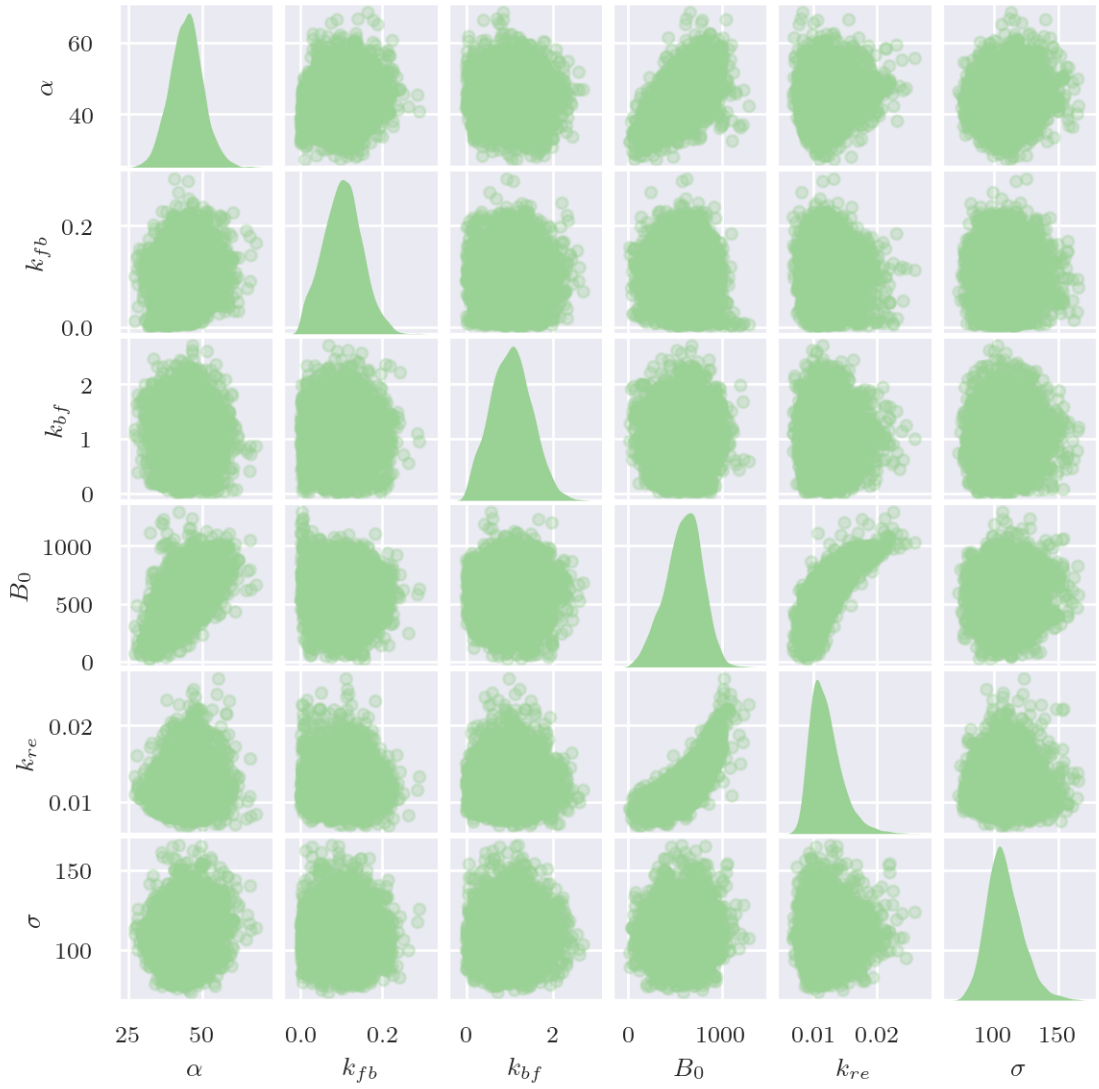

Figure 4.5: Scatter matrix plot of parameter samples for the Bayesian approximation of the CIV^+ model given by eqs. (2.4) and (2.5) with Gaussian noise added (s.d. $100\,\mathrm{nmol\,L^{-1}}$) and sampling time frequency corresponding to the time points used in data [PD].

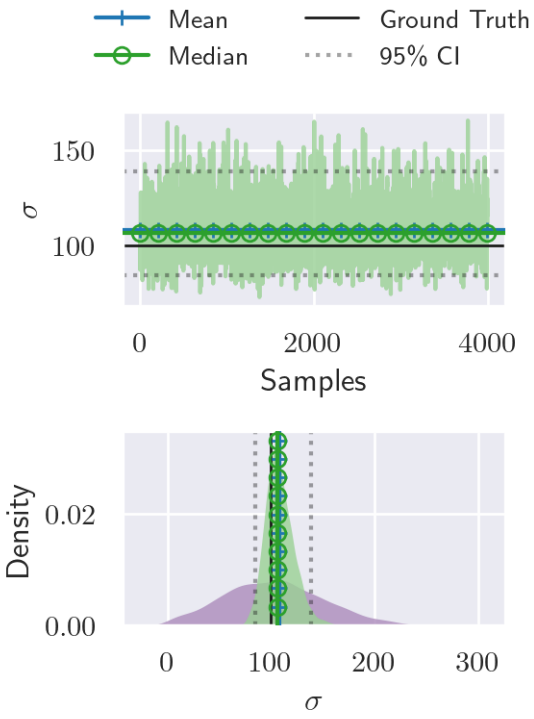

Figure 4.6: Trace, prior distributions and posterior distributions for the noise parameter σ, for the Bayesian approximation of the CIV$^+$ model given by eqs. (2.4) and (2.5) with Gaussian noise added (s.d. 100 nmol L^{-1}) and sampling time frequency corresponding to the time points used in data [PD].

as discussed above is likely a bias introduced from the high level of noise.

Choice of Prior Distributions

We examine the influence of the choice of prior distributions on the posterior estimates. We first consider different widths of normal prior. In the previous section, the standard deviation of each prior was chosen to be half of the mean that the normal distribution is centred around for each parameter. In what follows, when we refer to a wide prior, we choose the standard deviation to be 10 times the mean. Similarly, when we refer to a narrow prior, we choose the standard deviation to be a tenth of the respective mean. We also note that in each case we are using truncated norms to maintain the condition that all of the model parameters are positive, however we will later consider whether gamma prior distributions will affect the posterior outcome. A summary of the different choices

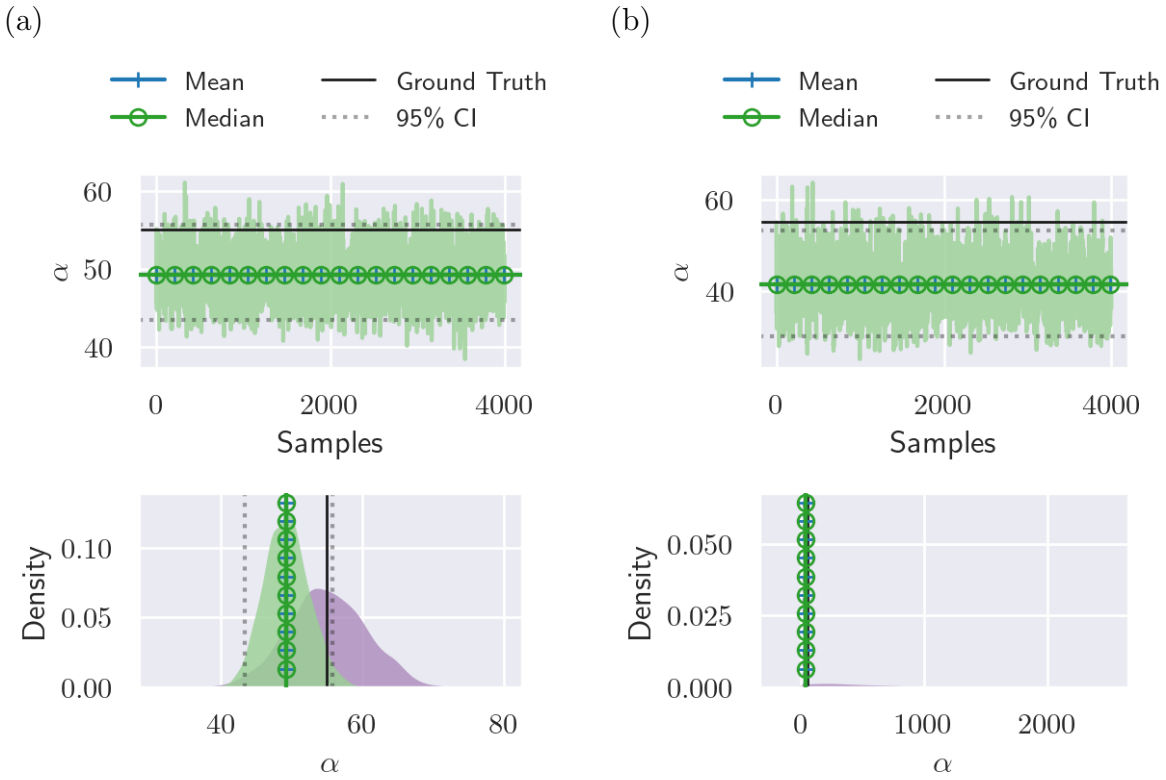

Figure 4.7: Trace, prior distributions and posterior distributions of dilution factor α, for the Bayesian approximation of the CIV$^+$ model given by eqs. (2.4) and (2.5) with Gaussian noise added (s.d. 100 nmol L^{-1}), sampling time frequency corresponding to the time points used in data [PD] and for varying widths of normal prior: (a) Narrow, (b) Wide.

of prior and the corresponding posterior distributions is shown in Table 4.2.

For all parameters, the narrow prior results in posterior distributions with similar standard deviations to their respective prior distributions which suggests that the prior distributions are leading the posterior over the data. For α, the ground truth remains at the edge of the 95% credible interval (Figure 4.7). For k_{fb} and k_{bf}, the width of the posterior distributions remains the same as the prior distributions (with a little movement from k_{fb} in the wide prior case), confirming that the model is insensitive to these values (Figure 4.8). The slight movement in the k_{fb} wide prior could be due to the parameter reaching the bounds at which the model is insensitive to that parameter value. When using wide prior distributions, we also see a relationship between B_0 and k_{fb} (Figure 4.9). In chapter 2, we saw that the parameter recovery CIV$^\pm$ models resulted in a overestimate

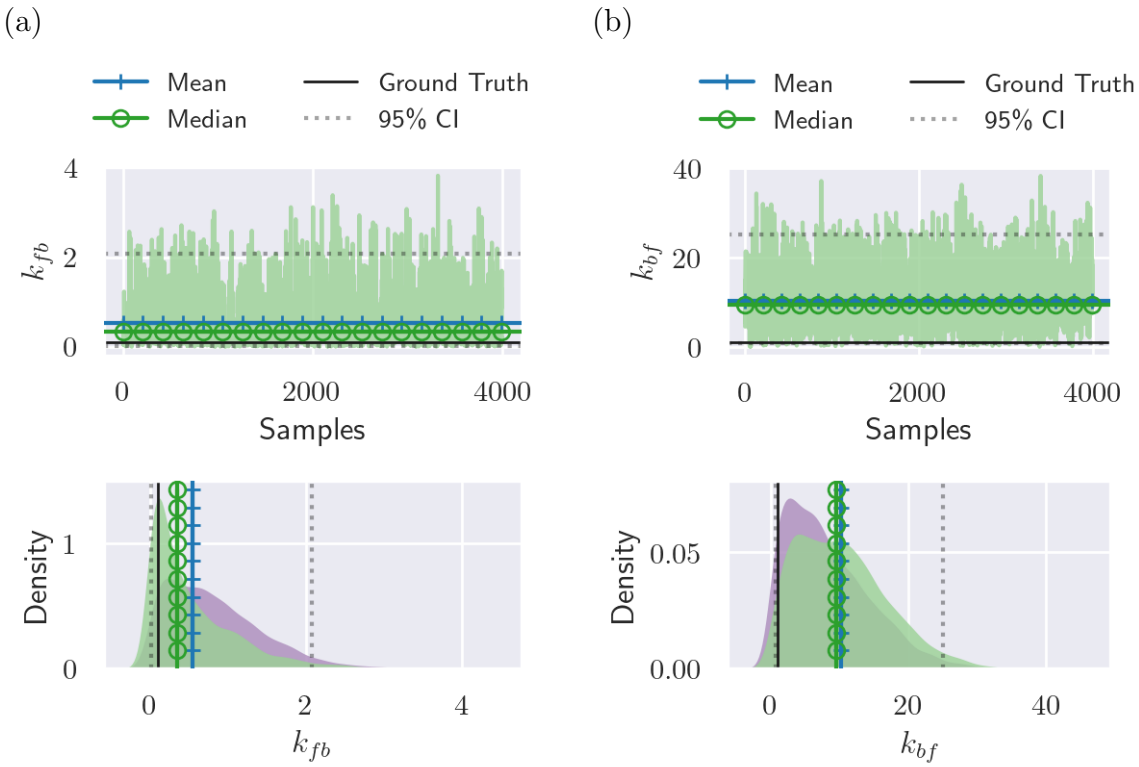

Figure 4.8: Trace, prior distributions and posterior distributions of binding and unbinding rates, k_{fb} and k_{bf} respectively, for the Bayesian approximation of the CIV$^+$ model given by eqs. (2.4) and (2.5) with Gaussian noise added (s.d. $100\,\mathrm{nmol\,L^{-1}}$), sampling time frequency corresponding to the time points used in data [PD] and for wide normal prior distributions.

of B_0 and so here the wider prior is allowing for B_0 to explore these much larger values. The posterior distribution for k_{fb} has shifted left in this case. The binding rate k_{fb} and physiological level of binding protein B_0 combined determine the amount of bound cortisol so a smaller k_{fb} compensates for a larger B_0. The posterior for k_{re} becomes very similar to the prior in the wide case, and could be due to larger values of k_{bf} (more unbinding) in the wider prior, which then requires a faster clearance rate (larger k_{re}) to maintain a good qualitative fit (Figure 4.10).

Gamma prior distributions can be imposed to inform the sampler that model parameters are small but positive [66, 67]. The shape and scale parameters for each prior are summarised in table Table 4.2. We find that the posterior for α is still biased away from the ground truth. We further confirm the insensitivity of the model to parameters k_{fb} and k_{bf} as they remain following the imposed gamma prior distributions (Figure 4.11). Finally, the posterior distributions for B_0 and k_{re} remain similar in shape to the posterior distributions when using normal prior distributions, suggesting they are not being influenced by the imposed prior. Overall, the gamma prior distributions do not seem to offer any significant improvements over using normal prior distributions, and computation is marginally longer.

Finally, uniform prior distributions are not recommended within Stan, instead it is recommended to use weakly informative prior distributions that indicate the order of magnitude of parameters [66].

4.2 Parameter inference in the CIV$^-$ model

We consider a Bayesian approximation of the CIV$^-$ model described by eqs. (2.34) and (2.35). For synthetic data with Gaussian noise added (s.d. $1\,\mathrm{nmol\,L^{-1}}$) and sampling time frequency corresponding to the time points used in data [PD], the Bayesian median estimate of total cortisol is a qualitatively good fit of the data (Figure 4.12). Fitting the CIV$^-$ model is significantly faster than the full model (approx. 40 seconds for a

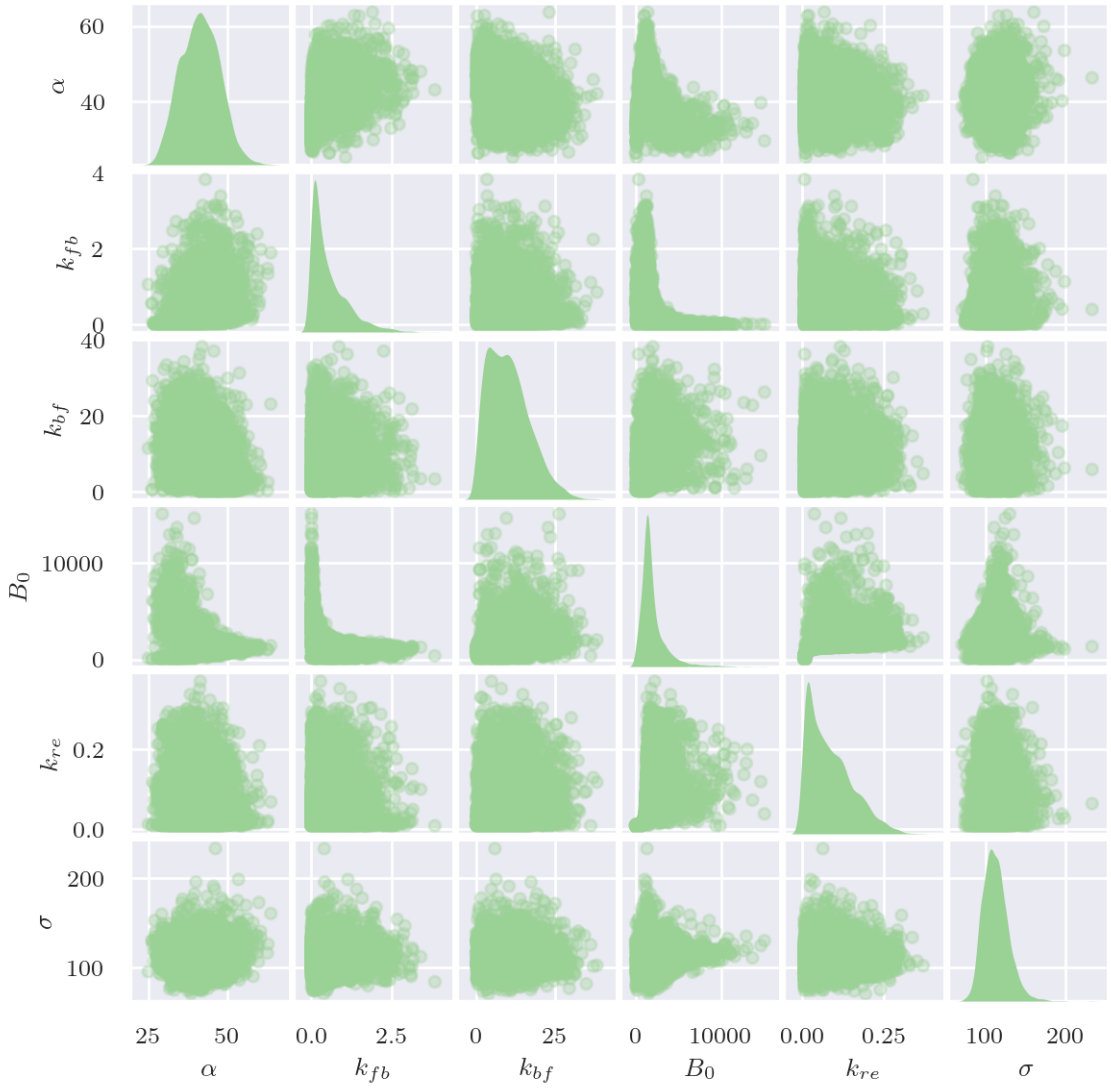

Figure 4.9: Scatter matrix plot of parameter samples for the Bayesian approximation of the CIV^+ model given by eqs. (2.4) and (2.5) with Gaussian noise added (s.d. $100\,\mathrm{nmol\,L^{-1}}$), sampling time frequency corresponding to the time points used in data [PD] and using wide normal prior distributions.

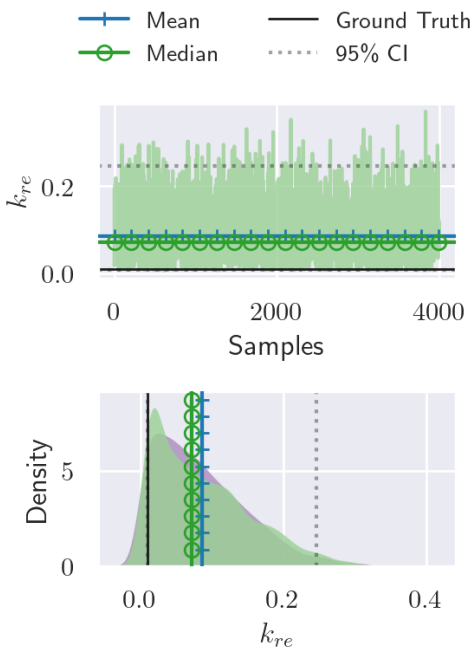

Figure 4.10: Trace, prior distributions and posterior distributions for the clearance rate parameter k_{re}, for the Bayesian approximation of the CIV$^+$ model given by eqs. (2.4) and (2.5) with Gaussian noise added (s.d. 100 nmol L^{-1}), sampling time frequency corresponding to the time points used in data [PD] and using wide normal prior distributions.

2000-sample chain versus 2500 seconds, see Table 4.4 for time comparison of all models). We now consider the behaviour of each parameter in turn.

For α, we see the same bias in the posterior away from the ground truth value that we saw in the CIV$^+$ model. Figure 4.13 shows that the ground truth is further from the mean and median of the posterior as noise increases as with the full model and is outside of the 95% CI for large noise.

The parameter grouping δ now behaves as the k_{fb} and k_{bf} behaved in the full model; the model seems insensitive to the value and the posterior distribution remains around the imposed prior (Figure 4.14(a)). In Figure 4.14, we show the posterior distribution for δ for both normal and gamma prior distributions. In Figure 4.14(b), we consider a normal prior where the true value is not at the mean of the prior, and we see that the posterior shows no shift towards the true value, suggesting the posterior distribution is entirely led by the imposed prior.

Figure 4.15 shows that the posterior distributions for the physiological level of binding

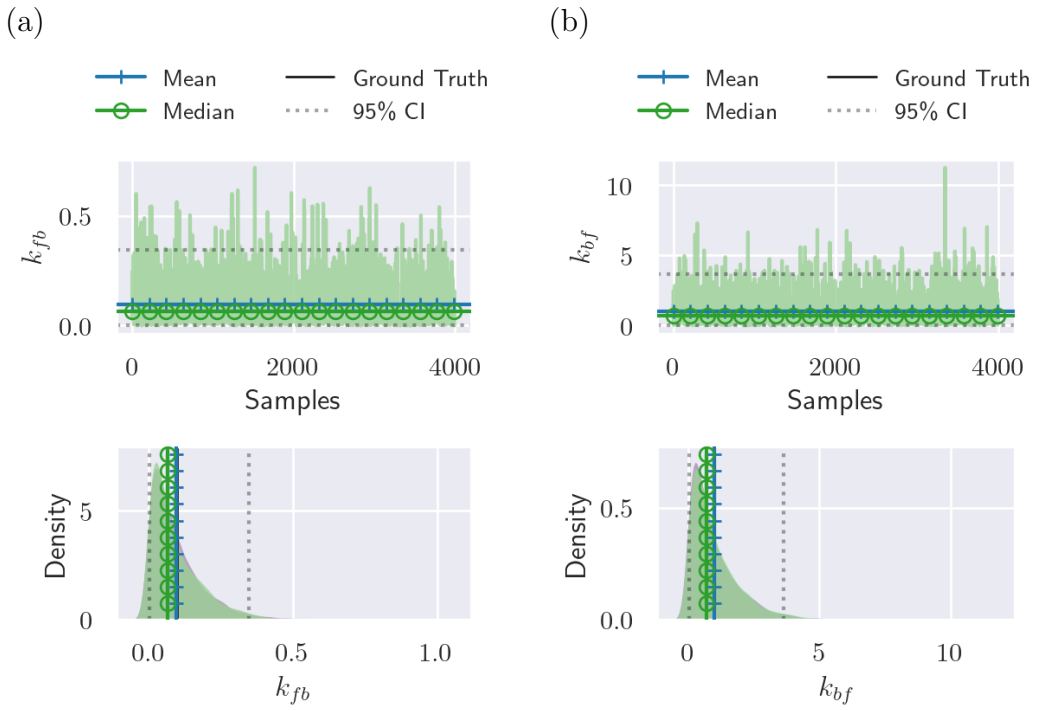

Figure 4.11: Trace, prior distributions and posterior distributions of binding and unbinding rates, k_{fb} and k_{bf} respectively, for the Bayesian approximation of the CIV$^+$ model given by eqs. (2.4) and (2.5) with Gaussian noise added (s.d. $100\,\mathrm{nmol\,L^{-1}}$), sampling time frequency corresponding to the time points used in data [PD] and for gamma prior distributions.

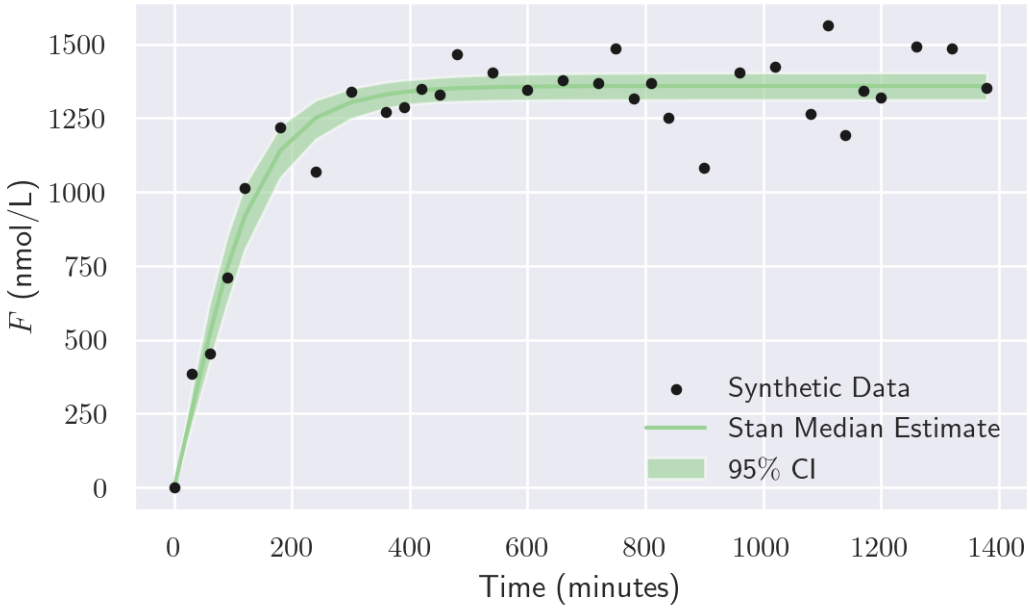

Figure 4.12: Bayesian approximation of synthetic data generated using the CIV$^-$ model given by eqs. (2.34) and (2.35) with Gaussian noise added (s.d. $100\,\mathrm{nmol\,L^{-1}}$), sampling time frequency corresponding to the time points used in data [PD] and for normal prior distributions.

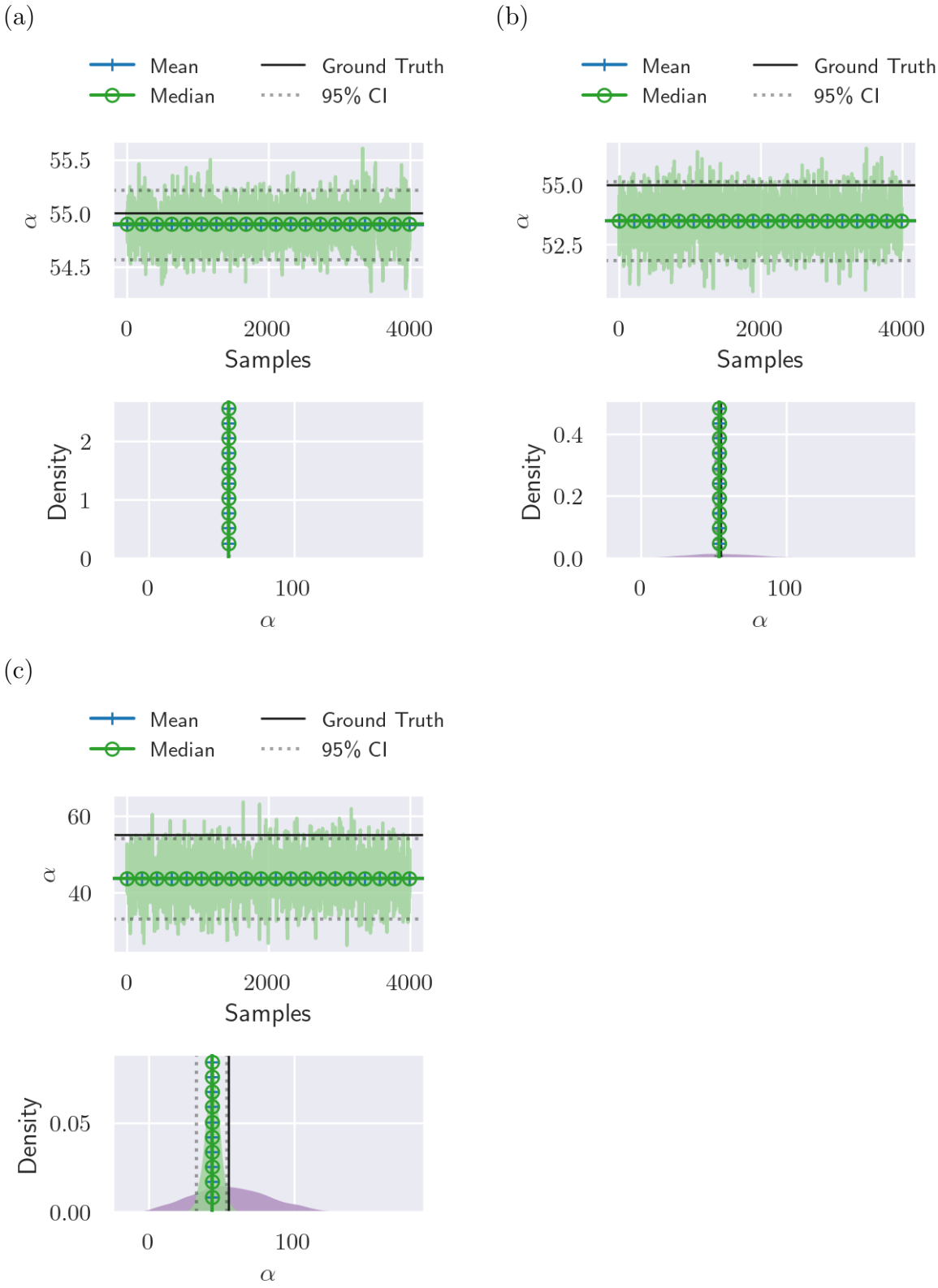

Figure 4.13: Trace, prior distributions and posterior distributions of dilution factor, α, for the Bayesian approximation of the CIV$^-$ model given by eqs. (2.34) and (2.35) with normal prior distributions imposed, sampling time frequency corresponding to the time points used in data [PD] and for varying amounts of noise: (a) 1 nmol L^{-1}, (b) 10 nmol L^{-1}, (c) 100 nmol L^{-1}.

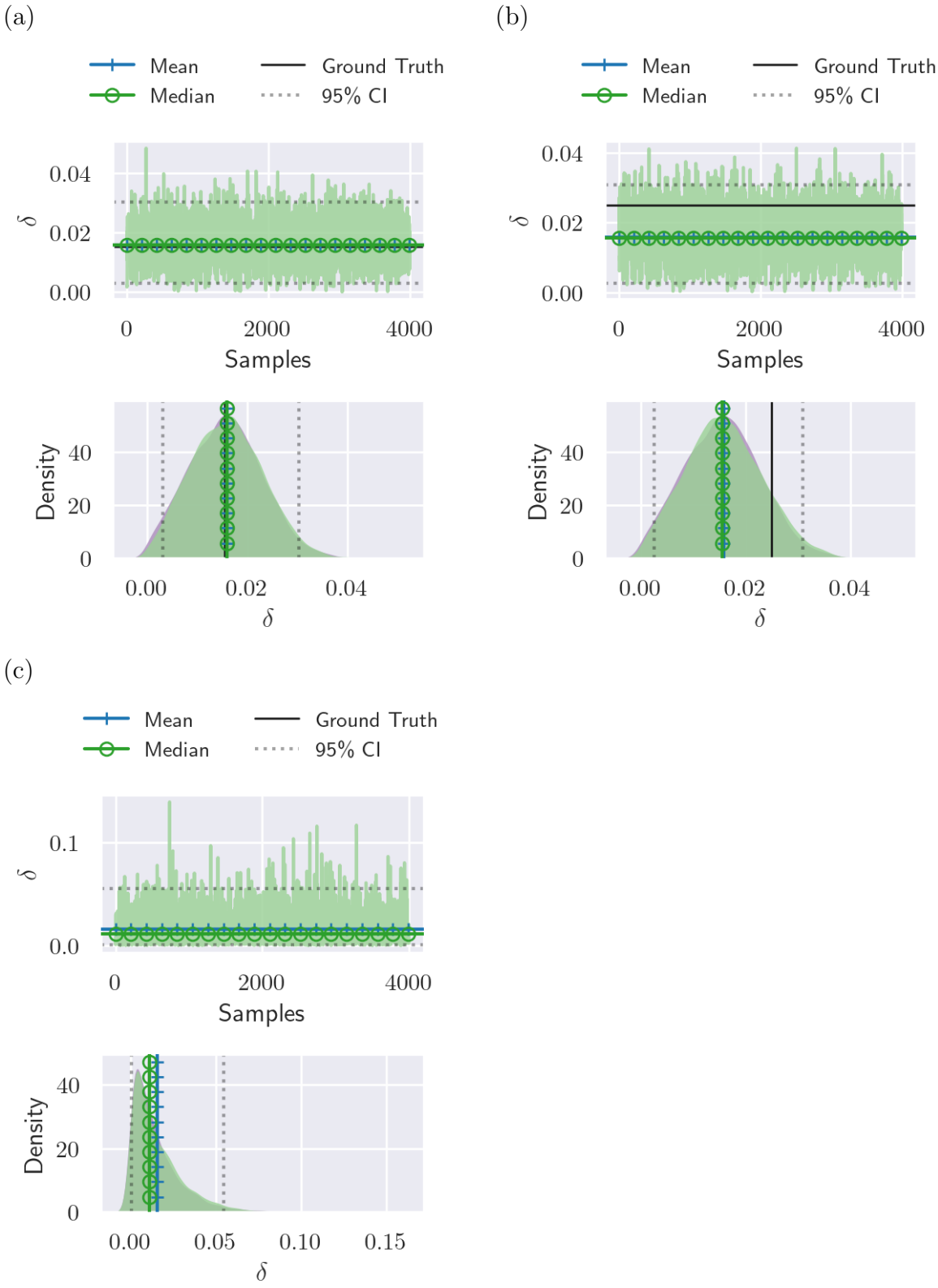

Figure 4.14: Trace, prior distributions and posterior distributions of the parameter grouping δ, for the Bayesian approximation of the CIV$^-$ model given by eqs. (2.34) and (2.35) with Gaussian noise added (s.d. $100\,\mathrm{nmol\,L^{-1}}$), sampling time frequency corresponding to the time points used in data [PD] and for varying imposed prior distributions: (a) Normal prior with the ground truth at the mean, (b) Normal prior with the ground truth away from the mean, (c) Gamma prior.

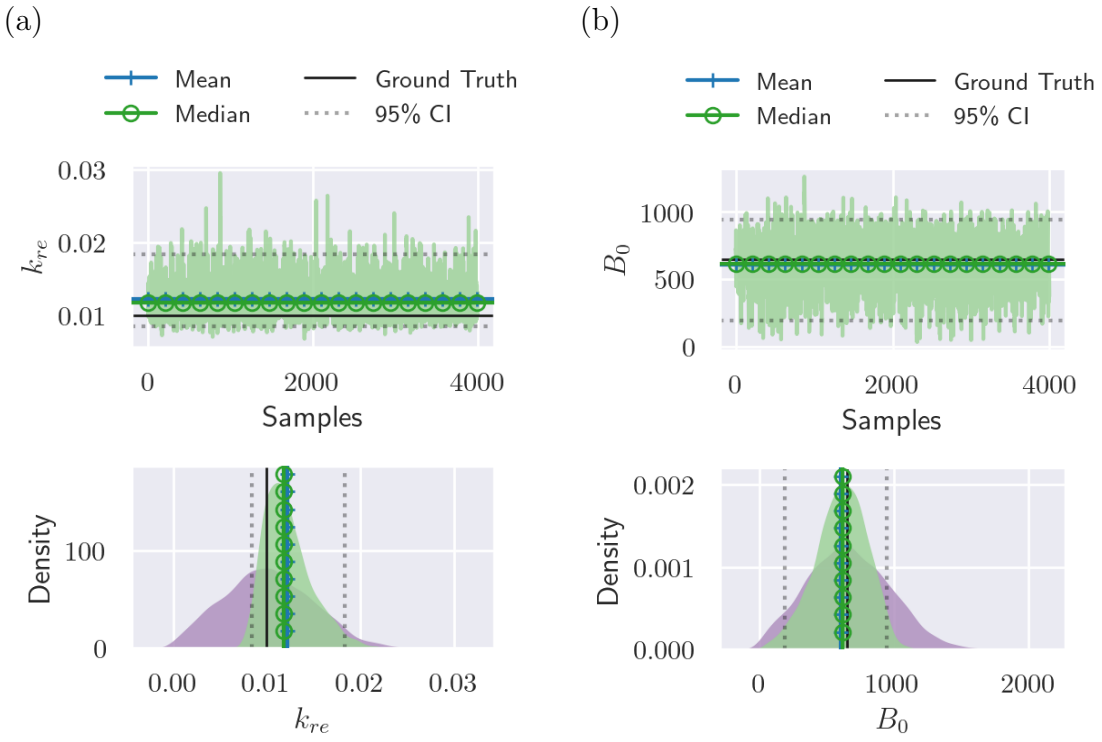

Figure 4.15: Trace, prior distributions and posterior distributions of clearance rate parameter k_{re} and physiological level of binding protein B_0, for the Bayesian approximation of the CIV$^-$ model given by eqs. (2.34) and (2.35) with Gaussian noise added (s.d. 100 nmol L^{-1}), sampling time frequency corresponding to the time points used in data [PD] and normal prior distributions imposed.

protein, B_0, and the clearance rate parameter, k_{re}, follow similarly from the CIV$^+$ model and there still appears to be a relationship between them shown in the scatter plot matrix (Figure 4.16). Therefore we conclude that this model retains the information of the full model whilst decreasing computation time significantly.

Comparison of Prior Distributions

We assess how the choice of prior distribution influences the parameter posterior distribution. Narrowing the normal prior distributions has a similar effect to the CIV$^+$ case, where the posterior distributions do not differ much (see summary of posterior standard deviations in Table 4.2). The posterior distributions are also similar to the CIV$^+$ case when gamma prior distributions are imposed. We do see a notable change when we implement wide prior distributions on all parameters (Figure 4.17). All of the parameter

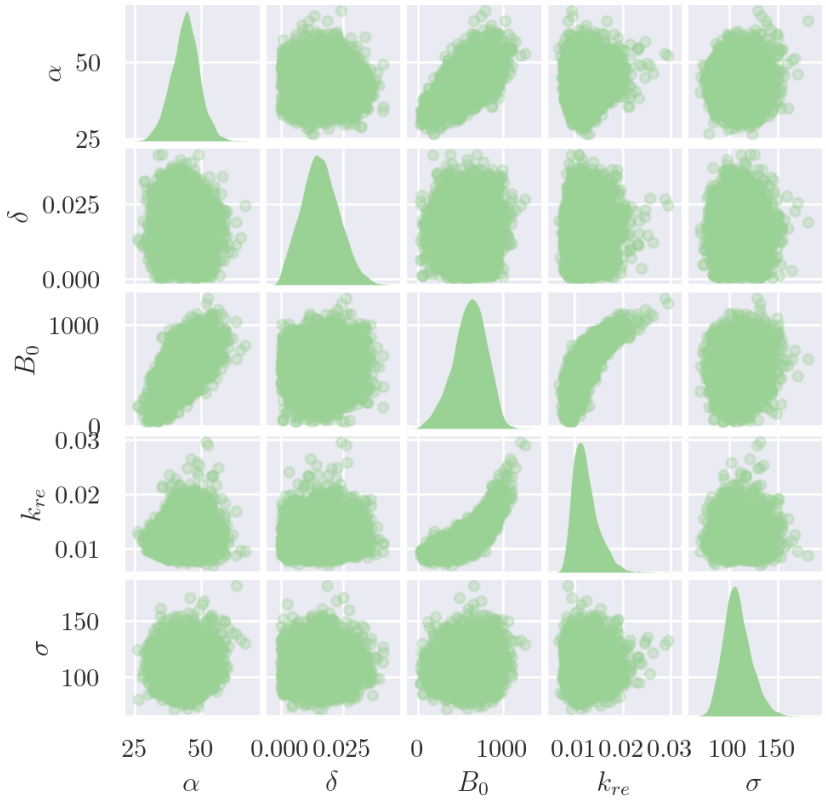

Figure 4.16: Scatter matrix plot of parameter samples for the Bayesian approximation of the CIV^- model given by eqs. (2.34) and (2.35) with Gaussian noise added (s.d. $100\,\mathrm{nmol\,L^{-1}}$), sampling time frequency corresponding to the time points used in data [PD] and normal prior distributions imposed.

ground truths (except noise parameter σ) are at the border or outside of the 95% credible interval of the posterior, with the ground truth for α far outside of the 95% credible interval. The posterior for δ has shifted marginally from the prior but is still very wide, supporting the conclusion that the model is insensitive to this value within certain bounds. The posterior remains very wide on B_0 in the normal wide prior case. The qualitative fit of the total cortisol trajectory still matches the data (Figure 4.18) which could suggest there is some local identifiability introduced for the physiological level of binding protein B_0 under large noise. The wide prior allows B_0 to reach physiologically unrealistic values which suggests a more informative prior is necessary on this parameter. In Figure 4.19 when noise is small and the same prior distributions are imposed, the posterior estimates are much closer to the ground truth values.

Error and Time Resolution

We now consider the influence of noise and time-resolution of data on the posterior distribution for the model parameters, in particular to see if increased time-resolution will reduce the level of uncertainty around the parameter grouping δ. Figure 4.14(a) showed that in the large noise, low time-resolution case, the posterior for δ is similar to the prior.

Figure 4.20 shows the prior versus posterior distributions for δ for varying time resolution and amounts of noise atop synthetic data. Decreasing the noise makes the posterior distribution for δ narrower ($\sim$ 33% width of the prior compared to $\sim$ 93% of width in the high noise case), and then increasing time-resolution of time samples to approximate resolution of current wearable and implantable sensors makes the posterior distribution narrower still [53, 52] ($\sim$ 15% width of the prior). However, when noise is high, increasing the time-resolution to every 10 minutes does not reduce the uncertainty in the estimates of δ (posterior distribution is $\sim$ 92% of the width of prior). Increasing the time-resolution beyond the current physically feasible limits to 1 minute creates a slight shift in the posterior, however there is still large uncertainty in the posterior distribution. We show the corresponding behaviour of the clearance rate parameter k_{re} to demonstrate the difference

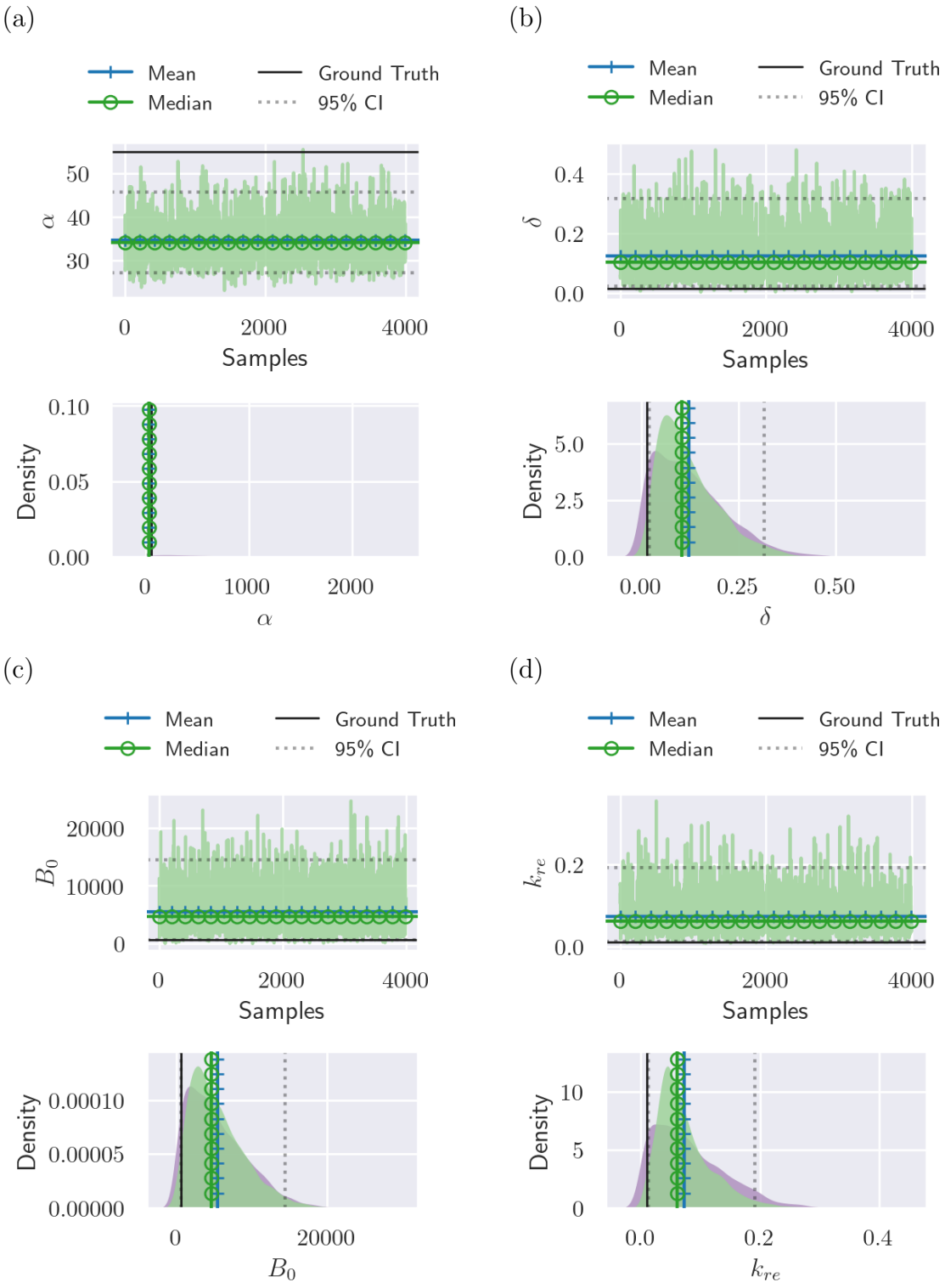

Figure 4.17: Trace, prior distributions and posterior distributions of model parameters for the Bayesian approximation of the CIV$^-$ model given by eqs. (2.34) and (2.35) with Gaussian noise added (s.d. 100 nmol L^{-1}), sampling time frequency corresponding to the time points used in data [PD] and wide normal prior distributions imposed: (a) for dilution factor α, (b) for parameter grouping δ, (c) for physiological level of binding protein B_0, (d) free cortisol clearance rate k_{re}.

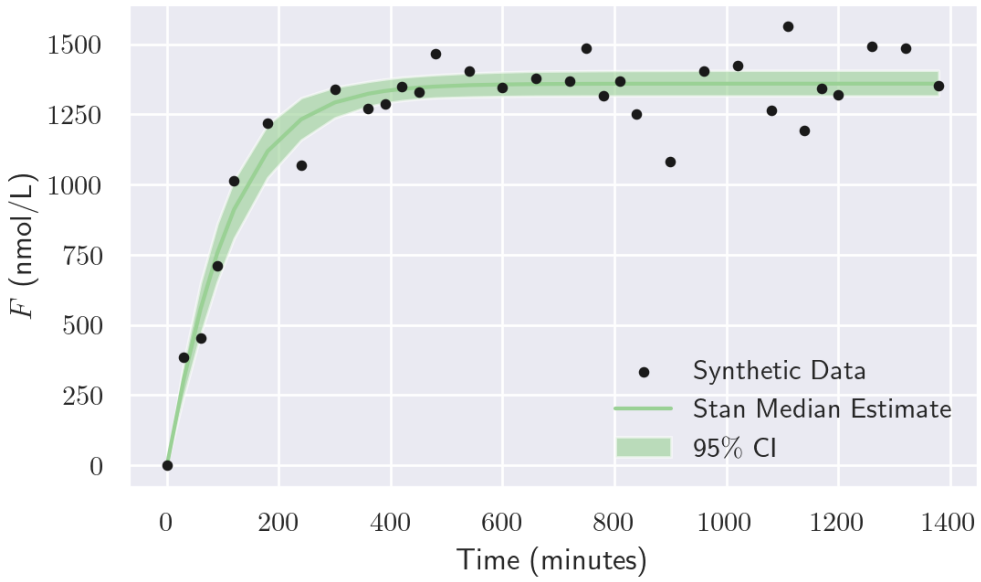

Figure 4.18: Bayesian approximation of synthetic data generated using the CIV^- model given by eqs. (2.34) and (2.35) with Gaussian noise added (s.d. $100\,\mathrm{nmol\,L^{-1}}$), sampling time frequency corresponding to the time points used in data [PD] and wide normal prior distributions imposed.

in posterior for varying time-resolution and error in Figure 4.21.

The level of noise atop the synthetic data has a large influence here on the ability to obtain a decent estimate for δ. Time-resolution can go some way to mitigating high noise, but the time-resolution needed for a realistic amount of error is currently physically implausible. The 95% credible intervals are narrower for all other parameter posterior distributions for both lower noise and higher time-resolution. We also see that the high time-resolution (every 1 minute) has eliminated some of the bias on the α estimate in the high noise case and the mean is much closer to the ground truth, with a standard deviation that is $\sim 4\%$ of the width of the imposed prior (compared to $\sim 20\%$ for the [PD] time case).

The value of δ value seems to have little to no effect on the model trajectory within sensible bounds as confirmed by the analysis in appendix D.2.

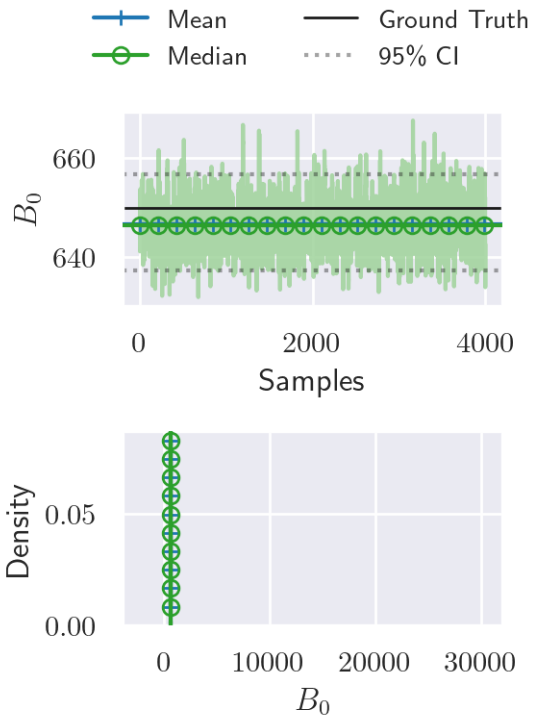

Figure 4.19: Trace, prior distributions and posterior distributions for the physiological level of binding protein B_0, for the Bayesian approximation of the CIV$^-$ model given by eqs. (2.34) and (2.35) with Gaussian noise added (s.d. $1\,\mathrm{nmol\,L^{-1}}$), sampling time frequency corresponding to the time points used in data [PD] and using wide normal prior distributions. The prior distribution is unseen due to the very narrow posterior distribution.

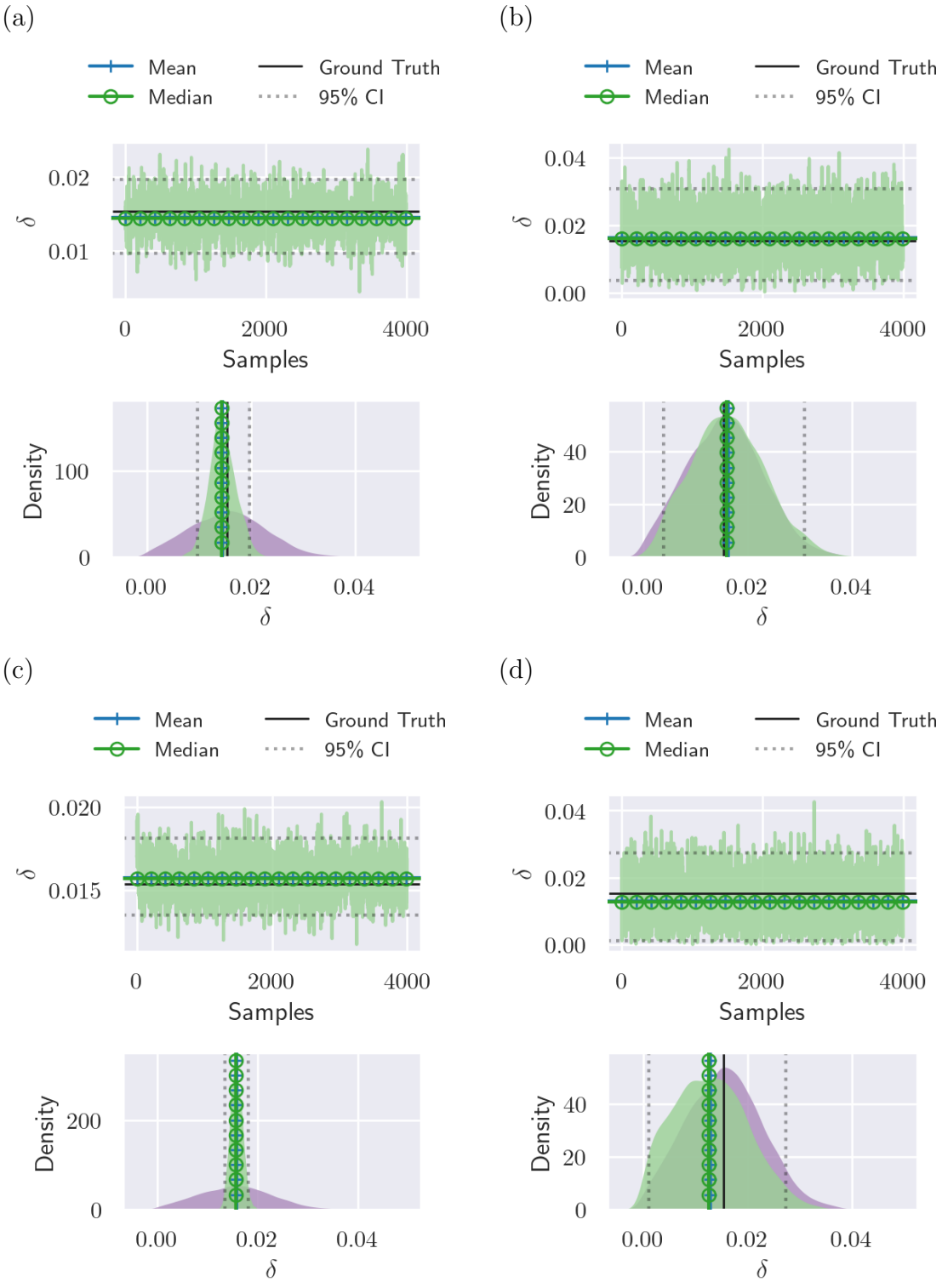

Figure 4.20: Trace, prior distributions and posterior distributions of model parameter grouping δ for the Bayesian approximation of the CIV$^-$ model given by eqs. (2.34) and (2.35) with normal prior distributions imposed and for varying noise and time-resolution: (a) low error (s.d. $1\,\mathrm{nmol\,L^{-1}}$), low time-resolution ([PD]), (b) high error (s.d. $100\,\mathrm{nmol\,L^{-1}}$), time-resolution (every 10 minutes), (c) low error (s.d. $1\,\mathrm{nmol\,L^{-1}}$), high time-resolution (every 10 minutes), (d) high error (s.d. $100\,\mathrm{nmol\,L^{-1}}$), high time-resolution (every 1 minute).

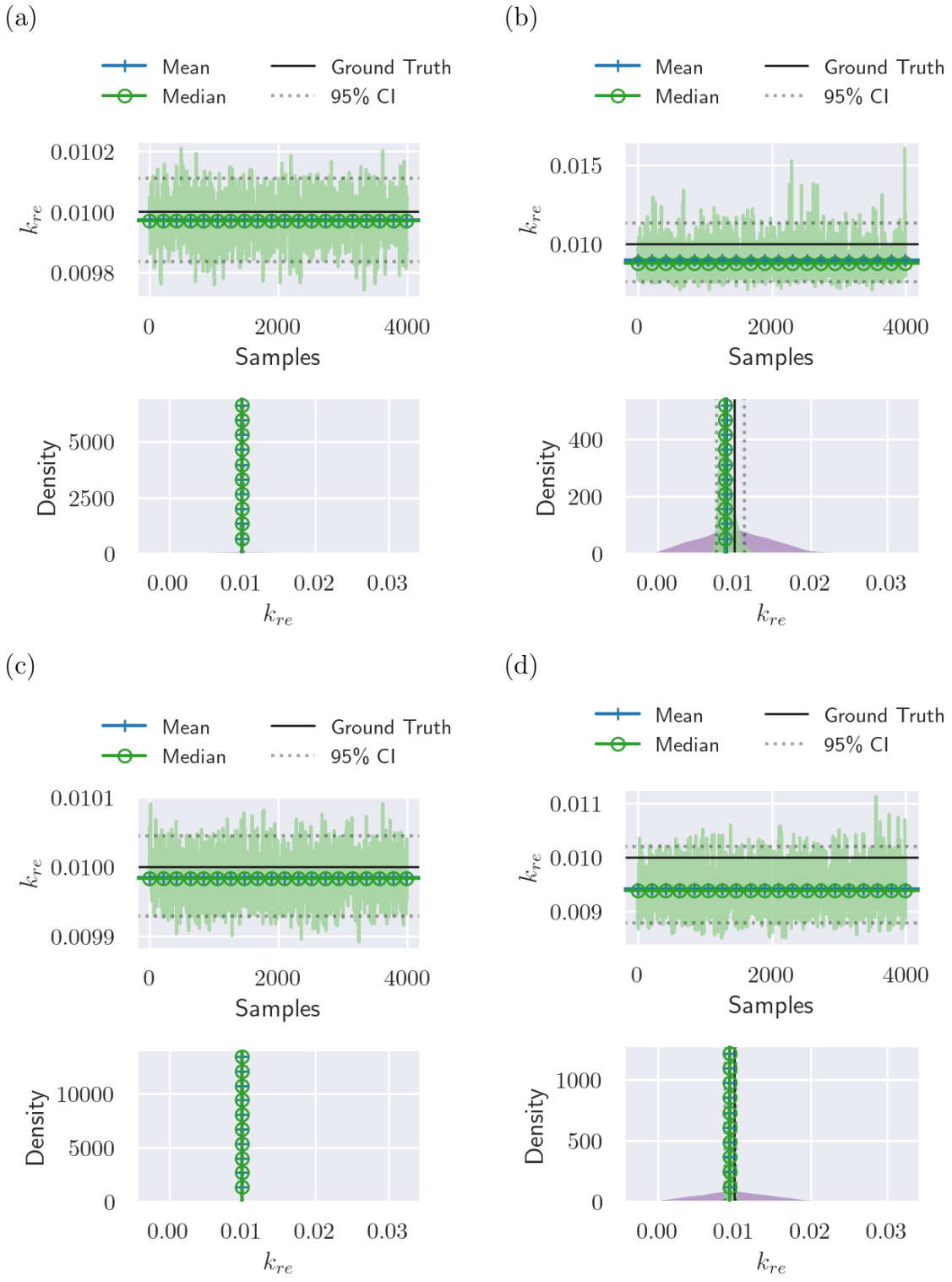

Figure 4.21: Trace, prior distributions and posterior distributions of free cortisol clearance rate k_{re} for the Bayesian approximation of the CIV^{-} model given by eqs. (2.34) and (2.35) with normal prior distributions imposed and for varying noise and time-resolution: (a) low error (s.d. $1\,\mathrm{nmol\,L^{-1}}$), low time-resolution ([PD]), (b) high error (s.d. $100\,\mathrm{nmol\,L^{-1}}$), time-resolution (every 10 minutes), (c) low error (s.d. $1\,\mathrm{nmol\,L^{-1}}$), high time-resolution (every 10 minutes), (d) high error (s.d. $100\,\mathrm{nmol\,L^{-1}}$), high time-resolution (every 1 minute).

Table 4.1: Comparing high and low time res and high and low noise for CIV$^-$ model given by eqs. (2.34) and (2.35).

			α	δ	B_0	k_{re}	σ
Ground truth			55	0.0154	650	0.01	-
Prior		Mean	55	0.0154	650	0.01	1/100
		SD	27.5	0.0077	325	0.005	0.5/50
Posterior	Low error (1), [PD] time	Mean	54.897	0.0145	646.368	0.009973	1.1043
		SD	0.166	0.00256	4.879	0.000068	0.1482
	High error (100), [PD] time	Mean	43.629	0.01586	614.609	0.01235	108.868
		SD	5.2524	0.007192	191.457	0.002563	13.743
	Low error (1), Time-res (10)	Mean	54.8978	0.015714	647.84	0.009985	1.01791
		SD	0.082553	0.001211	2.18516	0.00003	0.061587
	High error (100), Time-res (10)	Mean	45.7859	0.016284	388.997	0.008967	101.085
		SD	4.84969	0.007063	172.096	0.000975	6.00354
	Low error (1), Time-res (1)	Mean	55.044	0.014402	647.81	0.00997	0.980705
		SD	0.025338	0.000368	0.654284	0.000009	0.018456
	High error (100), Time-res (1)	Mean	53.9026	0.01291	584.869	0.009417	98.2435
		SD	1.21945	0.00706	38.6493	0.000358	1.81047

Table 4.2: Comparing prior and posterior distributions for the CIV$^+$ model (eqs. (2.4) and (2.5)) and the CIV$^-$ model (eqs. (2.34) and (2.35)). The mean and SD given are numerically calculated from the Bayesian approximations from each parameter, however some of the posterior distributions are not normally distributed, in particular in the case of gamma prior distributions.

			α	k_{fb}	k_{bf}	B_0	k_{re}	δ	σ
Ground truth			55	0.1	1	650	0.01	0.001538	100
Normal	Prior	Mean	55	0.1	1	650	0.01	0.01538	100
		SD	27.5	0.05	0.5	325	0.005	0.00769	50
	Posterior (CIV$^+$)	Mean	43.44	0.1019	1.035	617.2	0.0124	-	108.3
		SD	5.44	0.0477	0.464	193.6	0.0026	-	14.35
	Posterior (CIV$^-$)	Mean	43.9727	-	-	606.246000	0.012228	0.015860	108.376000
		SD	5.239	-	-	193.289000	0.002636	0.007325	13.830300
Normal Narrow	Prior	Mean	55	0.1	1	650	0.01	0.001538	100
		SD	5.5	0.01	0.1	65	0.001	0.00769	10
	Posterior (CIV$^+$)	Mean	49.27	0.1004	0.997	636.8	0.0106	-	103.1
		SD	3.15	0.01	0.102	51.5	0.0007	-	7.97
	Posterior (CIV$^-$)	Mean	49.3299	-	-	635.373	0.010583	0.015319	103.072
		SD	3.09878	-	-	52.4661	0.00074	0.00153	7.8342
Normal Wide	Prior	Mean	55	0.1	1	650	0.01	-	100
		SD	550	1	10	6500	0.1	-	1000
	Posterior (CIV$^+$)	Mean	41.32	0.5373	10.220	1966.6	0.0869	-	112.3
		SD	6.07	0.5642	6.547	1587.1	0.0675	-	15.85
	Posterior (CIV$^-$)	Mean	34.6736	-	-	5466.29	0.073137	0.1223	109.32
		SD	4.67248	-	-	3678.81	0.046471	0.078159	14.8189
Gamma	Prior	Scale	1	1	1	1	1	-	Mean 100
		Shape	55	0.1	1	650	0.01	-	SD 50
	Posterior	Mean	39.5939	0.095622	1.00964	398.009	0.010969	-	108.408
		SD	6.47113	0.095169	0.986495	282.192	0.003476	-	14.2186

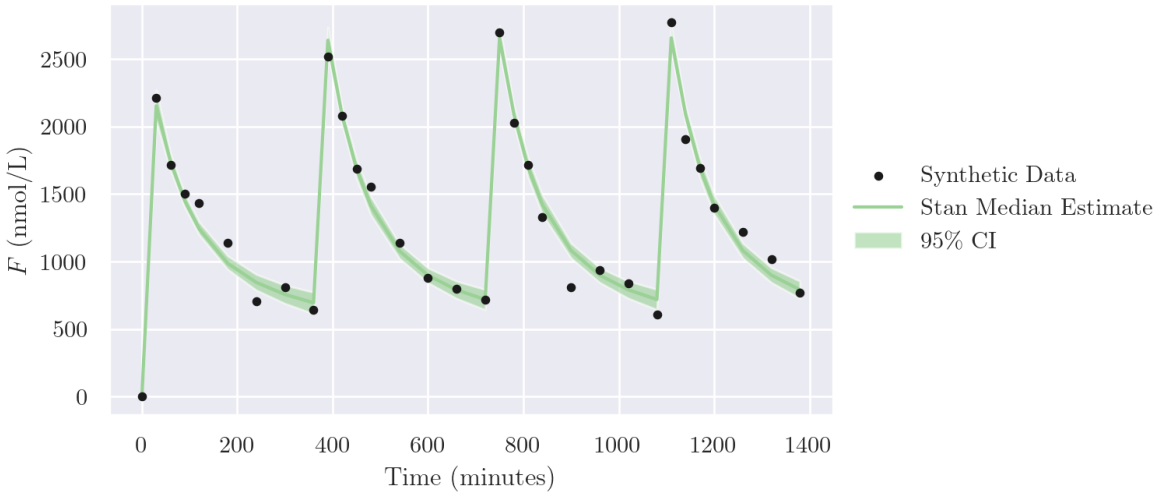

Figure 4.22: Bayesian approximation of synthetic data generated using the BIV$^+$ model given by eqs. (3.1) and (3.2) with Gaussian noise added (s.d. 100 nmol L^{-1}), sampling time frequency corresponding to the time points used in data [PD] and normal prior distributions imposed.

4.3 Parameter inference in the BIV$^\pm$ models

We fit the BIV$^\pm$ models to synthetic data for [PD] time-resolution and Gaussian noise added (s.d. 100 nmol L^{-1}) and the Bayesian approximation is shown in Figure 4.22. The posterior distributions for each model parameter are shown in Figures 4.23 and 4.24 for the BIV$^+$ model and Figures D.3 and D.4 for the BIV$^-$ model.

For both BIV$^\pm$ models, the bias on the posterior estimate of the dilution factor α remains. We see the same issues with binding and unbinding posterior distributions staying the same as the imposed normal prior distributions, although there is a very slight shift in the BIV$^+$ case. This difference could be a reflection of the movement of the ridge in Figure 3.11(a) which calculated the loss function for varying both binding and unbinding parameters simultaneously under high noise. Therefore, high noise may be introducing both a bias and practical identifiability issues on the ratio between binding and unbinding parameters.

The posterior distribution for B_0 has a narrower credible interval than both the CIV models and narrower still for the BIV$^-$ model (s.d. of posterior $\sim$190 nmol L^{-1} for CIV$^\pm$, $\sim$126 for BIV$^+$ and $\sim$58 for BIV$^-$, see Table 4.5). However for the BIV$^+$ model, the

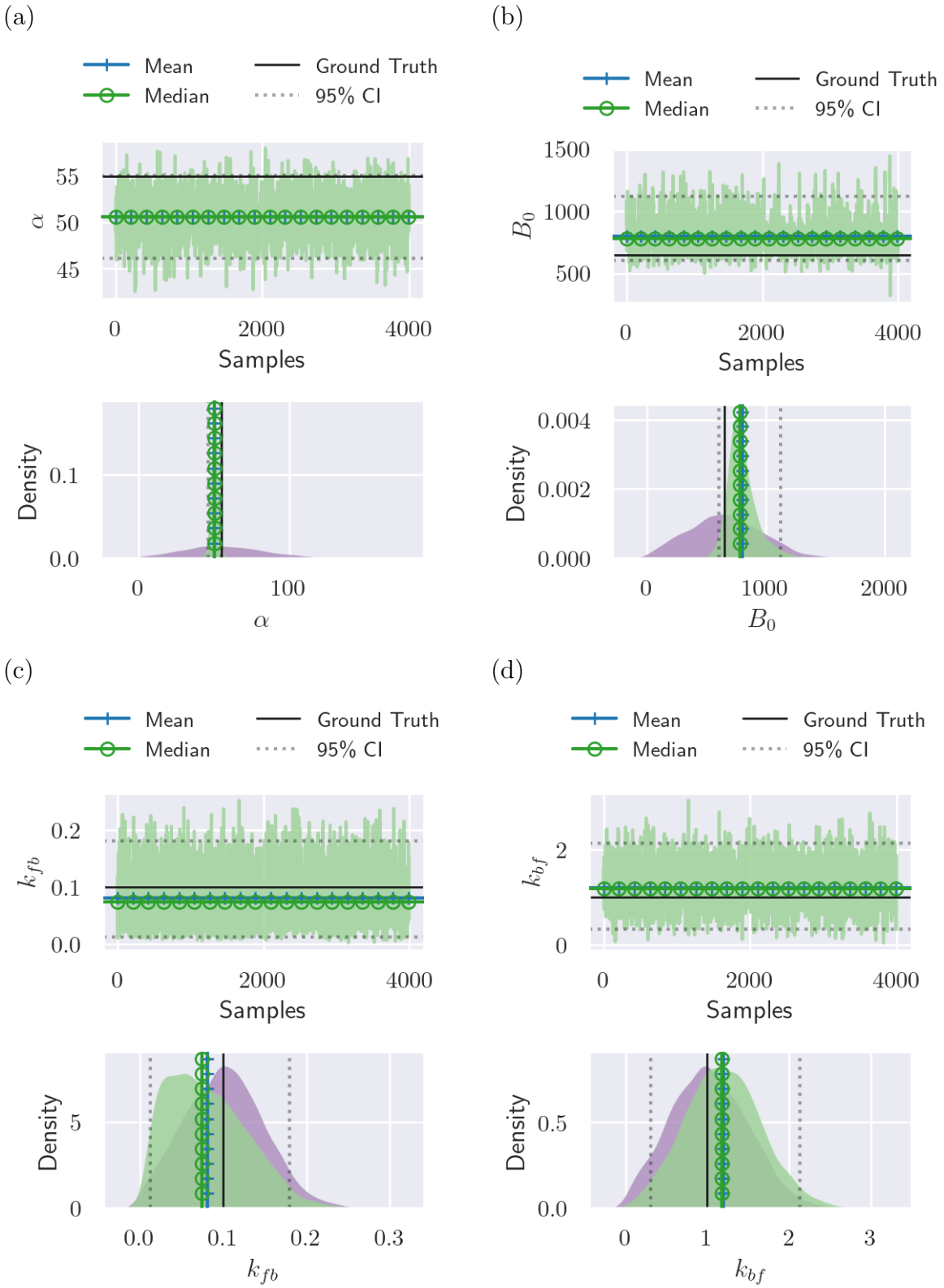

Figure 4.23: Trace, prior distributions and posterior distributions of model parameters for the Bayesian approximation of the BIV$^+$ model given by eqs. (3.1) and (3.2) with Gaussian noise added (s.d. 100 nmol L^{-1}), sampling time frequency corresponding to the time points used in data [PD] and normal prior distributions imposed: (a) for dilution factor α, (b) for physiological level of binding protein B_0, (c) for binding rate k_{fb}, (d) for unbinding rate k_{bf}.

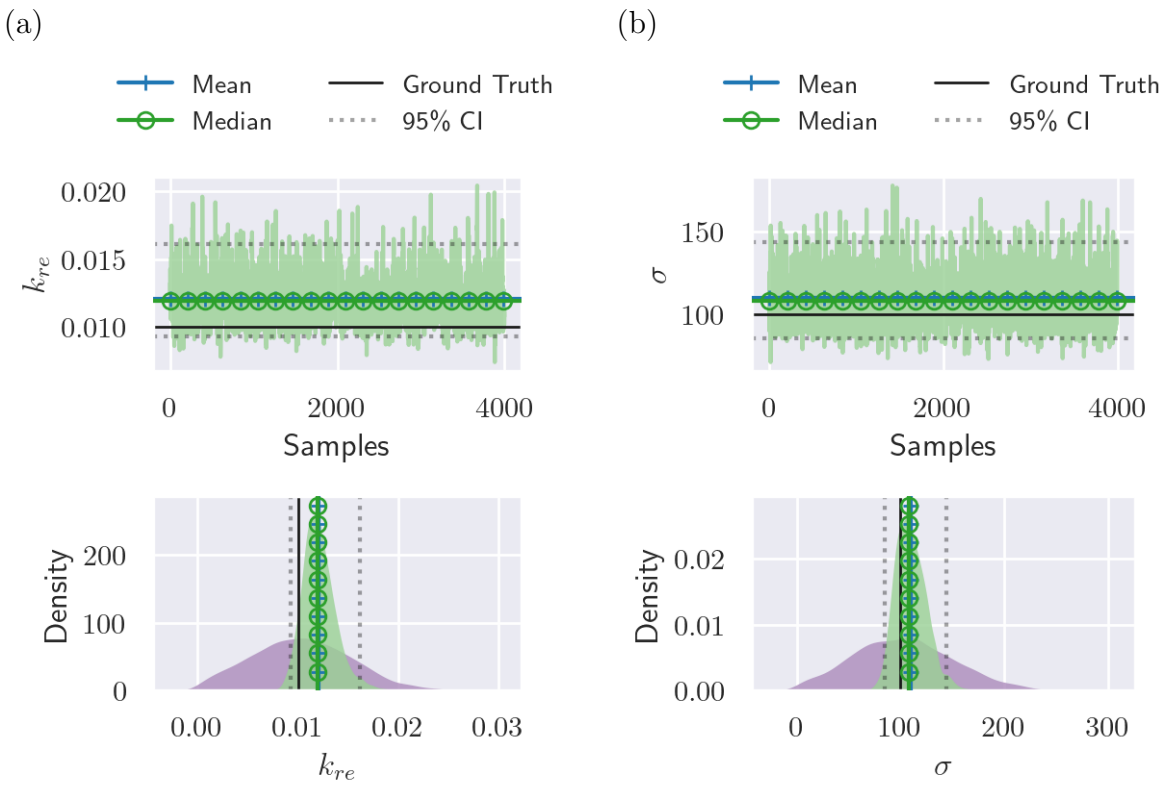

Figure 4.24: Trace, prior distributions and posterior distributions of model parameters for the Bayesian approximation of the BIV$^+$ model given by eqs. (3.1) and (3.2) with Gaussian noise added (s.d. 100 nmol L^{-1}), sampling time frequency corresponding to the time points used in data [PD] and normal prior distributions imposed: (a) for free cortisol clearance rate k_{re}, (b) for noise parameter σ.

ground truth is close to the 95% credible interval boundary.

As we found in section 3.5.5, the BIV$^{\pm}$ models retains more information about the physiological level of binding protein B_0 than the CIV$^{\pm}$ models, with a narrower posterior in both the full and reduced case. However, frequentist fitting in chapter 3 showed that the BIV^{+} model retained information about the ratio between binding and unbinding rates. The Bayesian posterior estimates have not significantly moved from the imposed prior distributions so even though the posterior means appear to retain the correct ratio, the width of the posterior is still wide so we do not have much certainty in this mean estimate.

The posterior distributions for both α and k_{re} are narrower in the BIV$^{\pm}$ models than they are in the CIV$^{\pm}$ models (see Table 4.5), suggesting this model retains more information about the model parameters than the CIV$^{\pm}$ models.

The relationship between B_0 and k_{re} is still apparent but is now linear in the scatter plot matrix compared to the CIV$^{\pm}$ case (Figures 4.5 and 4.16). We also see another correlation between estimates of α and k_{re} (BIV^{+} - Figure 4.25, BIV^{-} - Figure D.5).

Fitting the BIV^{-} model is much faster than the full model; approx. 280 seconds for 2000–sample chain versus 5515 seconds (Table 4.4).

Small noise behaviour

We now fit both BIV$^{\pm}$ models to synthetic data with very small noise (s.d. $1\,\mathrm{nmol\,L^{-1}}$).

The high noise case hides the correlation between binding and unbinding rates (see Figure 4.25). We see the expected correlation between binding and unbinding rates under small noise for the full model (Figure 4.26). Also, we see the same correlation as in the other cases between B_0 and k_{re}. It is likely that when fitting large noise, the values of k_{fb} and k_{bf} are insensitive in comparison to the other parameters, but under small noise, the binding and unbinding rates become comparable in their influence on the trajectory. We also see a negative correlation between α and k_{re} and the ground truth values are not within the 95% CI of the very narrow posterior distributions (Figure 4.27).

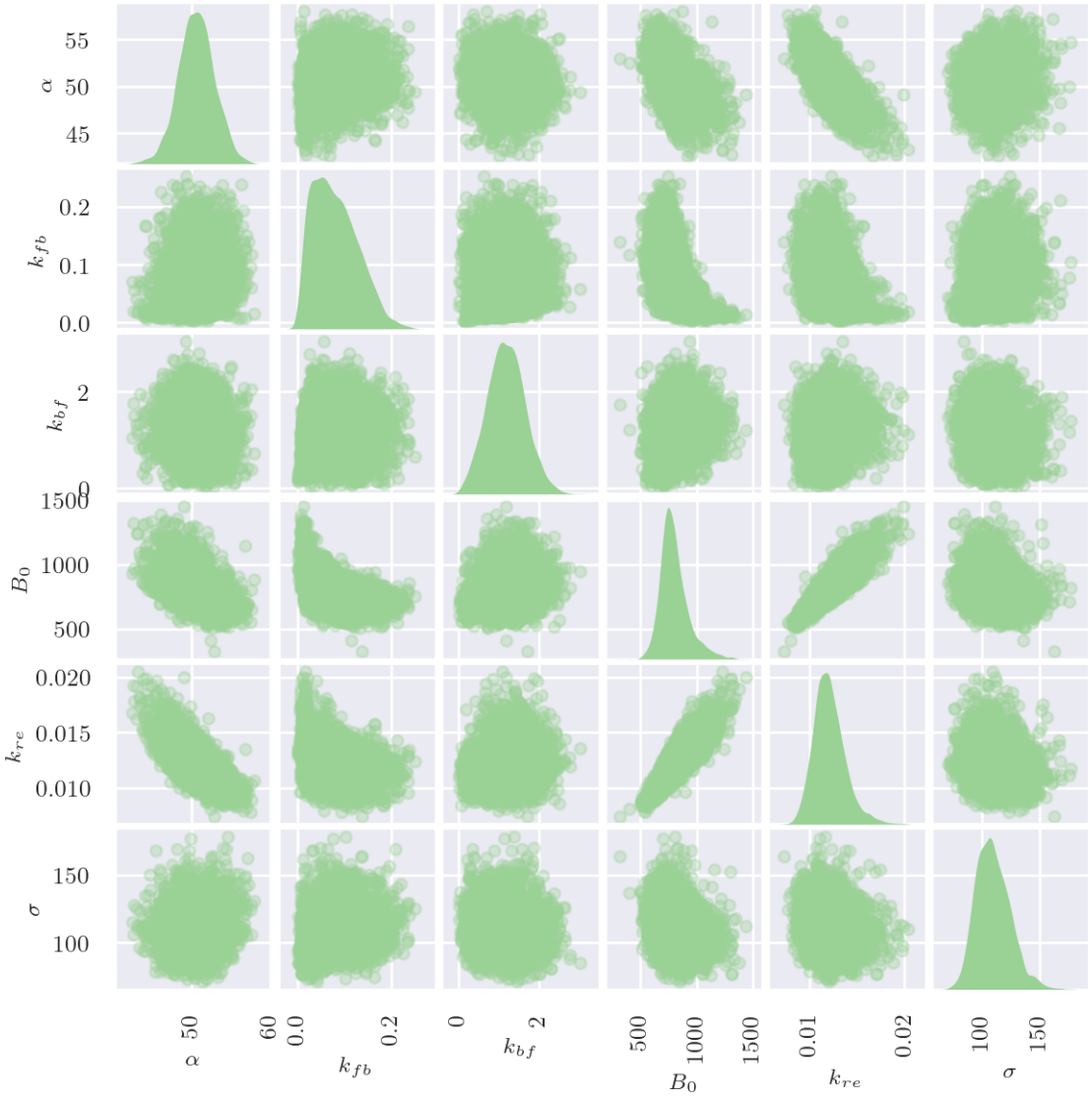

Figure 4.25: Scatter plot matrix of parameter estimates for Bayesian approximation of synthetic data generated using the BIV$^+$ model given by eqs. (3.1) and (3.2) with Gaussian noise added (s.d. 100 nmol L^{-1}), sampling time frequency corresponding to the time points used in data [PD] and normal prior distributions imposed.

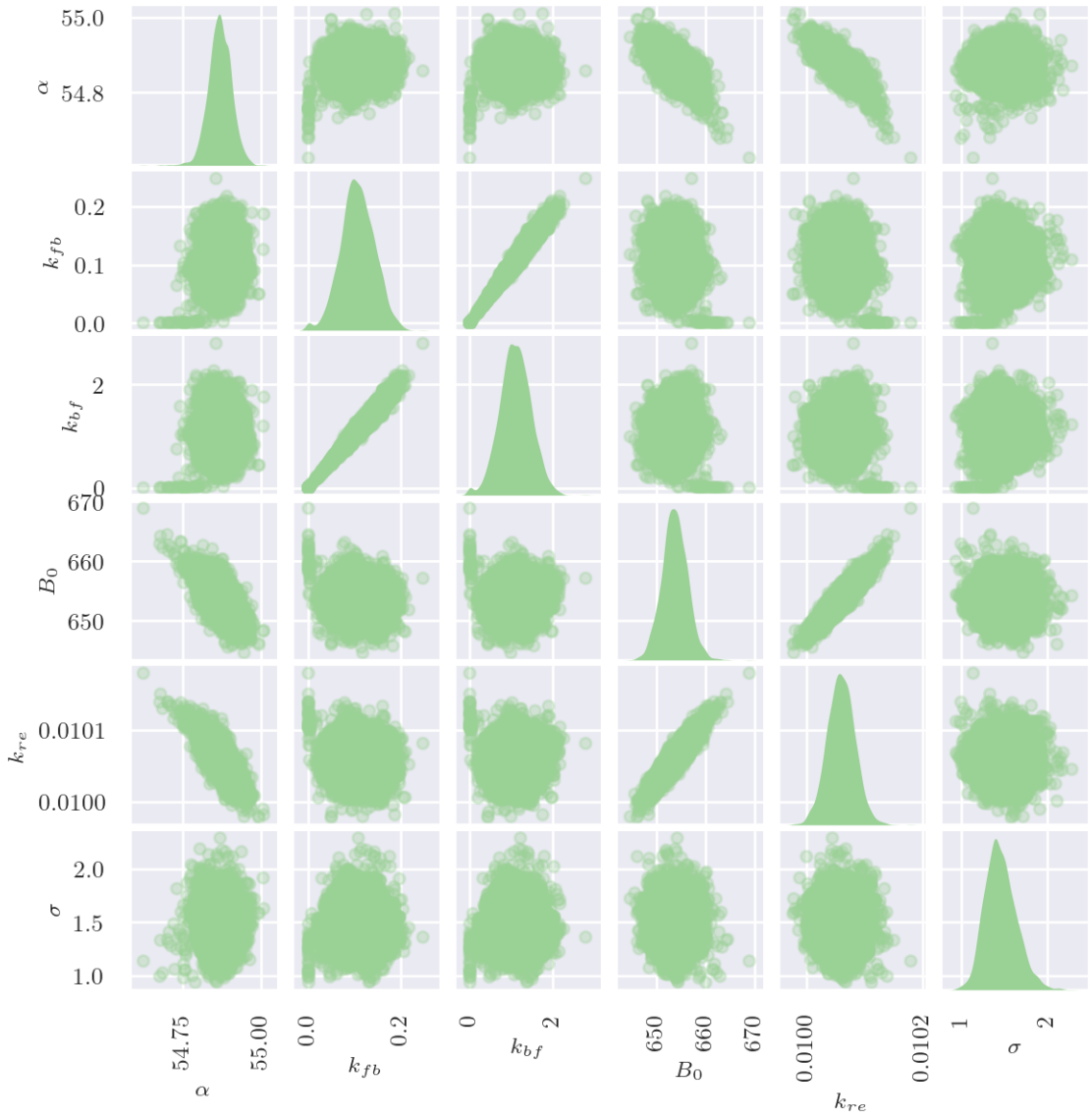

Figure 4.26: Scatter plot matrix of parameter estimates for Bayesian approximation using the BIV$^+$ model given by eqs. (3.1) and (3.2) with Gaussian noise added (s.d. $1\,\mathrm{nmol\,L^{-1}}$), sampling time frequency corresponding to the time points used in data [PD] and normal prior distributions imposed.

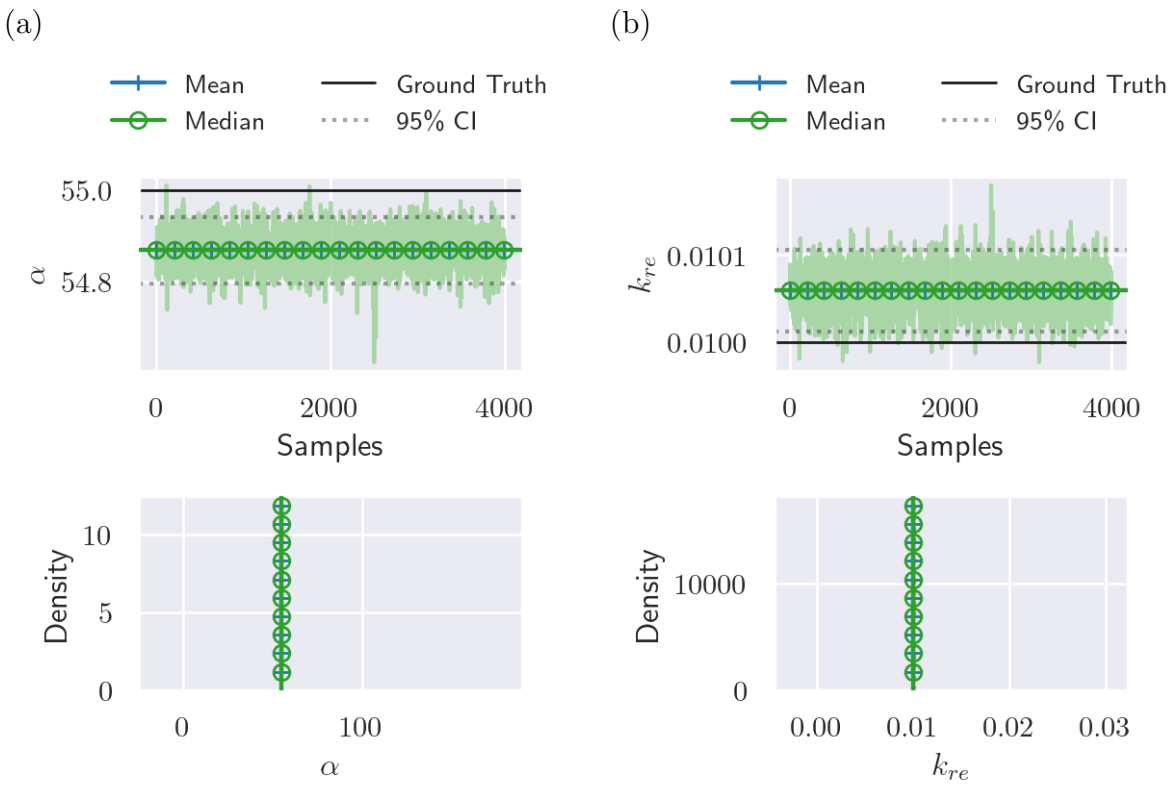

Figure 4.27: Trace, prior distributions and posterior distributions of model parameters for the Bayesian approximation of the BIV$^+$ model given by eqs. (3.1) and (3.2) with Gaussian noise added (s.d. $1\,\mathrm{nmol\,L^{-1}}$), sampling time frequency corresponding to the time points used in data [PD] and normal prior distributions imposed: (a) for dilution factor α, (b) for free cortisol clearance rate k_{re}.

The BIV$^-$ model does not show as strong correlation between k_{fb} and k_{bf}, or between any of the parameter pairs (Figure 4.28). Additionally, the means from the BIV$^-$ posterior distributions are much farther from the ground truth than the BIV$^+$ (Figure 4.29). The low noise case reflects what we found in the frequentist section, that the BIV$^-$ model does not retain the ratio between k_{fb} and k_{bf}, as the posterior for k_{bf} has now shifted and the mean has shifted (Figure 4.29).

4.4 Parameter inference in the CIV$^-$ and BIV$^+$ models simultaneously

We simultaneously fit synthetic data to the CIV$^-$ model and to the BIV$^+$ model and see a good qualitative fit to both synthetic data sets in Figure 4.30. We see that the means of the posterior distributions are similar to the estimates for fitting BIV alone suggesting that the BIV behaviour is dominating the inference (see Table 4.5) which is in agreement with the frequentist parameter recovery in chapter 3.

4.4.1 Parameter inference of experimental data

Finally, we fit the model to data [PD] to assess the capability of the model to replicate the qualitative behaviour of patient response. The Bayesian approximation for the CIV$^-$ model to [PD] using normal prior distributions is shown in Figure 4.31. We see a fairly good qualitative fit, the model is able to estimate the sharp rise initially and the plateau after about 6 hours. However, the data suggests there could be an overshoot after the initial rise before settling to an equilibrium that the model is unable to capture.

If we model both dosing regimes simultaneous using both reduced models, we seem to have again a reasonable fit of the patient data. The simultaneous fit results in the CIV$^-$ model having a slower initial rise and longer time to reach equilibrium (Figure 4.32(a)). For the BIV fit, the data appears to decay linearly. However the model is similar to exponential decay (Figure 4.32(b)). The linear clearance term in the model may not be

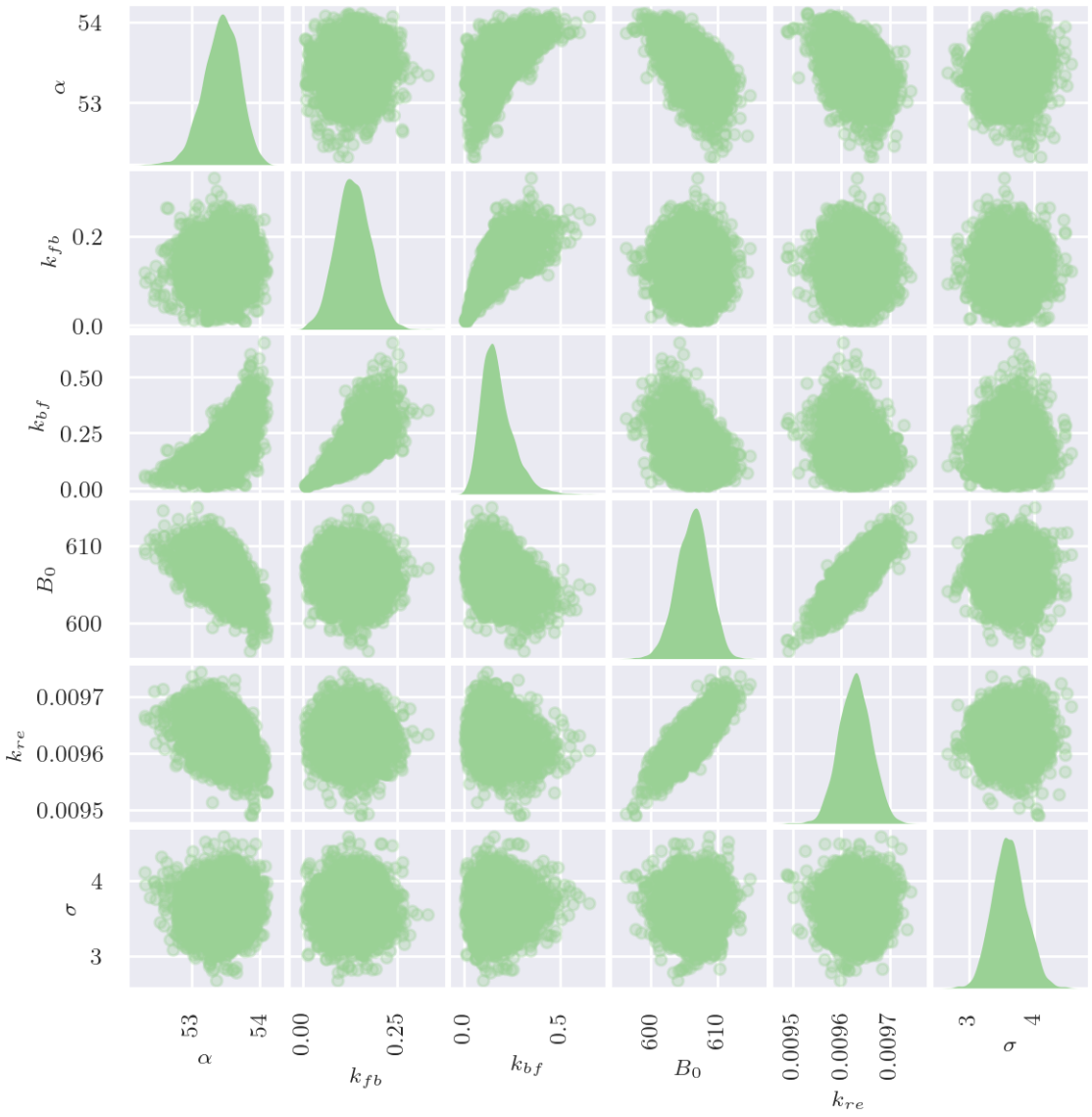

Figure 4.28: Scatter plot matrix of parameter estimates for the Bayesian approximation of the BIV$^-$ model given by eqs. (3.97) and (3.100) with Gaussian noise added (s.d. $1\,\mathrm{nmol\,L^{-1}}$), sampling time frequency corresponding to the time points used in data [PD] and normal prior distributions imposed.

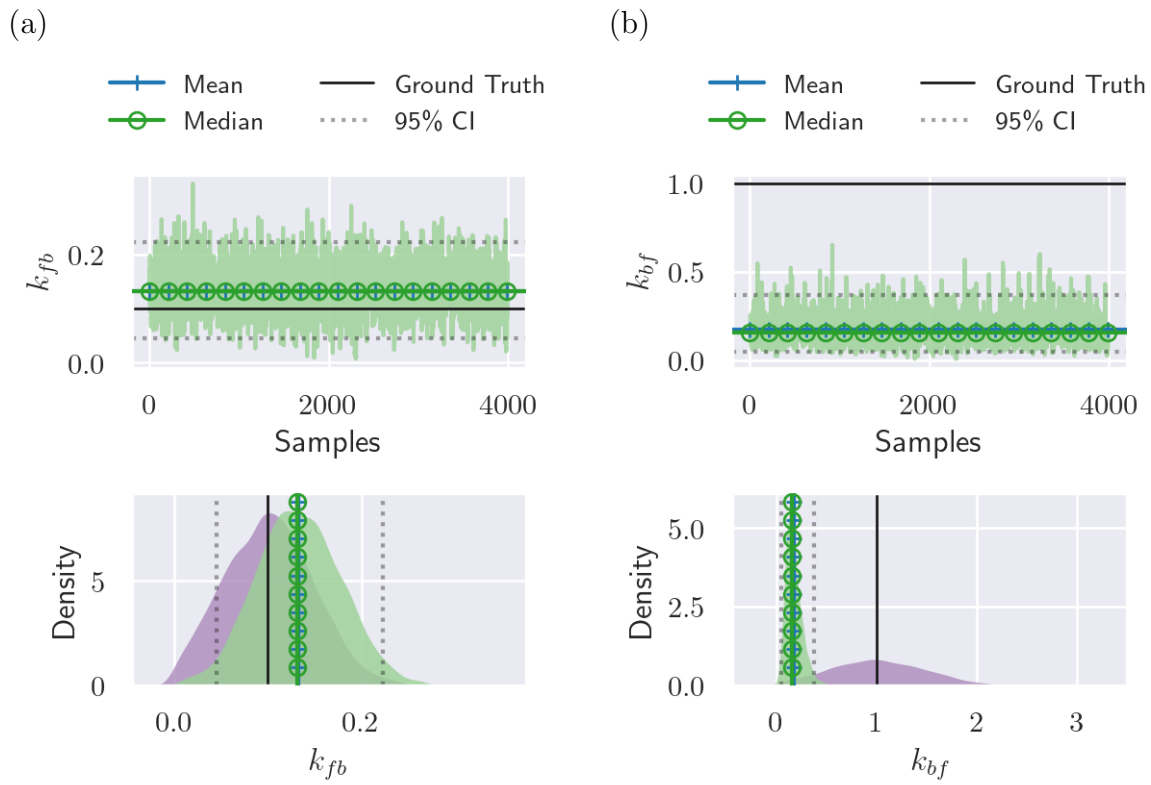

Figure 4.29: Trace, prior distributions and posterior distributions of model parameters for the Bayesian approximation of the BIV$^-$ model given by eqs. (3.97) and (3.100) with Gaussian noise added (s.d. $1\,\mathrm{nmol\,L^{-1}}$), sampling time frequency corresponding to the time points used in data [PD] and normal prior distributions imposed: (a) for binding rate k_{fb}, (b) for unbinding rate k_{bf}.

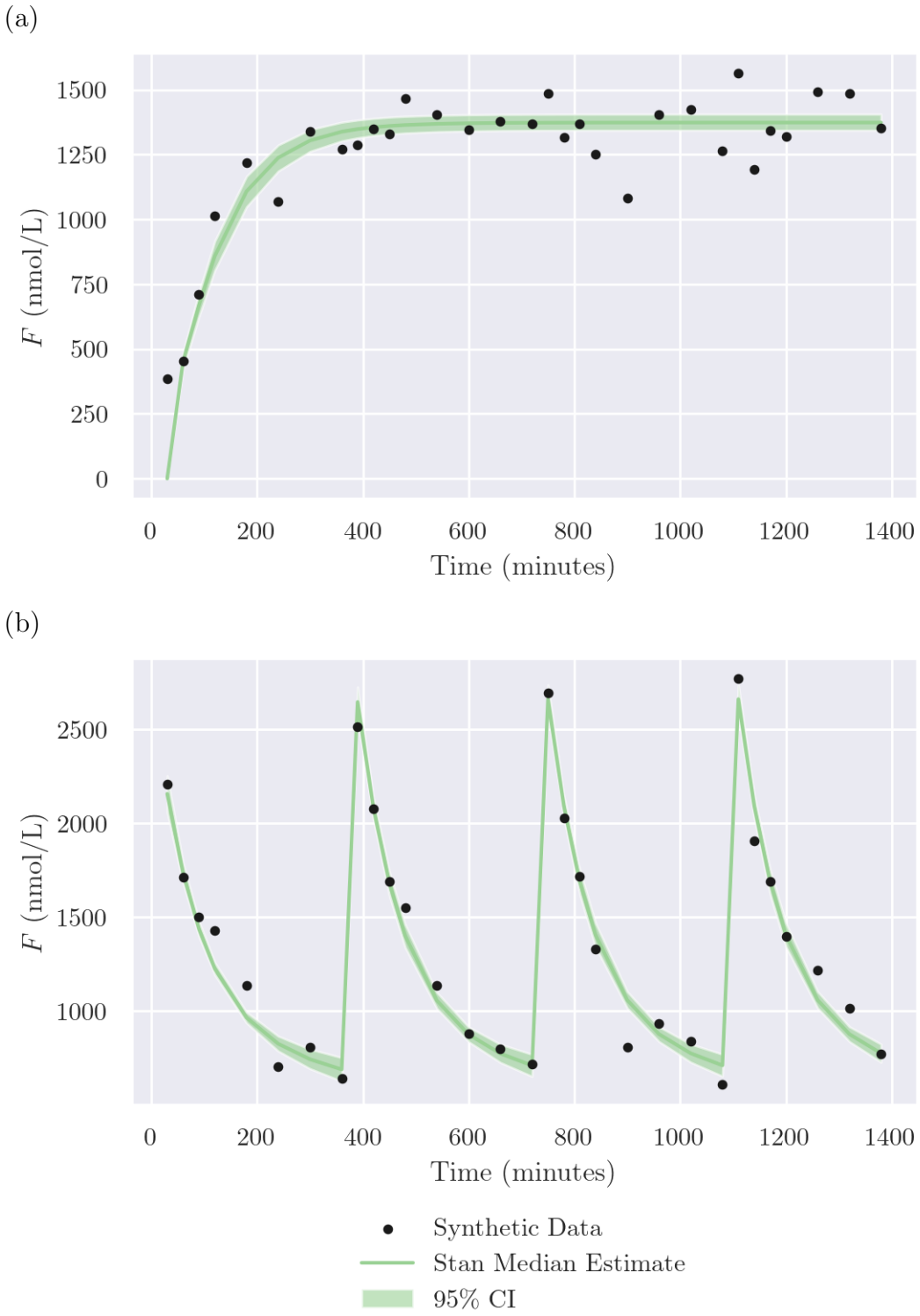

Figure 4.30: Bayesian approximation of simultaneous synthetic data generated using the BIV^{+} model given by eqs. (3.1) and (3.2) and the CIV^{-} model given by eqs. (2.34) and (2.35) with Gaussian noise added (s.d. $100\,\mathrm{nmol\,L^{-1}}$), sampling time frequency corresponding to the time points used in data [PD] and normal prior distributions imposed: (a) CIV, (b) BIV.

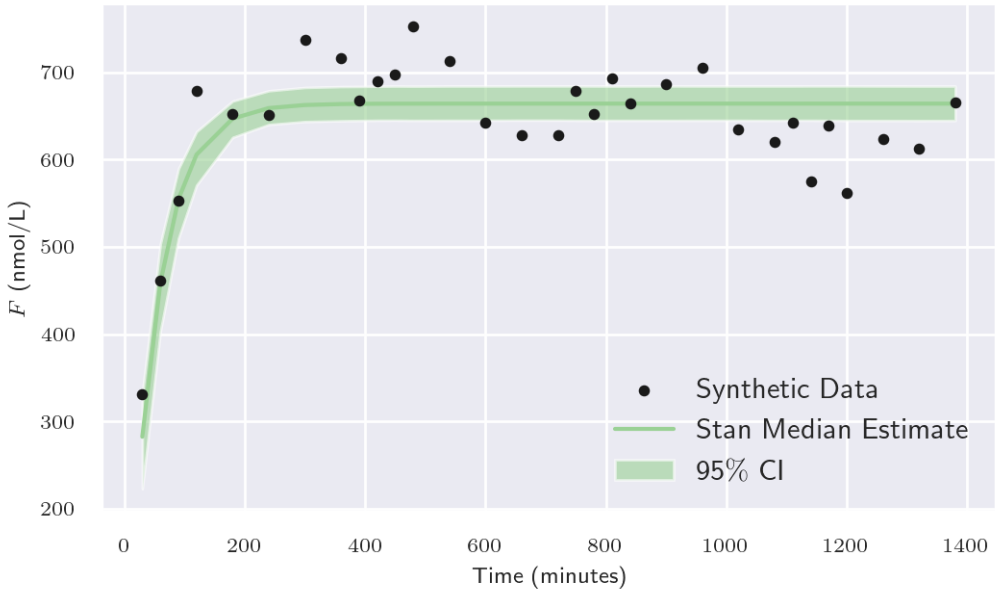

Figure 4.31: Bayesian approximation of the CIV$^-$ model given by eqs. (2.34) and (2.35) fitted to data [PD] when normal prior distributions are imposed.

sufficient to replicate the real data, which we begin to explore in appendix E.1.3. Altering the clearance term may also allow for the overshoot in the CIV data to be replicated, where there is additional evidence to suggest that clearance is not linear over a 24–hour timescale.

The Bayesian approximations suggest a much lower value of B_0 (mean from posterior $\sim$250 nmol L^{-1} rather than proposed value of 650 nmol L^{-1} and a much higher value for α. The estimates for α and k_{re} are mildly negatively correlated, suggesting the model requires more unbound cortisol and faster clearance to replicate data [PD] (see Figure 4.33).

4.5 Discussion

In this chapter, we have explored Bayesian inference of all model variations against synthetic data. Table 4.3 summarises whether parameters are recovered well or are insensitive when using Bayesian inference when normal prior distributions are imposed for data under high noise and time sampling corresponding to data [PD].

In all cases we found parameter estimates of the dilution factor α to be biased, which

(a)

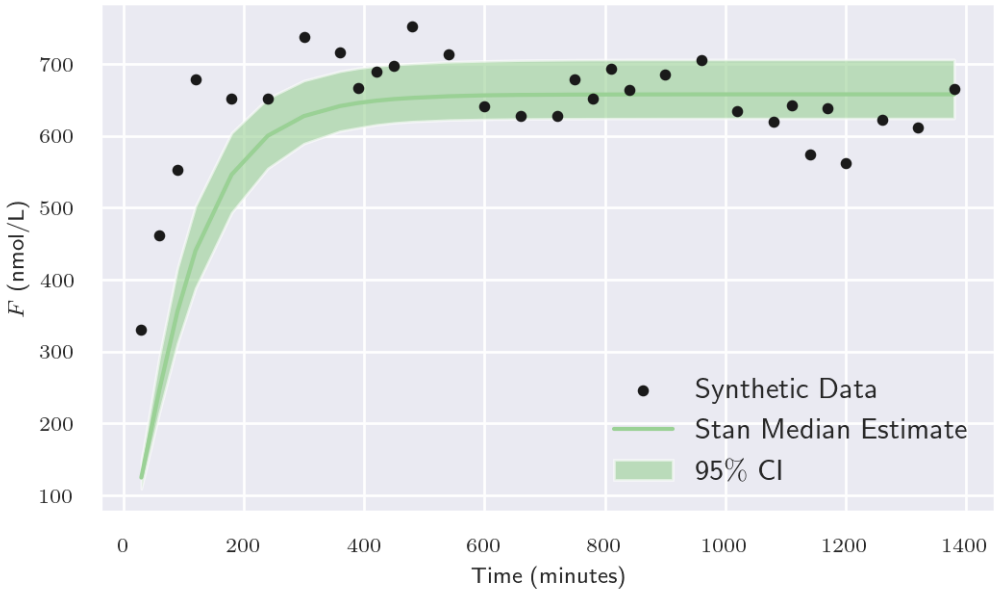

(b)

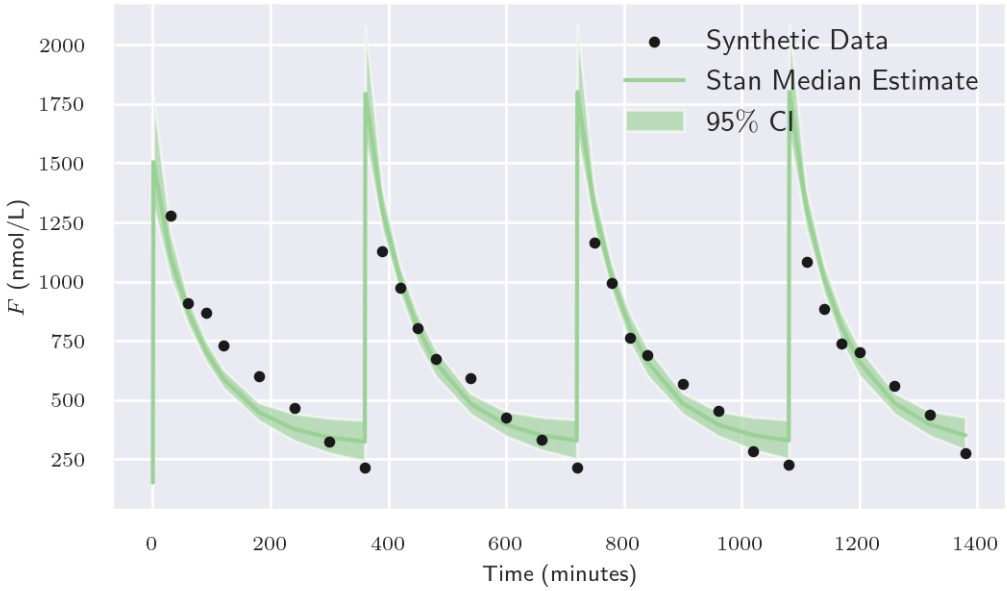

Figure 4.32: Bayesian approximation of the CIV$^-$ model given by eqs. (2.34) and (2.35) and the BIV$^-$ model given by eqs. (3.97) and (3.100) fitted to data [PD] when normal prior distributions are imposed, (a) CIV, (b) BIV.

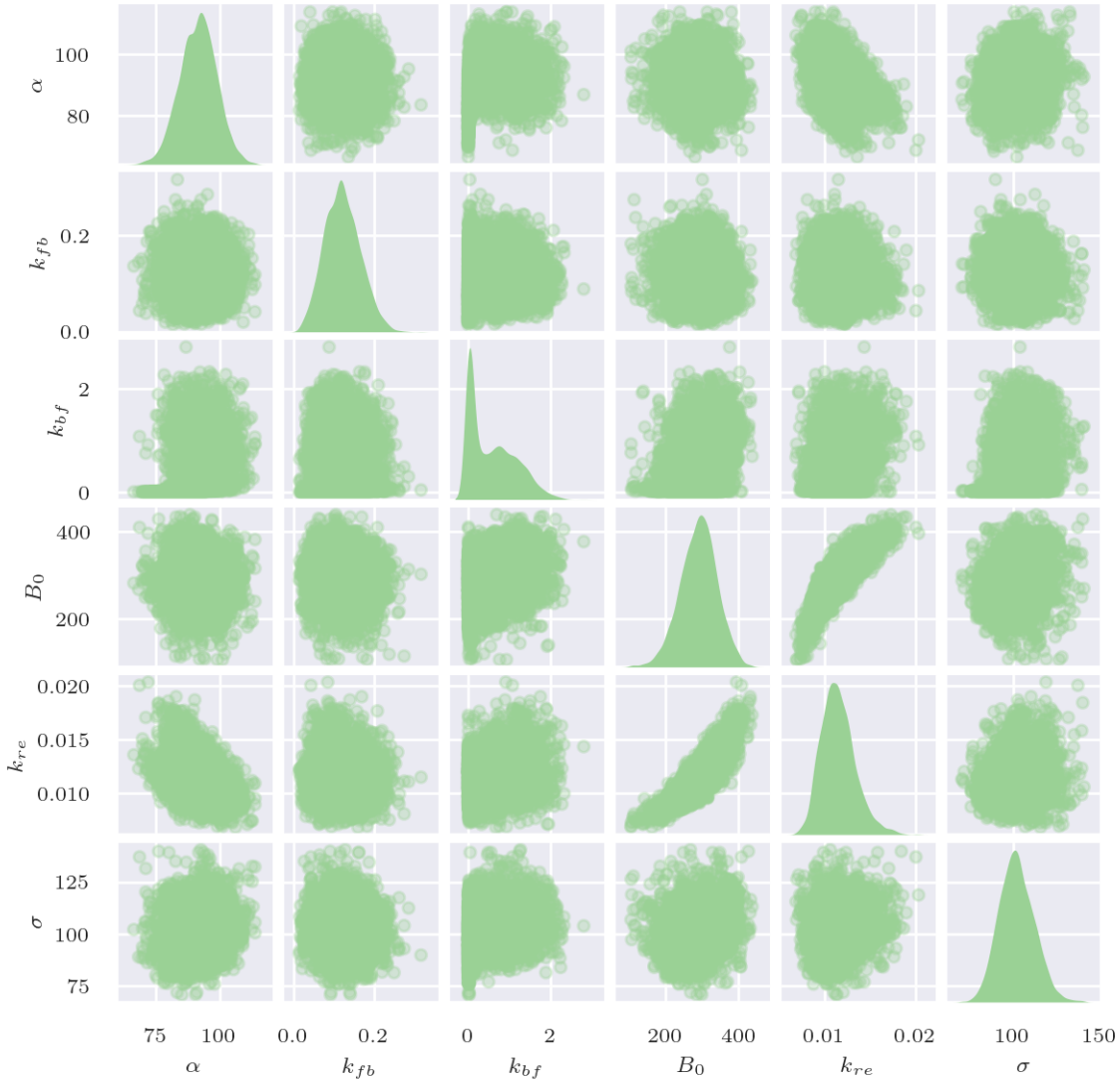

Figure 4.33: Scatter plot matrix of parameter estimates for the Bayesian approximation of the BIV$^-$ model given by eqs. (3.97) and (3.100) and the CIV$^+$ model given by eqs. (2.4) and (2.5) fitted to data [PD] and normal prior distributions imposed.

Table 4.3: Summary of which parameters are recovered well (✓) or are insensitive (✗) using Bayesian inference under high noise with time sampling corresponding to data [PD] and normal prior distributions imposed on each parameter.

	α	k_{fb}	k_{bf}	B_0	k_{re}	δ
CIV^+	✓	✗	✗	✓	✓	-
CIV^-	✓	-	-	✓	✓	✗
BIV^+	✓	✗	✗	✓	✓	-
BIV^-	✓	✗	✗	✓	✓	-
CIV^- and BIV^-	✓	✗	✗	✓	✓	-
CIV^- and BIV^+	✓	✗	✗	✓	✓	-

we suggest is due to noise on the synthetic data. This bias can be removed either by reducing noise or by increasing time-resolution of samples (see Table 4.1), suggesting that wearable sensors may be useful for mitigating the effects of noise for some parameters more than others.

Both BIV and CIV models are insensitive to binding and unbinding rates, k_{fb} and k_{bf} respectively, which concurs with frequentist fitting in Chapters 2 and 3. By considering a Bayesian approximation when reducing the noise on the synthetic data, we conclude that the BIV^- model does not retain the ratio between binding and unbinding rates like the full model. We also found that the posterior distributions for physiological level of binding protein, B_0, are narrower for the $BIV^\pm$ models suggesting that these models retain more information than the $CIV^\pm$ models in agreement with Chapters 2 and 3. However, in contrast to Chapter 2, Bayesian inference provides a better estimate for B_0 than frequentist fitting for the $CIV^\pm$ models which is likely due to the imposition of prior knowledge provided in the model. There is an apparent relationship between physiological level of binding protein and clearance rate, which echoes findings from exploring the loss function. This relationship is expected as a lower amount of binding protein, resulting in more circulating free cortisol, or a higher clearance rate both lead to more removal.

There is a significant reduction in computation time when using reduced over full models for both dosing regimes (see Table 4.4). For the CIV case, this reduction does not

result in losing information about the parameters. For the BIV case, there is a trade-off between faster computation time and the loss of information about the physiological level of binding protein B_0.

Practical identifiability issues have arisen even at small noise, in particular for the binding and unbinding rate parameters and these issues can be disguised under large noise (with wide posterior distributions for individual parameters but no visible correlation across parameters).

The CIV case showed how noise has more of an impact on hindering estimates of model parameters than time-resolution. This finding suggests that even with investment into implantable sensors to increase time-resolution of measurements, estimates of parameter values that are practically unidentifiable may still be indistinguishable if there is large noise introduced during data collection.

Bayesian inference has allowed for the visualisation of the relationships between model parameters, in particular between the physiological level of binding protein and the free cortisol clearance rate. This finding suggests that obtaining an estimate for the level of binding protein in a patient could be used to estimate their free cortisol clearance rate. However we do not yet have an explicit algebraic expression to relate these two parameters.

Table 4.4: Time comparison for Bayesian approximation across models.

Model	Runtime for 1 chain (2000 samples) (seconds)
CIV^{+}	2479.5
CIV^{-}	38.743
BIV^{+}	5514.85
BIV^{-}	280.456
CIV^{+} and BIV^{+}	5665.65
CIV^{-} and BIV^{-}	396.526
CIV^{-} and BIV^{+}	4841.45

Table 4.5: Parameter Inference estimate summary for synthetic data generated with Gaussian noise added (100) and data points evaluated to match [PD] time.

			α	k_{fb}	k_{bf}	B_0	k_{re}	δ	σ
Ground truth			55	0.1	1	650	0.01	0.015385	100
Prior		Mean	55	0.1	1	650	0.01	0.0154	100
		SD	27.5	0.05	0.5	325	0.005	0.0077	50
Posterior	CIV^+	Mean	43.442	0.101946	1.03471	617.239	0.012425	-	108.347
		SD	5.44369	0.04774	0.464414	193.557	0.002632	-	14.3535
	CIV^-	Mean	43.6287	-	-	614.609	0.01235	0.015863	108.868
		SD	5.25243	-	-	191.457	0.002563	0.007192	13.743
	BIV^+	Mean	50.5963	0.08064	1.19219	799.512	0.012093	-	109.638
		SD	2.28183	0.047191	0.463009	126.049	0.001667	-	14.911
	BIV^-	Mean	50.7489	0.095335	1.0787	634.991	0.010375	-	113.003
		SD	2.17764	0.047655	0.473413	58.175	0.000992	-	15.1397
	Simultaneous CIV^- and BIV^-	Mean	49.8478	0.10867	0.997447	658.138	0.010844	-	108.37
		SD	1.76787	0.043902	0.461213	44.5771	0.000851	-	9.98182
	Simultaneous CIV^- and BIV^+	Mean	50.4096	0.10569	1.04312	727.535	0.011613	-	107.804
		SD	1.80875	0.042673	0.446674	56.2625	0.001025	-	9.94943

CHAPTER 5

CONCLUSIONS

In this thesis we have developed and studied a pharmacokinetic model for cortisol dynamics for two dosing methods: via a continuous infusion and a series of intravenous boluses. We used asymptotic analysis to reduce both systems by exploiting the fast process of free cortisol binding and defining a dimensionless parameter grouping δ. Structural identifiability of all models was assessed and showed that all parameters should be identifiable under the assumption that we have perfect, high time-resolution data.

However, when considering synthetic data with additive noise we found that practical identifiability issues arose in both types of dosing models. When using frequentist parameter fitting, the BIV$^+$ model was better able to retain parameter values under physiologically realistic levels of noise, however the reduced model was unable to retain the exact values of binding and unbinding rate parameters, k_{fb} and k_{bf}. The CIV$^\pm$ models did not retain information about the physiological level of binding protein, B_0, however the overall estimated values of δ were close to the true value. Notwithstanding the poor estimates for k_{fb}, k_{bf} and δ individually, the qualitative fits of the CIV$^\pm$ models to the data were good. Similarly, the BIV$^-$ model was able to fit the data well despite losing the true ratio between k_{fb} and k_{bf}.

Bayesian inference allowed for more effective exploration of parameter space to fit synthetic data for all model parameters. The ability to impose prior information on parameter estimates allowed for a more sensible set of estimates for the CIV case. The

posterior distributions from the fits showed that all models were insensitive to the binding and unbinding parameter rates, confirming the findings in chapters 2 and 3.

We also investigated the impact of noise and time-resolution on the ability to infer certain parameters. We found that although higher time-resolution could reduce uncertainty and mitigate some of the biases introduced by the noise on the data (in particular when fitting the dilution factor α), there was not a physically realistic time resolution to eliminate the practical identifiability issues around the binding and unbinding parameters. The model appeared to be insensitive to changes in k_{fb} and k_{bf} within reasonable bounds, so wearable technology may still be beneficial in improving the remaining parameter estimates which have a larger impact on the model trajectory. In appendix B.2, we considered optimising the time sampling to find when samples should be drawn to retrieve the binding and unbinding rate parameters. An optimum time sampling is found for an individual under large noise, however this choice does not translate to the optimum time sampling for another individual and requires *a priori* knowledge of the parameters k_{fb} and k_{bf}. This work could therefore direct better experimental design in terms of time sampling regimes to reduce biased parameter estimates. Additionally, the assessment of practical identifiability allows experimentalists to anticipate which parameter values need to be pre-determined.

In both frequentist and Bayesian methods, it was found that the BIV model was driving parameter estimates when considering simultaneous fitting. In particular, the influence of the physiological level of binding protein proved to be significant in the model trajectory compared to binding and unbinding rates. This finding is beneficial for patients as BIV dosing is less invasive than a 24–hour continuous infusion and provides more information for predicting a patient's response to other forms of dosing.

There are many possible avenues for extending the models presented in this thesis. Firstly, an alternative removal term may be a useful addition based on the qualitative fit of the original model to data [PD] as shown in chapter 4. This addition is considered in appendix B, by introducing a variable which accounts for an enzyme that binds and

removes cortisol from the system. By adding this variable, the rate of removal can fluctuate over a 24–hour period which may better approximate the sharp increase seen in the CIV data before it settles to an equilibrium level. Similarly, the current BIV^+ model undercuts the data in the post-dosing period, suggesting that exponential decay is not a sufficient approximation of the dynamics.

In this thesis, we chose to focus on the continuous infusion and intravenous bolus due to their very different behaviour. A natural next step would be to consider additional compartments to compare the other two dosing methods (intramuscular and oral tablets), which would help to further verify the estimates we found for the first two dosing methods. Considering the response to oral tablets would also be very helpful as this choice is the most practical for long-term adrenal insufficiency management.

Finally, the physiological level of binding protein was shown to be an important parameter in determining the behaviour of the model. We also found that having prior knowledge of this level improved the Bayesian estimates for the CIV case. Therefore, another possible extension of this work would be to consider the influence of accounting for additional binding proteins such as albumin, of which there is a higher concentration but a lower binding affinity.

The cortisol deficient state in which this thesis is based provides a simple test ground for combining modelling and model reduction with identifiability and Bayesian inference techniques, which may prove valuable among other areas of pharmacology and medicine.

APPENDIX A

IDENTIFIABILITY ANALYSIS

A.1 Laplace transform approach

A.1.1 A structurally globally identifiable example

We first consider the following system

$$\frac{dx}{dt} = -kx, \qquad x(0) = x_0, \tag{A.1}$$

for $t \in [0, T]$ with parameter set $\boldsymbol{\theta} = (x_0, k)$. We take the state variable x to be observed and hence $y = x$. Defining the Laplace transform as

$$\tilde{x}(r) = \int_0^\infty e^{-rt} x(t)\ dt, \tag{A.2}$$

the expression for the transformed solution becomes

$$\tilde{x}(r) = \frac{\Phi_1}{r + \Phi_2}, \tag{A.3}$$

where $\Phi_1 = x_0$ and $\Phi_2 = k$. Therefore x_0 and k are both globally identifiable.

A.1.2 An unidentifiable example

We can easily adapt the above problem to illustrate where unidentifiability could arise. Now considering the system with parameter set $\boldsymbol{\theta} = (x_0, k, h)$, we define a system such as,

$$\frac{dx}{dt} = -\frac{k}{h}x, \qquad x(0) = x_0. \tag{A.4}$$

Following the method, we find the same transformed solution, this time with rational functions $\Phi_1 = x_0$ and $\Phi_2 = \frac{k}{h}$. In this case, the quotient $\frac{k}{h}$ is globally identifiable, but the individual parameters k and h are unidentifiable. For the system to be globally structurally identifiable, either k or h would need to be known. We could have equally chosen a system such as

$$\frac{dx}{dt} = -khx, \qquad x(0) = x_0, \tag{A.5}$$

or

$$\frac{dx}{dt} = -(k+h)x, \qquad x(0) = x_0, \tag{A.6}$$

where now $\Phi_2 = kh$ or $\Phi_2 = k + h$ respectively. In these cases, the product and the sum would be globally identifiable, but again the individual parameters would not be. We draw the same conclusion that either k or h would need to be known for the system to be globally structurally identifiable.

A.1.3 A structurally locally identifiable example

We now consider a pair of linear ODEs with only one observed variable, x_2, and the parameter set is $\boldsymbol{\theta} = (x_0, k, h)$:

$$\begin{aligned} \frac{dx_1}{dt} &= -kx_1, & x_1(0) &= x_0, \\ \frac{dx_2}{dt} &= kx_1 - hx_2, & x_2(0) &= 0. \end{aligned} \tag{A.7}$$

We suspect a parameter indeterminacy connected with the transformation $h \to k$, $k \to h$, $x_0 \to x_0 h/k$. To analyse this potential identifiability issue, we follow the method as in [15]. We write the two-compartmental model compactly as,

$$\frac{d\boldsymbol{\mu}}{dt} = A\boldsymbol{\mu}, \quad A = \begin{pmatrix} -k & 0 \\ k & -h \end{pmatrix}, \quad \boldsymbol{\mu}(0) = [x_0, 0]^T, \tag{A.8}$$

where $\boldsymbol{\mu}(t) = [x_1(t), x_2(t)]^T$. We also express which variables are observed as:

$$\begin{pmatrix} y_1(t) \\ y_2(t) \end{pmatrix} = \begin{pmatrix} 0 & 0 \\ 0 & 1 \end{pmatrix} \begin{pmatrix} x_1(t) \\ x_2(t) \end{pmatrix}, \tag{A.9}$$

which can be written compactly as $\boldsymbol{y} = C\boldsymbol{\mu}$. Using the Laplace transform as before, the initial value problem becomes,

$$-\boldsymbol{\mu}(0) + r\bar{\boldsymbol{\mu}}(r) = A\bar{\boldsymbol{\mu}}(r), \tag{A.10}$$

which means the transformed solution can be written as:

$$\bar{\boldsymbol{\mu}}(r) = (rI - A)^{-1}\boldsymbol{\mu}(0). \tag{A.11}$$

By calculating the inverse matrix $(rI - A)^{-1}$, we find the solution in Laplace space:

$$\bar{\boldsymbol{\mu}}(r) = \begin{pmatrix} \bar{x}_1(r) \\ \bar{x}_2(r) \end{pmatrix} = \frac{1}{(r+h)(r+k)} \begin{pmatrix} x_0(r+h) \\ kx_0 \end{pmatrix}. \tag{A.12}$$

Expressing the observed solution in terms of rational functions yields:

$$\bar{x}_2(r) = \frac{\Phi_1}{r^2 + \Phi_2 r + \Phi_3}, \tag{A.13}$$

where $\Phi_1 = kx_0$, $\Phi_2 = h + k$, $\Phi_3 = hk$. Thus, the products kx_0 and hk and the sum $h + k$ are structurally globally identifiable. Rearranging Φ_3 and substituting into Φ_2 yields the polynomial:

$$f(k) = k^2 - \Phi_2 k + \Phi_3 = 0. \tag{A.14}$$

Using Descartes' rule of signs, it can be seen that eq. (A.14) has two changes of signs in the coefficients, which means that it has either two or zero positive, real roots. The negative polynomial $f(-k)$ has no change of sign and so we deduce that there are zero negative roots. In summary, the structural identifiability analysis yields:

- k is locally identifiable with up to two possible solutions,
- x_0 is locally identifiable (from $\Phi_1 = kx_0$),
- h is locally identifiable (from $\Phi_3 = hk$).

Therefore, the model is structurally locally identifiable unless k is known, in which case the model would be structurally globally identifiable.

A.1.4 Prednisone Model - A structurally locally identifiable model

Finally, we consider the pharmacokinetic model presented by Bunte *et al.* [15] which models oral dosing of prednisone:

$$\begin{aligned} \frac{dS}{dt} &= -k_{abs}S, & S(0) &= S_0, \\ \frac{dP}{dt} &= k_{abs}S - (k_{Pex} + k_{PL})P + k_{LP}L, & P(0) &= 0, \\ \frac{dL}{dt} &= k_{PL}P - (k_{Lex} + k_{LP})L, & L(0) &= 0. \end{aligned} \tag{A.15}$$

In this scenario, we have three states: the stomach compartment, S, and the inactive and active metabolite prednisone, P and prednisolone, L respectively. Bunte *et al.* carried out identifiability analysis on the five model parameters subject to observing only P and L on their full model. They found the model to be structurally locally identifiable, with three possible solutions for all parameters except k_{PL}, which they found to be structurally globally identifiable.

Under the assumption that the conversion between P and L occurs much faster than absorption from the stomach and removal from the system, a quasi-steady approximation was used to reduce the system to:

$$\begin{aligned} \frac{dS}{dt} &= -k_{abs}S, & S(0) &= S_0, \\ \frac{dM}{dt} &= k_{abs}S - \frac{k_{Pex}k_{LP} + k_{PL}k_{Lex}}{k_{LP} + k_{PL}}M, & M(0) &= 0, \end{aligned} \tag{A.16}$$

where $M(t) = P(t) + L(t)$. Bunte *et al.* did not perform identifiability analysis on the reduced model, which we do so here to compare to the conclusions of the full model. The system in compact form is given by $\frac{d\boldsymbol{\mu}}{dt} = A\boldsymbol{\mu}$, where:

$$\boldsymbol{\mu}(t) = [S(t), M(t)]^T, \quad A = \begin{pmatrix} -k_{abs} & 0 \\ k_{abs} & -\frac{k_{Pex}k_{LP}+k_{PL}k_{Lex}}{k_{LP}+k_{PL}} \end{pmatrix}, \quad \boldsymbol{\mu}(0) = [S_0, 0]^T. \tag{A.17}$$

The observed variable is the sum of the prednisone and prednisolone levels ($\boldsymbol{y} = M(t)$) and the parameter set is $\boldsymbol{\theta} = [k_{abs}, k_{LP}, k_{PL}, k_{Pex}, k_{Lex}, S_0]$. Applying the Laplace transform, we find the new solution in Laplace space for the observable components only:

$$\bar{\boldsymbol{\mu}}(r) = \begin{pmatrix} \bar{S}(r) \\ \bar{M}(r) \end{pmatrix} = \frac{1}{\det(rI - A)} \begin{pmatrix} r + \frac{k_{Pex}k_{LP} + k_{PL}k_{Lex}}{k_{LP} + k_{PL}} & 0 \\ k_{abs} & r + k_{abs} \end{pmatrix} \begin{pmatrix} S_0 \\ 0 \end{pmatrix}. \tag{A.18}$$

Now, we express the observed transformed variable in terms of rational functions:

$$\bar{M}(r) = \frac{\Phi_1}{\Phi_2 r^2 + \Phi_3 r + \Phi_4}, \tag{A.19}$$

where,

$$\Phi_1 = k_{abs} S_0 (k_{LP} + k_{PL}), \tag{A.20}$$

$$\Phi_2 = k_{LP} + k_{PL}, \tag{A.21}$$

$$\Phi_3 = k_{abs}(k_{LP} + k_{PL}) + k_{Pex}k_{LP} + k_{Lex}k_{PL}, \tag{A.22}$$

$$\Phi_4 = k_{abs}(k_{Pex}k_{LP} + k_{Lex}k_{PL}). \tag{A.23}$$

Substituting eq. (A.21) into eq. (A.20) it follows that,

$$\frac{\Phi_1}{\Phi_2} = k_{abs} S_0. \tag{A.24}$$

In contrast to the full model, we can rearrange eqs. (A.21) to (A.23) to now find a quadratic in k_{abs}:

$$\Phi_2 k_{abs}^2 - \Phi_3 k_{abs} + \Phi_4 = 0. \tag{A.25}$$

Using Descartes' rule of signs, it can be seen that eq. (A.25) has 2 changes of signs in the coefficients, which means it has up to two positive, real roots. We conclude that:

- k_{abs} is locally identifiable (with up to two solutions),

- S_0 is locally identifiable (from eq. (A.24)),
- $k_{LP} + k_{PL}$ is globally identifiable (from eq. (A.21)),
- $k_{Pex}k_{LP} + k_{Lex}k_{PL}$ is locally identifiable (from eq. (A.23)).

Prior knowledge is needed about one out of k_{PL} and k_{LP} and one out of k_{Pex} or k_{Lex} for the model to be structurally locally identifiable, and additional prior knowledge is needed about k_{abs} for the model to be structurally globally identifiable. Hence, quasi-steady approximations have worsened the structural identifiability. However, the reduction in parameters given by the quasi-steady approximations does provide some improvement when statistically fitting due to the limited temporal resolution of the sample data.

A.2 Taylor series approach

A.2.1 A structurally globally identifiable example

We consider the system eq. (A.1), calculating the first two Taylor coefficients at $t_0 = 0$:

$$y(0, \boldsymbol{\theta}) = x(0, \boldsymbol{\theta}) = x_0, \tag{A.26}$$

$$\frac{dy}{dt}(0, \boldsymbol{\theta}) = -kx(0, \boldsymbol{\theta}) = -kx_0. \tag{A.27}$$

From the first coefficient, it can be seen that x_0 is unique. We can then conclude from the second coefficient that k is also unique. Therefore, this model is structurally globally identifiable which is in agreement with the Laplace Transform method outcome.

A.2.2 An unidentifiable example

We consider the system eq. (A.4), calculating the first three Taylor coefficients at $t_0 = 0$:

$$y(0, \boldsymbol{\theta}) = x(0, \boldsymbol{\theta}) = x_0, \tag{A.28}$$

$$\frac{dy}{dt}(0, \boldsymbol{\theta}) = -\frac{k}{h} x_(0, \boldsymbol{\theta}) = -\frac{k}{h} x_0, \tag{A.29}$$

$$\frac{d^2y}{dt^2}(0, \boldsymbol{\theta}) = -\frac{k}{h}\left(-\frac{k}{h}\right) x_0. \tag{A.30}$$

From the first coefficient, x_0 is unique. The second coefficient shows that the quotient k/h is unique. Further derivatives provides no mode information, hence we have the same two rational functions as in the Laplace Transform method. Thus, we conclude that the parameters k and h are unidentifiable and therefore the model is structurally unidentifiable.

A.2.3 A linear example

We consider the system given by eq. (A.7), calculating the first four Taylor coefficients at $t_0 = 0$:

$$y(0, \boldsymbol{\theta}) = x_2(0, \boldsymbol{\theta}) = 0, \tag{A.31}$$

$$\frac{dy}{dt}(0, \boldsymbol{\theta}) = kx_1(0, \boldsymbol{\theta}) - hx_2(0, \boldsymbol{\theta}) = kx_0, \tag{A.32}$$

$$\frac{d^2y}{dt^2}(0, \boldsymbol{\theta}) = -kx_0(k + h), \tag{A.33}$$

$$\frac{d^3y}{dt^3}(0, \boldsymbol{\theta}) = kx_0(k^2 + hk + h^2). \tag{A.34}$$

From the second coefficient, it can be seen that kx_0 is unique, meaning that we can eliminate this term from the third coefficient. Hence, the sum $k + h$ is also unique. Rewriting the fourth coefficient as $kx_0((k + h)^2 - hk)$, we see that the product hk is unique. Therefore, this leaves the same set of rational functions that was found using the Laplace transform approach, thus confirming that the model is structurally locally

identifiable.

A.2.4 Prednisone model

We return to the system given by eq. (A.16) and begin by evaluating the observable $y = [M]$ at initial time,

$$M(0) = 0. \tag{A.35}$$

From this, we obtain no information and so continue on to determine the next three coefficients,

$$\Phi_1 = \frac{d}{dt}M(0) = k_{abs}S_0, \tag{A.36}$$

$$\Phi_2 = \frac{d^2}{dt^2}M(0) = -\,k_{abs}S_0\frac{(k_{abs}\,(k_{LP}+k_{PL}) + k_{Pex}k_{LP} + k_{PL}k_{Lex})}{k_{LP}+k_{PL}}, \tag{A.37}$$

$$\begin{aligned}\Phi_3 = \frac{d^3}{dt^3}M(0) = k_{abs}S_0\frac{1}{(k_{LP}+k_{PL})^2}\cdot((k_{Pex}k_{LP}+k_{PL}k_{Lex})^2 \\ + k_{abs}(k_{LP}+k_{PL})(k_{Pex}k_{LP}+k_{PL}k_{Lex}) + k_{abs}^2(k_{LP}+k_{PL})^2)\end{aligned} \tag{A.38}$$

We can obtain a quadratic from these first 3 expressions,

$$(\Phi_1\Phi_3 - \Phi_2^2)S_0^2 - \Phi_1^2\Phi_2 S_0 - \Phi_1^4 = 0 \tag{A.39}$$

where using the original variables we can show that $\Phi_1\Phi_3 - \Phi_2^2 < 0$. Therefore, by Descartes' rule of signs, we have 2 changes of sign and so up to 2 positive, real roots. This is in agreement with our results using the Laplace transform, as we can conclude that both S_0 and k_{abs} are SLI (using eq. (A.36)).

Subsequent coefficients are of the form,

$$\Phi_j = (-1)^{j-1}\frac{k_{abs}S_0}{(k_{LP}+k_{PL})^{j-1}}\sum_{i=0}^{j-1}(k_{abs}(k_{LP}+k_{PL}))^i(k_{Pex}k_{LP}+k_{PL}k_{Lex})^{j-1-i}, \tag{A.40}$$

and hence do not provide further information into the identifiability of the remaining 4 parameters. Using MAPLE to attempt to solve the first 6 coefficients for the 6 parameters yields no answer, which would normally indicate calculating further coefficients. However, from the Laplace Transform method we know that the remaining 4 parameters are not identifiable. From eq. (A.37), we find that the fraction,

$$\frac{\left(k_{abs}\left(k_{lp}+k_{pl}\right)+k_{pex}k_{lp}+k_{pl}k_{lex}\right)}{k_{lp}+k_{pl}} \tag{A.41}$$

will be SLI, however it's not easily seen that the numerator and denominator are identifiable individually as it was using the Laplace Transform method. We could try calculating more coefficients, but there is an increasing complexity of coefficients with no guarantee of gaining more information.

A.2.5 A non-linear example

We now illustrate the Taylor series expansion method on a nonlinear system:

$$\frac{dx}{dt} = ax(b-x), \qquad x(0) = x_0, \tag{A.42}$$

$$y = x. \tag{A.43}$$

We calculate the first two Taylor coefficients at $t_0 = 0$:

$$y(0,\boldsymbol{\theta}) = x(0,\boldsymbol{\theta}) = x_0, \tag{A.44}$$

$$\frac{d}{dt}y(0,\boldsymbol{\theta}) = ax_0(b-x_0), \tag{A.45}$$

from which we deduce that both x_0 and $a(b - x_0)$ are unique. We now find the third coefficient:

$$\frac{d^2}{dt^2}y(t, \boldsymbol{\theta}) = \frac{d}{dt}(ax(b - x)), \tag{A.46}$$

$$= ab\frac{dx}{dt} - 2ax\frac{dx}{dt}, \tag{A.47}$$

$$= a^2x(b - 2x)(b - x). \tag{A.48}$$

As x_0 and $a(b - x_0)$ are both unique, the product $a(b - 2x_0)$ is also unique. Rewriting this term as $a(b - x_0) - ax_0$, we find a to be unique and therefore globally identifiable. Thus, b is also unique and so the system is structurally globally identifiable.

A.3 Extended observability

A.3.1 A linear unidentifiable example

We illustrate the method with an example, returning to the system given by eq. (A.4). In this method, it is assumed that initial conditions of observed variables are known (ref needed), and so we define the augmented vector as,

$$\tilde{\boldsymbol{x}} = [x, k, h], \tag{A.49}$$

where we have $n = 1$ states and $q = 2$ parameters. We then generate the observability-identifiability matrix with columns of partial derivatives of the model output with respect to each state and parameter in the augmented vector. Evaluating at the initial condition gives,

$$\mathcal{O}_I(\tilde{\boldsymbol{x}}_{\mathbf{0}}) = \begin{pmatrix} 1 & 0 & 0 \\ -\frac{k}{h} & -\frac{x_0}{h} & \frac{kx_0}{h^2} \\ \frac{k^2}{h^2} & 2\frac{kx_0}{h^2} & -2\frac{k^2x_0}{h^3} \end{pmatrix}. \tag{A.50}$$

Using Gaussian elimination, we put the matrix into row echelon form to calculate the matrix rank,

$$\mathcal{O}_I(\tilde{\boldsymbol{x}}_0) = \begin{pmatrix} 1 & 0 & 0 \\ 0 & 1 & -\frac{k}{h} \\ 0 & 0 & 0 \end{pmatrix}. \tag{A.51}$$

In order to be globally structurally identifiable, this matrix must have full rank, in this case we would require $\text{rank}(\mathcal{O}_I(\tilde{\boldsymbol{x}})) = 3$ [25]. We see here that the rank of this matrix is 2 so is not of full rank, meaning the system is structurally unidentifiable. Due to the structure of the matrix, the columns correspond to the partial derivatives with respect to each parameter and so we can determine the identifiability of each parameter or state as well as the whole model. We note that it is specifically the second and third columns that are linearly dependent, and the removal of either one does not reduce the matrix rank. This shows that it is both k and h that are unidentifiable. We also note by pausing after row echelon elimination that the expression in the 3rd column shows the algebraic expression for the cause of the identifiability issue. In this small example, it is easy to spot the algebraic expressions, however this would not be as clear with increased complexity.

The STRIKE_GOLDD software has an extension called 'AutoRepar' (added in 2021) which searches for reparameterisations for an unidentifiable model [46]. Running this algorithm on the above model, it is able to identify and suggest the transformation of $\frac{k}{h} \to k$ which would remove the nonidentifiability.

It is of note that the matrix may reach maximum rank with fewer derivatives, (in this case, the matrix was of rank 2 after just one derivative). Therefore, when analysing larger models, the rank is calculated after each derivative and if the rank is equal to $n + q$ then the method concludes in order to reduce excessive calculations.

A.3.2 Prednisone model

For the reduced Prednisone model (Equation (A.15)), the augmented vector is $\tilde{x} = [S, M, k_{abs}, k_{PL}, k_{LP}, k_{Pex}, k_{Lex}, S_0]$. The first 2 rows of the observability-identifiability matrix evaluated at the initial condition is,

$$\mathcal{O}_I(\tilde{\boldsymbol{x}}_0) = \begin{pmatrix} 0 & 1 & 0 & 0 & 0 & 0 & 0 & 0 \\ k_{abs} & -\frac{k_{PL}k_{Lex}+k_{LP}k_{Pex}}{k_{PL}+k_{LP}} & S_0 & 0 & 0 & 0 & 0 & 0 \end{pmatrix}. \tag{A.52}$$

The maximum number of derivatives needed to assess identifiability is $n + q - 1 = 2 + 6 - 1 = 7$. The complexity of the terms in the matrix is increasing swiftly and this method would be arduous and prone to error if done by hand. We input our system into the STRIKE_GOLDD software which can readily compute the observability-identifiability matrix and calculate the rank. It outputs that k_{abs} is identifiable and all other parameters are unidentifiable. However, it also tells us that both state variables are observable and their initial conditions, if unknown, are identifiable. Hence, we conclude that S_0 is also identifiable. This outcome agrees with our conclusions from the previous two methods. AutoRepar is unable to suggest a reparameterisation that would completely eliminate the unidentifiability, but does suggest a transformation that would reduce the 4 remaining parameters to 2.

A.3.3 A nonlinear identifiable example

We again consider the simple nonlinear system given by eq. (A.42) and construct the corresponding nonlinear observability-identifiability matrix. Our augmented vector here is $[x, a, b]$. The first row will correspond to the partial derivatives of the output variables with respect to the augmented vector,

$$\frac{\partial y}{\partial \tilde{\boldsymbol{x}}} = [1, 0, 0]. \tag{A.53}$$

This matrix has rank equal to 1. We calculate the next two rows using the Lie derivative definition given by eq. (1.5). We find the first Lie derivative,

$$L_{\boldsymbol{f}}\boldsymbol{g}(\tilde{\boldsymbol{x}}) = \frac{\partial \boldsymbol{g}(\tilde{\boldsymbol{x}})}{\partial \tilde{\boldsymbol{x}}}\boldsymbol{f}(\tilde{\boldsymbol{x}}) = [ax(b-x)]. \tag{A.54}$$

Thus the second row of the observability-identifiability matrix is,

$$\frac{\partial}{\partial \tilde{\boldsymbol{x}}}\left(L_{\boldsymbol{f}}\boldsymbol{g}(\tilde{\boldsymbol{x}})\right) = \begin{pmatrix} a(b-2x) & x(b-x) & ax \end{pmatrix}. \tag{A.55}$$

The second Lie derivative is given by,

$$L^2_{\boldsymbol{f}}\boldsymbol{g}(\tilde{\boldsymbol{x}}) = \frac{\partial L_{\boldsymbol{f}}\boldsymbol{g}(\tilde{\boldsymbol{x}})}{\partial \tilde{\boldsymbol{x}}}\boldsymbol{f}(\tilde{\boldsymbol{x}}) = [a^2b^2x - 3a^2bx^2 + 2a^2x^3], \tag{A.56}$$

hence the third row will be,

$$\frac{\partial}{\partial \tilde{\boldsymbol{x}}}\left(L^2_{\boldsymbol{f}}\boldsymbol{g}(\tilde{\boldsymbol{x}})\right) = \begin{pmatrix} a^2(b^2-6bx+6x^2) & 2ax(b^2-3bx+2x^2) & a^2x(2b-3x) \end{pmatrix}. \tag{A.57}$$

Combining these rows and evaluating at the initial condition $x(0) = x_0$, we have,

$$\mathcal{O}_I(\tilde{\boldsymbol{x}}_0) = \begin{pmatrix} 1 & 0 & 0 \\ a(b-2x_0) & x_0(b-x_0) & ax_0 \\ a^2(b^2-6bx_0+6x_0^2) & 2ax_0(b^2-3bx_0+2x_0^2) & a^2x_0(2b-3x_0) \end{pmatrix}. \tag{A.58}$$

In this particular example where we have no input, we see that the Lie derivatives agree with the time derivatives of the output variables. In order to calculate the rank, we use elementary row operations to obtain the following:

$$\begin{pmatrix} 1 & 0 & 0 \\ 0 & x_0(b-x_0) & ax_0 \\ 0 & 0 & a^2x_0^2 \end{pmatrix}. \tag{A.59}$$

In this case, the matrix has full rank (=3) as each column is linearly independent, under the conditions that $x_0 \neq 0$, $a \neq 0$ and $b - x_0 \neq 0$. These results concur with the conclusions drawn from the Taylor series method. We can also run this model through the STRIKE_GOLDD software that concludes that all states are observable and all parameters are locally structurally identifiable (in ≈ 0.29 seconds).

A.4 Identifiability of the BIV$^-$ model

To establish the identifiability of this model, we proceed by calculating successive Taylor coefficients to determine the identifiability for each model parameter. We calculate the first 4 coefficients,

$$\Phi_1 = -B_0(c_4 - 1), \tag{A.60}$$

$$\Phi_2 = \frac{D}{\alpha} - \frac{\alpha B_0^2 \delta}{(-B_0\alpha + D)}, \tag{A.61}$$

$$\Phi_3 = \frac{D}{\alpha}, \tag{A.62}$$

$$\Phi_4 = -k_{re}\left(\frac{(B_0^2\alpha^2 - DB_0(\delta+2)\alpha + D^2)}{2\,\alpha\,(-B_0\alpha + D)}\right. \tag{A.63}$$

$$+ \frac{(B_0\alpha)^4(2\delta^2+\delta+1) - D(B_0\alpha)^3(\delta^2+\delta+4)}{2R\,\alpha^2\,(-B_0\alpha+D)^2} \tag{A.64}$$

$$\left. + \frac{-D^2(B_0\alpha)^2(\delta-6)\,D^3B_0\alpha(\delta-4) + D^4}{2R\,\alpha^2\,(-B_0\alpha+D)^2}\right) \tag{A.65}$$

where

$$R = \sqrt{\frac{((d+1)\,a^2B_0^2 - 2DB_0a + D^2)^2}{a^2\,(-B_0a+D)^2}} \tag{A.66}$$

Using MAPLE, we are able to express 3 of the model parameters as a function of the rational functions above,

$$\alpha = \frac{D}{\Phi_3}, \tag{A.67}$$

$$\delta = -\frac{(c_4 - 1)(\Phi_2 - \Phi_3)(\Phi_1 + (c_4 - 1)\Phi_3)}{\Phi_1^2}, \tag{A.68}$$

$$B_0 = -\frac{\Phi_1}{c_4 - 1}, \tag{A.69}$$

$$\tag{A.70}$$

and conclude that these 3 parameters are globally identifiable. We write the final parameter in terms of the 3 globally identifiable parameters,

$$k_{re} = -\frac{2B_0 Q\,\Phi_4\,\alpha^2}{\begin{array}{r}(-B_0^2\alpha^2 + D(B_0 + \Phi_2)\alpha - D^2)\,Q + B_0\alpha^2(B_0^2 + B_0\Phi_2 + 2\Phi_2^2) \\ - 3D\alpha\left(B_0 + \frac{\Phi_2}{3}\right)(B_0 + \Phi_2) + 3D^2\left(B_0 + \frac{\Phi_2}{3}\right)\end{array}} \tag{A.71}$$

where

$$Q = \sqrt{\frac{(B_0 a + \Phi_2 a - 2D)^2}{a^2}} \tag{A.72}$$

Due to the square root, we have up to 2 solutions possible for k_{re}. It can be shown numerically that for the values suggested in section 2.2, only one solution is valid in order to satisfy the constraint that $k_{re} > 0$.

Table A.1: Summary of identifiability analysis on all toy problems.

System	Parameters	Laplace Transform	Taylor Series	Extended Observability	**SIAN** [43, 68, 69]
A.1	$[k, x_0]$	SGI GI: $[k, x_0]$	SGI GI: $[k, x_0]$	SLI LI: $[k, x_0]$	SGI: GI: $[k, x_0]$
A.4	$[k, h, x_0]$	SU GI: $[x_0]$ U: $[k, h]$	SU GI: $[x_0]$ U: $[k, h]$	SU LI: $[x_0]$ U: $[k, h]$	SU GI: $[x_0]$ U: $[k, h]$
A.7	$[k, h, x_0]$	SLI LI: $[k, h, x_0]$ (with up to 2 solutions)	SLI LI: $[k, h, x_0]$ (with up to 2 solutions) 4 coefficients calculated	SLI LI: $[k, h, x_0]$	SLI LI: $[k, h, x_0]$ (with up to 2 solutions)
A.16	$[k_{abs}, k_{PL}, k_{LP}, k_{Pex}, k_{Lex}, S_0]$	SU LI: $[k_{abs}, S_0]$ (with up to 2 solutions) U: $[k_{PL}, k_{LP}, k_{Pex}, k_{Lex}]$	SU LI: $[k_{abs}, S_0]$ (with up to 2 solutions) U: $[k_{PL}, k_{LP}, k_{Pex}, k_{Lex}]$ 6 coefficients calculated	SU LI: $[k_{abs}, S_0]$ U: $[k_{PL}, k_{LP}, k_{Pex}, k_{Lex}]$	SU LI: $[k_{abs}, S_0]$ (with up to 2 solutions) U: $[k_{PL}, k_{LP}, k_{Pex}, k_{Lex}]$
A.42	$[a, b, x_0]$	N/A	SGI GI: $[a, b, x_0]$	SLI LI: $[a, b, x_0]$	SGI GI: $[a, b, x_0]$

Table A.2: Outcome of identifiability analysis for each variation of the CIV and BIV models.

System	Parameters	Taylor Series	Extended Observability
CIV$^+$ Model Equations (2.22) and (2.23)	$[\alpha, k_{fb}, k_{bf}, B_0, k_{re}]$	SGI GI: $[\alpha, k_{fb}, k_{bf}, B_0, k_{re}]$	SLI LI: $[\alpha, k_{fb}, k_{bf}, B_0, k_{re}]$
CIV$^-$ Model Equations (2.34) and (2.35)	$[\alpha, \delta, B_0, k_{re}]$	SGI GI: $[\alpha, \delta, B_0, k_{re}]$	SLI LI: $[\alpha, \delta, B_0, k_{re}]$
CIV Model (non-zero initial cortisol level) Equations (2.57) and (2.58)	$[\alpha, k_{fb}, k_{bf}, B_0, k_{re}, F_0]$	SLI LI: $[\alpha, k_{fb}, k_{bf}, B_0, k_{re}, F_0]$	UI LI: $[\alpha, k_{fb}, k_{bf}, B_0, k_{re}]$ UI: $[F_0]$
BIV Model Equations (3.4) to (3.7)	$[\alpha, k_{fb}, k_{bf}, B_0, k_{re}]$	SGI: GI: $[\alpha, k_{fb}, k_{bf}, B_0, k_{re}]$	SLI: LI: $[\alpha, k_{fb}, k_{bf}, B_0, k_{re}]$
BIV Model - Asymptotic Equations (3.97) and (3.100)	$[\alpha, \delta, B_0, k_{re}]$	SGI: GI: $[\alpha, \delta, B_0, k_{re}]$	SLI: LI: $[\alpha, \delta, B_0, k_{re}]$

APPENDIX B

CALCULATIONS FOR MODEL DEVELOPMENT

B.1 Loss function behaviour for CIV dosing

B.2 Optimising time sampling

Using the current time sampling, we have seen that practical identifiability issues have arisen for the binding and unbinding rate parameters. We want to determine whether there is an optimum time sampling that would allow the true binding and unbinding parameters to be found at high noise. An optimisation problem is defined with a total number of sampling points fixed. Figure B.3 shows the set up of our optimisation problem with 4 parameters to fit: N_1 and N_2 are the number of time points in the first two regions respectively and T_1 and T_2 define the end time point of the intervals for the first two regions, i.e., N_1 time points will be sampled while $0 < t \leq T_1$ and N_2 time points will be sampled while $T_1 < t \leq T_2$. The remaining time points will be sampled within the final region while $T_2 < t \leq 1440$. The points within each region will be evenly spaced between the two end points of the region. The number of points in the first two regions must be positive and collectively must not exceed the total number of time points N,

$$0 \leq N_1 + N_2 \leq N. \tag{B.1}$$

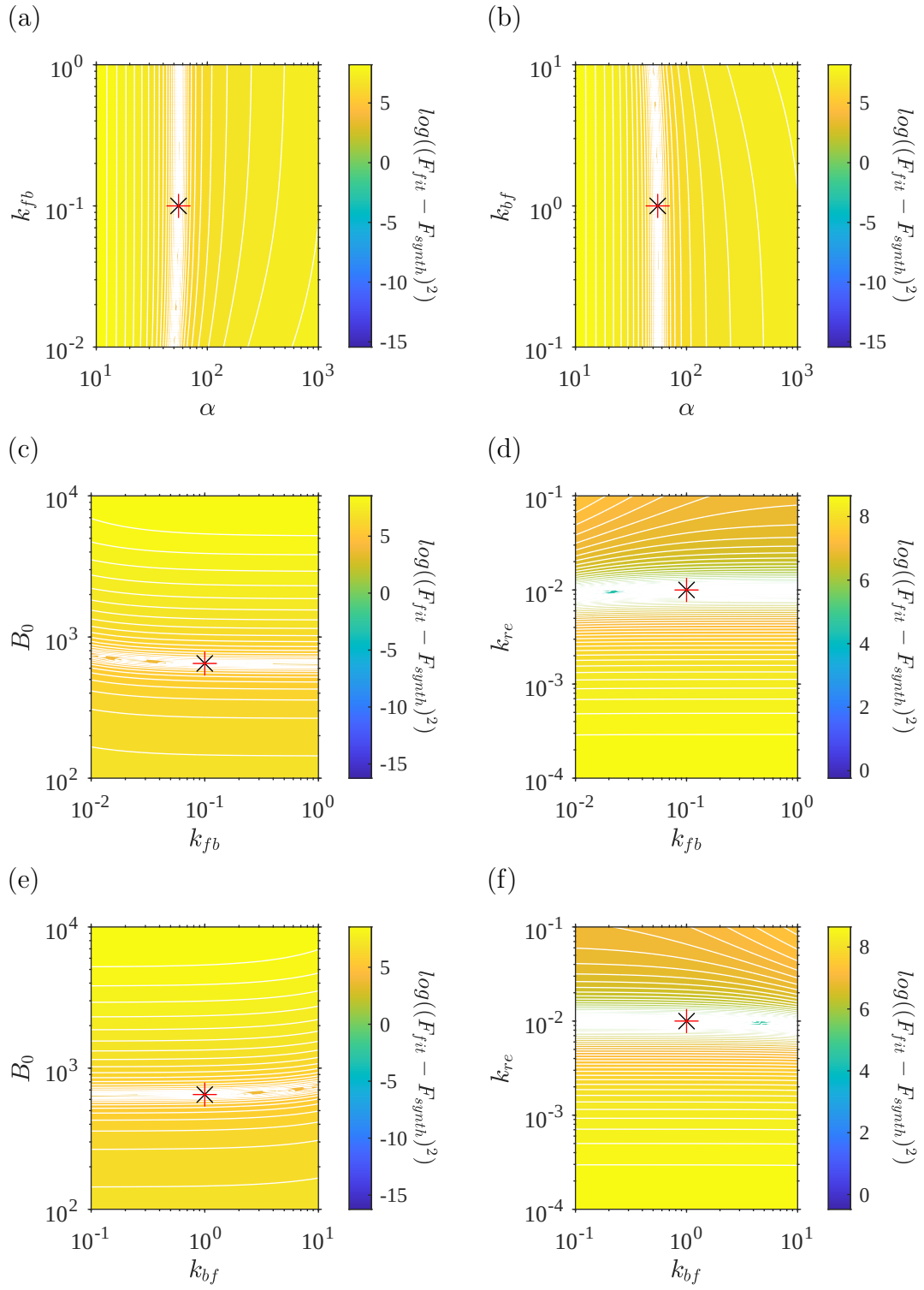

Figure B.1: Loss function value for varying pairs of model parameters for CIV dosing with zero noise added to synthetic data and sampling time frequency corresponding to the time points used in data [PD]. The red plus indicates the true parameter value pair, while the loss function numerical minimum are shown with a black cross: (a) α versus k_{fb}, (b) α versus k_{bf}, (c) k_{fb} versus B_0, (d) k_{fb} versus k_{re}, (e) k_{bf} versus B_0, (f) k_{bf} versus k_{re}.

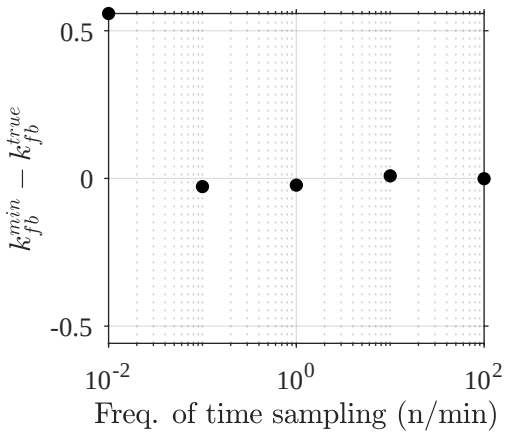

Figure B.2: Varying k_{fb} and k_{bf} for CIV dosing with Gaussian noise (s.d. $1\,\mathrm{nmol\,L^{-1}}$) added to synthetic data and sampling time frequency ranging from 0.01-100 timepoints per minute: difference between true parameter value for k_{fb} and corresponding k_{fb} value that generates minimum loss function.

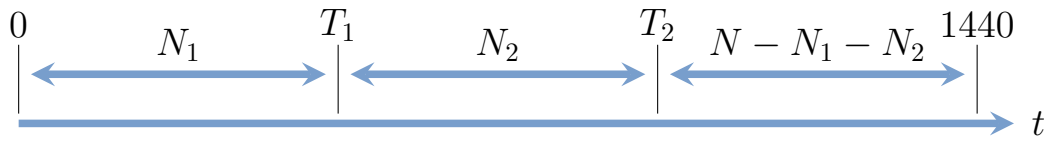

Figure B.3: Schematic of the time sampling within a 24-hour region.

We impose the constraint that there will be at least one point in each of the three regions,

$$N_1 \geq 1, \tag{B.2}$$

$$N_2 \geq 1. \tag{B.3}$$

Currently, the highest frequency that cortisol concentration could be measured would be approximately every 10 minutes via some implantable sensor which yields a frequency of samples constraint in each of the regions,

$$\frac{T_1}{N_1} \geq 10, \qquad \frac{T_2}{N_2} \geq 10, \qquad \frac{1440 - T_2}{N - N_1 - N_2} \geq 10. \tag{B.4}$$

Finally, due to the frequency constraint there must be at least 10 minutes between T_1 and T_2,

$$T_2 \geq T_1 + 10. \tag{B.5}$$

The CIV$^+$ model

For zero to small noise, the time sampling is of little importance. Optimising for an individual allows each parameter to be uniquely determined even at high noise, however this requires *a priori* knowledge of the parameters k_{fb} and k_{bf}. An optimum time sampling is found for an individual under large noise (Figure B.4), however this choice is not necessarily the optimal distribution for any other individual when generating new data and assessing the match to the true value of k_{fb} (Figure B.5). This motivates a more in depth study into the optimal spacing distribution for an individual versus a group.

The CIV$^-$ model

If we optimise the time sampling as we did for the CIV$^+$ model, we are able to identify δ with just 24 time points (Figure B.6).

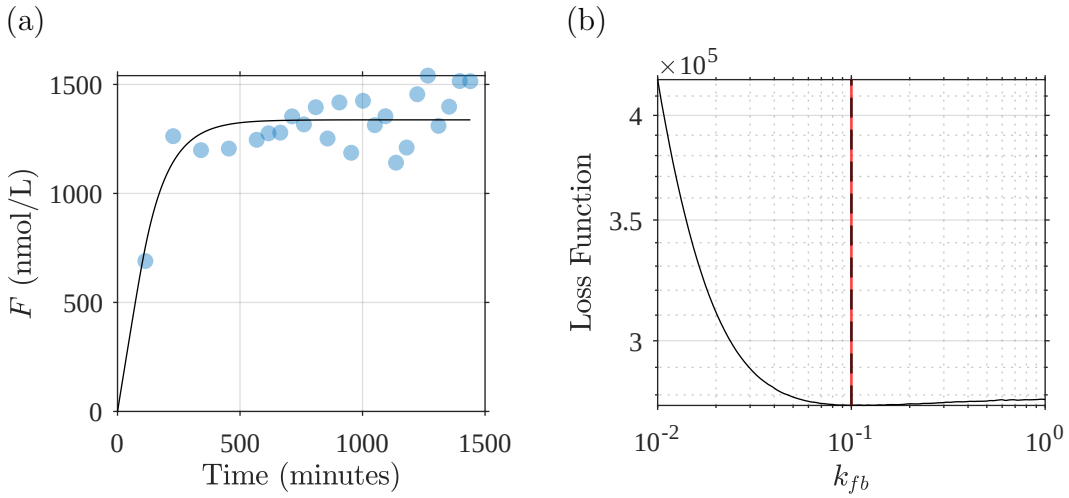

Figure B.4: Results of optimising the time sampling for $N = 24$ for one set of synthetic data with $N_1 = 5$, $N_2 = 10$, $T_1 = 568$, $T_2 = 1050$: (a) synthetic data at the optimised timepoints, (b) the corresponding loss function for varying k_{fb} where the red line indicates the true value of k_{fb} and the black dashed line indicates the numerical minimum of the loss function.

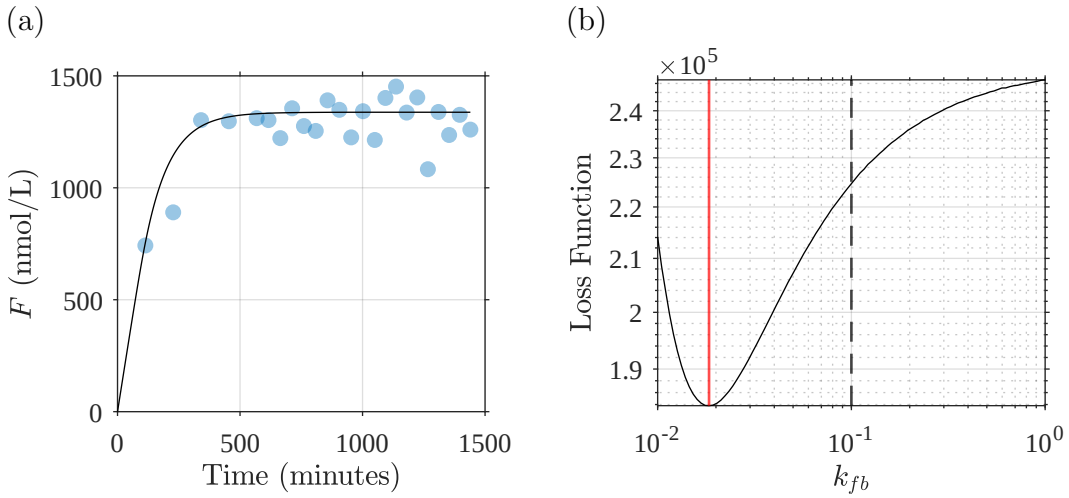

Figure B.5: Using the optimised time sampling and generating a new set of synthetic data for the same timepoints: (a) synthetic data at the optimised timepoints for a different individual, (b) the corresponding loss function for varying k_{fb} where the red line is the true value of k_{fb} and the black dashed line is the numerical minimum of the loss function.

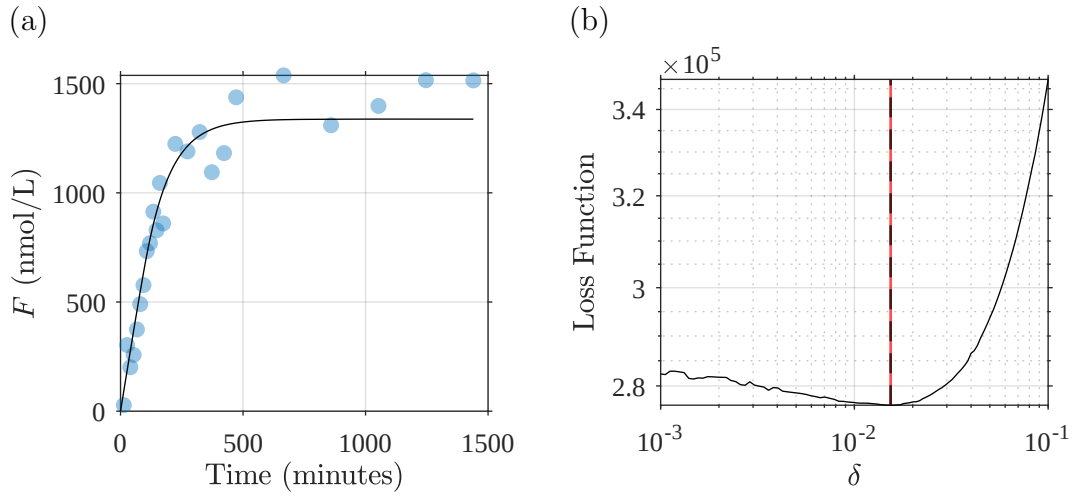

Figure B.6: Results of optimising the time sampling for $N = 24$ for the CIV-A model for one set of synthetic data giving a result of $N_1 = 13$, $N_2 = 6$, $T_1 = 174$, $T_2 = 472$: (a) synthetic data at the optimised timepoints, (b) the corresponding loss function for varying δ where the red line indicates the true value of δ and the black dashed line is the numerical minimum of the loss function.

However, as previously, this time sampling is only optimal for an individual, so the same time points for another individual are unable to match the true δ value to the minimum in the loss function (Figure B.7).

The BIV$^+$ model

As in the CIV case, we want to determine whether there is an optimum time sampling to that would allow the true binding and unbinding parameters to be found at high noise. Figure B.8 shows a similar case to CIV (see Figures B.4 and B.5) - an optimum time sampling can be found for an individual but requires a priori knowledge of k_{fb} and also does not represent the optimum time sampling of another individual.

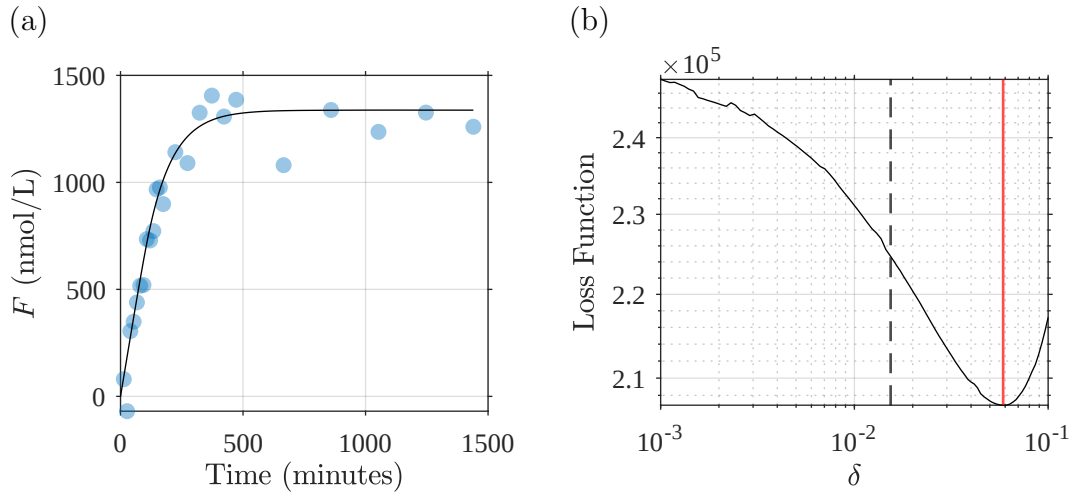

Figure B.7: Using the optimised time sampling for the CIV-A model and generating a new set of synthetic data for the same timepoints: (a) synthetic data at the optimised timepoints for a different individual, (b) the corresponding loss function for varying δ where the red line is the true value of δ and the black dashed line is the numerical minimum of the loss function.

B.3 Model reductions

B.3.1 Continuous intravenous infusion

We have the single ODE in B'

$$\frac{dB'}{dt'} = \left(\delta\frac{1}{B'^2} + 1\right)^{-1}\left(-1 + \delta\rho\frac{1-B'}{B'}\right), \tag{B.6}$$

which can be solved using separation of variables to find an implicit solution,

$$\frac{B'}{(B'-\delta\tilde{\rho})^{1+\delta\tilde{\rho}^2}}\exp(-\tilde{\rho}B') = \exp(\rho(t'+\tilde{c})), \tag{B.7}$$

where,

$$\tilde{\rho} = \frac{\rho}{1+\delta\rho}, \tag{B.8}$$

.

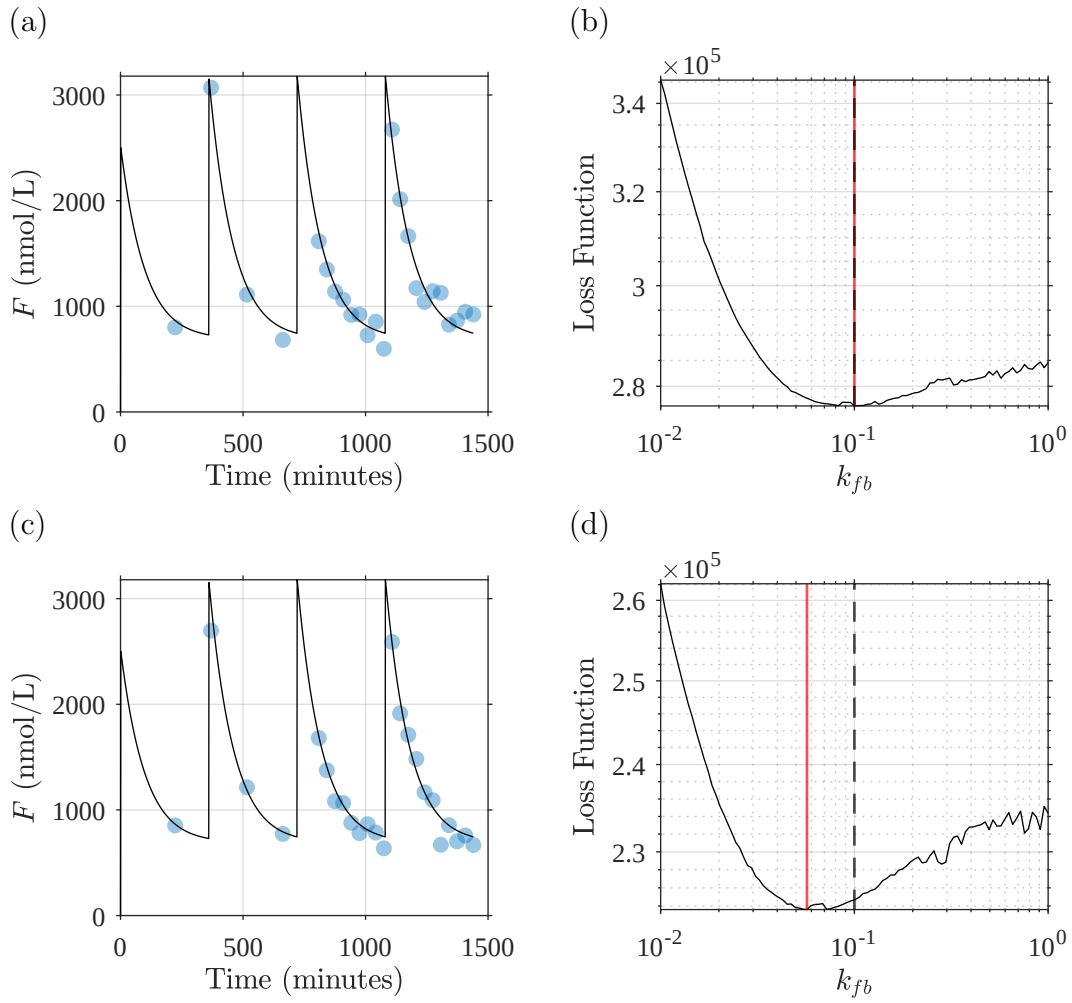

Figure B.8: Results of optimising the time sampling for $N = 24$ for one set of synthetic data with $N_1 = 1$, $N_2 = 4$, $T_1 = 223$, $T_2 = 809$: (a) synthetic data at the optimised time points, (b) the corresponding loss function for vartying k_{fb} where the red line indicates the true value of k_{fb} and the black dashed line indicates the calculated minimum of the loss function, (c),(d) generating a new set of synthetic data for the same time points.

B.3.2 Intravenous bolus injections

Returning once more to the post dosing nondimensional system for the BIV case given by eqs. (3.58) and (3.59). We consider scalings that reflect low levels of binding protein and high levels of free cortisol,

$$B' = \delta \grave{B}', \qquad F'_f = \grave{F}'_f, \qquad t' = \delta^{-1}\grave{t}^{-1} + t_{cr}, \tag{B.9}$$

which yields the following system,

$$\delta \frac{d\grave{F}'_f}{d\grave{t}'} = -\frac{\beta}{\delta}\grave{F}'_f\grave{B}' + \frac{\beta}{\delta}(1 - \delta\grave{B}') - \delta\psi\grave{F}'_f, \tag{B.10}$$

$$\delta^2 \frac{d\grave{B}'}{d\grave{t}'} = -\frac{\beta}{\delta}\grave{F}'_f\grave{B}' + \frac{\beta}{\delta}(1 - \delta\grave{B}'). \tag{B.11}$$

Taking leading order terms gives us the relation,

$$\grave{F}'_f\grave{B}' = 1. \tag{B.12}$$

We also subtract eq. (B.11) from eq. (B.10) and take leading order terms to find a single ODE in $\grave{F}'_f$,

$$\frac{d\grave{F}'_f}{d\grave{t}'} = -\psi\grave{F}'_f, \tag{B.13}$$

which gives an exponential solution for this region,

$$\grave{F}'_f = A\exp(-\psi\grave{t}'), \qquad \grave{B}' = \frac{1}{A}\exp(\psi\grave{t}'). \tag{B.14}$$

In original dimensionless variables,

$$F'_f = A\exp(-\delta\psi(t' - t_{cr})), \qquad B' = \frac{\delta}{A}\exp(\delta\psi(t' - t_{cr})). \tag{B.15}$$

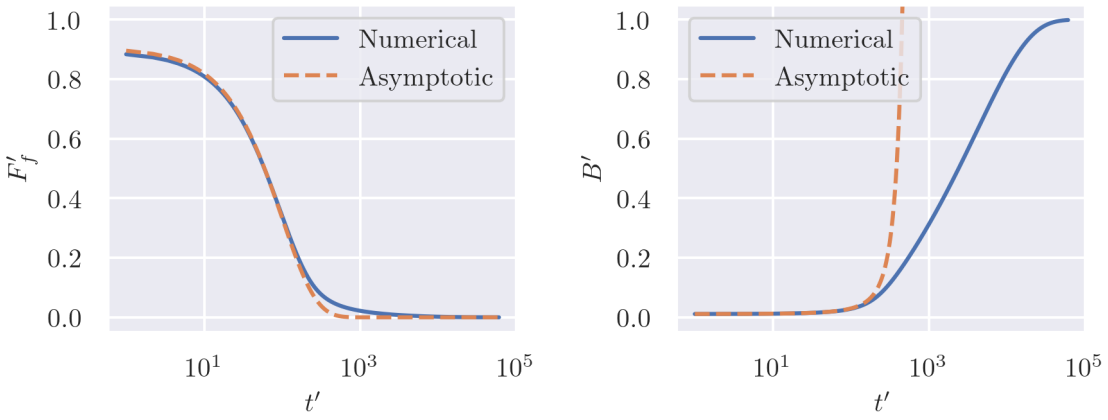

Figure B.9: Comparison of the midterm exponential asymptotic solution to the full numerical solution.

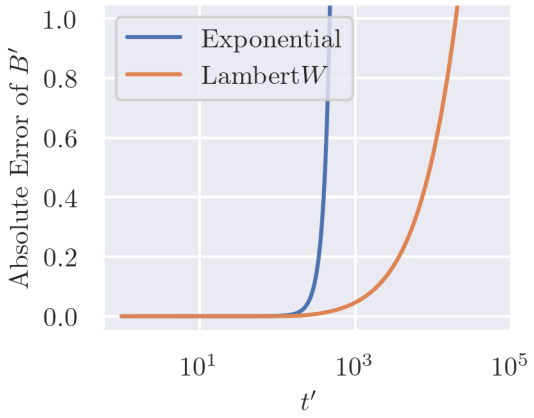

Figure B.10: Comparison of error of the two midterm asymptotic solutions against the full numerical solution for the post dosing region.

where the constant A is determined by matching to the end of the dosing region. Figure B.9 shows good agreement initially between the asymptotic and numerical solution, however the solution for B' begins to rapidly diverge as time increases.

We compare error between the full numerical solution and the 2 asymptotic solutions given by eqs. (3.66) and (B.15) in Figure B.10. The exponential solution diverges from the full numerical solution sooner than the Lambert W solution, however neither solution is able to match for large time.

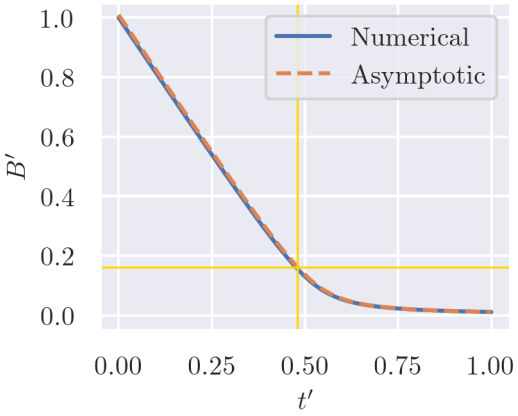

Figure B.11: The crossover asymptotic solution. The yellow lines highlight the point where binding protein is proportional to the golden ratio at $t' = \rho(1 - \delta^{\frac{1}{2}})$.

The Golden Ratio

The solution to the crossover region in the dosing period is,

$$B' = \frac{-\rho^{-1}(t' - t_{cr}) + \sqrt{(\rho^{-1}(t' - t_{cr}))^2 + 4\delta}}{2}. \tag{B.16}$$

When taking $t' = \rho(1 - \delta^{\frac{1}{2}})$ and substituting $t_{cr} = \rho$, we find,

$$B' = \delta^{\frac{1}{2}} \left(\frac{1 + \sqrt{5}}{2} \right), \tag{B.17}$$

i.e., the golden ratio (Figure B.11).

Similarly, recalling the slow manifold solution in the post dosing period,

$$B' = h'_0 + \delta^{\frac{1}{2}} h'_1, \tag{B.18}$$

where,

$$h'_0(x') = \frac{-x' + (x'^2 + 4\delta)^{\frac{1}{2}}}{2}, \tag{B.19}$$

$$h'_1(x') = \delta^{\frac{1}{2}} \frac{x' - (x'^2 + 4\delta)^{\frac{1}{2}}}{2(x'^2 + 4\delta)^{\frac{1}{2}}}. \tag{B.20}$$

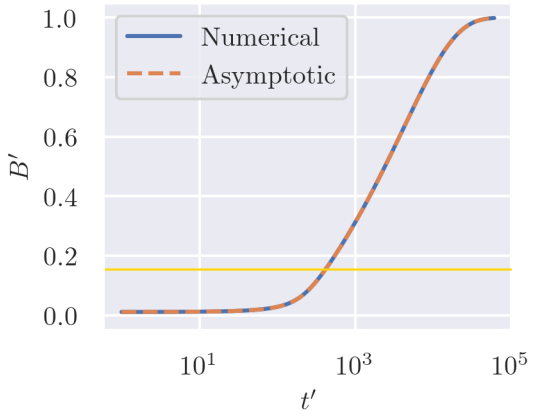

Figure B.12: The slow manifold asymptotic solution. The horizontal yellow line highlights the point where binding protein is proportional to the golden ratio.

Therefore, when $x' = -\delta^{\frac{1}{2}}$, we have,

$$h_0'(-\delta^{\frac{1}{2}}) = \delta^{\frac{1}{2}} \left(\frac{1+\sqrt{5}}{2} \right), \tag{B.21}$$

$$h_1'(-\delta^{\frac{1}{2}}) = -\frac{\delta}{\sqrt{5}} \left(\frac{1+\sqrt{5}}{2} \right). \tag{B.22}$$

Figure B.12 shows the golden ratio point on the slow manifold asymptotic solution for the post dosing region. As the solution is dependent on the numerical solution of the ODE for slow variable x', we do not have an analytic expression for t' at this point.

APPENDIX C

BAYESIAN INFERENCE - TOY PROBLEMS

C.1 Setting up a Stan model for inference

A Stan model is made up of blocks which include:

- Function block, where any external functions are defined, e.g., an ODE system,
- Data block, where the observed data is inputted alongside any known quantities,
- Parameters block, which defines any parameters to be fitted and their necessary constraints,
- Model block, this is the section where the likelihood function and any parameter prior distributions are defined,
- Generated quantities block (optional), defining outputs that the user would like calculated alongside the prior distributions. In this work, we generate model trajectories based on the accepted parameter samples.

We provide Stan with prior distributions based on previous knowledge of the parameter set. For ODE models, we also provide a likelihood function of the form:

$$\boldsymbol{y} \sim \mathcal{N}(F(\boldsymbol{\theta}, t), \sigma^2). \tag{C.1}$$

where $F(\boldsymbol{\theta}, t)$ is the observed variable and we assume that the observed data has some normal additive noise with standard deviation σ [61].

C.2 Toy Problems

We run the following workflow on the toy problems discussed in section 1.3 to analyse how identifiability issues may present when fitting parameters to data with noise:

1. Define parameter prior distributions and choose "true values" for each model parameter.

2. Generate synthetic data with additive Gaussian noise using selected "true values".

3. Run a prior predictive check - generate 100 draws of model parameters from the given prior distributions and calculate the model trajectory for each set. Visually compare these to the data to see whether they provide a sensible estimate of the qualitative behaviour.

4. Fit the data using Stan with 4 chains (1000 warm up and 1000 samples per chain) to find posterior distributions for model (and noise) parameters.

5. Plot the trace and posterior distribution of each parameter.

C.2.1 Globally identifiable case

We first run a fit for the structurally globally identifiable ODE system described by eq. (A.1). In Figure C.1, we see that the true trajectory that was used to generate the synthetic data falls within the 95% credible interval (CI) of trajectory estimates. Similarly, Figure C.2 shows that the individual parameter estimates are both within their respective 95% CIs. The samples for both parameters resemble random walks, which suggests that the Markov chains have reached convergence as desired. The posterior for k is much narrower than the prescribed prior, which suggests the data is leading the posterior

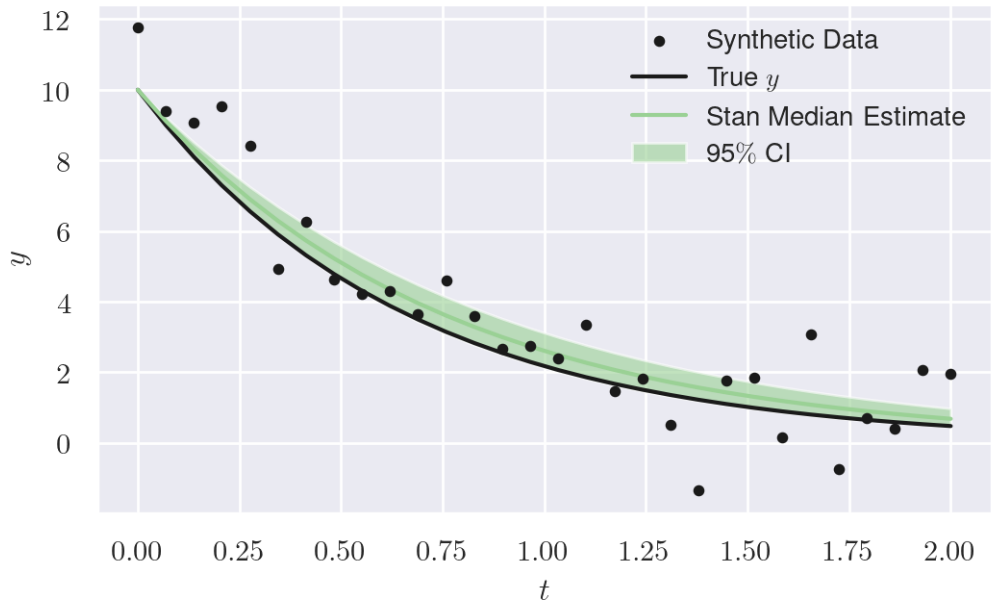

Figure C.1: Bayesian approximation of synthetic data generated using the system described by eq. (A.1).

rather than the prior. However, the ground truth of k sits very close to upper bound of the credible interval, which could suggest some bias has been introduced from the noise on the data. Finally, the scatter plot matrix of parameter estimates (Figure C.3) shows little sign of correlation between parameters. Overall, we conclude that the model retains identifiability when data has noise added with some bias introduced into the estimates due to noise.

C.2.2 Unidentifiable case

We now look at the structurally unidentifiable ODE system described by eq. (A.4). We see in Figure C.4 that the model trajectory is still a good fit to the synthetic data and true curve, however we can immediately see an issue in Figure C.5 where the parameters estimates are plotted against one another in a scatterplot matrix. There is a strong correlation between parameters k and h, which is expected due to the algebraic linear relationship (k/h) that was found when testing structural identifiability. Similarly, we see in Figure C.6 that the posterior distributions for k and h are not much narrower than

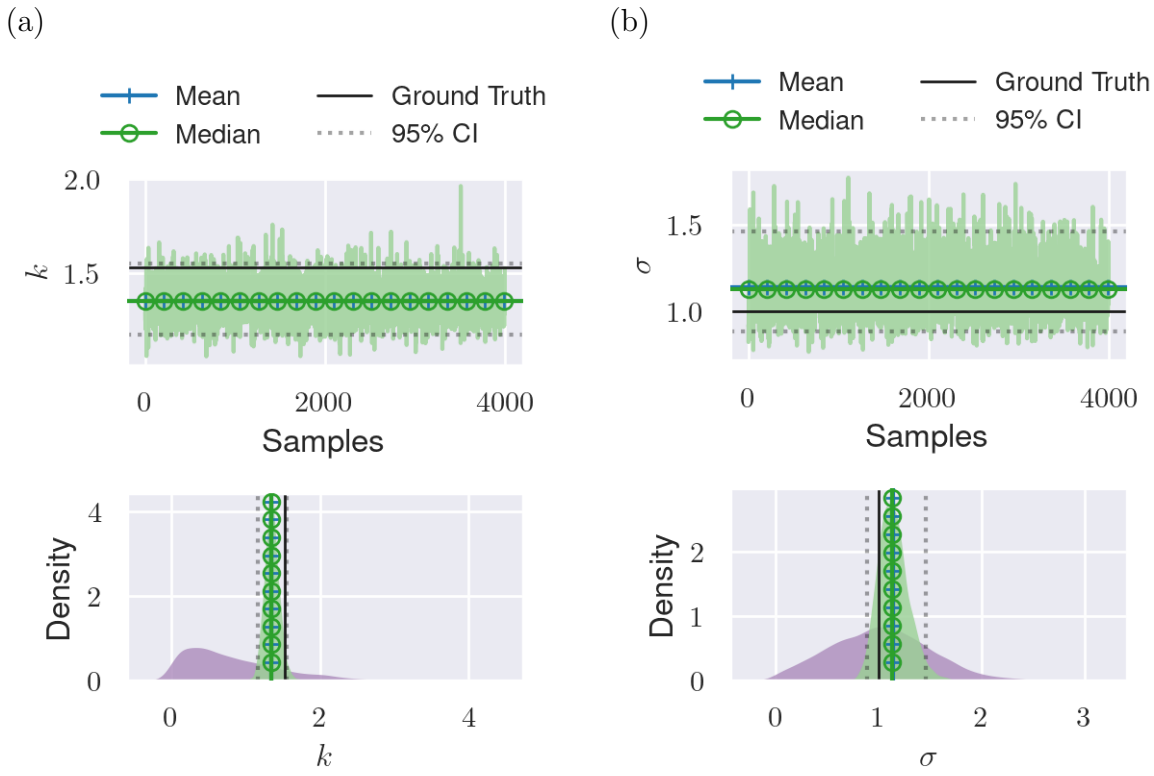

Figure C.2: Trace, prior distributions and posterior distributions of model parameters for the Bayesian approximation of the system described by eq. (A.1): (a) for model parameter k, (b) noise parameter σ.

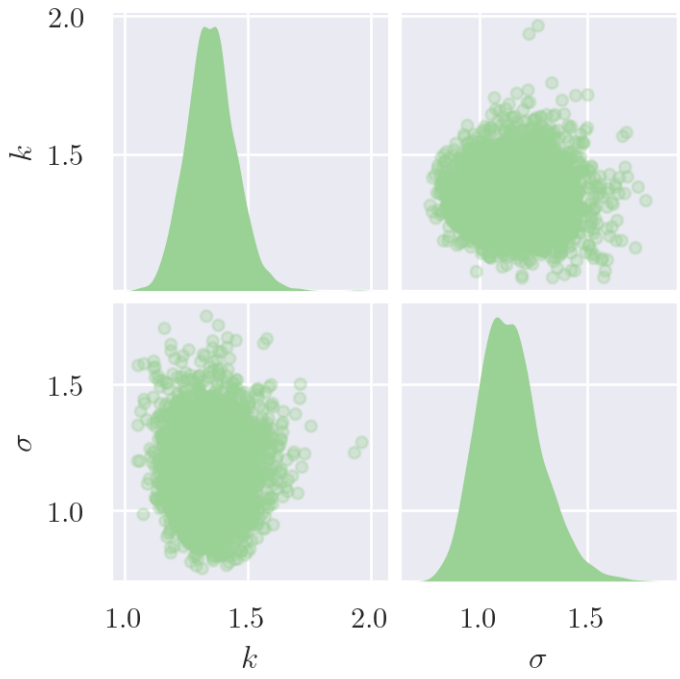

Figure C.3: Scatter matrix plot of parameter samples for the Bayesian approximation of the system described by eq. (A.1).

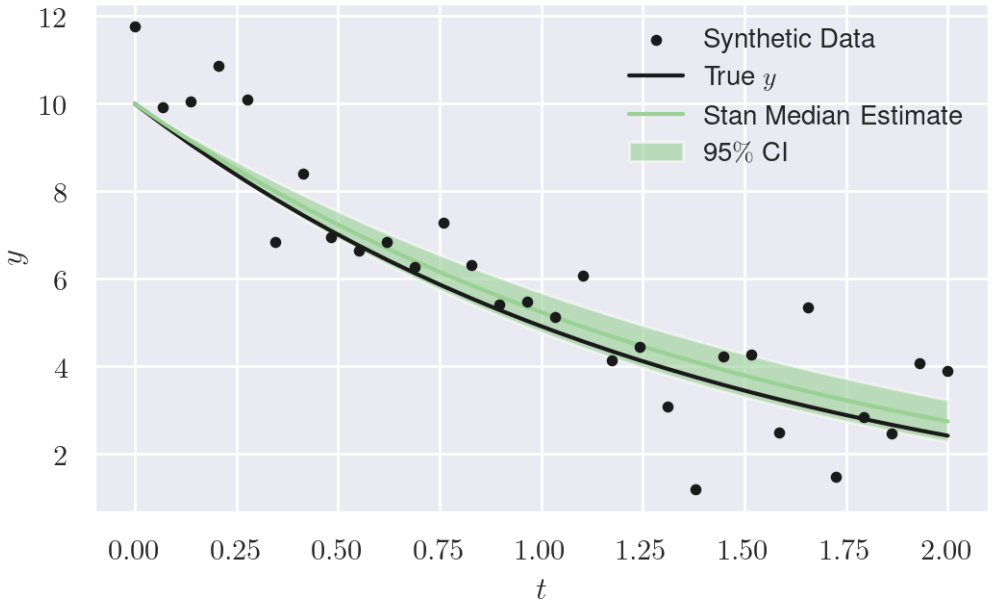

Figure C.4: Bayesian approximation of synthetic data generated using the system described by eq. (A.4).

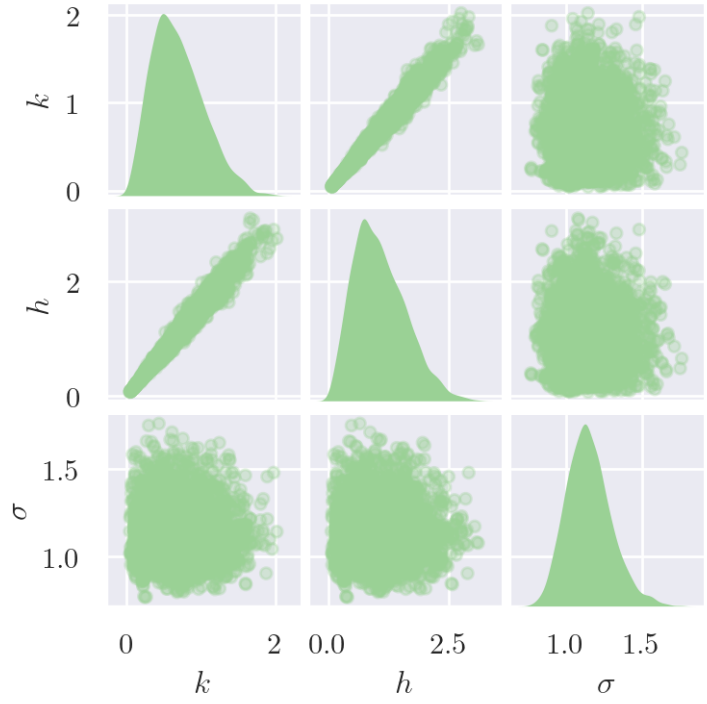

Figure C.5: Scatter matrix plot of parameter samples for the Bayesian approximation of the system described by eq. (A.4).

the initial prior distributions, suggesting a lot of uncertainty in the posterior estimates. We have chosen ground truth values that sit at the tail of the prior, and hence we also run a Bayesian approximation with values nearer the peaks in the prior distributions (see Figure C.7). We find that although the peaks of the posterior distributions appear to align with the ground truth values, the width of the posterior distributions have not narrowed from the prior suggesting the fit is led by the prior rather than the data. We also still see the strong correlation in the scatter matrix which indicates a problem with the estimates. In this case, the structural unidentifiability is visible in the Bayesian Inference and for this simple case, a possible reparameterization could be inferred from the correlation between k and h in the scatter plot matrix.

C.2.3 Locally identifiable case

The remaining case to consider was the system given by eq. (A.7) which we found to be structurally locally identifiable with up to 2 solutions. We try fitting in Stan for synthetic data with low noise and see that although the model trajectory gives a qualitatively good fit against the true curve (Figure C.8), we see similar strong relationships between parameters as we did in the unidentifiable case (Figure C.9). Additionally in Figure C.10, we see bimodal distributions in the posterior distributions for k, h and x_0 that correspond to the algebraic solutions we found in the identifiability analysis. Here, the medians and means are misleading due to the bimodal distributions. The trace plots of the estimates also show some problems, as they appear to be stuck in places, suggesting that the Markov chains may have not reached convergence, likely due to shifting between two peaks.

Adding noise to this model and rerunning the fit shows that the bimodal distributions disappear from the posterior distributions and the trace plots appear to resemble Markov chains signifying convergence (Figure C.11), implying that sufficient noise on data can hide identifiability issues. In Figure C.12, the relationships are still visible within the scatterplot, but it has already become more difficult to infer the algebraic relationships between the parameters from visualising alone.

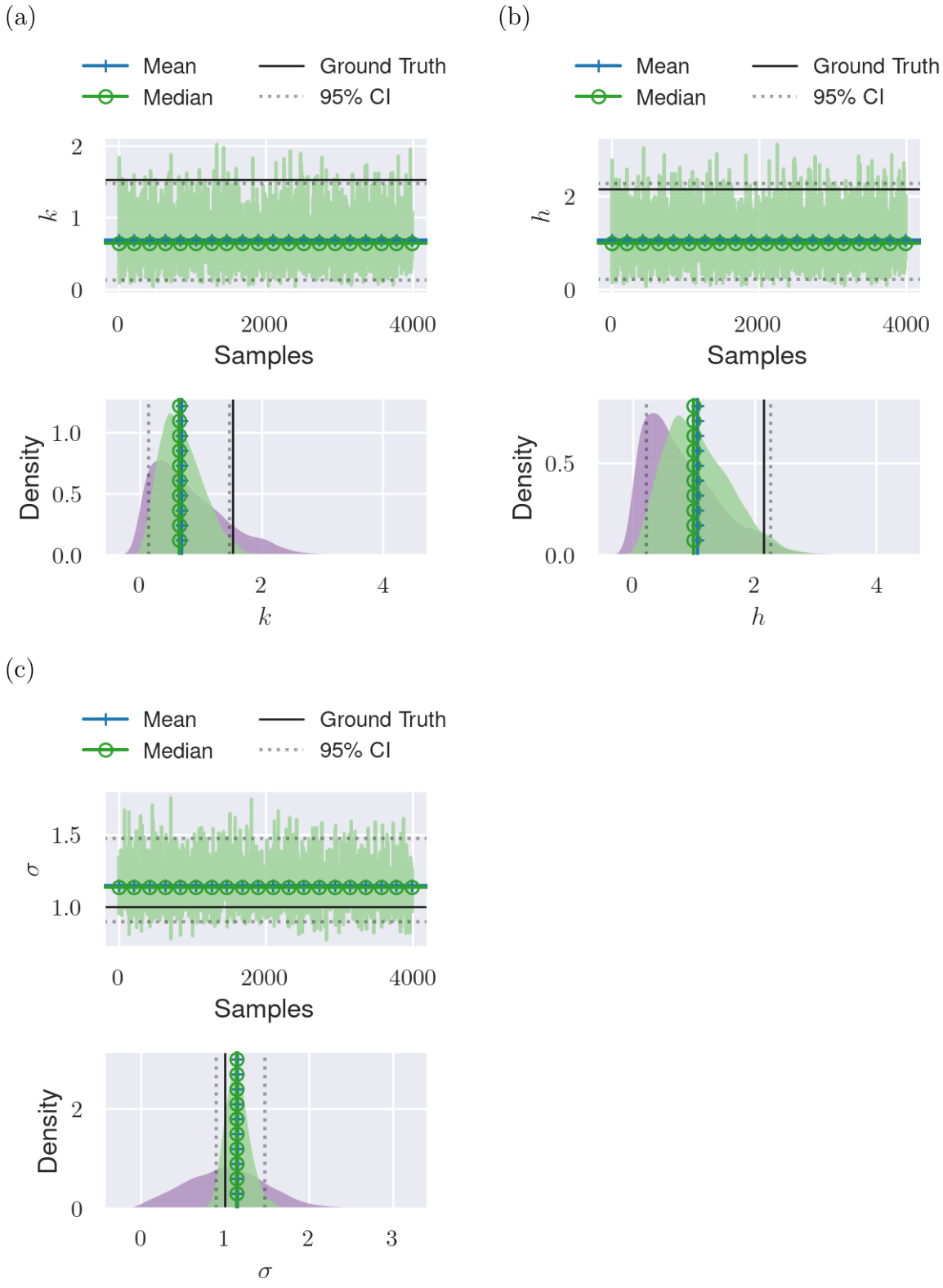

Figure C.6: Trace, prior distributions and posterior distributions of model parameters for the Bayesian approximation of the system described by eq. (A.4) where true values were chosen in the tails of the prior distributions: (a) for model parameter k, (b) for model parameter h, (c) noise parameter σ.

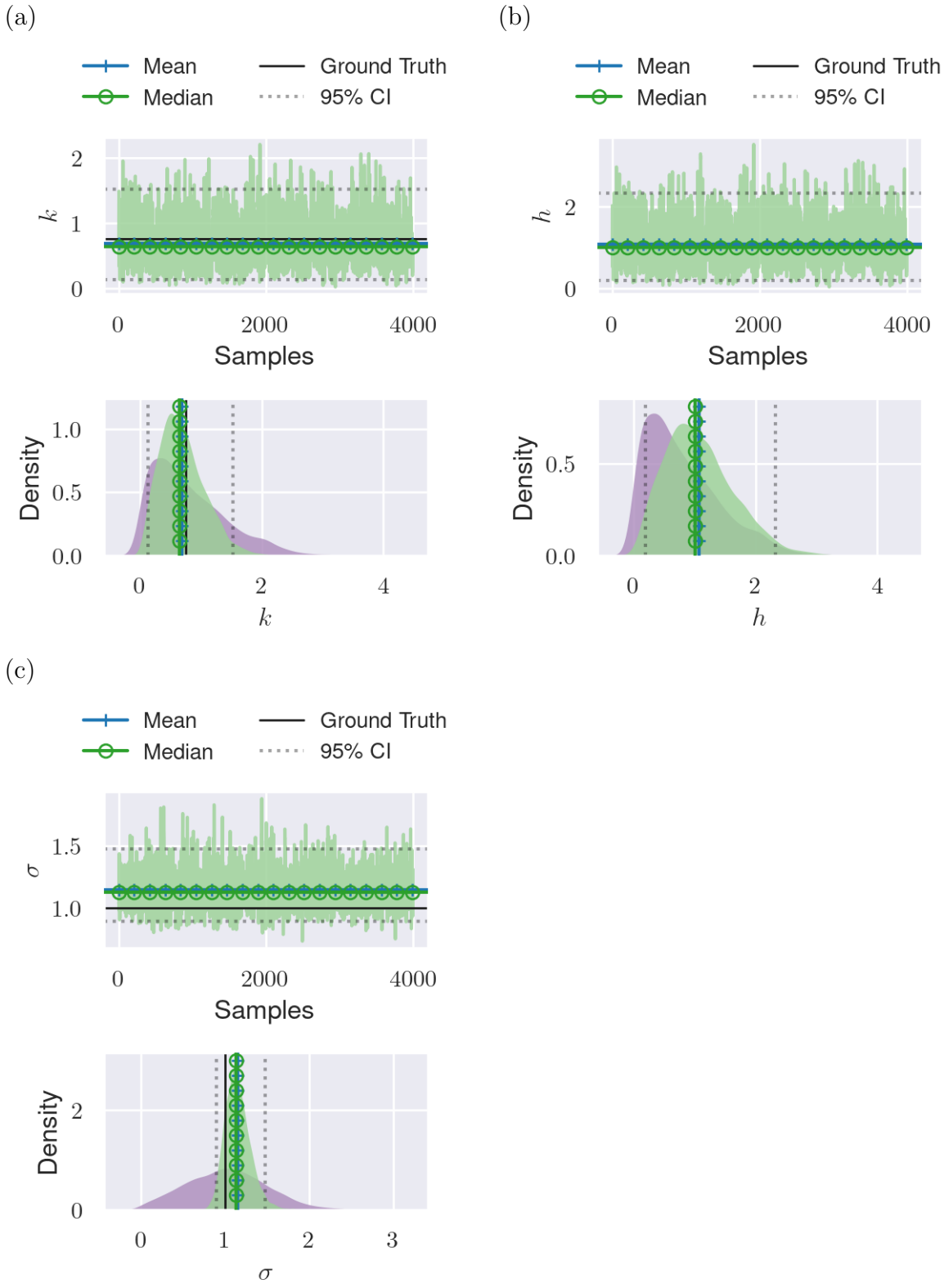

Figure C.7: Trace, prior distributions and posterior distributions of model parameters for the Bayesian approximation of the system described by eq. (A.4) where true values were chosen in the centre of the prior distributions: (a) for model parameter k, (b) for model parameter h, (c) noise parameter σ.

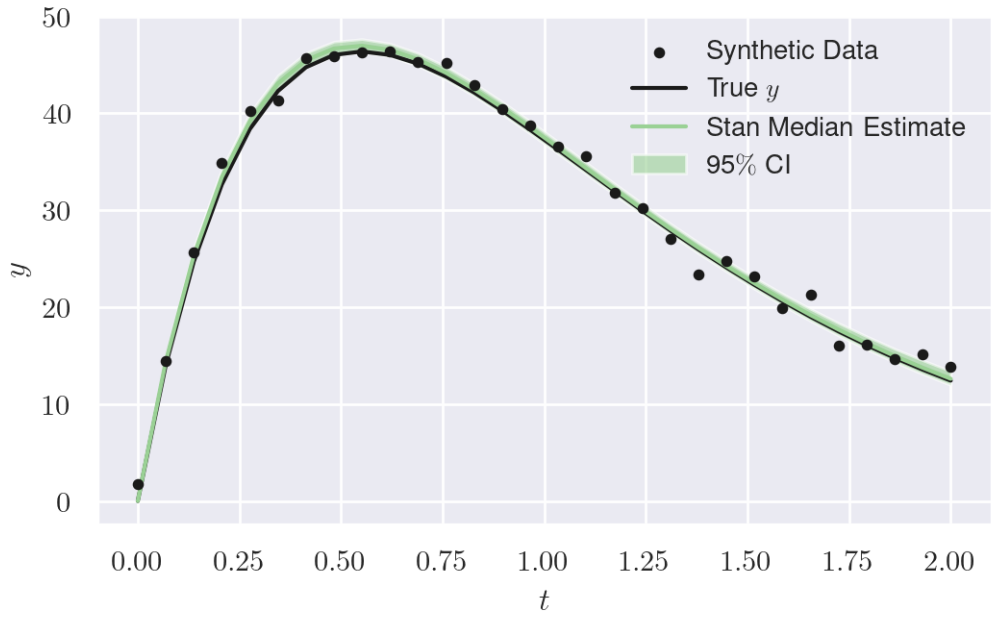

Figure C.8: Bayesian approximation of synthetic data generated using the system described by eq. (A.7).

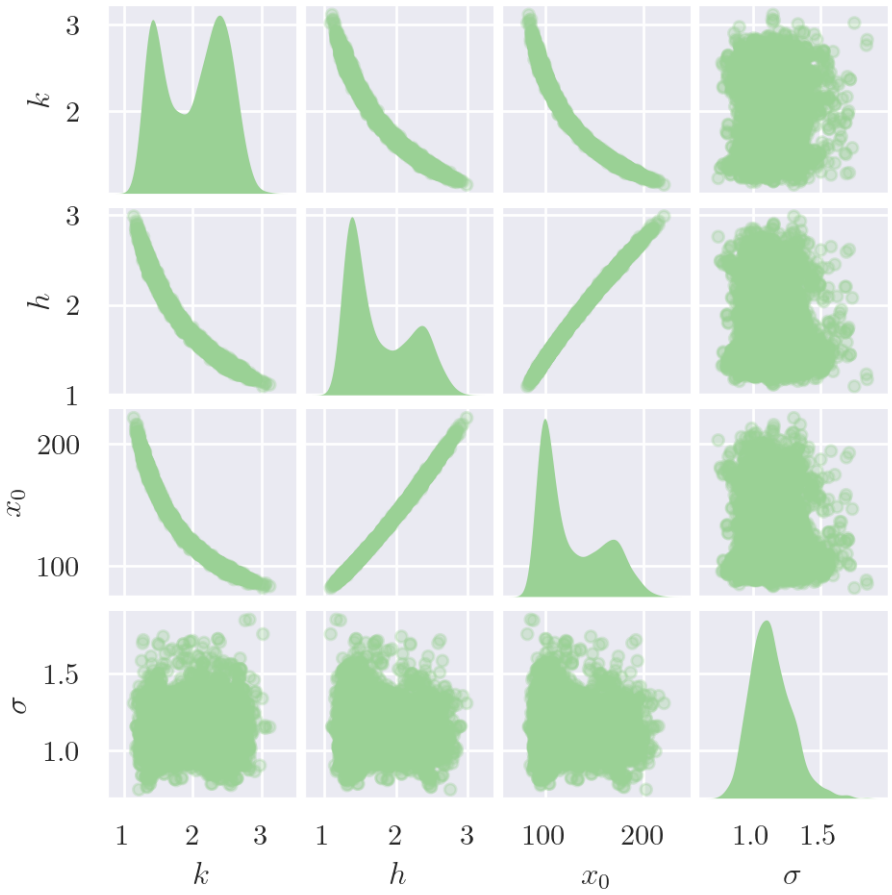

Figure C.9: Scatter matrix plot of parameter samples for the Bayesian approximation of the system described by eq. (A.7).

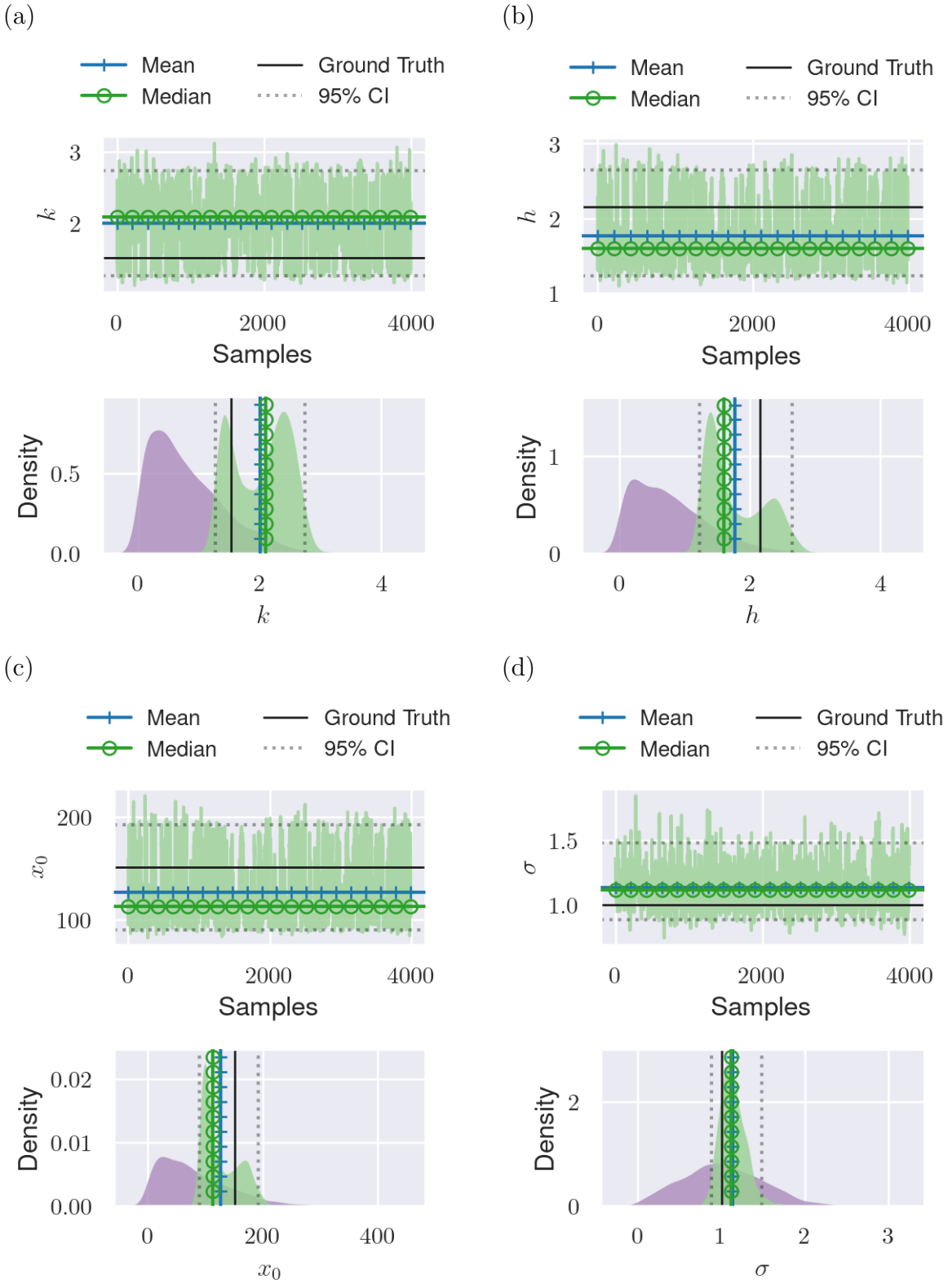

Figure C.10: Trace, prior distributions and posterior distributions of model parameters for the Bayesian approximation of the system described by eq. (A.7): (a) for model parameter k, (b) for model parameter h, (c) for unknown initial condition x_0, (d) noise parameter σ.

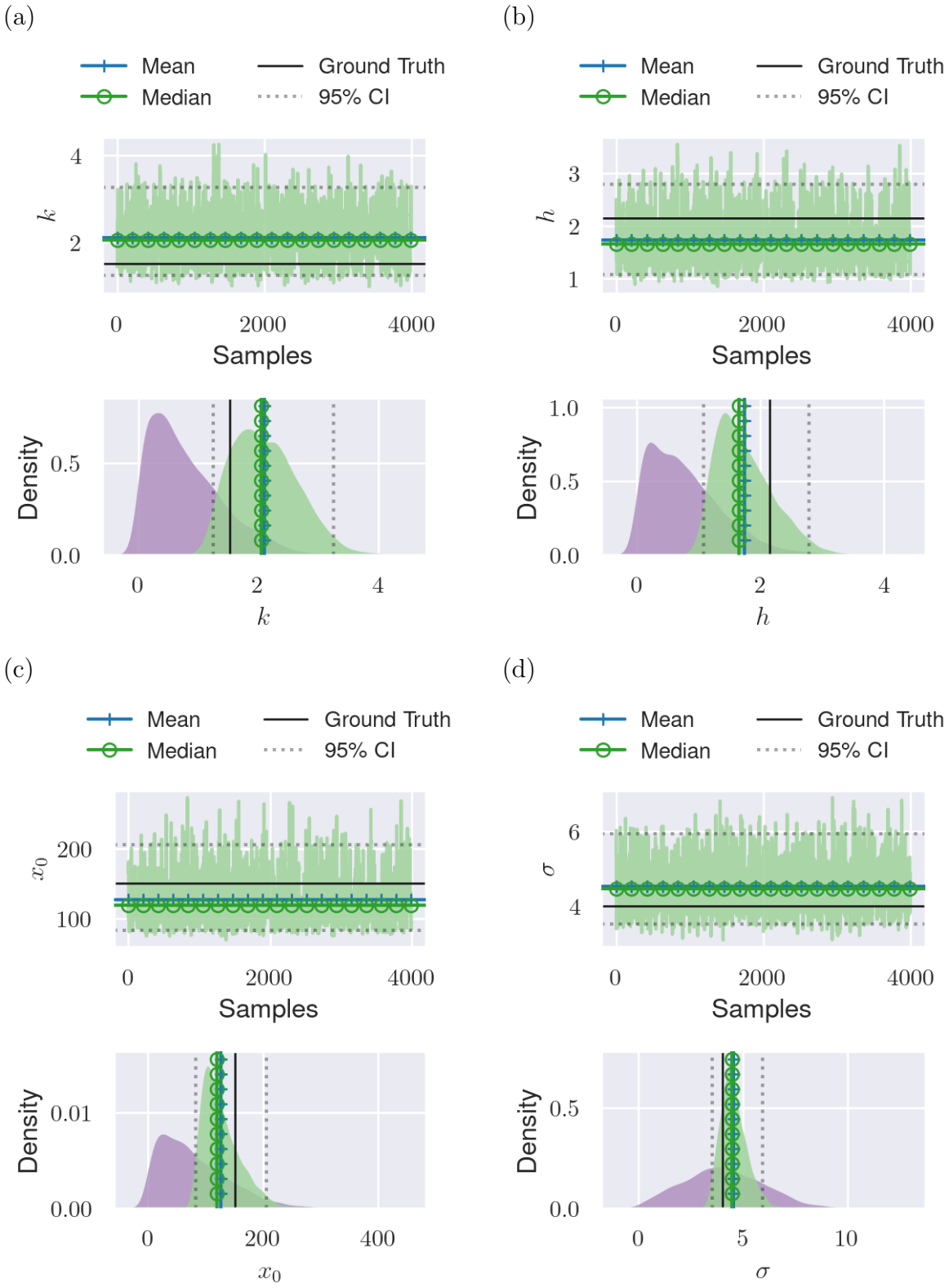

Figure C.11: Trace, prior distributions and posterior distributions of model parameters for the Bayesian approximation of the system described by eq. (A.7) when noise on the generated synthetic data has been increased: (a) for model parameter k, (b) for model parameter h, (c) for unknown initial condition x_0, (d) noise parameter σ.

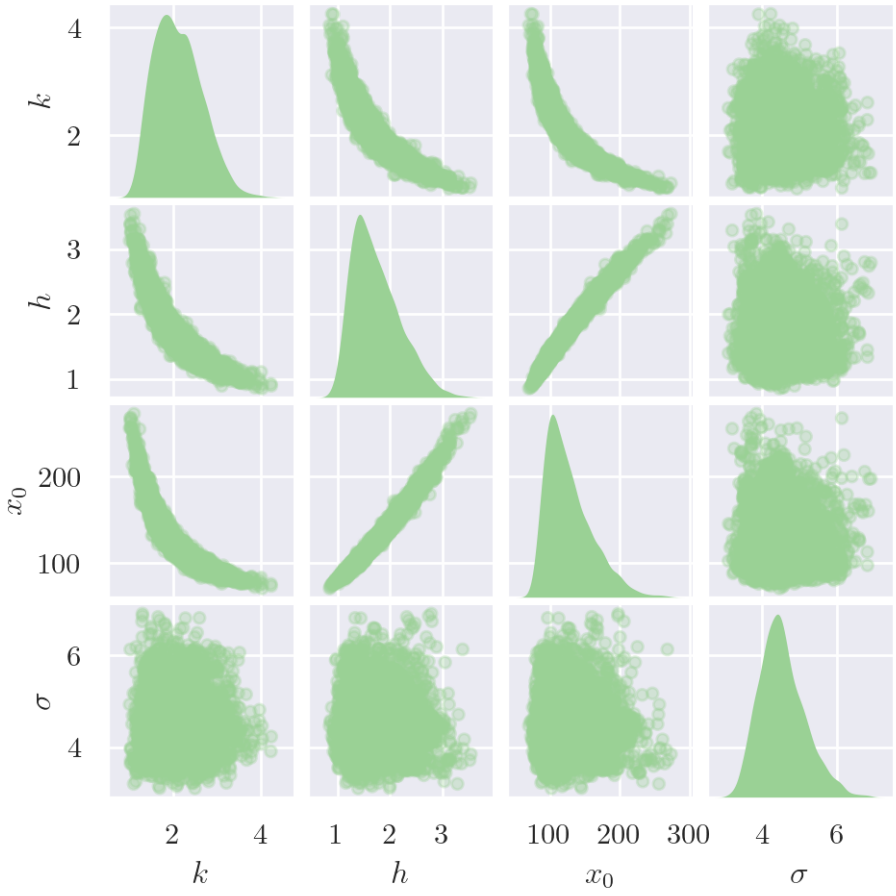

Figure C.12: Scatter matrix plot of parameter samples for the Bayesian approximation of the system described by eq. (A.7) when noise on the generated synthetic data has been increased.

APPENDIX D

ADDITIONAL RESULTS FROM BAYESIAN INFERENCE

D.1 The CIV$^+$ model

The trace, prior and posterior distribution of the model parameters when treating the noise parameter σ as known is shown in Figure D.1.

D.2 The CIV$^-$ model

A scatter plot matrix of the posterior distribution of the model parameters when treating δ as known is shown in Figure D.2. The posterior distributions are unchanged compared to when δ is included as a parameter to be fitted, which is expected as at high noise the model trajectory was insensitive to δ.

D.3 The BIV$^-$ model

We fit the BIV$^-$ model to synthetic data for [PD] time-resolution and Gaussian noise added (s.d. $100\,\mathrm{nmol\,L^{-1}}$) and the posterior distributions are shown in Figures D.3 and D.4.

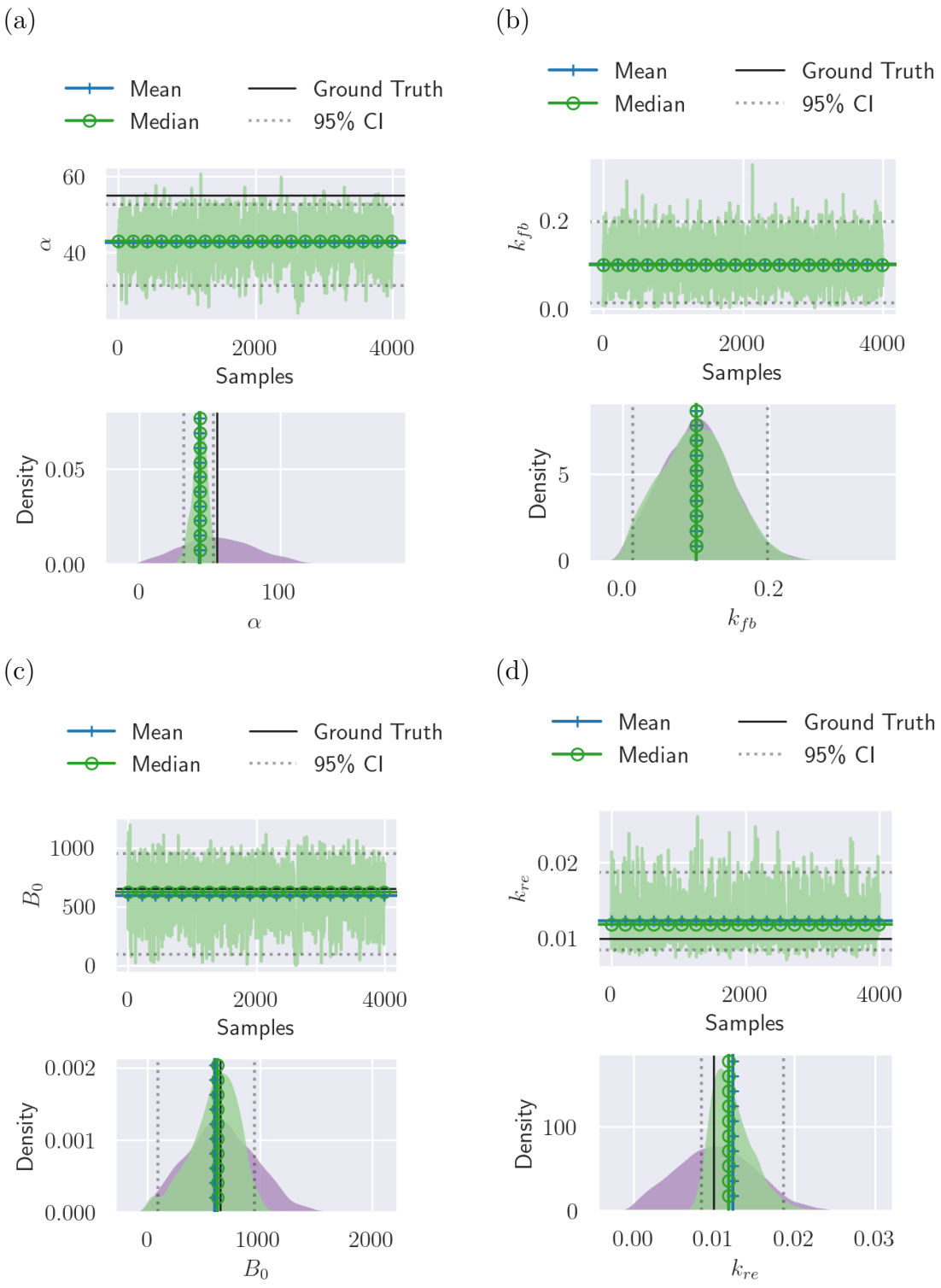

Figure D.1: Trace, prior distributions and posterior distributions of a selection of the model parameters for the Bayesian approximation of the CIV$^+$ model with Gaussian noise added (s.d. 100 nmol L^{-1}) when the noise parameter σ is treated as known: (a) α, (b) k_{fb}, (c) B_0, (d) k_{re}.

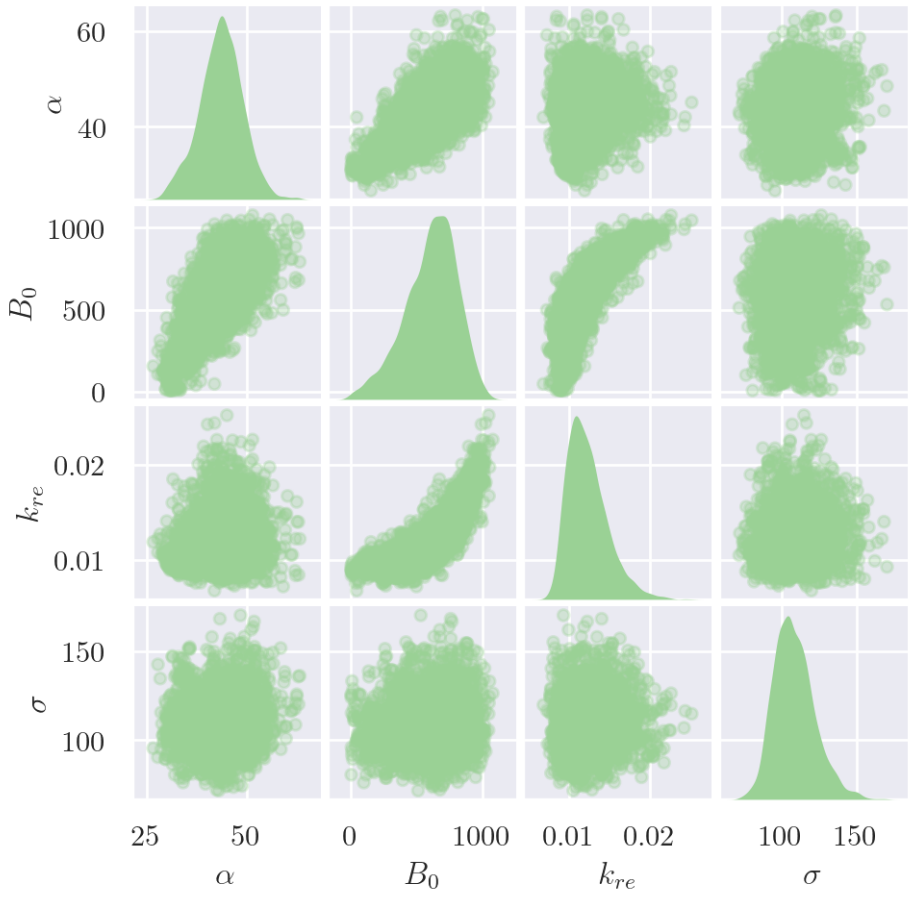

Figure D.2: Scatter plot matrix of parameter estimates for Bayesian approximation of synthetic data generated using the CIV^- model with Gaussian noise added (s.d. $100\,\text{nmol}\,\text{L}^{-1}$) when normal prior distributions are imposed and δ is treated as known.

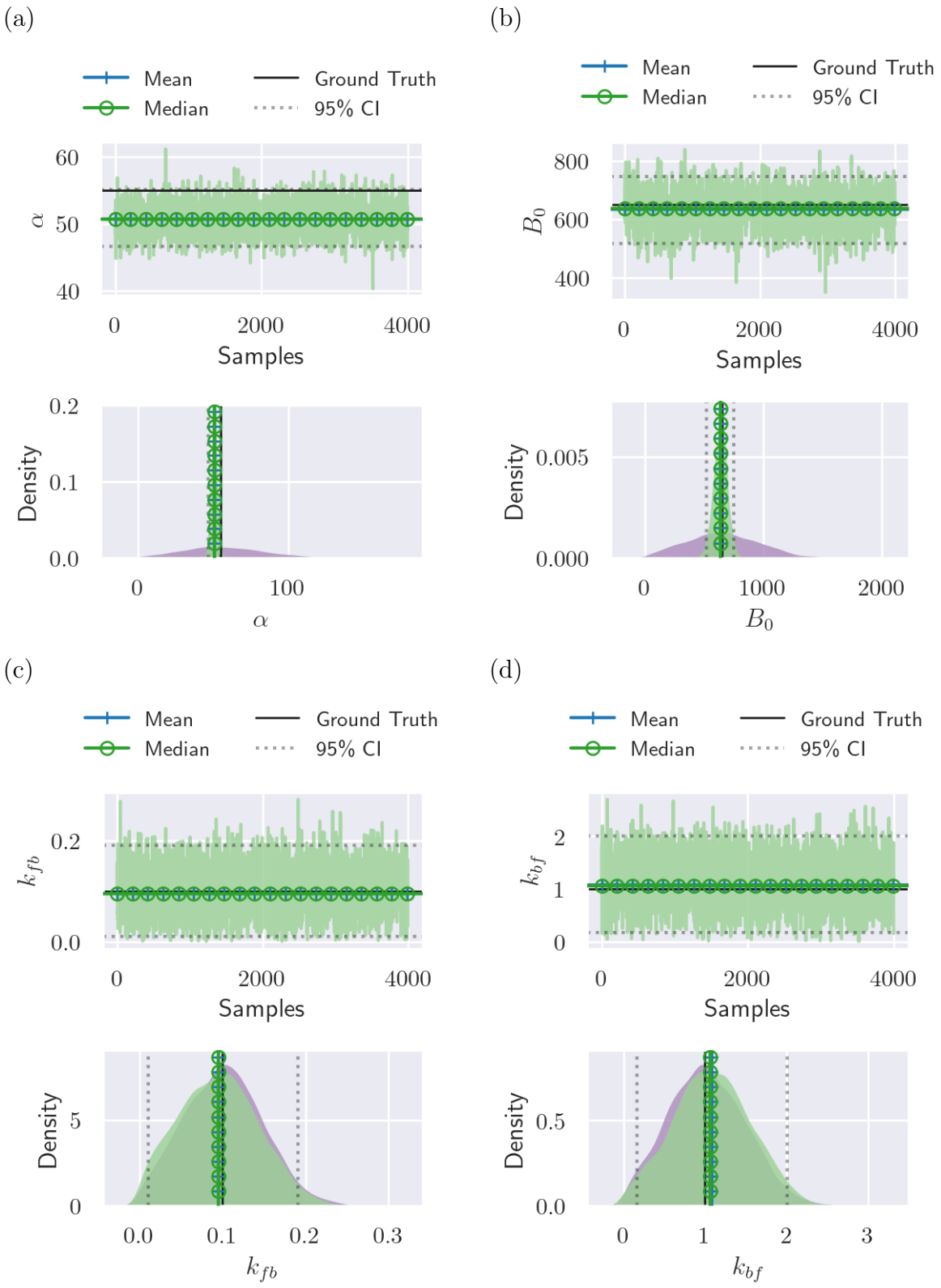

Figure D.3: Trace, prior distributions and posterior distributions of model parameters for the Bayesian approximation of the BIV$^-$ model when a normal prior is imposed: (a) for dilution factor α, (b) for physiological level of binding protein B_0, (c) for binding rate k_{fb}, (d) for unbinding rate k_{bf}.

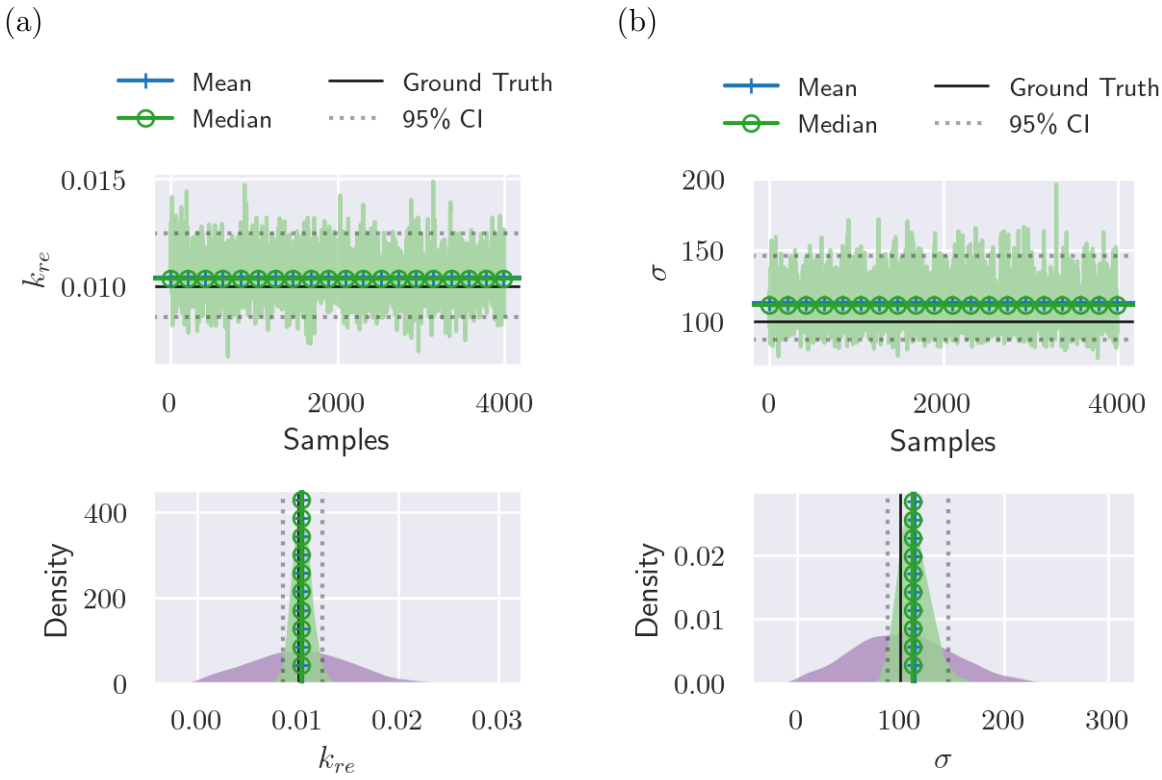

Figure D.4: Trace, prior distributions and posterior distributions of model parameters for the Bayesian approximation of the BIV$^-$ model when a normal prior is imposed: (a) for free cortisol clearance rate k_{re}, (b) for noise parameter σ.

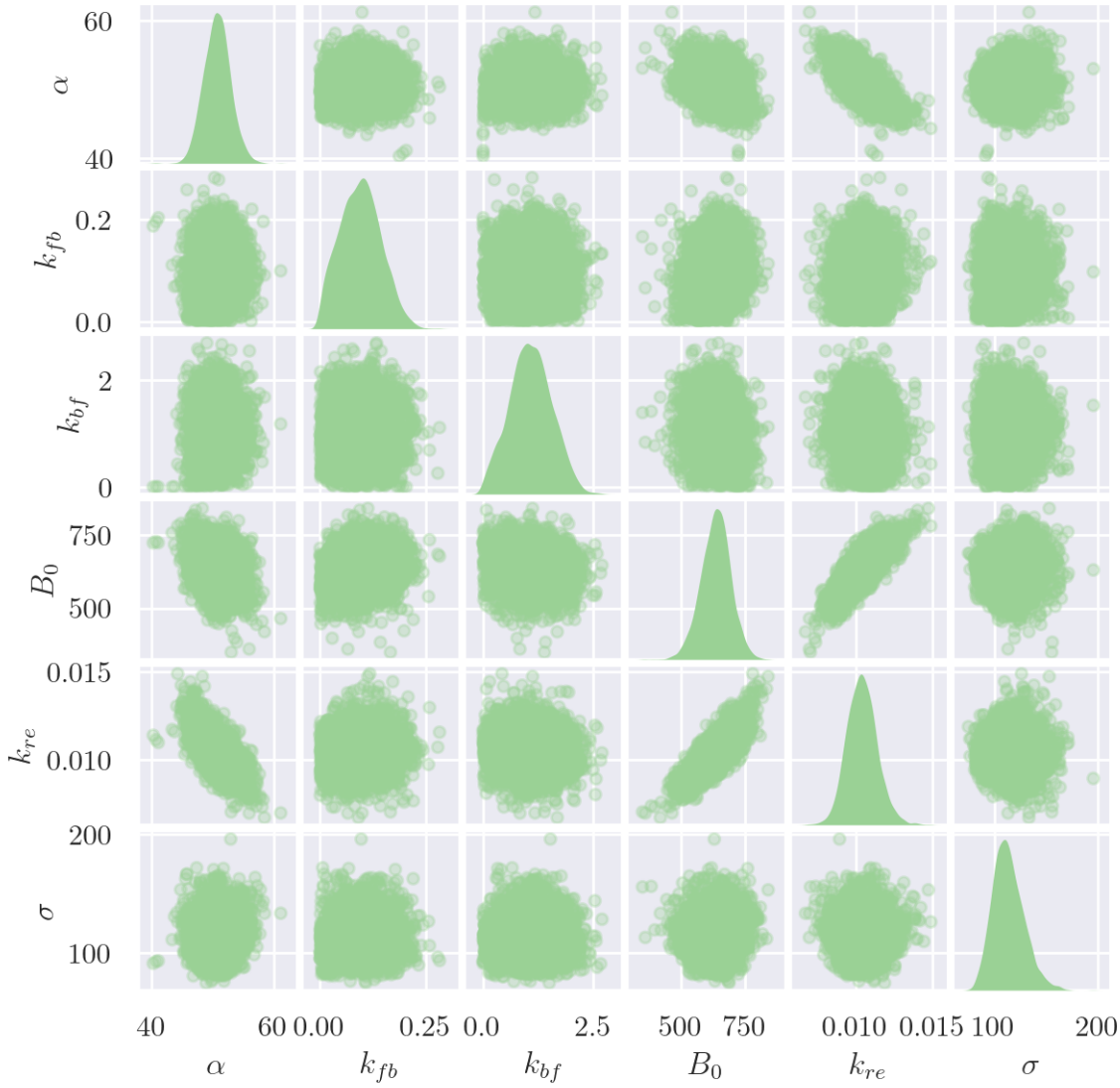

Figure D.5: Scatter plot matrix of parameter estimates for Bayesian approximation of synthetic data generated using the BIV^{-} when normal prior distributions are imposed.

APPENDIX E

POTENTIAL MODEL EXTENSIONS

E.1 Model Extensions

E.1.1 Incorporating a non-zero initial level of cortisol

We have carried out an initial assessment of the practical identifiability of the extended CIV model with a non-zero initial level of cortisol incorporated given by eqs. (2.57) and (2.58). Again using a frequentist approach, results in Figure E.1 show the loss function behaviour for varying pairs of model parameters.

E.1.2 Other Binding Proteins

Binding to albumin could also be considered to ascertain whether the overshoot in the CIV data can be obtained without the incorporation of an additional ODE accounting for a removal enzyme. Cortisol has a much higher affinity to bind with CBG however albumin has a much higher capacity, therefore this may become relevant when patients receive an intravenous bolus dose of cortisol when CBG may become saturated [12].

The ODE system for modelling cortisol delivery when considering binding to both CBG and albumin, denoted by B^C and B^A respectively, is defined by eqs. (E.1) and (E.3). The binding and unbinding rates are given by k_{fb}^C and k_{bf}^C respectively for CBG and k_{fb}^A and k_{bf}^A respectively for albumin. The physiological level of CBG and albumin is denoted by

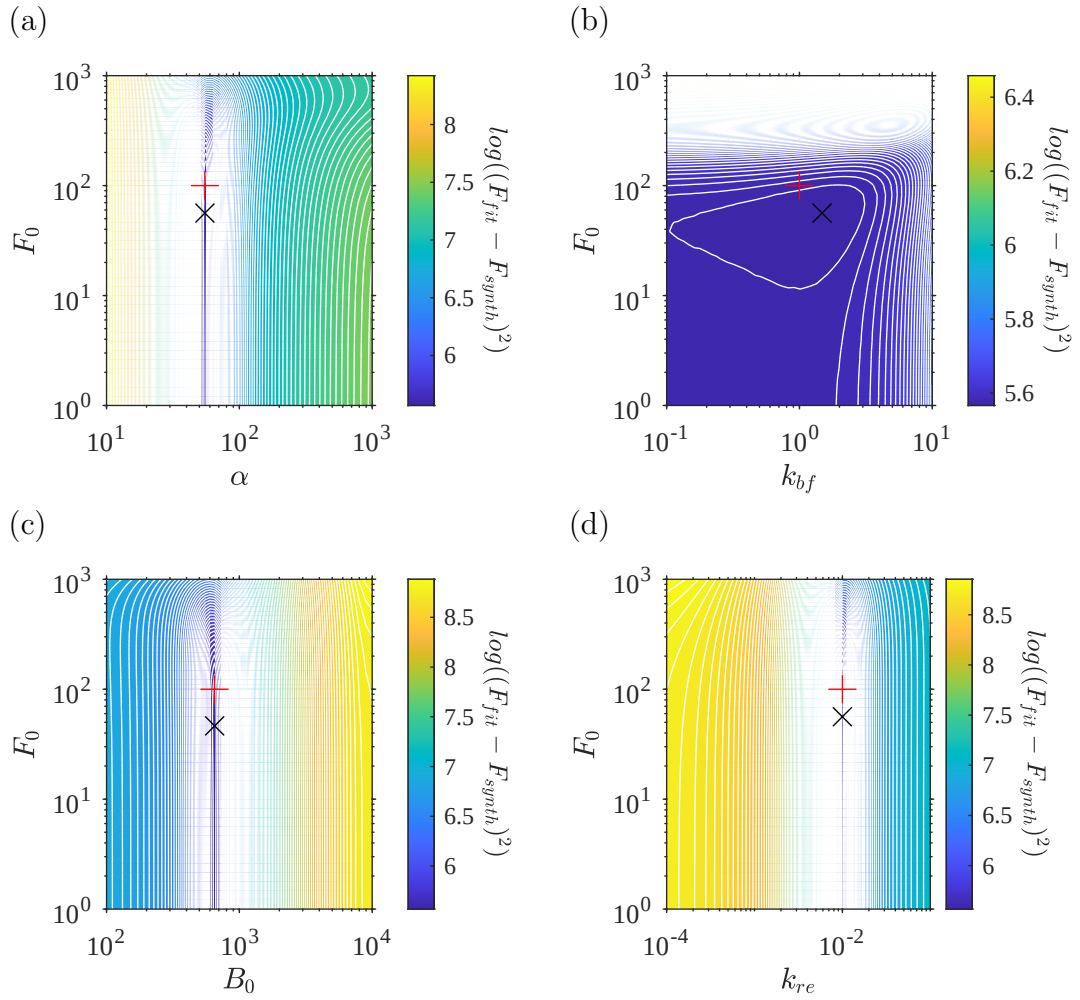

Figure E.1: Loss function for varying pairs of model parameters for the extended CIV model with Gaussian noise added (s.d. 100 nmol L^{-1}) and sampling time frequency corresponding to the time points used in data [PD]. The red plus indicates the true parameter value pair, while the loss function numerical minimum are shown with a black cross: (a) α versus F_0, (b) k_{bf} versus F_0, (c) B_0 versus F_0, (d) k_{re} versus F_0.

B_0^C and B_0^A respectively.

$$\frac{dF_f}{dt} = \alpha q(t) - k_{fb}^C F_f B^C + k_{bf}^C (B_0^C - B^C) \; - k_{fb}^A F_f B^A + k_{bf}^A (B_0^A - B^A) - k_{re} F_f, \quad \text{(E.1)}$$

$$\frac{dB^C}{dt} = \qquad - k_{fb}^C F_f B^C + k_{bf}^C (B_0^C - B^C), \quad \text{(E.2)}$$

$$\frac{dB^A}{dt} = \qquad\qquad\qquad\qquad - k_{fb}^A F_f B^A + k_{bf}^C (B_0^A - B^A), \quad \text{(E.3)}$$

with initial conditions $F_f = 0, B^C(0) = B_0^C, B^A(0) = B_0^A$.

This model has 3 variables (B now split into B^C and B^A) and 8 parameters compared to 2 variables and 5 parameters in the original model ***(reword)***.

E.1.3 Alternative Removal

Returning to our full ODE system given by eqs. (2.4) and (2.5), we currently have a pair of ODEs with 5 parameters to fit to data.

From inspection of the data, the CIV cortisol levels in Figure 1.3(a) seem to peak at around five hours before coming down to a slightly lower equilibrium level. The existence of this peak implies implies that there may be some upregulation of cortisol removal over 24 hours. A linear removal model (i.e., where the removal rate, k_{re}, is constant) is able to rise to the peak but then stays at this increased level for the rest of time. We also note that this removal term has the form of exponential decay in the BIV case, whereas the data in Figure 1.3(c) appears more linear.

We therefore consider introducing an additional variable, H, which accounts for an enzyme that binds and removes cortisol from the system. We anticipate that more enzyme is produced in response to higher free cortisol concentrations, but on a slower timescale in order to describe the upregulation of cortisol removal, motivating the model,

$$\frac{dE}{dt} = Q(F_f) - k_0 E, \quad \text{(E.4)}$$

where,

$$Q(F_f) = Q_{min} + \frac{(Q_{max} - Q_{min})F_f}{\tilde{F}_f + F_f}, \tag{E.5}$$

and the enzyme degrades at a rate k_0. Therefore, when there is very little free cortisol, production of the removal enzyme is at a some minimum rate Q_{min}. When free cortisol levels are very high, this production rate reaches a maximum rate Q_{max}. Additionally, $\tilde{F}_f$ is the value of free cortisol such that the production rate is at the midpoint between Q_{min} and Q_{max}, i.e., $Q(\tilde{F}_f) = (Q_{min} + Q_{max})/2$. We consider three specific cases of fixed F_f to demonstrate the behaviour of variable E (shown in Figure E.2). When there is very little free cortisol, we find:

$$\frac{dE}{dt} \approx Q_{min} - k_0 E, \tag{E.6}$$

hence over time, $E \to \frac{Q_{min}}{k_0}$. When $F_f = \tilde{F}_f$:

$$\frac{dE}{dt} = \frac{Q_{min} + Q_{max}}{2} - k_0 H, \tag{E.7}$$

hence $E \to \frac{Q_{min}+Q_{max}}{2k_0}$ as $t \to \infty$. Finally, when $F_f \gg \tilde{F}_f$:

$$\frac{dE}{dt} \approx Q_{max} - k_0 E, \tag{E.8}$$

therefore the amount of removal enzyme is bounded by $\frac{Q_{max}}{k_0}$.

Another refinement to the model which may explain the peak in the CIV data is to adapt the removal term in the ODE for F_f to account for this dependence on the amount

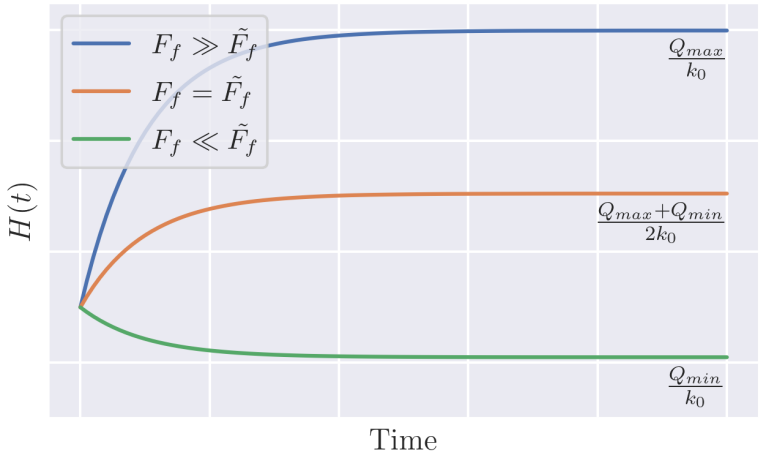

Figure E.2: Schematic of the dynamics of E for updated model over time under three different clamped levels of cortisol.

of removal enzyme. This creates the following system,

$$\frac{dF_f}{dt} = \alpha q(t) - k_{fb}F_f B + k_{bf}(B_0 - B) - k_{re}\frac{EF_f}{K_m + F_f}, \tag{E.9}$$

$$\frac{dB}{dt} = -k_{fb}F_f B + k_{bf}(B_0 - B), \tag{E.10}$$

$$\frac{dE}{dt} = Q_{min} + \frac{(Q_{max} - Q_{min})F_f}{\tilde{F}_f + F_f} - k_0 E, \tag{E.11}$$

with initial conditions,

$$F_f(0) = 0, \qquad B(0) = B_0, \qquad E(0) = E_0. \tag{E.12}$$

Here, E_0 is some initial physiological level of removal enzyme. We see that when there is little free cortisol, removal is also very small; when free cortisol levels are very high, the removal is bounded by the value of E. We also have a parameter K_m, which is the value of free cortisol such that removal is half its maximum for some level of E, i.e., $-k_{re}\frac{E}{2}$.

There are now 11 parameters to fit ($\alpha, k_{fb}, k_{bf}, k_{re}, Q_{min}, Q_{max}, k_0, K_m, \tilde{F}_f, B_0, E_0$) and another unobserved compartment, E, which increases the complexity of the model. One thing we note is that our data only has one observable, which raises potential issues with identifiability. There may be multiple or even infinite parameter sets that fit the data

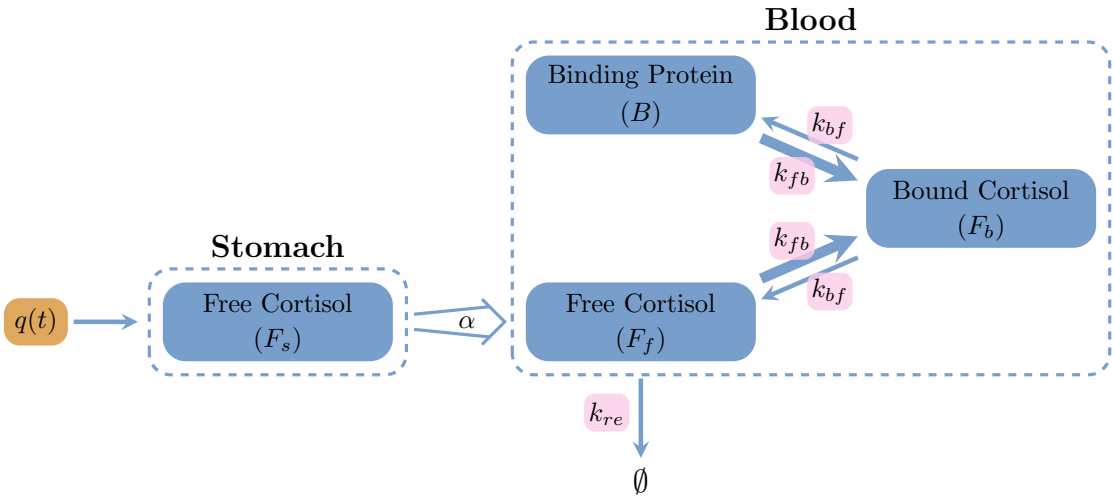

Figure E.3: Two-compartment model of hydrocortisone delivery with an additional stomach compartment to reflect oral dosing.

equally well. We would like to assess the reliability of the parameter estimates in a model with this level of complexity.

E.1.4 Additional Stomach Compartment

The model for oral dosing is shown schematically in Figure E.3. There is an additional variable, F_s, which represents free cortisol in the stomach compartment, and a rate, k_{abs}, for absorption from the stomach into the bloodstream.

This gives the ODE system,

$$\frac{dF_s}{dt} = q(t) - k_{abs}F_s, \tag{E.13}$$

$$\frac{dF_f}{dt} = \alpha k_{abs}F_s \quad - k_{fb}F_f B + k_{bf}(B_0 - B) - k_{re}F_f, \tag{E.14}$$

$$\frac{dB}{dt} = \quad - k_{fb}F_f B + k_{bf}(B_0 - B), \tag{E.15}$$

with initial conditions $F_s(0) = F_f(0) = 0, B(0) = B_0$.

E.1.5 Additional Muscle Tissue Compartment

The previous models ignore transfer of free cortisol into muscle tissue. We would like to assess the effect of neglecting this by formulating a model with an additional peripheral compartment. Melin *et al.* [70] found that adding a peripheral compartment allowed for a better match against the patient data compared to a one-compartment model. Additionally, a model by Lee *et al.* [16] aimed to tune a cortisol sensor by considering transport into adipose, brain and muscle distinctly and modelling both free and bound cortisol in each. Cortisol is used for different processes within different parts of the body, therefore the ability to measure these distinctly and continuously would allow dosages to be tweaked and fitted to a specific individuals quicker and more precisely.

For simplicity, we consider just one collective peripheral compartment, however this could be divided to account for different rates of transfer into muscle and other tissue types. Denoting free cortisol being taken up by muscle tissue as F_m, we introduce 3 new parameters: a dilution factor, γ, to account for the change in volume between blood and muscle tissue, and rates of conversion from blood to muscle and back, k_{fm} and k_{mf} respectively. Combining this with the original system given by eqs. (2.4) and (2.5) gives the following model:

$$\frac{dF_f}{dt} = \alpha q(t) - k_{fb}F_f B + k_{bf}(B_0 - B) - \quad k_{fm}F_f + \frac{1}{\gamma}k_{mf}F_m - k_{re}F_f, \tag{E.16}$$

$$\frac{dB}{dt} = \qquad - k_{fb}F_f B + k_{bf}(B_0 - B), \tag{E.17}$$

$$\frac{dF_m}{dt} = \qquad\qquad\qquad\qquad + \gamma k_{fm}F_f - \quad k_{mf}F_m, \tag{E.18}$$

with initial conditions $F_f(0) = F_m(0) = 0, B(0) = B_0$. We are able to eliminate the

Table E.1: Model Variables

Variable	
F	Total cortisol
F_f	Free cortisol
F_b	Bound cortisol
F_m	Muscle free cortisol
F_s	Stomach free cortisol
B	Binding protein (unoccupied)
B^A	Albumin (unoccupied)
B^C	Corticosteroid-binding globulin (CBG) (unoccupied)
E	Cortisol removal enzyme

dilution factor γ in this case by rescaling. Setting $F_m = \gamma \bar{F}_m$, the system becomes:

$$\frac{dF_f}{dt} = \alpha q(t) - k_{fb}F_f B + k_{bf}(B_0 - B) \; - k_{fm}F_f + k_{mf}\bar{F}_m - k_{re}F_f, \tag{E.19}$$

$$\frac{dB}{dt} = \qquad - k_{fb}F_f B + k_{bf}(B_0 - B), \tag{E.20}$$

$$\frac{d\bar{F}_m}{dt} = \qquad\qquad\qquad\qquad + k_{fm}F_f - k_{mf}\bar{F}_m. \tag{E.21}$$

and we subsequently drop the bars.

Table E.2: Model Parameters

Parameter	
	One-Compartment Model
α	Blood dilution factor
k_{fb}	Binding rate
k_{bf}	Unbinding rate
B_0	Physiological level of binding protein
k_{re}	Removal rate
	Non-zero Initial Cortisol Model
F_{f0}	Initial level of free cortisol
F_{b0}	Initial level of bound cortisol
F_0	Initial level of total cortisol
	Albumin Model
k_{fb}^C	CBG binding rate
k_{bf}^C	CBG unbinding rate
B_0^C	Physiological level of CBG
k_{fb}^A	Albumin binding rate
k_{bf}^A	Albumin unbinding rate
B_0^A	Physiological level of albumin
	Alternative Removal Model
Q_{min}	Enzyme minimal production rate
Q_{max}	Enzyme maximum production rate
$\tilde{F}_f$	Mid-point enzyme production level of free cortisol
K_m	Mid-point removal level of free cortisol
k_0	Enzyme degradation rate
E_0	Physiological level of cortisol removal enzyme
	Stomach Model
k_{abs}	Stomach to blood absorption rate
	Muscle Tissue Model
k_{fm}	Blood to muscle conversion rate
k_{mf}	Muscle to blood conversion rate
γ	Muscle to blood dilution factor

LIST OF REFERENCES

[1] A Prete, AE Taylor, I Bancos, DJ Smith, MA Foster, S Kohler, V Fazal-Sanderson, J Komninos, DM O'Neil, DA Vassiliadi, CJ Mowatt, R Mihai, JL Fallowfield, D Annane, JM Lord, BG Keevil, JAH Wass, N Karavitaki, and W Arlt. Prevention of adrenal crisis: cortisol responses to major stress compared to stress dose hydrocortisone delivery. *J. Clin. Endocrin. Metab.*, 03 2020. https://doi.org/10.1210/clinem/dgaa133.

[2] W Arlt and B Allolio. Adrenal insufficiency. *Lancet*, 361(9372):1881–1893, 2003. https://doi.org/10.1016/s0140-6736(03)13492-7.

[3] NC Nicolaides, GP Chrousos, and E Charmandari. Adrenal insufficiency. In KR Feingold, B Anawalt, A Boyce, G Chrousos, WW de Herder, K Dhatariya, K Dungan, A Grossman, JM Hershman, J Hofland, S Kalra, G Kaltsas, C Koch, P Kopp, M Korbonits, CS Kovacs, W Kuohung, B Laferrère, EA McGee, R McLachlan, JE Morley, M New, J Purnell, R Sahay, F Singer, CA Stratakis, DL Trence, and DP Wilson, editors, *Adrenal disease and function*. Endotext, South Dartmouth, MA, 2017. https://www.ncbi.nlm.nih.gov/books/NBK279083/.

[4] EN Brown, PM Meehan, and AP Dempster. A stochastic differential equation model of diurnal cortisol patterns. *Am. J. Physiol. Endocrinol. Metab.*, 280(3):E450–E461, 2001. https://doi.org/10.1152/ajpendo.2001.280.3.E450.

[5] R Megha, CJ Wehrle, S Kashyap, and SW Leslie. Anatomy, abdomen and pelvis, adrenal glands (suprarenal glands). *StatPearls [Internet]*, 2020. https://www.ncbi.nlm.nih.gov/books/NBK482264/.

[6] CG Brook and NJ Marshall. *Essential endocrinology*. Blackwell Publishing, 4th edition, 2001.

[7] E Zavala, KCA Wedgwood, M Voliotis, J Tabak, F Spiga, SL Lightman, and K Tsaneva-Atanasova. Mathematical modelling of endocrine systems. *Trends Endocrinol. Metab.*, 30(4):244–257, 2019. https://doi.org/10.1016/j.tem.2019.01.008.

[8] R Giordano, F Guaraldi, R Berardelli, I Karamouzis, V D'Angelo, C Zichi, S Grottoli, E Ghigo, and E Arvat. Dual-release hydrocortisone in addison's disease–a review of the literature. *Eur. Endocrinol.*, 10(1):75, 2014. http://doi.org/10.17925/EE.2014.10.01.75.

[9] E Charmandari, NC Nicolaides, and GP Chrousos. Adrenal insufficiency. *Lancet*, 383(9935):2152–2167, 2014. https://doi.org/10.1016/S0140-6736(13)61684-0.

[10] PC Hindmarsh and K Geertsma. Chapter 18 - glucocorticoid treatment. In PC Hindmarsh and K Geertsma, editors, *Congenital Adrenal Hyperplasia*, pages 211–218. Academic Press, 2017.

[11] CW Le Roux, GA Chapman, WM Kong, WS Dhillo, J Jones, and J Alaghband-Zadeh. Free cortisol index is better than serum total cortisol in determining hypothalamic-pituitary-adrenal status in patients undergoing surgery. *J. Clin. Endocrinol. Metab.*, 88(5):2045–2048, 2003. https://doi.org/10.1210/jc.2002-021532.

[12] GE Mattos, J Heinzmann, S Norkowski, J Helbling, AM Minni, M Moisan, and C Touma. Corticosteroid-binding globulin contributes to the neuroendocrine phenotype of mice selected for extremes in stress reactivity. *J. Endocrinol.*, 219(3):217–229, 2013. https://doi.org/10.1530/JOE-13-0255.

[13] N El-Farhan, DA Rees, and C Evans. Measuring cortisol in serum, urine and saliva–are our assays good enough? *Ann. Clin. Biochem.*, 54(3):308–322, 2017. https://doi.org/10.1177/0004563216687335.

[14] Ian Wallace, Sean Cunningham, and John Lindsay. The diagnosis and investigation of adrenal insufficiency in adults. *Ann. Clin. Biochem.*, 46(5):351–367, 2009. https://doi.org/10.1258/acb.2009.009101.

[15] K Bunte, DJ Smith, MJ Chappell, ZK Hassan-Smith, JW Tomlinson, W Arlt, and P Tiňo. Learning pharmacokinetic models for in vivo glucocorticoid activation. *J. Theor. Biol.*, 455:222–231, 2018. https://doi.org/10.1016/j.jtbi.2018.07.025.

[16] MA Lee, N Bakh, G Bisker, EN Brown, and MS Strano. A pharmacokinetic model of a tissue implantable cortisol sensor. *Adv. Healthc. Mater.*, 5(23):3004–3015, 2016. https://doi.org/10.1002/adhm.201600650.

[17] Y Lenbury and P Pornsawad. A delay-differential equation model of the feedback-controlled hypothalamus–pituitary–adrenal axis in humans. *Math. Med. Biol.*, 22(1):15–33, 2005. https://doi.org/10.1093/imammb/dqh020.

[18] N Bairagi, S Chatterjee, and J Chattopadhyay. Variability in the secretion of corticotropin-releasing hormone, adrenocorticotropic hormone and cortisol and understandability of the hypothalamic-pituitary-adrenal axis dynamics—a mathematical study based on clinical evidence. *Mathematical medicine and biology: a journal of the IMA*, 25(1):37–63, 2008. https://doi.org/10.1093/imammb/dqn003.

[19] W Arlt, SE Baldeweg, SHS Pearce, and HL Simpson. Endocrinology in the time of covid-19: management of adrenal insufficiency. *Eur. J. Endocrinol.*, 183(1):G25–G32, 2020. https://doi.org/10.1530/EJE-20-0361.

[20] M Debono, C Ghobadi, A Rostami-Hodjegan, H Huatan, MJ Campbell, J Newell-Price, K Darzy, DP Merke, W Arlt, and RJ Ross. Modified-release hydrocortisone to provide circadian cortisol profiles. *J. Clin. Endocrin. Metab.*, 94(5):1548–1554, 2009. https://doi.org/10.1210/jc.2008-2380.

[21] G Johannsson, AG Nilsson, R Bergthorsdottir, P Burman, P Dahlqvist, B Ekman, BE Engström, T Olsson, O Ragnarsson, M Ryberg, B Wahlberg, BMK Biller, JP Monson, PM Stewart, H Lennernäs, and S Skrtic. Improved cortisol exposure-time profile and outcome in patients with adrenal insufficiency: a prospective randomized trial of a novel hydrocortisone dual-release formulation. *J. Clin. Endocrin. Metab.*, 97(2):473–481, 2012. https://doi.org/10.1210/jc.2011-1926.

[22] Judith A Whitworth et al. Mechanisms of glucocorticoid–induced hypertension. *Kidney Int.*, 31(5):1213–1224, 1987. https://doi.org/10.1038/ki.1987.131.

[23] M Whitaker, M Debono, H Huatan, D Merke, W Arlt, and RJ Ross. An oral multiparticulate, modified-release, hydrocortisone replacement therapy that provides physiological cortisol exposure. *Clin. Endocrinol. (Oxf)*, 80(4):554–561, 2013. https://doi.org/10.1111/cen.12316.

[24] A Mallappa, N Sinaii, P Kumar, MJ Whitaker, L Daley, D Digweed, DJA Eckland, C Van Ryzin, LK Nieman, W Arlt, et al. A phase 2 study of chronocort, a modified-release formulation of hydrocortisone, in the treatment of adults with classic congenital adrenal hyperplasia. *J. Clin. Endocrin. Metab.*, 100(3):1137–1145, 2015. https://doi.org/10.1210/jc.2014-3809.

[25] AF Villaverde, ND Evans, MJ Chappell, and JR Banga. Input-dependent structural identifiability of nonlinear systems. *IEEE Control Syst. Lett.*, 3(2):272–277, 2018. https://doi.org/10.1109/LCSYS.2018.2868608.

[26] V Shivva, J Korell, IG Tucker, and SB Duffull. An approach for identifiability of population pharmacokinetic–pharmacodynamic models. *CPT: Pharmacomet. Syst. Pharmacol.*, 2(6):1–9, 2013.

[27] ND Evans, SYA Cheung, and JWT Yates. Structural identifiability for mathematical pharmacology: models of myelosuppression. *J Pharmacokinet. Pharmacodyn.*, 45:79–90, 2018.

[28] B Hochwald and A Nehorai. Identifiability in array processing models with vector-sensor applications. *IEEE Transactions on signal processing*, 44(1):83–95, 1996.

[29] M Anguelova. *Observability and identifiability of nonlinear systems with applications in biology*. Chalmers Tekniska Hogskola (Sweden), 2007.

[30] H Singhal and G Michailidis. Identifiability of flow distributions from link measurements with applications to computer networks. *Inverse Probl.*, 23(5):1821–1849, 2007.

[31] L Gibiansky and E Gibiansky. Target-mediated drug disposition model: approximations, identifiability of model parameters and applications to the population pharmacokinetic–pharmacodynamic modeling of biologics. *Expert Opin. Drug Metab. Toxicol.*, 5(7):803–812, 2009.

[32] H Miao, X Xia, AS Perelson, and H Wu. On identifiability of nonlinear ode models and applications in viral dynamics. *SIAM Review*, 53(1):3–39, 2011.

[33] DLI Janzén, M Jirstrand, MJ Chappell, and ND Evans. Three novel approaches to structural identifiability analysis in mixed-effects models. *Comput. Methods Programs Biomed.*, 171:141–152, 2019. https://doi.org/10.1016/j.cmpb.2016.04.024.

[34] RE Bellman and KJ Åström. On structural identifiability. *Math. Biosci.*, 7(3-4):329–339, 1970. https://doi.org/10.1016/0025-5564(70)90132-X.

[35] H Pohjanpalo. System identifiability based on the power series expansion of the solution. *Math. Biosci.*, 41(1-2):21–33, 1978. https://doi.org/10.1016/0025-5564(78)90063-9.

[36] AF Villaverde, A Barreiro, and A Papachristodoulou. Structural identifiability of dynamic systems biology models. *PLoS Comput. Biol.*, 12(10):e1005153, 2016. https://doi.org/10.1371/journal.pcbi.1005153.

[37] K Srinivasarengan, J Ragot, Christophe Aubrun, and D Maquin. An approach to parameter identifiability for a class of nonlinear models represented in lpv form. *arXiv preprint arXiv:2003.10297*, 2020.

[38] KR Godfrey. The identifiability of parameters of models used in biomedicine. *Math. Model.*, 7(9-12):1195–1214, 1986. https://www.sciencedirect.com/science/article/pii/027002558690076X.

[39] KR Godfrey and JJ DiStefano III. Identifiability of model parameters. *IFAC Proceedings Volumes*, 18(5):89–114, 1985. https://www.sciencedirect.com/science/article/pii/S1474667017605445.

[40] SV Chin and MJ Chappell. Structural identifiability and indistinguishability analyses of the minimal model and a euglycemic hyperinsulinemic clamp model for glucose–insulin dynamics. *Comput. Methods Programs Biomed.*, 104(2):120–134, 2011. https://www.sciencedirect.com/science/article/pii/S0169260710002233.

[41] RN Gunn, MJ Chappell, and VJ Cunningham. Reparameterisation of unidentifiable systems using the taylor series approach. *IFAC Proceedings Volumes*, 30(2):247–252, 1997. https://www.sciencedirect.com/science/article/pii/S1474667017445794.

[42] O Chis, JR Banga, and E Balsa-Canto. Structural identifiability of systems biology models: a critical comparison of methods. *PloS One*, 6(11):e27755, 2011. https://doi.org/10.1371/journal.pone.0027755.

[43] Hoon Hong, Alexey Ovchinnikov, Gleb Pogudin, and Chee Yap. Sian: software for structural identifiability analysis of ode models. *Bioinformatics*, 35(16):2873–2874, 2019. https://doi.org/10.1093/bioinformatics/bty1069.

[44] H Hong, A Ovchinnikov, G Pogudin, and C Yap. Global identifiability of differential models. *Commun. Pure Appl. Math.*, 73(9):1831–1879, 2020. https://onlinelibrary.wiley.com/doi/abs/10.1002/cpa.21921.

[45] AF Villaverde and JR Banga. Structural properties of dynamic systems biology models: Identifiability, reachability, and initial conditions. *Processes*, 5(2):29, 2017. https://doi.org/10.3390/pr5020029.

[46] Gemma Massonis, Julio R Banga, and Alejandro F Villaverde. Autorepar: a method to obtain identifiable and observable reparameterizations of dynamic models with mechanistic insights. *International Journal of Robust and Nonlinear Control*, 33(9):5039–5057, 2023.

[47] A Raue, C Kreutz, FJ Theis, and J Timmer. Joining forces of bayesian and frequentist methodology: a study for inference in the presence of non-identifiability. *Philos. Trans. R. Soc. A: Math. Phys. Eng. Sci.*, 371(1984):20110544, 2013. https://doi.org/10.1098/rsta.2011.0544.

[48] I Bancos, S Hahner, J Tomlinson, and W Arlt. Diagnosis and management of adrenal insufficiency. *Lancet Diabetes Endocrinol.*, 3(3):216–226, 2015. https://doi.org/10.1016/S2213-8587(14)70142-1.

[49] A Prete, AE Taylor, I Bancos, DJ Smith, MA Foster, S Kohler, V Fazal-Sanderson, J Komninos, DM O'Neil, DA Vassiliadi, et al. Response to letter to the editor:"prevention of adrenal crisis: cortisol response to major stress compared to stress dose hydrocortisone delivery". *The Journal of Clinical Endocrinology & Metabolism*, 106(1):e404–e406, 2021. https://doi.org/10.1210/clinem/dgaa712.

[50] PJ Wood. Disorders of the adrenal cortex. In *Scientific Foundations of Biochemistry in Clinical Practice*, pages 681–706. Elsevier, 1994.

[51] S Lee, HS Lim, HJ Shin, SA Kim, J Park, HC Kim, H Kim, HJ Kim, YT Kim, KR Lee, et al. Simultaneous determination of cortisol and cortisone from human serum by liquid chromatography-tandem mass spectrometry. *J. Anal. Methods Chem.*, 2014(1):787483, 2014.

[52] TJ Upton, E Zavala, P Methlie, O Kämpe, S Tsagarakis, M Øksnes, S Bensing, DA Vassiliadi, MA Grytaas, IR Botusan, et al. High-resolution daily profiles of tissue adrenal steroids by portable automated collection. *Science translational medicine*, 15(701):eadg8464, 2023.

[53] NK Singh, S Chung, A Chang, J Wang, and DA Hall. A non-invasive wearable stress patch for real-time cortisol monitoring using a pseudoknot-assisted aptamer. *Biosensors and Bioelectronics*, 227:115097, 2023.

[54] E Shchepakina, V Sobolev, and MP Mortell. *Singular Perturbations: Introduction to system order reduction methods with applications*, volume 2114. Springer, 2014.

[55] Aaron M Ellison. Bayesian inference in ecology. *Ecology letters*, 7(6):509–520, 2004.

[56] GE Backus. Bayesian inference in geomagnetism. *Geophysical Journal International*, 92(1):125–142, 1988.

[57] EJ Wagenmakers, J Love, M Marsman, T Jamil, A Ly, J Verhagen, R Selker, QF Gronau, D Dropmann, B Boutin, et al. Bayesian inference for psychology. part ii: Example applications with jasp. *Psychonomic bulletin & review*, 25:58–76, 2018.

[58] U Von Toussaint. Bayesian inference in physics. *Reviews of Modern Physics*, 83(3):943–999, 2011.

[59] EJ Wagenmakers, M Marsman, T Jamil, A Ly, J Verhagen, J Love, R Selker, QF Gronau, M Šmíra, S Epskamp, et al. Bayesian inference for psychology. part i: Theoretical advantages and practical ramifications. *Psychonomic bulletin & review*, 25:35–57, 2018.

[60] P Dellaportas and GO Roberts. An introduction to mcmc. In *Spatial statistics and computational methods*, pages 1–41. Springer, 2003.

[61] Stan Development Team. *Stan Modeling Language Users Guide and Reference Manual, Version 2.29*. 2019. `https://mc-stan.org`.

[62] B Carpenter, A Gelman, MD Hoffman, D Lee, B Goodrich, M Betancourt, M Brubaker, J Guo, P Li, and A Riddell. Stan: A probabilistic programming language. *J. Stat. Softw.*, 76(1), 2017. `https://doi.org/10.18637/jss.v076.i01`.

[63] Stan Development Team. *CmdStanPy, Version 0.9.76*. 2021. `https://pypi.org/project/cmdstanpy`.

[64] RM Neal. Mcmc using hamiltonian dynamics. In S Brooks, A Gelman, G Jones, and X Meng, editors, *Handbook of Markov Chain Monte Carlo*, pages 113–162. CRC Press LLC, 2011.

[65] M Betancourt. A conceptual introduction to hamiltonian monte carlo. *arXiv*, 2017. `https://doi.org/10.48550/ARXIV.1701.02434`.

[66] Prior choice recommendations. `https://github.com/stan-dev/stan/wiki/prior-choice-recommendations`, (accessed: 18.09.2024).

[67] NR Ging-Jehli. Setting reasonable priors for computational modeling. https://www.gingjehli.com/single-post/choosing-effective-samplers-and-setting-priors, (accessed: 18.09.2024).

[68] Ilia Ilmer. *Structural Identifiability Toolbox*. https://maple.cloud/app/6509768948056064, (accessed: 07.09.2024).

[69] Ilia Ilmer, Alexey Ovchinnikov, and Gleb Pogudin. Web-based structural identifiability analyzer. In *Computational Methods in Systems Biology: 19th International Conference, CMSB 2021, Bordeaux, France, September 22–24, 2021, Proceedings 19*, pages 254–265. Springer, 2021.

[70] J Melin, ZP Parra-Guillen, N Hartung, W Huisinga, RJ Ross, MJ Whitaker, and C Kloft. Predicting cortisol exposure from paediatric hydrocortisone formulation using a semi-mechanistic pharmacokinetic model established in healthy adults. *Clin. Pharmacokinet.*, 57(4):515–527, 2017. https://doi.org/10.1007/s40262-017-0575-8.